CHAPTER I

Introduction

1.1 Biogenic Volatile Organic Compounds

Biogenic volatile organic compounds (BVOCs or VOCs) account for more than 1,200 Tg yr^{-1} of emitted carbon in the atmosphere [Guenther et al., 1995, 2003], more than tenfold that of anthropogenic sources [Tsigaridis and Kanakidou, 2007; Heald et al., 2008]. Globally detected BVOC species include the highly reactive isoprene (C_5H_8), monoterpenes ($C_{10}H_{16}$), and sesquiterpenes ($C_{15}H_{32}$), which are hydrocarbons emitted in large quantities by vegetation [Kesselmeier and Staudt, 1996; Aschmann et al., 1998]. The reasons why vegetation emit so much of the carbon it expends considerable energy to fix through photosynthesis (~10% can be lost through BVOC emission [Peñuelas and Llusià, 2003; Chen and Cao, 2005]) remains elusive, although studies have shown that isoprene and monoterpene emission rates tend to increase with increasing temperature or other environmental stress stimuli including injuries, parasites, or atmospheric pollutants such as tropospheric ozone [Kesselmeier and Staudt, 1996]. Other BVOCs include alkanes, other alkenes, carbonyls, alcohols, esters, and acids although these are of minor importance compared to isoprene and monoterpenes in terms of total emissions and reactivity [Kesselmeier and Staudt, 1996; Atkinson and Arey, 2003].

Major constituent BVOCs commonly detected in North American air samples include isoprene and monoterpenes, such as α-pinene, β-pinene, camphene, 2-carene,

sabinene, Δ^3-carene, α-terpinene and d-limonene (Figure 1.1) [Apel et al., 2002; Wisthaler et al., 2001; Grossenbacher et al., 2005]. Ambient concentrations of BVOCs range from a few parts-per-trillion by volume (pptv) to several parts-per-billion by volume (ppbv) [Grossenbacher et al., 2005]. Each of the compounds in Figure 1.1 is characterized by a reactive olefinic double bond making it highly susceptible to oxidation in the atmosphere.
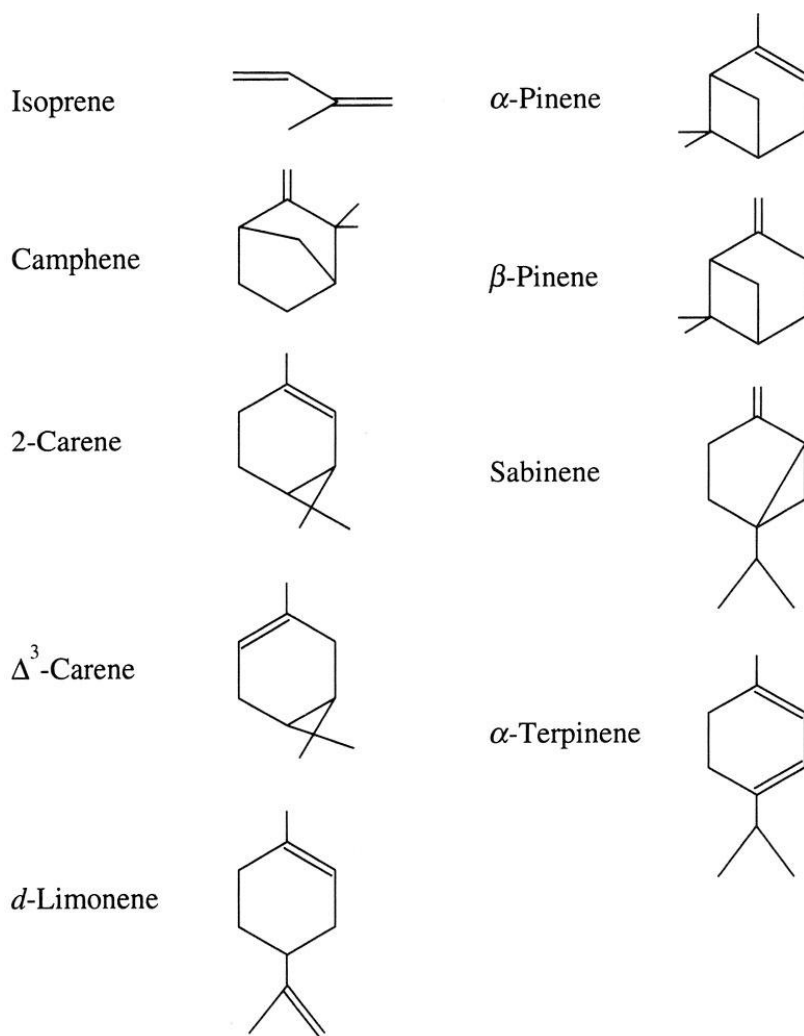

Isoprene

α-Pinene

Camphene

β-Pinene

2-Carene

Sabinene

Δ^3-Carene

α-Terpinene

d-Limonene

Figure 1.1: Molecular structures of common BVOCs emitted from vegetation.

Isoprene and monoterpenes account for over 50% of global BVOC emissions, with isoprene emitting at a rate of ~500 Tg yr^{-1} and monoterpenes emitting at a rate of

~127 Tg yr^{-1} [Guenther et al., 2003, 2006]. While not as dominant as isoprene in terms of total emissions, global α-pinene emissions of 50-60 Tg yr^{-1} [Guenther et al., 2003, 2006] are on the order of global anthropogenic hydrocarbon emissions [Isaksen and Hov, 1987]. In mid-latitude regions such as the Mediterranean and North America, α-pinene has been measured to significantly exceed isoprene [Kalabokas et al, 1997; Owen et al., 1997; Seufert et al., 1997]. When compared to isoprene, α-pinene has similar reactivity to the hydroxyl radical (OH) but higher reactivity to ozone (O_3) and nitrate (NO_3) radicals, making its reaction pathway significant in the accounting of tropospheric O_3 and NO_x ($NO_x = NO + NO_2$) [Atkinson and Arey, 2003]. The oxidation products of α-pinene, similar to isoprene, other monoterpenes, and sesquiterpenes, have recently been discovered to generate large amounts of secondary organic aerosols (SOA) in the atmosphere, which contributes to the global radiation budget [Andreae and Crutzen, 1997; Larsen et al., 2001; Librando and Tringali, 2005; Pathak et al., 2007; Steinbrecher et al., 2009].

Secondary organic aerosols differ from primary aerosols, which are directly emitted as liquids or solids from biomass burning, fossil fuel combustion, volcanic eruptions, and wind-driven uptake of a variety of materials. SOAs are formed via gas-to-particle phase conversion directly in the atmosphere or via condensation of gases onto existing particles [Monks et al., 2009]. Figure 1.2 shows the physical and chemical processing that affects both primary and secondary aerosols in the atmosphere. The most notable atmospheric impact of aerosols is a net negative radiative forcing to the Earth's atmosphere [Andreae and Crutzen, 1997]. Atmospheric SOA formation can increase cloud condensation nuclei (CCN) by a factor of more than 2 over the course of one day

[Lihavainene et al., 2003], increasing the amount of cloud droplets in the atmosphere, which acts to cool temperatures [Kerminen et al., 2005].
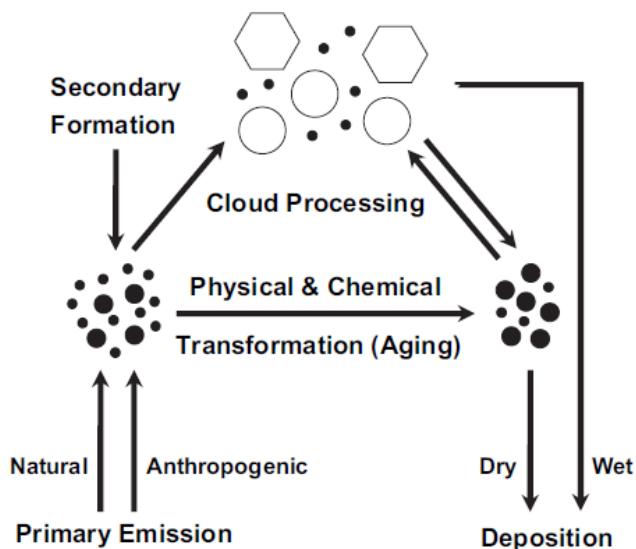

Figure 1.2: Biogenic and anthropogenic aerosols processing in the atmosphere [Fuzzi et al., 2006].

Estimates of global annual aerosol SOA production yields continue to be very uncertain, ranging from 13-24 Tg yr^{-1} [Griffin et al., 1999a] to 140-490 Tg yr^{-1} [Goldstein and Galbally, 2007]. SOA production can form through a variety of reaction pathways and the dominant formation channel is different for each BVOC. For example, SOA formed from the α-pinene ozonolysis process is very efficient, with the ratio of aerosol produced to precursor consumed as high as 0.67 in chamber studies [Hoffman et al., 1997]. The SOAs produced by ozonolysis contributes up to 80% of total SOA formation from α-pinene [Griffin et al., 1999a]. The detailed mechanism creating SOA precursors from monoterpenes continues to be largely unmapped and is an area of active research [Zhang et al., 1992; Hoffmann et al., 1997; Librando and Tringali, 2005; Pathak et al., 2007]. Kanakidou et al. [2000] estimated present day levels of annual biogenic SOA formation to be between 61–79 Tg yr^{-1}, compared to pre-industrial levels of between 17–

28 Tg yr^{-1}. Field observations and measurements of ambient air and particles have revealed a link between SOA formation and nucleation events to monoterpene oxidation [Kavouras et al., 1998; Yu et al., 1999]. Research to determine the as-yet unknown processes that lead to SOA formation from monoterpene oxidation chemistry will fill a current gap in the knowledge of climate forcing processes.

BVOCs are very active in the atmosphere, as shown in Figure 1.3, which depicts the sources, sinks, and wide variety of physical and chemical processes affecting these compounds in the troposphere. These compounds react with all major atmospheric radicals and halogens to form lower-volatility reaction products that can be transported horizontally into remote regions, vertically to the upper troposphere and across the tropopause into the stratosphere, or partition out of the gas phase to form SOA products. Eventually biological and deposition processes provide a sink for BVOC oxidation products to terminate its atmospheric reactions.
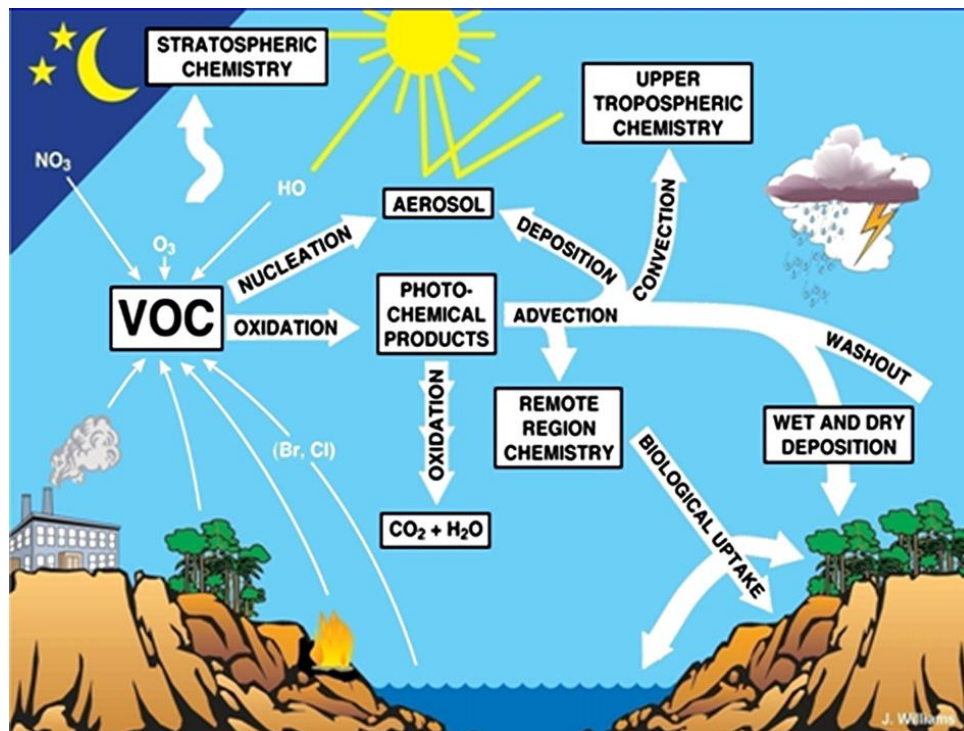

Figure 1.3: Schematic of BVOC processes in the atmosphere [Monks et al., 2009].

In the atmosphere BVOCs react mainly with OH, O_3, and NO_3 [Atkinson et al., 1997; Atkinson and Arey, 1998, 2003]. Rate constants obtained in laboratory studies of the oxidation of major BVOCs [Atkinson and Arey, 2003] show that reaction with OH is the most important pathway during the daytime when both OH and α-pinene concentration levels reach their daily maximum. Although absolute OH concentration is only a few tenths of a pptv at its highest levels, OH nonetheless determines the oxidation capacity of Earth's environment by rapidly reacting with virtually every important neutral species in the atmosphere [Crutzen, 1995]. OH radicals are produced when O_3 is photolyzed to produce O_2 and excited atomic oxygen $O(^1D)$ in Reaction (henceforth written as "R") 1.1a followed by $O(^1D)$ combining with water in R1.1d to form two OH radicals.

$$O_3 + h\upsilon \quad\quad \rightarrow \quad O_2 + O(^1D) \quad\quad\quad\quad (1.1a)$$

$$O(^1D) + M \quad\quad \rightarrow \quad O(^3P) + M \quad\quad\quad\quad (1.1b)$$

$$O(^3P) + O_2 + M \rightarrow \quad O_3 + M \quad\quad\quad\quad (1.1c)$$

$$O(^1D) + H_2O \quad \rightarrow \quad 2OH \quad\quad\quad\quad (1.1d)$$

$$O_3 + H_2O + M \quad \rightarrow \quad O_2 + 2OH + M \quad\quad\quad\quad (1.1e)$$

Approximately 90% of $O(^1D)$ is quenched in the regeneration of O_3 and approximately 10% of $O(^1D)$ survives quenching in R1.1b to react with water vapor in R1.1d to form OH radicals. The net reaction is that ozone photolyzes and reacts with H_2O to form two OH radicals (R1.1e). In polluted areas OH can also be produced via photolysis of nitrous acid (HONO) in R1.2 and hydrogen peroxide (H_2O_2) in R1.3.

$$HONO + h\upsilon \rightarrow OH + NO \quad\quad\quad\quad (1.2)$$

$$H_2O_2 + h\upsilon \quad \rightarrow 2OH \quad\quad\quad\quad (1.3)$$

OH quickly transforms a large number of tropospheric trace species into their oxidized forms, such as CO to CO_2, NO_2 to HNO_3, and SO_2 to H_2SO_4. While OH is the dominant reactive oxidant during the daylight hours, at night NO_3 is the major oxidant. NO_3 is formed from NO_2 reacting with O_3 in R1.4. NO_3 photolyzes quickly during the day but at night it is present in concentrations higher than OH [Wayne et al., 1991], although there have been reports of high nighttime OH concentrations above a forested site [Faloona et al., 2001] and the reactions of RO_2 and NO_3 have been postulated as an indirect source of OH at night [Vaughan et al., 2006].

$$NO_2 + O_3 \quad \rightarrow \quad NO_3 + O_2 \tag{1.4}$$

Ozone photolysis produces the OH radical through the net reaction R1.1e. Tropospheric ozone is primarily formed from NO_2 photolysis liberating $O(^3P)$ and combining with O_2 to create O_3 (R1.5a and R1.5b).

$$NO_2 + h\upsilon \quad \rightarrow \quad O(^3P) + NO \tag{1.5a}$$

$$O(^3P) + O_2 + M \quad \rightarrow \quad O_3 + M \tag{1.5b}$$

Another reactive oxidant in the atmosphere is HO_2. HO_2 is formed when atomic hydrogen and molecular oxygen react with a third body molecule M (R1.6) or when an alkoxy radical (RO) reacts with O_2 forming a carbonyl and HO_2 (R1.7)
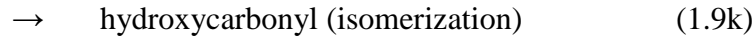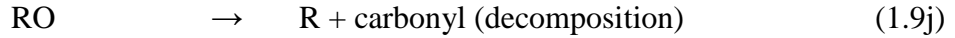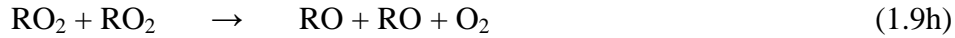
$$H + O_2 + M \quad \rightarrow \quad HO_2 + M \tag{1.6}$$

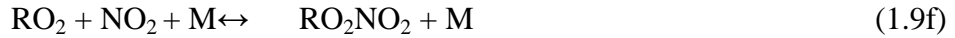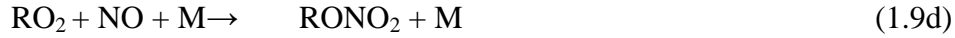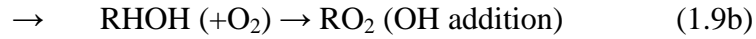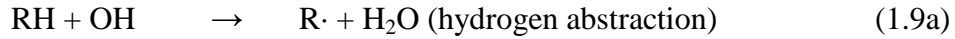$$RO + O_2 \quad \rightarrow \quad HO_2 + R_{-H}O \tag{1.7}$$

In the presence of HO_2 and NO_x, peroxy radicals can regenerate OH or be reduced to form an alkoxy radical and oxidize NO to NO_2 (reaction 1.8a and 1.8b). R1.8a and R1.8b both produce NO_2, which in turn can create O_3 through R1.5a and R1.5b.

$$HO_2 + NO \qquad \rightarrow \qquad OH + NO_2 \qquad\qquad (1.8a)$$

$$RO_2 + NO \qquad \rightarrow \qquad RO + NO_2 \qquad\qquad (1.8b)$$
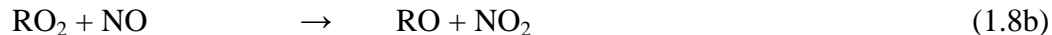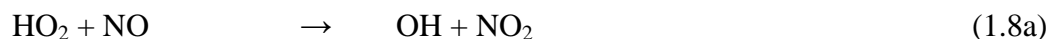
The detailed photochemical oxidation reaction mechanisms of monoterpenes such as α-pinene and β-pinene have not been studied as frequently as isoprene and, as a result, are much less well-understood. Previous laboratory studies of α-pinene oxidation products include those conducted by Aschmann et al. [2002], Arey et al., [1990], Hatakeyama et al. [1991], Grosjean et al. [1992], Hakola et al. [1994], Aschmann et al. [1998], Vinckier et al. [1998], Ruppert et al. [1999], Reissell et al. [1999], Nozière et al. [1999], Orlando et al. [2000]; van den Bergh et al. [2000], Larsen et al. [2001], Peeters et al. [2001], and Wisthaler et al. [2001]. The majority of these studies focused on the formation yields of one or more key α-pinene aldehyde and ketone products such as pinonaldehyde, formaldehyde, and acetone. Only Aschmann et al. [2002] and Nozière et al. [1999] presented total nitrate yields from α-pinene oxidation initiated by OH attack. Recent α-pinene oxidation experimental studies have focused on SOA production [Griffin et al., 1999a; Larsen et al., 2000; Iinuma et al, 2003; Pathak et al., 2007; Ma et al., 2008, 2009] from reactions with OH, O_3, and NO_3 radicals.

Several models have been developed to examine α-pinene oxidation reaction mechanisms in order to simulate previously published experimental results. Recent models include a quantum chemistry model utilizing quantitative structure-activity relationships combined with transition state theory calculations by Peeters et al. [2001], chemical mechanism models by Capouet et al. [2004] and Pinho et al. [2007], and hybrid chemical and particle gas-partitioning models for α-pinene SOA formation by Xia et al. [2008] and Chan et al. [2009].

A generalized mechanism for OH oxidation of BVOCs is shown in R1.9a-R1.9m.

$$RH + OH \quad \rightarrow \quad R\cdot + H_2O \text{ (hydrogen abstraction)} \quad (1.9a)$$

$$\rightarrow \quad RHOH \; (+O_2) \rightarrow RO_2 \text{ (OH addition)} \quad (1.9b)$$

$$R\cdot + O_2 \quad \rightarrow \quad RO_2 \quad (1.9c)$$

$$RO_2 + NO + M \rightarrow \quad RONO_2 + M \quad (1.9d)$$

$$\rightarrow \quad RO\cdot + NO_2 \quad (1.9e)$$

$$RO_2 + NO_2 + M \leftrightarrow \quad RO_2NO_2 + M \quad (1.9f)$$

$$RO_2 + HO_2 \quad \rightarrow \quad ROOH + O_2 \quad (1.9g)$$

$$RO_2 + RO_2 \quad \rightarrow \quad RO + RO + O_2 \quad (1.9h)$$

$$RO_2 + RO_2 + M \rightarrow \quad ROH \;\; + M \quad (1.9i)$$

$$RO \quad \rightarrow \quad R + \text{carbonyl (decomposition)} \quad (1.9j)$$

$$\rightarrow \quad \text{hydroxycarbonyl (isomerization)} \quad (1.9k)$$

$$NO_2 + h\upsilon \quad \rightarrow \quad NO + O(^1D) \quad (1.1l)$$

$$O(^1D) + O_2 + M \rightarrow \quad O_3 + M \quad (1.1m)$$

The mechanism of Reactions (R) 1.9a- 1.9k is schematically depicted in Figure 1.4.
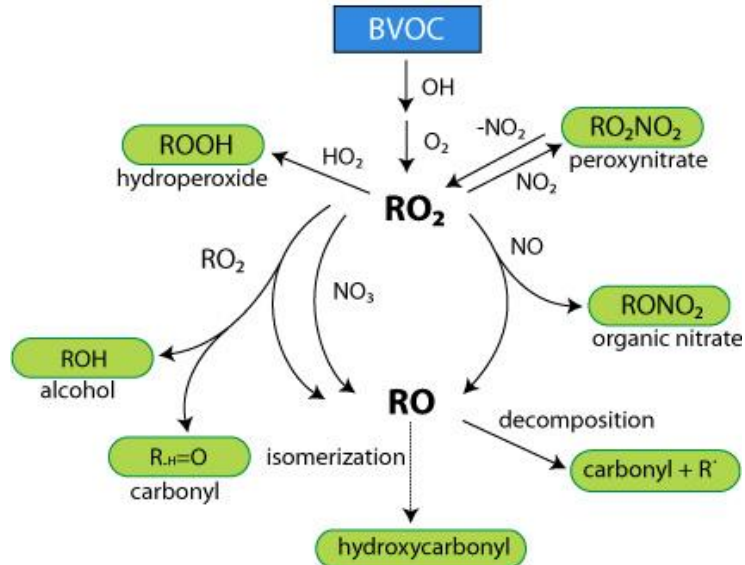

Figure 1.4: Simplified BVOC and OH reaction mechanism with NO_x [Adapted from Monks et al., 2009].

A BVOC (RH) reacting with OH undergoes either hydrogen abstraction or OH-addition across an olefinic double bond (if present). Both pathways can produce a radical that combines with O_2 to form a peroxy radical (RO_2). RO_2 can react with HO_2 form a hydroperoxide (ROOH) in R1.9g, react with another RO_2 to produce an alcohol or carbonyl in R1.9i, react with NO_3 to form RO and NO_2 in R1.9e, or react with NO to form an organic nitrate ($RONO_2$) in R1.9d or an alkoxy radical (RO) and NO_2 in R1.9e. In the presence of NO larger than 10-30 pptv, the peroxy radical reactions 1.9d and 1.9e dominate [Arey et al., 2001]. The reversible reaction 1.9f is not significant for monoterpenes from the results of experimental studies [Atkinson and Arey, 2003]. The production of $RONO_2$ in R1.9d sequesters NO_x and terminates further reactions that can lead to the formation of tropospheric O_3 (R1.9l and R1.9m). The formation of an organic nitrate in the reaction mechanism described above is often treated as an effective sink for NO_x. However, through thermal decomposition pathways and reactions with OH and other radicals, these nitrates can continue to participate in atmospheric reactions as has been suggested for isoprene nitrates [Paulson and Seinfeld, 1992; Horowitz et al., 2007]. Some 20-40% of isoprene nitrates are estimated to be lost via ozonolysis, indicating that the formation of a nitrate is not the absolute terminating step but a short- to long-term reservoir species for NO_x [Horowitz et al., 2007].

The general mechanism shown in R1.9a-R1.9k transforms a BVOC into a less volatile, water-soluble compound that can be removed either through possibly further chemical reactions, photolysis, decomposition, wet or dry deposition, or formation of a SOA [Monks et al., 2009]. One of the most important net results from the general degradation of a BVOC in the atmosphere is the formation of NO_2 that can then produce

tropospheric O_3 through R1.9l and R1.9m. Due to its participation in helping determine tropospheric ozone concentrations, the branching ratio that governs whether an NO_2 or $RONO_2$ is formed in reactions R1.9d and R1.9e is a key parameter in the oxidation reaction pathways of BVOCs.

Tropospheric O_3 impacts are felt most strongly through three major effects: 1) it is a significant input to the radiative forcing of Earth's atmosphere [Forster et al., IPCC AR4, 2007]; 2) it is a known plant phytotoxin and human health risk [Ashmore et al., 2005]; and 3) it is the main progenitor of hydroxyl (OH) radicals in the troposphere in unpolluted areas [Cape, 2009]. These factors and the high reactivity of the O_3 molecule make detailed accounting of the total sources, sinks and reaction pathways of tropospheric O_3 from atmospheric processing of BVOCs very important.

1.2 Tropospheric ozone

Ozone is present in both the troposphere and the stratosphere of Earth's lower atmosphere. The distribution of ozone is uneven, with 90% of global O_3 concentration located in the stratosphere while the remaining 10% is in the troposphere [Crutzen, 1995]. In the stratosphere incoming solar UV radiation produces O_3 from molecular oxygen (R1.10a and R1.10b) to $O(^3P)$. $O(^3P)$ can undergo a three body reaction with molecular oxygen and a third molecule M (usually N_2 or another O_2) to form O_3 [Chapman, 1930].

$$O_2 + h\upsilon \ (175nm < \lambda < 242nm) \rightarrow O(^3P) \qquad (1.10a)$$

$$O(^3P) + O_2 + M \rightarrow O_3 + M \qquad (1.10b)$$
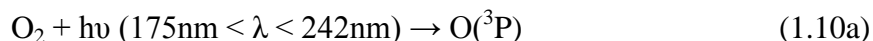
O_3 in the stratosphere filters harmful UV radiation and absorbs incoming solar radiation to warm the Earth's atmosphere. Tropospheric O_3, on the other hand, is a

component of photochemical smog and its presence can be harmful to vegetation due to damage to leaves and reduced photosynthesis rates [Karnosky et al., 2007]. Figure 1.5 shows major ozone reaction pathways, sources and sinks in the Earth's lower atmosphere.
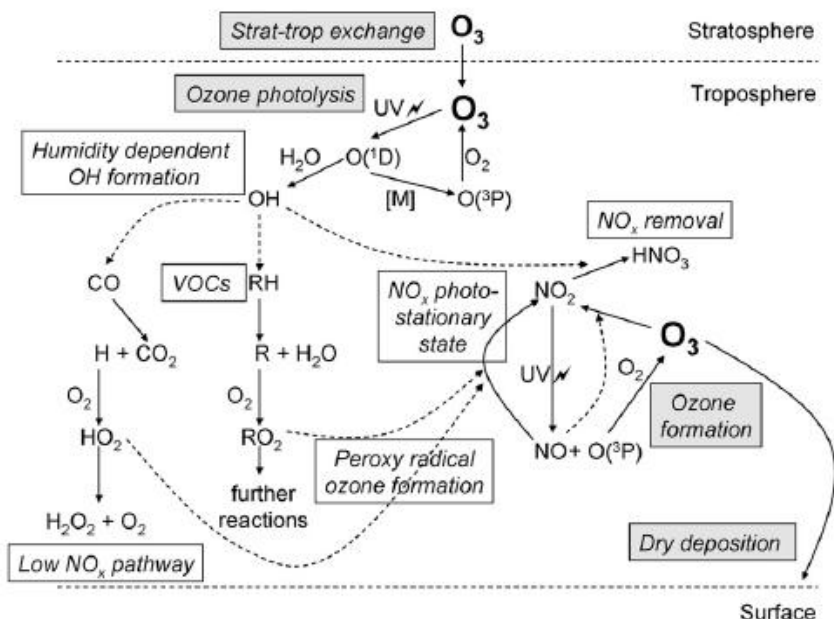

Figure 1.5: Major reaction pathways of ozone in the lower atmosphere including major sources and sinks [Cape, 2008].

Ozone can be transported from the stratosphere into the troposphere by a stratosphere-troposphere exchange (STE) process [Olsen et al., 2007]. The stratospheric source of tropospheric ozone contributes an estimated 550 ± 170 Tg yr^{-1} while photochemical tropospheric ozone source contributes 5100 ± 600 Tg yr^{-1} [Stevenson et al., 2006], with annual variability showing the ozone flux into the troposphere to be highest during the March-July period [Olsen et al., 2004]. Current global background levels of tropospheric ozone range between 20-45 ppbv in the northern hemisphere [Vingarzan, 2004] compared to peak values of 100-400 ppbv in urban areas [Kley et al., 1999].

Tropospheric ozone is known to be harmful crops and vegetation above a threshold concentration of 40ppbv [Fuhrer et al., 1997; Mauzerall and Wang, 2001].

Background ozone levels in the troposphere, the concentration attributable to anthropogenic activities, have risen steadily in the past 30 years by a rate of 0.5-2% per year [Vingarzan, 2004]. Models using current data and projecting backwards suggest that the tropospheric burden of ozone has increased by 40-65% since preindustrial times [Mickley et al., 2001; Shindell et al., 2003; Lamarque et al., 2005; Horowitz, 2006].

Models predicting future tropospheric ozone response to climate change scenarios generally show increases in the emissions of O_3 precursors globally, which could lead to ozone levels that would significantly affect natural vegetation and crop yields [Stevenson et al., 2000, 2006; Cape, 2009]. However, great variability remains in the model results. Increases from 0-9ppb of the daily maximum 8-hour average of O_3 concentrations have been reported in simulated responses to climate change scenarios [Dawson et al., 2007; Hogrefe et al., 2004; Racherla and Adams, 2006; Zhang et al., 2008; Ito et al., 2009]. Wu et al. [2008] speculated that inclusion of isoprene and other BVOC chemistry could account for most of the difference in model responses projecting O_3 production increase due to temperature rise.

Figure 1.6 shows model results for global tropospheric ozone in years 1860, 2000, and a predictive model for the year 2100 [Horowitz, 2006]. The global increase in background ozone concentrations is particularly marked in areas around dense urban population centers with high NO_x concentrations and the surrounding regions where prevailing geostrophic winds transport polluted air masses to remote areas. The predicted future ozone concentrations in 2100 could increase by up to 42% relative to 2000 levels due to projected increases in NO_x emissions and land-use changes [Horowitz, 2006].
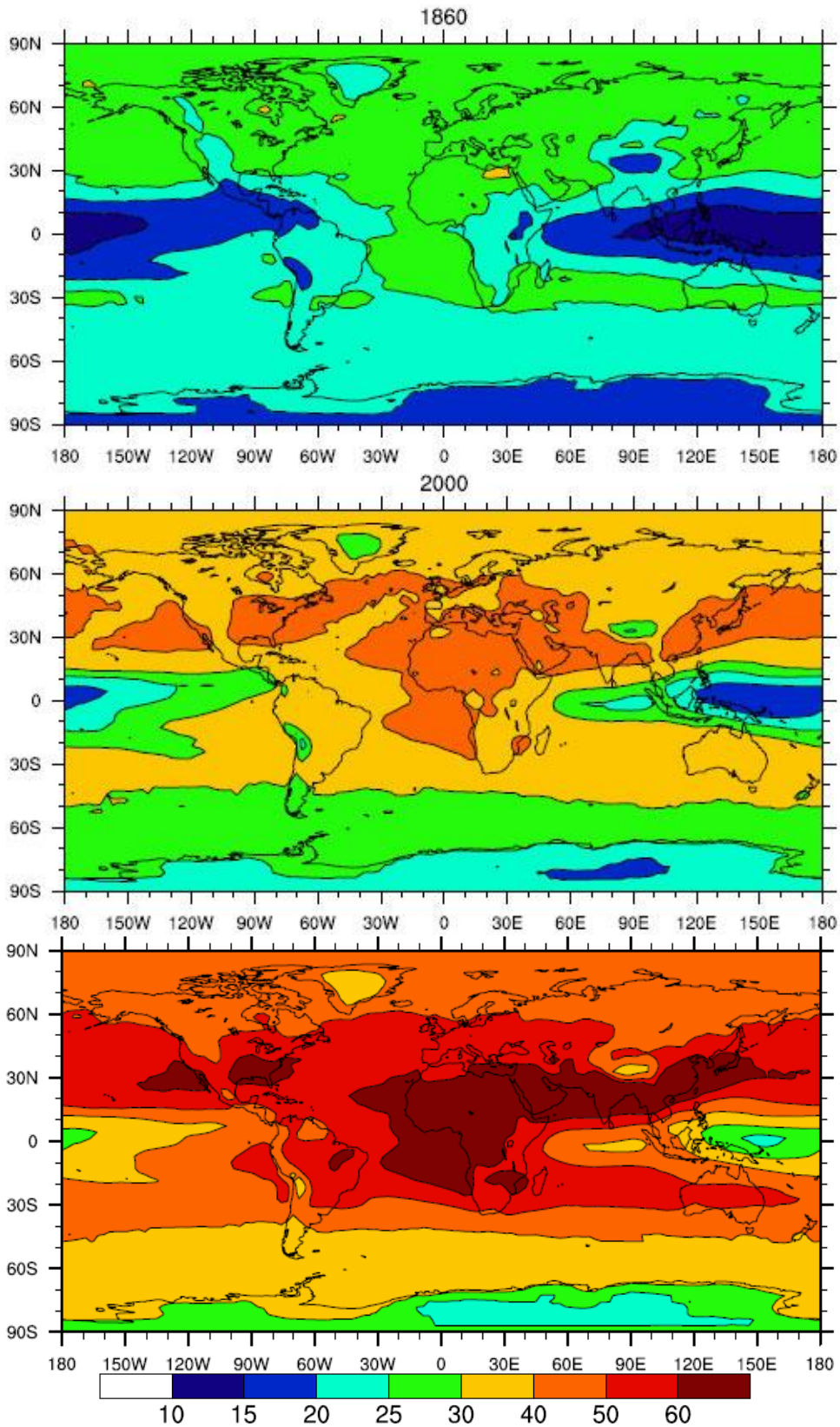
Figure 1.6: Simulated tropospheric ozone concentration for year 1860 (top), year 2000 (center), and year 2100 (bottom) [Horowitz, 2006].

Ito et al. [2009] introduced isoprene nitrate chemistry in a global modeling study that studied O_3 sensitivity to NO_x reactions in isoprene oxidation chemistry. An assumption was made in the model that isoprene hydroxynitrates continued to react and returned NO_x with 40% efficiency back into the atmosphere (known as "NO_x recycling") as estimated by Horowitz et al. [2007]. The results of this study showed that ozone levels may increase by as much as 7ppbv on a regional scale attributable to the inclusion of isoprene nitrate chemistry alone. Ozone sensitivity to isoprene nitrate chemistry from the study is shown in Figure 1.7 as green enhancements on the world map.
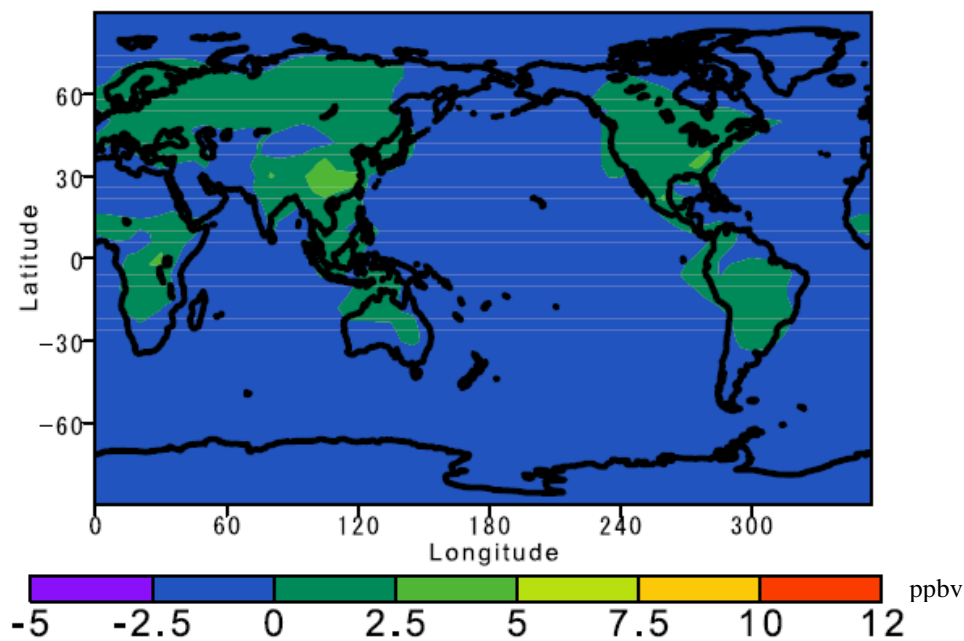
Figure 1.7: Enhancement of surface ozone due to isoprene nitrate chemistry assuming a 5°K increase in temperature and 40% NO_x recycling efficiency [Ito et al., 2009].

With isoprene nitrate chemistry showing significant regional impact on tropospheric ozone concentrations in Figure 1.7, including α-pinene nitrate chemistry and other monoterpene nitrate chemistry in global chemistry models is a logical next step. The longevity of α-pinene nitrate products, with atmospheric lifetimes of 1-2 days, allows

it to participate in regional transport processes and recycle sequestered NO_x back into the atmosphere to form tropospheric ozone. More research is needed for quantitative determination of reaction products and formation yields of nitrate species from a variety of BVOC species.

Tropospheric ozone is a component of smog and it also has direct impact on the climate as a greenhouse gas affecting radiative forcing in the Earth's atmosphere. Measured in units of Watts·m^{-2}, radiative forcing is a quantitative indicator of the perturbation of the energy in the sun-Earth atmosphere system. It can be a positive or negative quantity manifesting in temperature increase or decrease depending on the source of the forcing [Hofmann et al., 2006]. This quantity is frequently used for comparisons between the effects different human and natural agents have in perturbing the Earth's atmospheric energy budget [Forster et al., IPCC AR4 2007]. The production of aerosols is an example of a net negative perturbation leading to lower temperatures while the increase in compounds such as carbon dioxide (CO_2), methane (CH_4), nitrous oxide (N_2O), halocarbons, sulfur hexafluoride (SF_6), and other greenhouse gases are a net positive perturbation, which can increase the surface temperature of Earth.

The increase in greenhouse gas emissions due to industrial activity is estimated to have increased the net radiative forcing of the Earth's atmosphere by +1.6 [+1.0,-0.8] W·m^{-2} [Forster et al., IPCC AR4 2007]. Joos and Spahni [2008] showed rates of change in CO_2, CH_4, N_2O, and other greenhouse gas forcing in the twentieth century that were an order of magnitude or greater higher than during the past 20,000 years. Figure 1.8 shows the change in radiative forcing of Earth's atmosphere between the years 1750 and 2005. Radiative forcing due to tropospheric ozone is several times higher than that of

16

stratospheric ozone despite stratospheric ozone being an order of magnitude higher in global concentration [Forster et al., IPCC AR4 2007]. Increases in tropospheric ozone in the past three decades have been estimated to have caused an additional 0.3 - 0.6 W·m^{-2} of forcing [Forster et al., IPCC AR4 2007], with average levels of tropospheric O_3 having increased by 0.26 ppbv y^{-1} between 1988 and 2003 in North America [Jaffe et al., 2003; Jaffe and Ray, 2007].
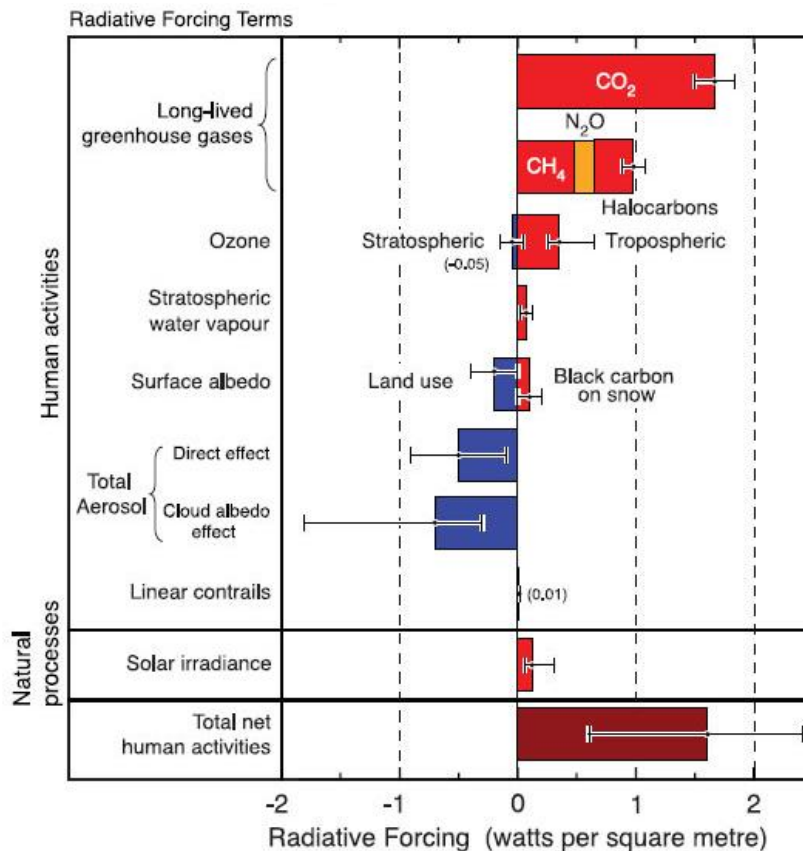

Figure 1.8: The change in radiative forcing terms from year 1750 to year 2005 [Forster et al., IPCC AR4 2007].

Contributions to radiative forcing from SOAs formed from oxidation products of BVOCs remain uncertain due to the large range in the estimated production of SOAs worldwide. The potential effects of climate change on isoprene and monoterpene

17

emissions have garnered increasing attention due to the many implications for altering

SOA and tropospheric ozone production [Steiner et al., 2006; Liao et al., 2009].

1.3 Organic Nitrates

Peroxy radical (RO_2) species originating from the OH-initiated oxidation of

BVOCs react predominantly with NO through R1.9d and R1.9e. The organic nitrate

$RONO_2$ formed from R1.9d serves as a reservoir of NO_x in the atmosphere. While often

treated as a terminating step in the oxidation pathway, it is likely that significant NO_x

recycling occurs [Horowitz et al., 2007; Monks et al., 2009] through further reactions

with OH and other radicals as well as thermal decomposition and other loss processes.

For every $RONO_2$ created, the chemical reaction pathway 1.9a-1.9k consumes NO and

does not form NO_2, which could otherwise participate in O_3 production. This makes O_3

concentrations sensitive to the formation of $RONO_2$ nitrates. While organic nitrates can

also be produced from NO_3 or O_3 reactions with alkenes, the results of this research

presents only the OH-initiated first generation organic nitrates because OH reactions are

the most important reaction pathway for monoterpenes.

RO_2 can react with NO to form an unstable peroxy nitrite intermediate [ROONO]

that decomposes into NO_2 and RO (R1.10b) or, less often, will de-radicalize and form a

stable organic nitrate (R1.10a) [Atkinson et al., 1982].

$$RO_2 \cdot \ + \ NO + M \ \rightarrow \quad [ROONO] + M \qquad\qquad (1.10a)$$

$$[ROONO] \quad \rightarrow \quad RO \cdot + NO_2 \qquad\qquad (1.10b)$$

$$\rightarrow \quad RONO_2 \qquad\qquad (1.10c)$$

The branching ratio "α" (calculated as $k_{1.10c}/(k_{1.10b}+k_{1.10c})$) determines the fraction

of [ROONO] molecules that produces $RONO_2$ rather than decomposes into an alkoxy

radical RO and NO_2. To experimentally determine the branching ratio, the yield of $RONO_2$ is divided by the fraction of the time its precursor RO_2 radical is produced from OH reactions with α-pinene. Organic nitrate branching ratios have been known to increase with increasing carbon number [Carter and Atkinson, 1989; Jenkin et al., 1997; O'Brien et al., 1998; Arey et al., 2001; Zhang et al., 2004]. This is related to the increased modes available in larger compounds to diffuse energy away from the critical dissociative vibrational mode [Shepson, 2007]. Branching ratios for smaller C_1-C_3 alkyl and alkene nitrates have been measured [O'Brien et al., 1998; Arey et al., 2001] as well as larger C_8-C_{12} n-alkenes [Matsunaga and Ziemann, 2009] and cyclic aromatic compounds [Espada and Shepson, 2005]. Quantum chemistry model predictions of alkyl and alkene nitrate branching ratios have also been reported [Barker et al., 2003; Zhang et al., 2004].

Besides its impact on NO_x and tropospheric ozone, alkyl and alkene nitrate compounds have long been suspected of being the major source of "missing NOy" [Fahey et al., 1986; Day et al., 2003; Williams, 2004]. NO_y ($NO_y = NO_X + HNO_3 + PAN + HONO + HO_2NO_2 + NO_3 + 2N_2O_5 +$ particulate nitrate NO_3^-) or "odd nitrogen", consists of all NO_x and NO_z (NO_y - NO_x) species. When the sum of individual NO_y species does not match total NO_y measurements this shortfall is considered "missing" NO_y. Day et al. [2003] found total large abundances of alkyl nitrates in three locations accounting for 10-20% of NO_y. These organic nitrates could constitute a large part of the missing NO_y first noted by Fahey et al. [1986].
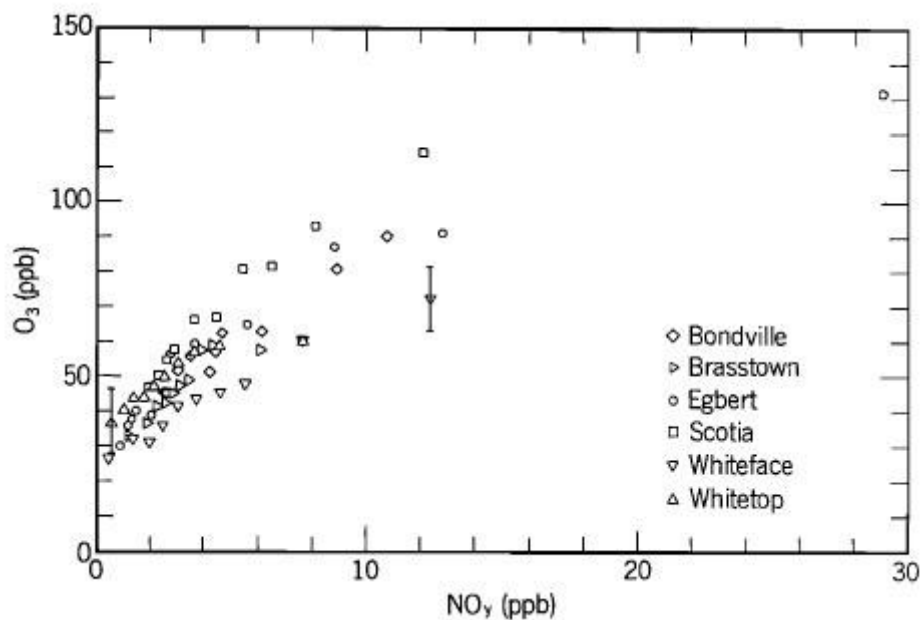
Figure 1.9: The relationship between NO_y and O_3 from six North American sites in the summer of 1988 [Trainer et al., 1993].

Finding and identifying the missing NO_y species is essential because of its direct relationship to tropospheric O_3. Figure 1.9 shows the relationship of O_3 and NO_y concentrations for six rural sites in North America in the summer of 1988 [Trainer et al., 1993]. The positive linear correlation between O_3 and NO_y concentrations is expected since NO_y includes NO_x, which is the catalyst in photochemical O_3 production.

In measurements of total reactive nitrogen and reactive nitrogen species at a rural forest site, Horii et al. [2006] found no missing NO_y in unpolluted air masses although in polluted air masses the concentration of the total reactive nitrogen species fell short of total NO_y. The deposition velocity measured the concentration of the reactive nitrogen shortfall species were consistent with measured amounts of total alkyl and hydroxynitrates, suggesting the missing NO_y is largely caused by anthropogenic NO_x emissions increasing nitrate formation in BVOC oxidation.

Among monoterpene BVOCs, α-pinene accounts for ~45% of global emissions annually, making it by far the dominant monoterpene in the atmosphere [Seinfeld and Pankow, 2003; Lathiere et al., 2005]. During OH-initiated reactions, α-pinene organic nitrates such as β-hydroxynitrates can be formed following the generalized reaction mechanism of R1.9a - R1.9k. Due to the presence of the olefinic double bond on the alkene, OH is calculated to add across the double bond ~95% of the time and undergo hydrogen abstraction ~5% of the time (Appendix A).

Previous experimental studies of α-pinene hydroxynitrates included Aschmann et al. [2002] and Nozière et al [1999]. Aschmann et al. [2002] used API-MS to detect the presence of β-hydroxynitrate (MW 215), dihydroxynitrates (MW 231), and dihydrocarbonyl products (MW 184) in chamber studies of α-pinene undergoing OH-initiated oxidation in the presence of NO. Nozière et al. [1999] studied α-pinene β-hydroxynitrates as part of a larger α-pinene and OH reaction experiment that measured total hydroxynitrate concentrations without individual speciation.

To date only two sets of published experimental results [Nozière et al., 1999; Aschmann et al., 2002] present total yields of α-pinene nitrates. Unfortunately the data from the studies are considerably divergent with no overlap - necessitating further experimental study of the reaction mechanism for α-pinene nitrate formation. The dearth of experimental α-pinene nitrate studies can largely be attributed to the difficulty in identifying these compounds due to the lack of commercial standards available for calibration. Studies of C_2-C_4 alkene hydroxynitrates (formed from OH addition reaction pathway) [Muthuramu et al., 1993; Shepson et al., 1996] have discussed the adsorptive nature of alkene hydroxynitrates due to their low volatility and high Henry's Law

constants. The much larger mass (C_{10}) α-pinene hydroxynitrate presents significant challenges for instrumental detection, requiring very specific instrument conditioning routines and starting conditions for successful laboratory analysis. These hydroxynitrates have yet to be detected in ambient air, although they have been detected in chamber experiments of α-pinene reactions with OH in the presence of NO_x [Aschmann et al., 1998, 2002; Nozière et al., 1999].

In this thesis Chapter 2 discusses the first successful synthesis of an authentic α-pinene hydroxynitrate reference standard ("authentic" refers to a standard that does not use a proxy compound) and the various analytical methods used to help identify the target α-pinene hydroxynitrates within the synthesis mixture. Chapter 3 discusses the first known effort to identify and quantify the yields and RO_2+NO branching ratios of individual first generation hydroxynitrates produced from α-pinene and OH-oxidation in the presence of NO_x. Chapter 4 discusses the chemical model created to describe and reproduce the experimental conditions incorporating RO_2+NO branching ratios from the experimental results into the reaction rate constant. Chapter 5 discusses the investigation of GCxGC (or "two-dimensional" chromatography) as a candidate for an alternative analysis technique in photochemical chamber experiments.

1.4 GCxGC Comprehensive Two-dimensional Chromatography

Current measurement instruments used to detect and quantify alkyl nitrates in the gas phase include gas chromatography – flame ionization detector (GC-FID), gas chromatography – mass spectrometer (GC-MS) [Atkinson et al., 1982; Aschmann et al., 2001], Fourier transform infrared spectroscopy (FTIR) [Tuazon and Atkinson, 1990; Nozière et al., 1999], and gas chromatography – electron capture detector (GC-ECD)

[Atlas, 1988; O'Brien et al., 1998; Giacopelli et al., 2005]. The FTIR technique gives total nitrate concentrations but it does not allow the identification of the possible types or numbers of nitrate products in the sample. Gas chromatography (GC) methods are well-established and have low pptv limits of detection although significant challenges remain in analyte identification and complex sample separation.

The large number of compounds typically found in laboratory and ambient air samples makes traditional GC analysis very challenging. There is a high probability of chromatography peak overlap or coelution in complex mixtures, making identification and quantification difficult during data analysis [Davis and Giddings, 1983]. A recent development in GC technology is the invention of comprehensive two-dimensional gas chromatograph (or "GCxGC"), which separates a sample with two analytical columns in series with different stationary phase coatings designed to separate via physical and chemical properties such as boiling point and polarity [Liu and Philips, 1991]. The chromatogram of a GCxGC is presented in a two-dimensional plane rather than a one-dimensional trace as is the case in traditional GC methods. The extra separation axis allows coeluting peaks the opportunity to separate via a property "orthogonal", or independent, to the first column, increasing the probability of complete separation.

In Chapter 5 a benchtop GCxGC instrument with a novel solid-state thermal modulator component was used in laboratory studies of α-pinene hydroxynitrates. A thermal modulator component placed in between the first and second column helps trap and then reinjects small plugs of analyte emerging from the end of the first column into the second column. A model of the heat transfer and heating profile of the thermal modulator using Indium as the heat-transfer material is presented. The initial results

support further development of this technique for possible use in sample separation, identification and quantification of complex gas phase mixtures in future laboratory and ambient applications.

1.5 Research Objectives

The results of four major research efforts are reported in this dissertation: 1) synthesis and analysis of an α-pinene β-hydroxynitrate standard; 2) detailed photochemical reaction chamber experiments to identify and speciate first-generation α-pinene nitrates produced from α-pinene OH-oxidation in the presence of NO_x; 3) creation of a chemical model to simulate the photochemical chamber experiments and compare the results to observational data to enhance understanding of the α-pinene β-hydroxynitrate formation mechanism; and 4) evaluation of comprehensive GCxGC gas chromatography method as a possible new analysis technique for atmospheric nitrate experiments.

To complete these research objectives, α-pinene nitrates were first synthesized by reacting α-pinene epoxide with nitric acid using a procedure adapted from Muthuramu et al. [1993], Lockwood [2008 doctoral dissertation], and Nichols et al. [1953]. Confirmation of the synthesized organic nitrate products was carried out with silica gel-plate separation, high-performance liquid chromatography, GC-MS, and GC-ECD. A series of photochemical reaction chamber experiments were carried out with high initial concentrations of NO and α-pinene. Analysis of the experimental data produced measured formation yields and branching ratios of α-pinene nitrates. A chemistry model was then created and the model results were compared with the experimental data.

Lastly, some preliminary work testing a novel solid-state thermal modulator in a comprehensive two-dimensional gas chromatograph is presented in the context of its efficacy in separating compounds in an α-pinene OH-oxidation experiment.

CHAPTER II

α-Pinene Hydroxynitrate Synthesis and Identification

2.1 *α-Pinene hydroxynitrate synthesis*

An authentic standard for gas chromatography peak identification and elution
time comparison was required to identify α-pinene β-hydroxynitrates (shortened to
"hydroxynitrates", "nitrates", or "APNs") in photochemical reaction chamber
experiments. Due to the lack of commercial availability, APNs were synthesized in the
laboratory using organic synthesis procedures established by Muthuramu et al. [1993],
Lockwood [2008 doctoral dissertation], and based on work originating from Nichols et al.
[1953]. The synthesis process reacted α-pinene epoxide (97% Sigma Aldrich) with high-
purity fuming nitric acid (>90% Sigma-Aldrich) to form α-pinene β-hydroxynitrates. The
molecular structure of α-pinene epoxide ($C_{10}H_{16}O$) is schematically shown in Figure 2.1.
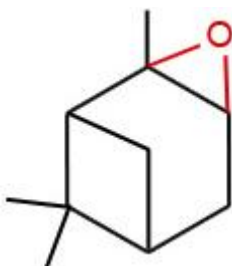
Figure 2.1: α-Pinene epoxide molecular structure.

In the α-pinene epoxide molecule, instead of a double bond across the 1,2 carbon
positions, as in the case of an α-pinene molecule, the presence of an oxygen atom creates

ring strain and polarity conditions dynamically favorable for the addition of a functional

group such as a nitrate (NO_3^-).

The synthesis reaction proceeds as shown in R 2.1.

$$C_{10}H_{16}O + HNO_3 \rightarrow C_{10}H_{16}OH^+ + NO_3^- \rightarrow HOC_{10}H_{16}ONO_2 \qquad (2.1)$$
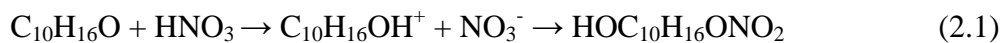
The α-pinene epoxide molecule was protonated to form $C_{10}H_{15}OH^+$, which led to

α-cleaving at the 1-carbon position followed by NO_3^- addition to the 2-carbon position to

form a hydroxynitrate (Figure 2.2b). An isomer could also be formed with α-cleaving of

the 2-carbon position followed by NO_3^- addition to the 1-carbon position (Figure 2.2a).

27
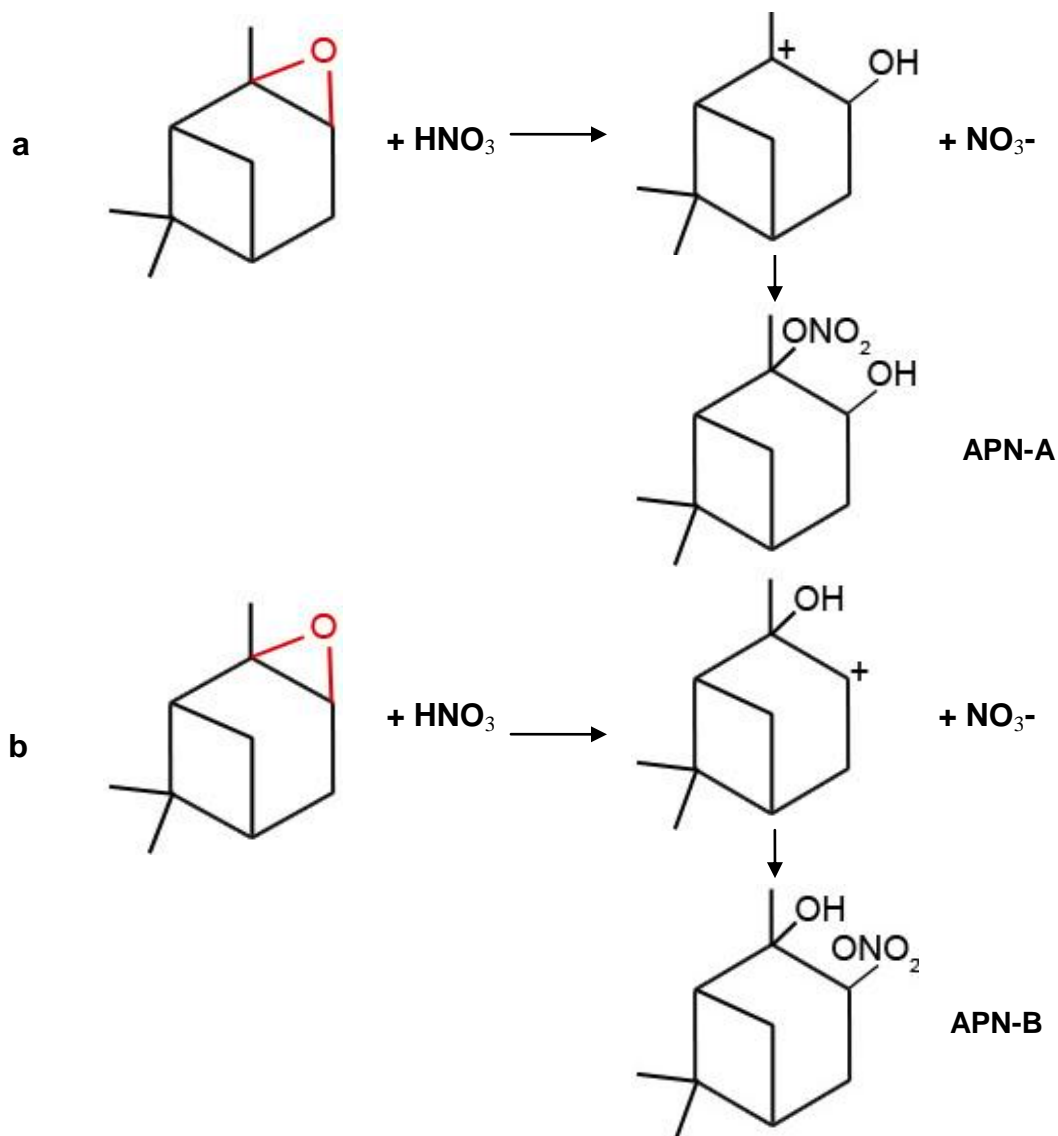
Figure 2.2: Formation of the hydroxynitrate isomers APN-A and APN-B via reaction of α-pinene epoxide with fuming nitric acid through protonation at the 1-carbon (a) or 2-carbon site (b) and addition of NO_3^-.
The structural asymmetry of the α-pinene epoxide molecule affects the synthesis

yields of the nitrate isomers. The cation of the first nitrate isomer (APN-A) precursor is

on a tertiary carbon, while the cation of the second nitrate isomer (APN-B) precursor is

on a secondary carbon. The protonated precursor of APN-B is as a result less stable than

APN-A and it is expected that a greater quantity of APN-A would form versus APN-B in

the synthesis process.

APNs can form through many different pathways including NO_3 addition,

ozonolysis, as well as OH-addition to the double-bond. In the synthesis process, due to

the presence of the oxygen across the 1,2 position and the absence of water or other

oxygen sources, the protonation step can only occur at the 1,2 site on the epoxide

molecule, leading to the formation of the two APNs isomers. In addition, the molecular

orientation of the OH and ONO_2 functional groups allows the formation of

conformational isomers (conformers). The possibility of multiple nitrates (counting all

conformers) in the mixture will be explored in the section on dipole moment calculations.

Model-based calculations of α-pinene OH-oxidation products have shown that the

four-membered ring in α-pinene is a destabilizing presence for the APN-A RO· precursor

[Vereecken and Peeters, 2000]. Rearrangement of the OH + α-pinene adduct precursor of

APN-A to break the four-membered ring to form an internal double bond was found to be

energetically favorable. The energy barrier associated with the breaking of the four-

membered ring and formation of an internal double bond was calculated to have a lower

energy barrier height than if the ring-breaking process had not occurred [Vereecken and

Peeters, 2000]. This rearrangement mechanism then leads to the formation of another

nitrate isomer, which, following the naming conventions presented in this thesis, is

referred to as APN-C [Dibble, 2000]. The molecular structure and formation pathway of
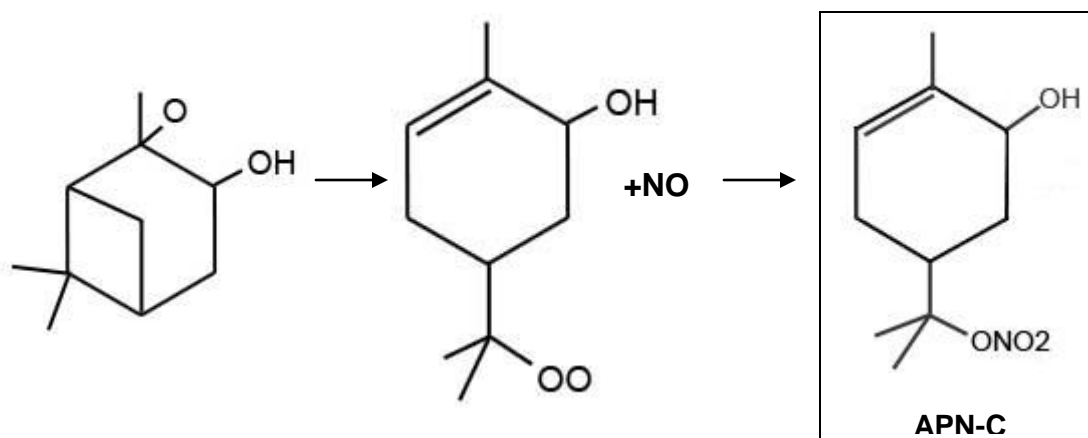
APN-C is shown in Figure 2.3.

Figure 2.3: Ring-breaking of the APN-A ROOH precursor forms an internal double bond and leads to reaction with NO forming APN-C.

2.1.1 Detailed synthesis

The following procedure was conducted with the room in semi-darkness due to

the sensitivity of organic nitrates to photo-decomposition. A "stock" sample of α-pinene

epoxide was diluted in cyclohexane (Sigma-Aldrich, anhydrous 99%) to 0.034M. 50mL

of the diluted starting material was typically sufficient for the synthesis process. This

starting material was transferred into an aluminum-foil-wrapped 250mL 3-neck round-

bottom flask placed in a bath of chilled water held to 15°C. Nitrogen gas (Praxair, UHP

5.0) purged the flask to reduce the condensation of water, atmospheric oxygen and

introduction of other contaminants during synthesis. A thermometer was inserted to

monitor the reaction temperature and a stir bar was added to the glass bulb to mix the

solution during the reaction. To initialize the synthesis process, nitric acid was added to

the diluted α-pinene epoxide solution mixed to a molar ratio of 1.2:1. The excess nitric acid in the solution helped to fully react with the epoxide. The monitoring of the appearance of reaction products with thin layer chromatography silica gel separations (detailed in Section 2.2.1) performed every 10 minutes during the synthesis process confirmed that the epoxide starting material was consumed after thirty minutes. After the synthesis was completed, the solution was transferred out of the round-bottom flask and into a clean amber bottle. A steady flow of dry nitrogen air flowing at ~3mL min^{-1} was blown over the solution to evaporate some of the cyclohexane and concentrate the nitrate material in the amber bottle.

To remove the excess HNO_3 from the synthesis mixture, the solution was washed once with ultrapure water. The water was then separated from the nitrate mixture using a separation funnel. After the ultrapure water wash and separation step, the synthesis solution was placed back into a clean amber glass bottle and refrigerated in a freezer to avoid photo-decomposition and evaporation.

The synthesized material was analyzed daily with a GC-ECD and less frequently with a GC-MS. The synthesized nitrates underwent both GC-MS and GC-ECD analyses to identify the synthesis compounds as well as the peak elution temperature. Fresh APN solutions were resynthesized every three months to avoid sample degradation.

2.2   α-Pinene Hydroxynitrate Identification

In addition to the GC-ECD and GC-MS analyses mentioned above, six other independent methods were used to assist in identifying the APNs in the synthesis solution. Thin layer chromatography (TLC), high-performance liquid chromatograph (HPLC), GC-MS (operating in negative-mode chemical ionization) chromatograms and

mass spectra, GC-ECD correlation to GC-MS data, photochemical reaction chamber experiments, Gaussian dipole moment calculations, and chemical modeling were the methods used to help isolate and identify the nitrates produced in the synthesis mixture and in the photochemical reaction chamber experiments.

2.2.1   TLC silica gel separation analysis

The time required for completion of the APN synthesis reaction was determined empirically by using thin layer chromatography (TLC) on a polar, glass-backed silica gel adsorbent layer (Sorbent Technologies UV 254 glass-backed, 250μm silica gel thickness) as the stationary phase. Every 10 minutes during the synthesis process, 6 drops taken from the synthesis mixture were carefully applied to a single point on a silica gel TLC plate alongside 6 drops of the diluted α-pinene epoxide. A photograph of the result from a TLC plate test is shown in Figure 2.4. The white line drawn down the middle of the plate is a demarcation between the unreacted material and the synthesized material.
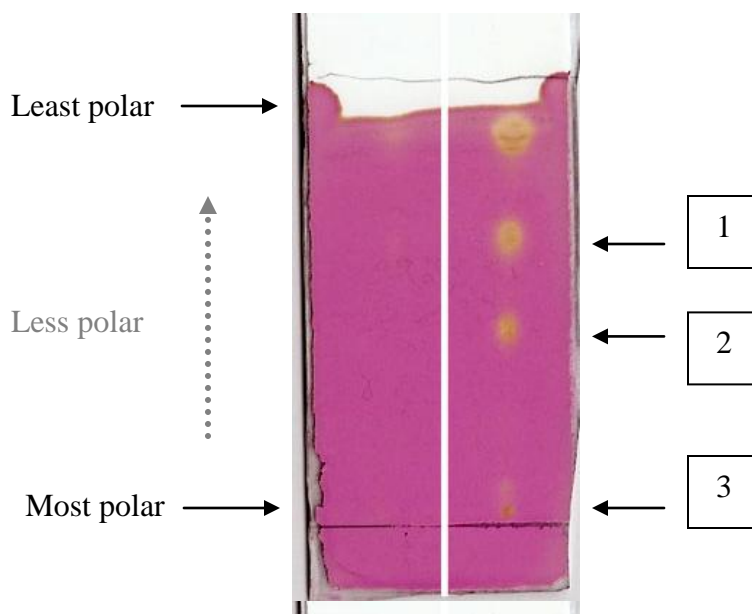
Figure 2.4: TLC silica gel plate separation of the unreacted starting material (left) and the synthesized APNs (right).

The separation process was started by dipping 5mm of the bottom of the TLC plate (indicated by a scribed black line at the base of Figure 2.4) in a 30% ethyl acetate/70% hexane solvent inside a sealed glass bottle for 5 minutes. The solvent moved up the plate by capillary action, dissolving the sample and moving the mixture up the plate separating by the sample's interactions with the stationary phase and solubility in the solvent. The use of a polar silica gel as the stationary phase caused the analyte to separate by order of decreasing polarity with the most polar products near the bottom of the plate and the least polar at the top (the polarity gradient is indicated in Figure 2.4). The plate was then stained using $KMnO_4$, which is deep purple in color, in order to highlight the separated products that appeared as yellow dots. In Figure 2.4 the unreacted starting material (left) had virtually no products present that were separable or reactive with the TLC plate, while the synthesis products (right) reached their peak in color intensity indicating maximum consumption of the starting epoxide material after 30 minutes. The unreacted starting material reaching the top of the TLC plate demonstrated the low polarity expected of an ether (α-pinene epoxide) diluted in a cycloalkane (cyclohexane), classes of compounds with low polarity. Three compounds (labeled 1-3 in Figure 2.4) that were not present in the starting material could be seen in the synthesis separation. It is very likely that at least two are the β-hydroxynitrates APN-A and APN-B due to the dominant reaction pathway of H^+ addition to the oxygen atom to break the epoxide's energetic three-membered ring to form a hydroxyl group. One of the three products could be the third nitrate APN-C although it is not possible to identify with TLC alone. It is worth noting here that three mid- to high polarity products in the synthesis mixture were separated by the TLC technique.

2.2.2   HPLC analysis

High performance liquid chromatography (HPLC) was also used to further
analyze the synthesized α-pinene nitrates. Unlike the open tubular capillary column used
in gas chromatography, liquid chromatography uses a packed column with packing
material selected to optimally separate the target analyte. During analysis the solvent
being continuously pumped through the column, or "mobile phase", carries sample
solution through the analytical column. The components of the sample solution migrate
according to the interactions of the analyte compounds with the column packing material
and the mobile phase. Figure 2.5 shows a schematic of a standard HPLC instrument
process.
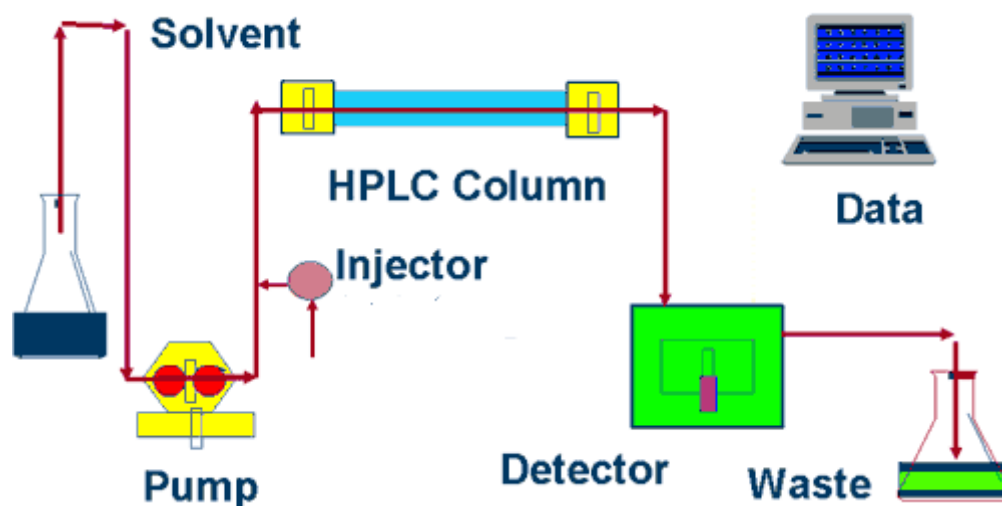
Figure 2.5: HPLC system analysis process.

Synthesized APNs were separated using a Waters 501 HPLC equipped with a
Zorbax Eclipse Extra Dense Bonding Cyano (XDB-CN) column (Agilent Technologies,
4.6 x 150 mm, 3.5 μm) and a Waters 990 photodiode array detector operating in normal
phase with isocratic (or "constant composition") flow. The packing material inside the
column was thick, hard-walled silica with a bonded monolayer of CN-silane on top of the

fully hydroxylated silica surface. The mobile phase used was HPLC-grade hexane (Sigma-Aldrich 99%) pumped at a flow rate of 1mL min^{-1} through the system. Prior to use in the HPLC, the mobile phase solvent was dried with anhydrous $MgSO_4$ (Sigma-Aldrich). An injector port was connected to a 20μL volume stainless steel sample loop that was pre-cleaned with an injection of 10mL of methanol and then with 20mL of hexane to clear it of residue remaining from previous experiments. After a sample was injected into the sample loop with a syringe, a manual valve was switched to push the sample on-column and begin the separation and data collection process.

The cyano-bonded chromatography column separated the synthesized mixtures in order of increasing polarity. Figure 2.6(a) shows the overlay of the chromatogram for the unreacted starting material (red trace) and the chromatogram for the separated synthesis material (black trace). When comparing the two traces it was apparent at least three new products were produced during the synthesis process that were not in the starting material (labeled A, B, and C). Two peaks from the starting material were chosen as reference peaks representative of the starting material (labeled S1 and S2). In the HPLC analysis of the starting material mixture a continuum of largely unseparated peaks eluting from 1.5 minutes to 16 minutes but front-loaded at the 2-5 minute mark was observed. This continuum of unseparated material eluted very shortly after the column dead time (minimum time required for carrier flow to flush eluent into the detector) elapsed, indicating it consisted of low-polarity products. The starting unreacted mixture sample included α-pinene epoxide diluted in cyclohexane with purities of 97% and 99% respectively, so impurities were known to be present in the sample. In the black trace of Figure 2.6(b) the amount of material from the "continuum region" decreased

dramatically. This was consistent with the material being largely cyclohexane in the starting mixture since an extra step had been taken in the organic synthesis process to evaporate cyclohexane to concentrate the nitrate compounds. Due to the evaporation step, the synthesized mixture should deplete the cyclohexane that had been in the starting material. Cyclohexane is also nonpolar so it would be expected to elute early in the analysis, which is the region where most of the "continuum" material was lost.
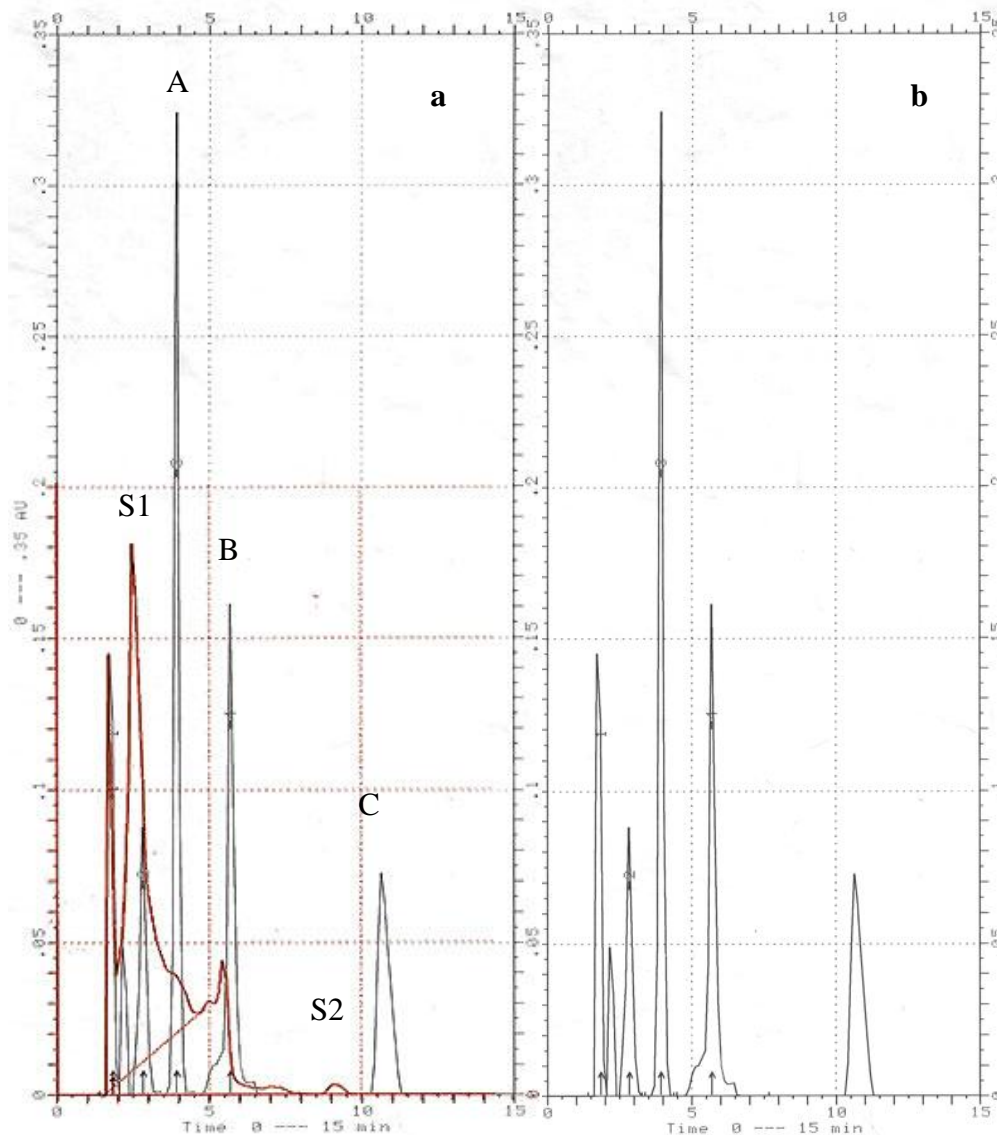

Figure 2.6: (a) Overlay of starting material (red trace) with reacted α-pinene nitrate (black trace) after HPLC separation analysis. (b) α-pinene nitrate separation without starting material overlay.

The absorption spectra for Peaks A, B, and C were examined and compared to the absorption spectra for peaks S1 and S2. As shown in Figure 2.7, the absorption spectra maxima for Peaks A,B, and C were red-shifted by ~ 5nm from the absorption maxima for Peaks S1 and S2 (located at ~ 200nm as indicated by the green line in Figure 2.7),
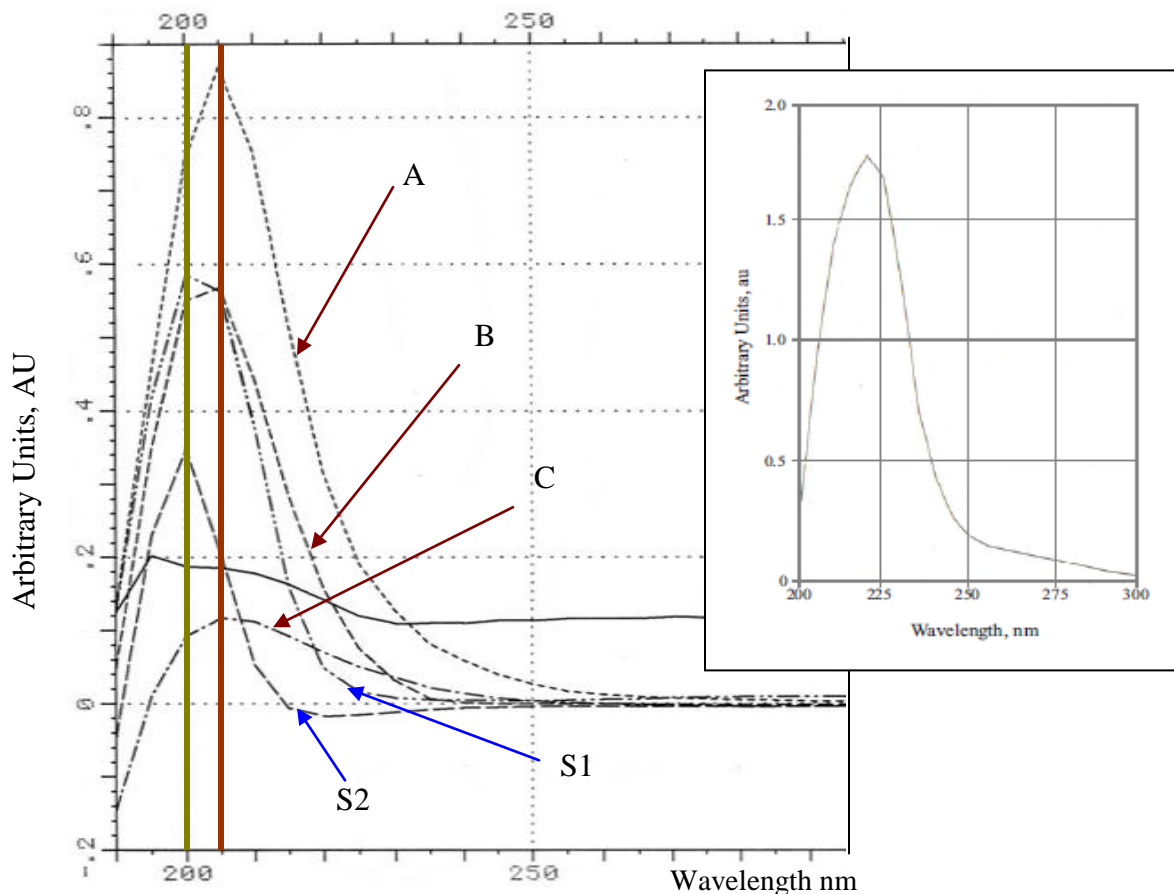
Figure 2.7: Absorption spectra of selected peaks in the HPLC analysis. (INSET) Isobutyl nitrate absorption spectra from a previous study [Lockwood, 2008 dissertation thesis].

The overall shape of the absorption spectra from Peaks A, B, and C was consistent and self-similar although Peak C was flat and broad, possibly indicative of the coelution of multiple compounds. A concurrently separated reference alkyl nitrate absorption spectra was not available for comparison but an isobutyl nitrate absorption spectra from Amanda Lockwood's dissertation thesis [2008] is shown in the inset of

Figure 2.7. The overall shape of the isobutyl nitrate absorption spectra is similar to that of Peaks A and B, but the red-shift is substantially different. The large temporal gap (more than 2 years) and operational differences between the analysis of the α-pinene hydroxynitrates and the Lockwood isobutyl nitrate sample makes comparisons difficult. An immediate future task is to analyze APN synthesis mixture with a reference alkyl nitrate absorption spectra at the same time. With the lack of concurrent alkyl nitrate absorption spectra to identify an α-pinene nitrate absorption profile in the synthesis mixture, the HPLC analysis of the synthesized mixture is inconclusive. Potential coelution and analyte elution order of α-pinene hydroxynitrates are explored in the examination of isomer dipole moments in the next section.

2.2.3   Dipole moment calculations

The total number of possible conformational isomers (conformers) of APNs from first-generation OH + α-pinene reactions was at least 20, consisting of 8 from OH-addition across the double bond and 12 from hydrogen abstraction at other sites of α-pinene. Ring-opening events could add to the count of conformers. From Kwok and Atkinson [1995] OH + α-pinene reaction rate constant calculations, approximately 95% of the time the initial OH attack results in OH-addition, thus the most important nitrate conformational isomers to consider should result from OH addition rather than hydrogen abstraction.

Dipole moment calculations for the APNs formed from OH addition reactions were carried out by Marc Fiddler using Gaussian 03 at the B3PW91/6-31g(d) level of theory, using Becke's three-parameter exchange and Perdew-Wang's correlation functional [Becke et al., 1993; Perdew et al., 1996]. Three-dimensional models of the

nitrate isomers were prepared as input for the calculations. Table 2.1 presents the

conformational isomers used as input to the dipole moment calculations. The results of

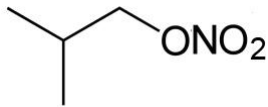the dipole moment calculations are listed below the molecular structure in Table 2.1.

A.1	A.2	A.3	A.4
3.89298	2.5806	2.3655	3.4169
B.1	B.2	B.3	B.4
4.1093	2.9637	2.6637	2.586
H.1	H.2	IBN	
3.4566	3.8147	3.6806	

Table 2.1: The molecular structure and corresponding calculated dipole moment for the 10 APN conformers. The number beneath each molecular structure is the dipole moment. The bond orientations are represented by a solid wedge (directed out of the page) or the hatched bond (directed into the page). The chirality at each chiral carbon position is indicated by "S" and "R" to mean "counterclockwise" or "clockwise" orientation respectively. Each nitrate is labeled by the location of the OH and ONO$_2$ positions.

Isobutyl nitrate (IBN) was included for comparison in Table 2.1 since IBN is often used as a substitute standard for alkene nitrates. In Table 2.1 the three rows "A", "B", and "H" differentiate the APN-A, APN-B, and hydrogen-abstracted nitrate types. The number following the column type and "." is an assigned conformer number. For example Nitrate A.1 is the first of 4 conformational isomers of APN-A.

The dipole moment analysis presented below is adapted from a treatment by Graetzel and Infelta in "The Bases of Chemical Thermodynamics" Vol. 2.

The effective equilibrium molecular dipole moment $\langle\mu\rangle$ for each APN can be written as a canonical ensemble representing a probability distribution that characterizes the microscopic states of each molecule's conformer i as shown in Equation 2.1.

$$\langle\mu\rangle = \sum_i p_i \mu_i \qquad\qquad \text{(Eqn 2.1)}$$

In Equation 2.1, μ_i is the dipole moment per nitrate conformer and p_i is the probability of each conformer contributing to the weighted equilibrium molecular dipole moment. Probability p_i can also be defined as a partition function representing the thermodynamic probability of the molecular conformer occupying an energy state q_i corresponding to the molecular energy level as written in Equation 2.2:

$$\langle\mu\rangle = \sum_i q_i \mu_i \qquad\qquad \text{(Eqn 2.2)}$$

From Equation 2.2, it can be seen that if all conformer energy states were equally probable, the individual partition function q_i for each conformer would be identical and q_i can be treated as a constant. Since q_i can be moved out of the summation, the effective dipole moment for the molecule would be the sum of the dipole moments of the conformers multiplied by the same $1/n$ probability for each dipole moment where n is the number of conformers for the species.

The partition functions of the energy states of APN conformers q_i is the product of the translational, rotational, vibrational, and electronic partition functions as written in Equation 2.3:

$$q_i = q_{trans}q_{rot}q_{vib}q_{elect}$$ (Eqn. 2.3)

Since these are all conformers, the translational partition function q_{trans} is not important due to it being a function of the mass raised to the 3/2 power. The vibrational partition function q_{vib} is related to the vibrational frequency υ and can be assumed to be similar due to their sharing of the same vibrational energy modes. Electronic partition functions q_{elect} can also be ignored because the conformers are all assumed to be in low energy equilibrium states. This leaves the rotational partition function q_{rot} and the relative energies of the molecular structures to consider. The rotational partition function q_{rot} can be related to energy via the Boltzmann distribution (Equation 2.4).

$$q_i = \frac{1}{\sum q_i} e^{\frac{-\Delta E}{k_B T}}$$ (Eqn 2.4)

In Equation 2.4, q_i is normalized by the total number of states in the canonical ensemble, k_B is the Boltzmann constant, T is the temperature in Kelvin, and $\Delta E = (E_i - E_0)$ is the difference between the energy of the system in the lowest energy conformer and an excited state. The larger the difference in energy, the smaller the partition function and the lesser its importance in the normalized effective dipole moment.

When analyzing the isomers' calculated dipole moments (Table 2.2), three distinct groupings of dipole moment clusters were found by selecting dipole moments within 10% of each other in value. These clusters indicate the likelihood of co-elution in HPLC and also help determine the elution order of the individual nitrates. The three

dipole moment groups in Table 2.2 are: Group 1 (μ1): 2.5 ± 0.25 Debye; Group 2: (μ2): 3.2 ± 0.3 Debye; Group 3 (μ3): 3.8 ± 0.38 Debye. The uncertainty indicated is the 1σ standard deviation of the dipole moments in the group.

Nitrate isomer	Dipole moment [Debye]	Group
A.1	3.8298	3
A.2	2.5806	1
A.3	2.3655	1
A.4	3.4169	2
B.1	4.1093	3
B.2	2.9637	2
B.3	4.0025	3
B.4	3.6922	3
H.1	3.4566	2
H.2	3.8147	3
IBN	3.6806	-

Table 2.2: Grouping of nitrate isomers by the dipole moment.

The individual dipole moments vary independent of the parent nitrate molecule such that, for example, not all APN-A isomers have conformers with dipole moments that all fall in the same group. Thus, when interpreting the HPLC data, it is incumbent to consider the possibility that the eluted compounds are not in fact individual APNs but conformers eluting by their dipole moment "grouping".

Revisiting Figure 2.6(a), the three peaks identified on the plot of the HPLC separation of the synthesized material may elute in the order of dipole moment although this is also a function of the analyte solubility in each of the two phases. Considering that μ1 is the least polar of the three dipole moment groups in Table 2.2 with an average group dipole moment of 2.47 Debyes, it would most likely correspond with Peak A, which is the first peak to be eluted in HPLC separations. Due to APN-A being the only nitrate source for μ1 conformers, Peak A is likely a mix of two APN-A conformers. When looking at μ2 the picture is more complex because its members are comprised of isomers from APN-A, APN-B, and a hydrogen abstraction nitrate H.1. However, the

41

small probability of hydrogen abstraction means it is likely not a major contributor of this group. Since this group is of intermediate average group dipole moment of 3.28 Debyes, it is likely to correspond to Peak B. Lastly μ_3 is the most polar of the three groups, with an average group dipole moment of 3.89 Debyes. This group has the most complex membership but is mainly comprised of APN-B conformers. This could explain why the absorption spectrum for Peak C in Figure 2.7 was so broad at the full-width half-height compared to Peaks A and B. Another problem was leaving out APN-C in the dipole moment calculations, which could have been used to compare its calculated dipole moment relative to the other nitrate isomers. The lack of clear dipole moment separation in the individual nitrate species of Table 2.2 indicates that the dipole moment calculation is unfortunately be of little value in nitrate identification.

2.2.4   GC-MS analysis of synthesis standard

The analytical instrument used in the detection and analysis of APNs during the chamber experiments was a GC-ECD (discussed in detail in Chapter 3.3). The instrument provided retention time and elution temperatures but lacked mass and structure information. To aid in the identification of APNs, a GC-MS was used to obtain mass information in the synthesized APN mixture. The GC-MS provided mass spectra at each point in the overall chromatogram (every 0.1s) whose fragments could be used to identify nitrate signatures and mass fragmentation patterns consistent with α-pinene nitrate compounds. The elution temperature of the nitrates found in the synthesis mixture using the GC-MS was then compared to the GC-ECD chromatogram data to allow the identification of nitrates using the GC-ECD during experiments.

The GC-MS used was an Agilent 5975C (Agilent Labs, Santa Clara, CA) operating in negative ion chemical ionization mode (NICI). NICI is a softer ionization method than the more common and more energetic electron-impact (EI) fragmentation technique used to ionize analyte before they reaches the detector. In NICI an electron is transferred between the neutral analyte [M] and ions from a reagent gas, in this case methane. A heated filament in the source region initially emits energetic electrons (230eV) that quickly decelerate by colliding with the reagent gas molecules to form low energy thermal electrons (<15eV) and ionized methane as shown in R2.2.

$$CH_4 + e^- \ (230eV) \rightarrow CH_4^+ + 2e^- \qquad (<15eV) \qquad\qquad (2.2)$$

Methane yields almost no negative ions during this process, thus preventing it from contributing electronic noise that would add to the background current generated by the low energy thermal electrons.

The reagent gas methane was maintained at a high partial pressure relative to the incoming analyte in the source region. This allowed a large cross-section for ion-molecule collisions and a correspondingly short path-length for the neutral molecule entering the source region of the detector. The incoming analyte molecule forms anions through dissociative electron capture, where the thermal electrons are captured followed by dissociation to form an anion and a neutral radical. The three possible anions and neutral radicals that can be formed when an alkyl nitrate undergoes negative-ion chemical ionization are shown in Reactions 2.3-2.5 [Worton et al., 2008].

$$RONO_2 + e^- \ (<15eV) \rightarrow NO_3^- + (R)\cdot \qquad\qquad (2.3)$$

$$\rightarrow NO_2^- + (RO)\cdot \qquad\qquad (2.4)$$

$$\rightarrow RO^- + (NO_2)\cdot \qquad\qquad (2.5)$$
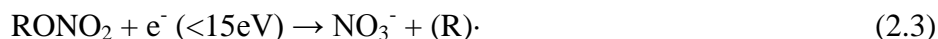
The neutral analyte M entering the detector cell adds a thermal electron to form [M-H]$^-$ before further fragmenting through R2.3-R2.5. The mass spectra results of the primary anayte [M] would then appear to have m/z value reduced by 1, which is factored in as part of the interpretation of the NICI GC-MS mass data. The technique lends itself well to detecting compounds with high electron affinity such as APN.

The column used in the GC-MS was a 30 meter Rtx-1 stationary phase coating with a 0.25μm film thickness (Restek). The carrier gas was helium (Praxair, UHP 5.0) with a flow rate of 10 mL min^{-1}. The temperature programming in the GC-MS was the same as the programming used in the GC-ECD and was set as follows:

1. 4 minutes holding at 30°C

2. 10°C per minute ramp to 105°C

3. 1°C per minute ramp to 125°C

4. 45°C per minute ramp to 250°C.

The NICI ionization process produces less fragmentation and often only two or three mass fragments are detected per mass scan compared to the much larger collection of low mass fragments typically obtained through EI bombardment.

Worton et al. [2008] and Sato et al. [2005] used NICI in a GC-MS similar to the one in this work to study the mass fragmentation of alkyl nitrates. They both suggested the loss of NO_3^- was a minor pathway, accounting for < 1% of the fragmentation reactions except in the case of very short chain alkyl nitrates such as ethyl and n-propyl nitrates. Instead they found that the fragmentation pathway proceeded largely via Reaction 2.4 or 2.5. When the fragmentation proceeds via Reaction 2.4, both observed

the elimination of molecular hydrogen from (RO)· to produce [RO-H$_2$]$^-$ fragments in NICI spectra.

It is reasonable to expect that the NICI fragmentation pattern of α-pinene nitrates would produce similar results to that of alkyl nitrates. Substituting α-pinene hydroxynitrates as the starting RONO$_2$, the [RO-H$_2$]$^-$ fragmentation pathway found by Worton et al. [2008] and Sato et al. [2005] can be described in R2.6 and R2.7:

$$C_{10}H_{16}OHONO_2 + e^- \ (<15eV) \ \rightarrow NO_2 + (C_{10}H_{16}OHO^-)\cdot \qquad (2.6)$$

$$(C_{10}H_{16}OHO^-)\cdot \rightarrow C_{10}H_{14}OHO^- + H_2 \qquad (2.7)$$

The fragment C$_{10}$H$_{14}$OHO$^-$ would be rendered as a fragment with a mass to charge ratio (m/z) of 167 in the GC-MS mass scans. The proximity of the OH group remaining in the activated alkoxy radical quickly facilitates the formation and break-off of an H$_2$O molecule from fragment m/z 167 creating a fragment with an m/z value of 149.

$$(C_{10}H_{14}OHO^-)\cdot \rightarrow C_{10}H_{13}O^- + H_2O \qquad (2.8)$$
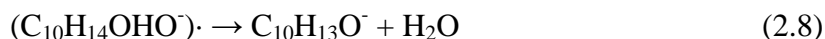
From R2.6 - R2.8, it would be expected that the major peaks in an APN GC-MS analysis undergoing NICI would be m/z 46 (NO$_2$) and m/z 149 ([RO-H$_2$]$^-$) with a small amount of m/z 167 (RO)·.

A GC-MS total chromatogram for the synthesized nitrate material is shown in Figure 2.8(a) with an enlarged view of the peaks of interest in Figure 2.8(b). The black trace is the total ion current, corresponding to the gas chromatography separation. The red trace identifies locations of mass fragment m/z 46. The green trace identifies locations of mass fragment m/z 149. The X-axis corresponds to the scan number, which can be converted to time in seconds when a mass scan is picked out and examined. The Y-axis corresponds to total ion-current in the detector and is related to absolute

45

abundance. Figures 2.8(c), 2.8(d), and 2.8(e) are mass scans from the peaks of interest,

Peak A, B, and C, where the only coincidence of m/z 46 and m/z 149 exist.
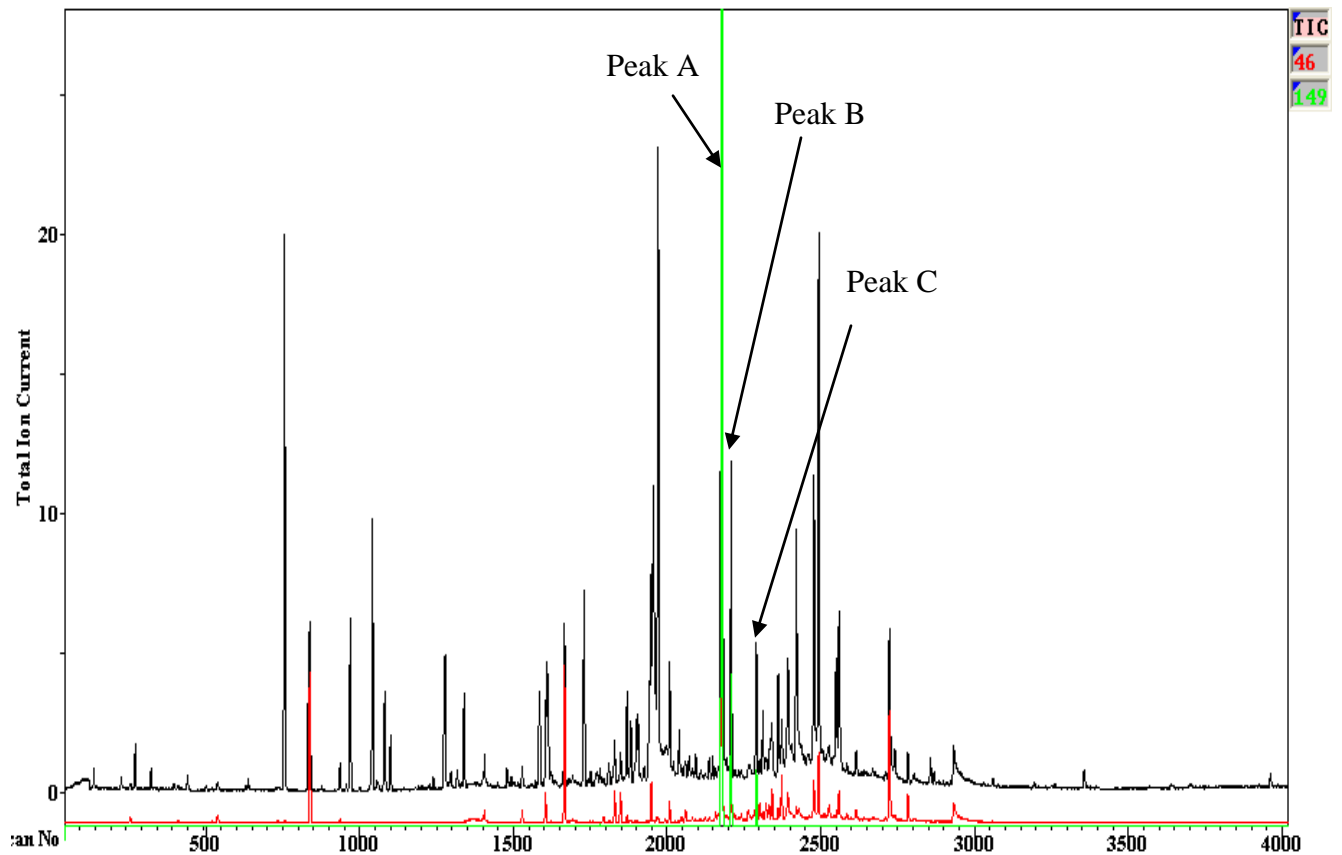
Figure 2.8(a): α-Pinene nitrate chromatogram with m/z 46 and m/z 149 fragments.
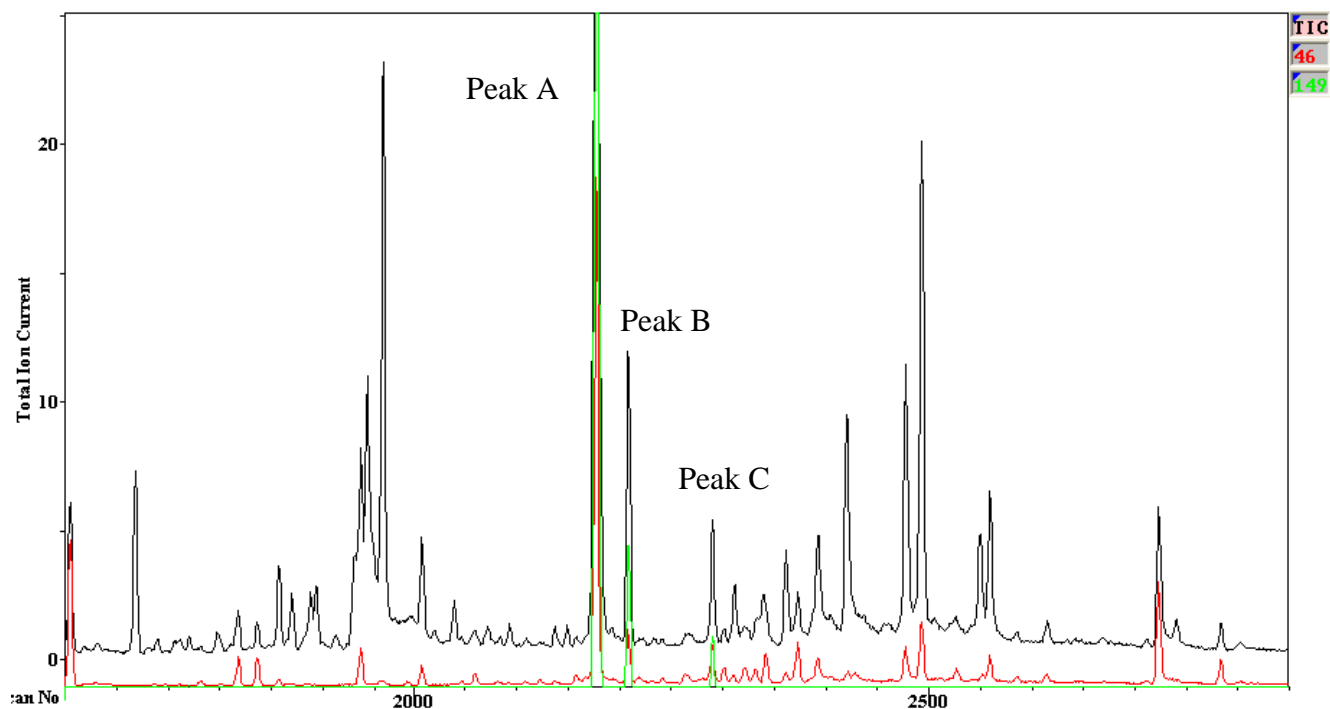
Figure 2.8(b): Enlarged view of the three peaks, A, B, and C with fragments m/z 46 and m/z 149.

When interpreting the mass spectra presented in Figures 2.8 (c) - 2.8(e), it is worth repeating that the initial analyte forms an [M-H]⁻ adduct before undergoing further fragmentations. For an α-pinene hydroxynitrate with molecular structure $HOC_{10}H_{16}ONO_2$, the neutral analyte's molecular mass is 215 amu prior to ionization. When inside the detector region the formerly neutral analyte captures an electron to form [M-H]⁻ and becomes an m/z 214 ion before further fragmentations proceed. Peak A's mass spectrum is shown in Figure 2.8(c) and is comprised of mass fragments with m/z values of 46, 133, 149, 150, 151, and a small amount of 167.
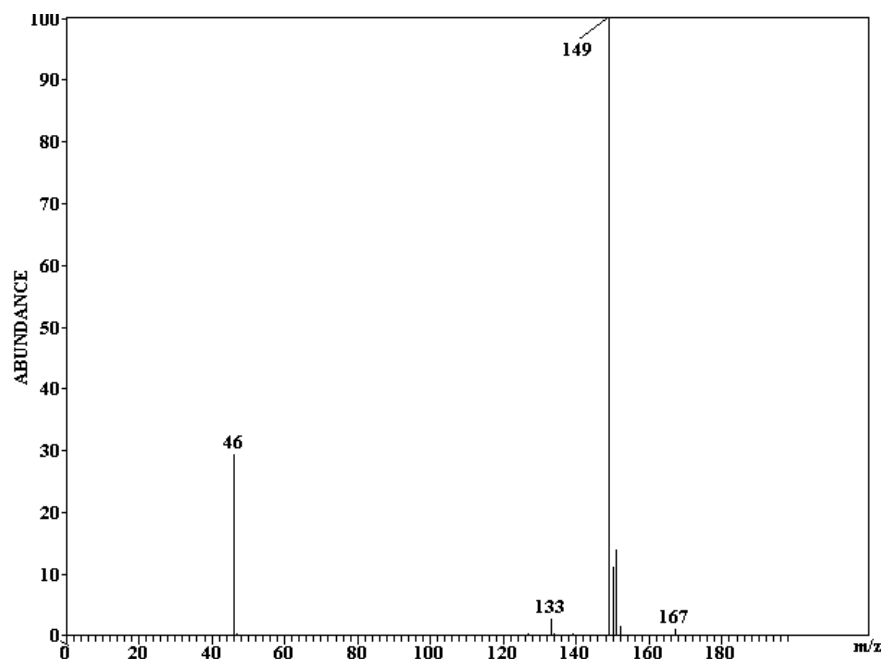
Figure 2.8(c): Peak A mass scan.

The m/z 46 fragment is common in nitrates due to the weak O-N bond [Worton et al., 2002]. The m/z 133 mass fragment is indicative of a loss of O and H_2O from [RO-H_2]⁻ (167-16-18=133). Fragment m/z 149 is indicative of [RO-H_2]⁻ subsequently losing H_2O (167-18=149). Fragment m/z 150 is indicative of the loss of NO_3 plus further abstraction of an H_2 molecule from APN (214-62-2=150) or is the result of the presence of ^{13}C in the nitrate. Fragment m/z 152 is indicative of APN losing NO_3 (214-64). Fragment m/z 151 could result from fragment m/z 152 losing additional hydrogen. Fragment m/z 167 could result from molecular H_2 elimination from the alkoxy neutral radical [RO-H_2]⁻ (169-2=167).

Peak B's mass scan in Figure 2.8(d) appears similar to Peak A's mass scan in Figure 2.8(c), except there is a m/z 127 fragment present instead of m/z 133. This is a very small fragment and there is no reasonable collisional process to form a m/z 127 fragment hence it is could indicate a small contaminant coeluted with the nitrate.
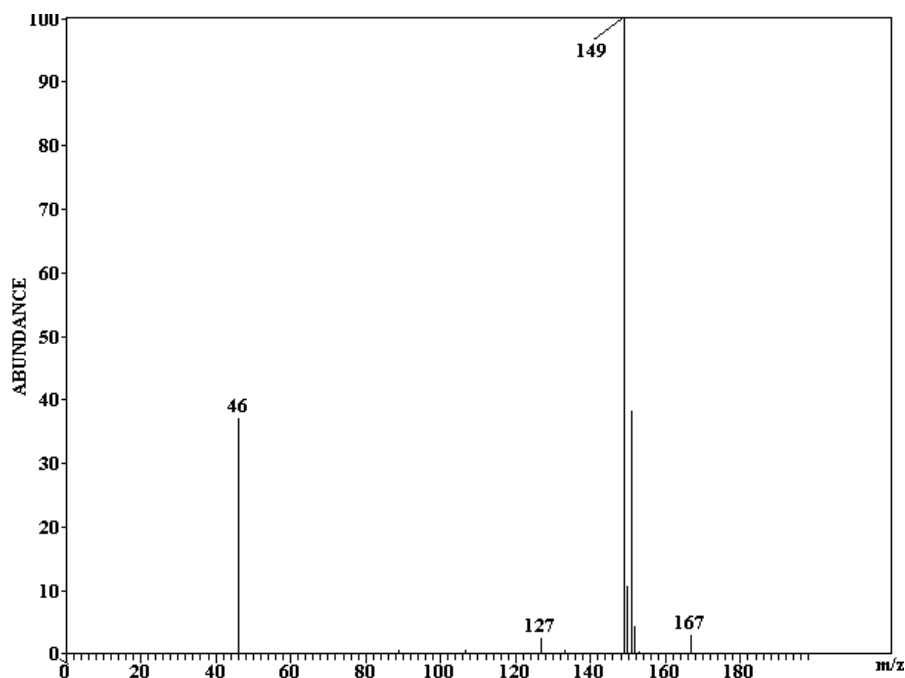
Figure 2.8(d): Peak B mass scan.

In Figure 2.8(e) the Peak C mass scan shows many of the same signature mass fragments as found in the mass scans for Peak A and Peak B, with two new minor fragments with m/z 89 and m/z 185. The fragment m/z 89 is not a large abundance in the mass scan and no reasonable fragmentation mechanism could be found to explain its presence. A small fragment m/z 185 is also present in the mass spectrum that is larger than any of the mass fragments in the previous Peak A and Peak B mass scans. This is consistent with Peak C having a larger starting neutral analyte molecular mass and indicates it is different from A and B or it could mean a m/z 29 mass fragment CH_3CH_2 was freed from the originating APN molecule to form m/z 185. Peak C has the mass fragment indicators of a hydroxynitrate but it could possibly be another class of nitrate, perhaps even a dihydroxynitrate as Aschmann et al. [1998] identified a m/z 231 product as a dihydroxynitrate. A dinitrate undergoing NO_2 fragmentation could give a mass fragment of m/z 184 and m/z 185 (with the presence of ^{13}C). The enhanced abundance

49

of m/z 133 over m/z 127 mass fragments in Peak C could be meaningful since those fragments are in Peak A and Peak B respectively. Without further investigation with another analytical technique, it is difficult to make further identification of Peak C.
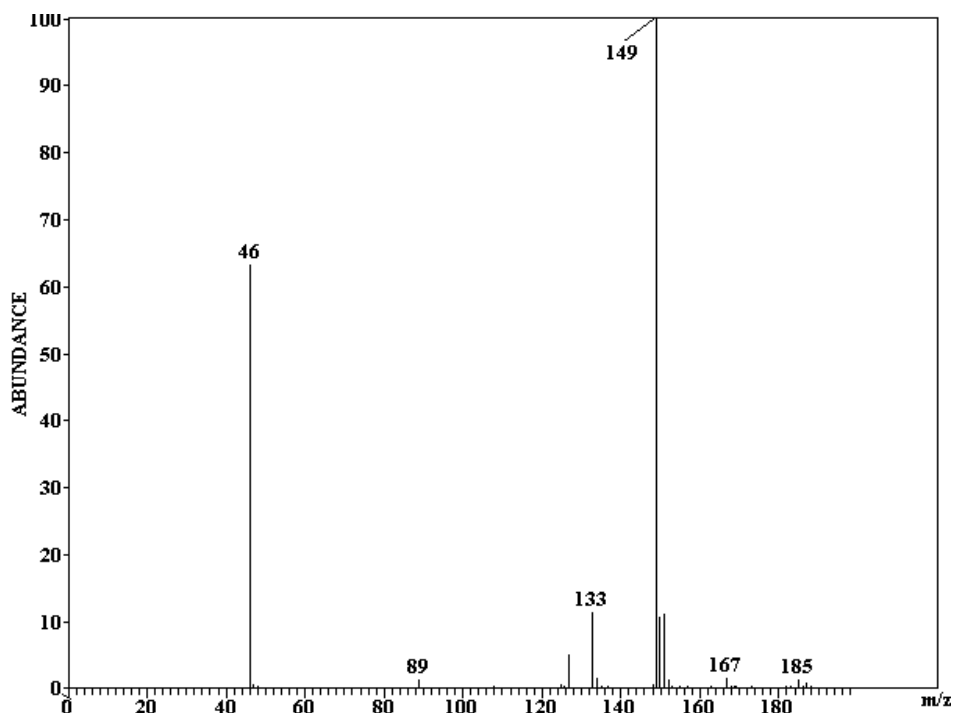
Figure 2.8(e): Peak C mass scan.

All of the fragments appearing in the mass spectra for Peaks A, B, and C are listed in Table 2.4 along with potential fragment identification mechanisms.

Mass Scan fragment m/z	Fragmentation Mechanism	Appears in Peak
46	NO_2 fragment from ONO_2	A,B,C
89	unknown	C
127	unknown	B,C
133	$[RO-H_2]^-$ -O -H_2O	A,C
149	$[RO-H_2]^-$ -H_2O	A,B,C
150	$RONO_2$-NO_3 - H_2	A,B,C
151	$RONO_2$-NO_3 - H	A,B,C
152	$RONO_2$ - NO_3	A,B,C
167	$[RO-H_2]^-$	A,B,C
185	$RONO_2$ – CH_3CH_2	C

Table 2.4: Fragmentation groups from mass scans of GC-MS applied to synthesis.

Comparison of the data obtained analysis of the synthesized material via the GC-ECD and GC-MS results was performed using relative elution temperature. From the GC-MS results the elution temperatures corresponding to Peaks A, B, and C were 115°C, 115.4°C and 116°C respectively.

2.2.5 GC-ECD Analysis of Synthesis Standard

The α-pinene nitrate synthesis standard solution was analyzed using the GC-ECD instrument to compare with GC-MS results discussed in the previous section by matching elution temperatures of identified α-pinene hydroxynitrates. By using a matching Rtx-1 column and duplicating the chromatography conditions used in the GC-MS as closely as possible, the identification information obtained through GC-MS analysis can be transferred to the GC-ECD. In the GC-ECD the starting conditions and column temperature programming were optimized for the separation of the nitrate compounds in the instrument.

The synthesis standards are separated with the GC-ECD at least three times before each experiment to coat the system's surfaces with nitrates and minimize the irreversible adsorption effects reported by Muthuramu et al. [1993]. Figure 2.9(b) shows a typical GC-ECD chromatogram of the synthesized α-pinene hydroxynitrate standard solution that was diluted in clean air to ~130ppbv (using 1-octyl-nitrate as a substitute proxy standard to determine the concentration) and sampled in the gas phase. Peaks A, B, and C are labeled in Figure 2.9(b) to correspond to Peaks A, B, and C in the GC-MS analysis of Figure 2.8(a). The peaks elute at 114°C and 115°C, and 116°C. This agrees with the GC-MS results for elution temperature within 1°C, a very solid correlation between the two analytical instruments. The synthesis standard chromatograms are also compared against

the photochemical reaction chamber time-series chromatographs to observe if the peaks

that grow with time correspond to peaks A,B, and C in the standard. Figure 2.9(a) is a

chromatogram of the starting unreacted material for comparison. There are no reactants

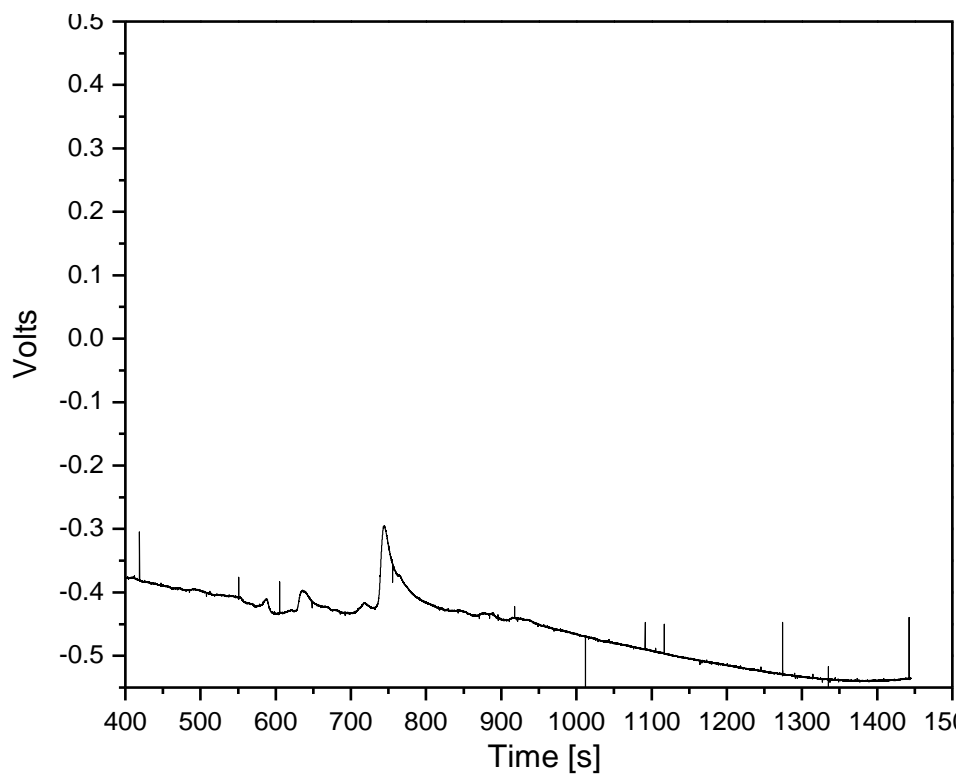beyond 900s compared to Figure 2.9(b).

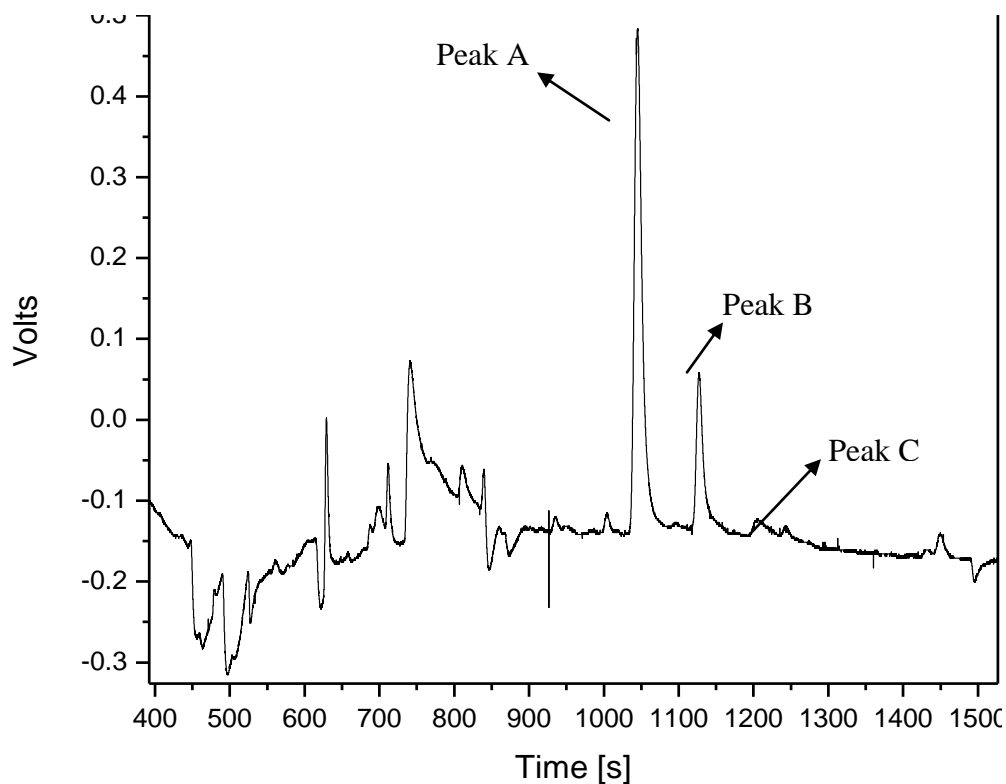**Figure 2.9 (a): GC-ECD chromatogram of starting diluted α-pinene epoxide material.**

Figure 2.9 (b): GC-ECD chromatogram of synthesized nitrate material.

2.3 1-Octyl-nitrate Synthesis and Calibration

While the synthesized α-pinene hydroxynitrate standard used in GC-MS and GC-ECD analyses was needed for qualitative identification of the nitrates, the standard itself was not usable for calibration or quantitative analysis. This was due in large part to the difficulty in isolating a single nitrate compound in sufficient purity for analysis in proton nuclear magnetic resonance (^{1}H NMR). The analysis technique of ^{1}H NMR offers structural information about the different types of hydrogen present in a molecule and quantitative estimates of sample purity. Usually a single highly purified molecule is analyzed to observe the resonance patterns of hydrogen. The results from the HPLC analysis of the APN synthesis mixture showed that only Peak C in Figure 2.6(b) was sufficiently separated from the rest of the peaks to be considered as a candidate for purification extraction. Because of its late elution time and separation from other peaks

Peak C could be isolated and collected through repeated HPLC separation. However its absorption spectra in Figure 2.6(a) showed that it did not resemble the spectra of a reference alkyl nitrate, isobutyl nitrate, and could be indicative of a mixture of compounds. Peak C was not extracted because of the lack of sufficient synthesized material to proceed with the purification step. The inability to produce a single purified compound for quantitative analysis in ^{1}H NMR from the synthesis mixture mandated a substitute calibration compound with sufficient functional group similarity to the synthesized hydroxynitrates.

From the works of Giacopelli et al. [2005] and Muthuramu et al. [1993], there is precedence for using an alkyl nitrate as a quantitative substitute standard for organic alkene nitrates. While isobutyl nitrate is a commercially available alkyl nitrate, its relative volatility resulted in a fast elution time in the GC-ECD that could coincide with the large air peak due to unretained material traveling through the system in the first two minutes of analysis. The only other commercial option was isopropyl nitrate, which is even more volatile. As a less volatile substitute standard was required to elongate the elution time, 1-octyl-nitrate was synthesized.

Silver nitrate (Sigma-Aldrich) and 1-bromooctane (95%, Fisher Scientific) mixed to form a molar ratio of 1.2:1 were reacted to create 1-octyl-nitrate and a silver bromide precipitate. The precipitate was separated from the 1-octyl-nitrate through a separation funnel and filter paper to eliminate trace amounts of precipitate. Figure 2.10 shows the chemistry of the reaction that produces the 1-octyl-nitrate from 1-bromooctane.
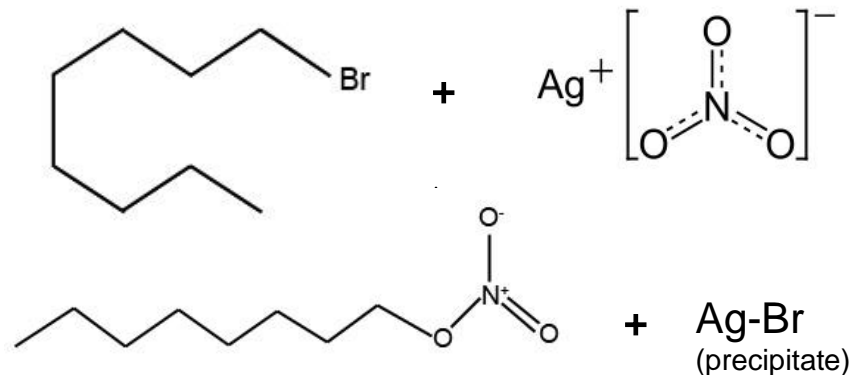
Figure 2.10: Reaction of 1-bromooctane and silver nitrate to form 1-octyl-nitrate.

2.3.1 ^{1}H NMR analysis of 1-bromooctane and 1-octyl-nitrate

Samples of the 1-octyl-nitrate and the starting material 1-bromooctane were diluted with chloroform (99.8% Chloroform-d with 0.03% TMS, Sigma-Aldrich) and analyzed with Proton Nuclear Magnetic Resonance (^{1}H NMR) Spectroscopy. The NMR spectrum provides information about the relative number of chemically distinct hydrogen groups that resonate at a resonance frequency. During NMR analysis, an external magnetic field is applied to the sample. The nuclear magnetic moment of a nucleus can align with the externally applied B-field in either parallel or opposing directions, though it is energetically preferred to be aligned parallel to the external field [Darbeau, 2006]. The rotation axis of a spinning nucleus precesses about the external B-field with an angular frequency called the Larmor frequency [Darbeau, 2006]. The NMR spectrum presents the difference between the Larmor frequency of the nucleus and that of a standard compound, generally tetramethylsilane, $Si(CH_3)_4$ (abbreviated as "TMS"), and this is known as the chemical shift in the spectra. Written as "δ", chemical shift is defined by the frequency of the resonance in the resonant hydrogen with reference to a standard compound. The chemical shift can be expressed in terms of the difference in sample and

reference resonance frequency in Equation 2.5 [Francis Carey, "Organic Chemistry" text].

$$\delta = \frac{\upsilon_{signal} - \upsilon_{reference}}{\upsilon_{reference}} \times 10^6 = ppm \qquad \text{(Eqn 2.5)}$$

The x-axis in a NMR spectrum is customarily expressed in parts-per-million (ppm), independent of the spectrometer frequency. The unitless ppm measurement of chemical shift can be related to the field strength of the induced B field of the resonant hydrogen group, expressed in units of Teslas (T). Figure 2.11 shows the ^{1}H NMR results from 1-bromooctane, the alkyl halide used in the synthesis reaction.

δ chemical shift, ppm
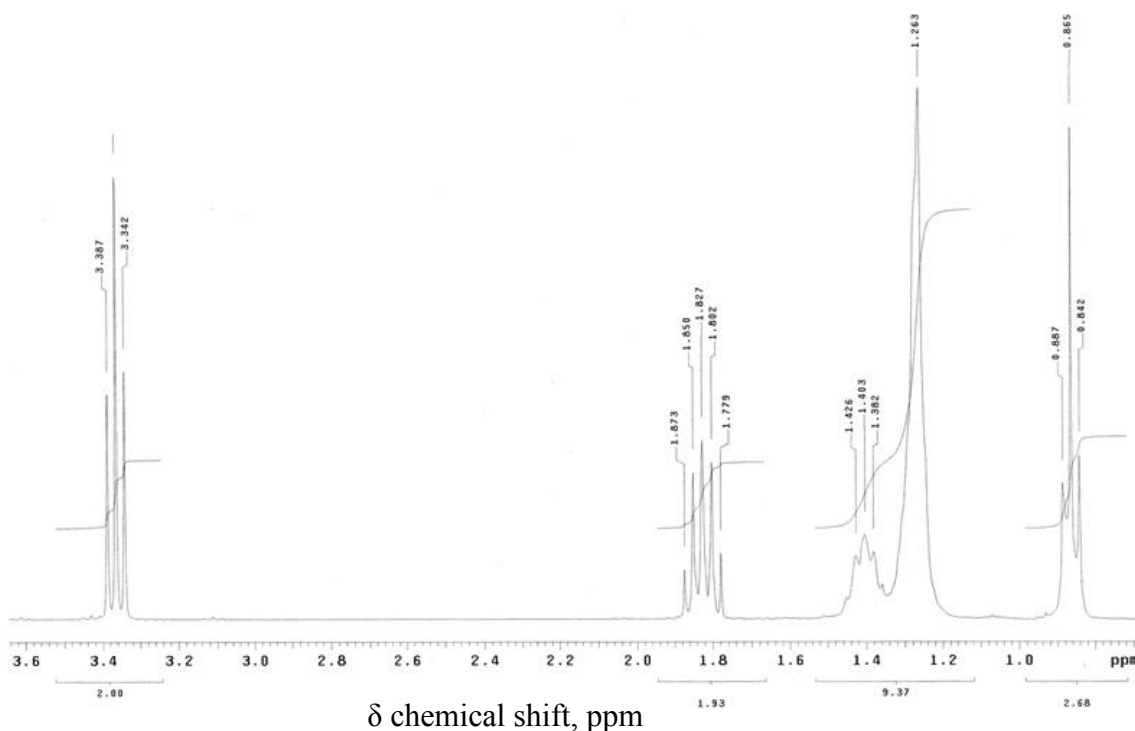
Figure 2.11: ^{1}H NMR spectrum of 1-bromooctane.

1-Bromooctane ($CH_3(CH_2)_7Br$) has 5 major different hydrogen groupings: CH_3, CH_2 next to CH_2, CH_2 next to CH_3, and a CH_2Br group. The CH_2Br triplet is shifted at 3.4ppm in Figure 2.11, the CH_2 multiplet next to the CH_2Br group is shifted to 1.8ppm, a

multiplet of the CH_2 adjacent to another CH_2 is shifted at 1.4ppm, and a multiplet for the CH_2 group adjacent to CH_3 shifted at between 1.2 to 1.4ppm. Lastly the CH_3 protons are the triplet at 0-1ppm.

Figure 2.12 shows the ^1H NMR spectrum of 1-octyl-nitrate ($CH_3(CH_2)_7ONO_2$). The presence of unreacted 1-bromooctane at 3.4ppm appears as a minor component. 1-octyl-nitrate also has the same proton groups except it now has an ONO_2 group at one end. The CH_2 attached to the ONO_2 group is shifted farther downfield than the CH_2Br triplet in 1-bromooctane NMR spectrum. The integration of the area of the starting material still left at 3.4ppm in Figure 2.12 divided by the integration of the starting material at 3.4ppm in Figure 2.11 gives the purity of the synthesized nitrate compound. This calculation showed that the purity of the 1-octyl-nitrate standard was 98.5%.
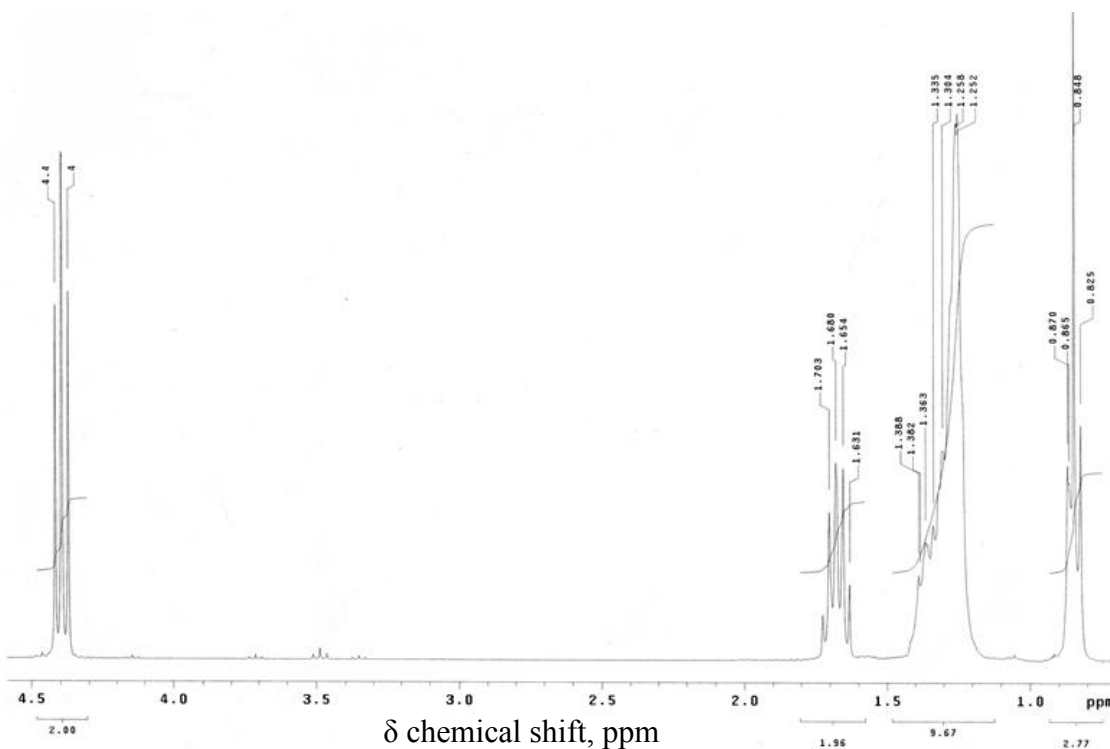
Figure 2.12: ^1H NMR spectrum of 1-octyl-nitrate.

2.3.2 GC-ECD analysis of 1-bromooctane and 1-octyl-nitrate

Samples of the 1-octyl-nitrate and 1-bromooctane were analyzed in the GC-ECD to determine elution times and detector linearity. The solutions were diluted in clean air to 200ppbv and analyzed with the same chromatographic conditions used for the α-pinene synthesized hydroxynitrates. Figure 2.13 shows the overlay of the unreacted 1-bromooctane and 1-octyl-nitrate standard chromatograms. The peak for 1-octyl-nitrate elutes at 700s compared to 600s for 1-bromooctane.
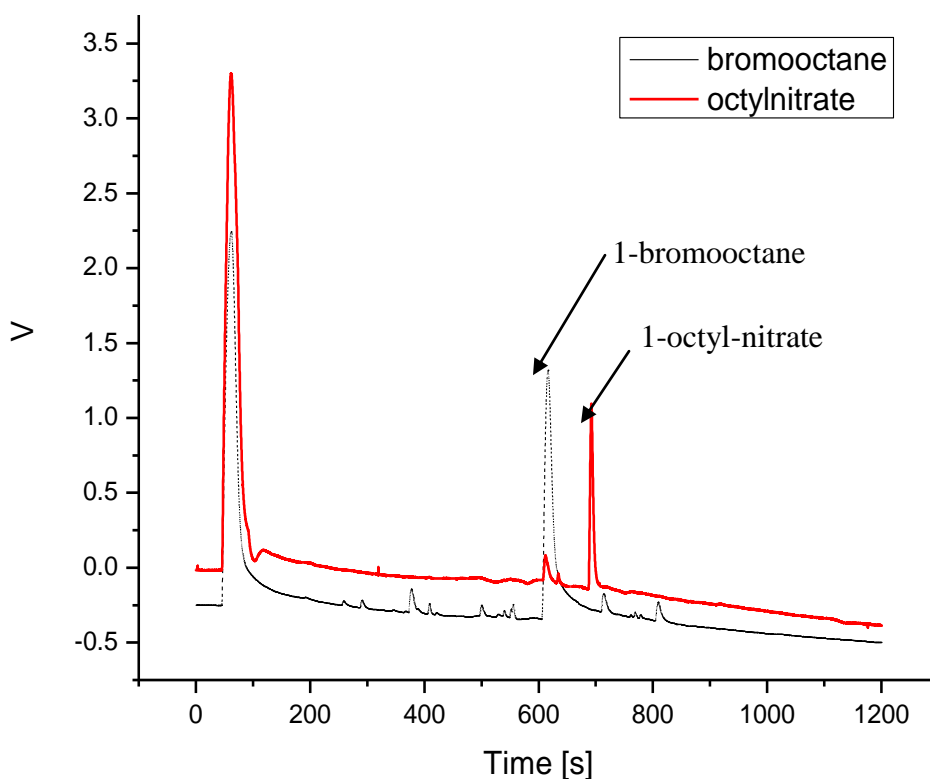
Figure 2.13: Overlay of the unreacted 1-bromooctane and the 1-octyl-nitrate standard chromatograms analyzed with the GC-ECD showed the 1-octyl-nitrate is right-shifted from 1-bromooctane and eluted at 700s.

The results of the calibration conducted using standard mixing ratios ranging from 5-60ppbv concentrations of 1-octyl-nitrate in the gas phase are shown in Figure 2.13. It shows the response of the GC-ECD is linear over this range.

The 1-octyl-nitrate synthesized standard was refrigerated and kept in a frozen state to prevent evaporation and photo-dissociation. The GC-ECD was calibrated with 0-60ppbv 1-octyl-nitrate prior to each experiment. Appendix F shows all the calibration plots for the full sets of data presented in this thesis.
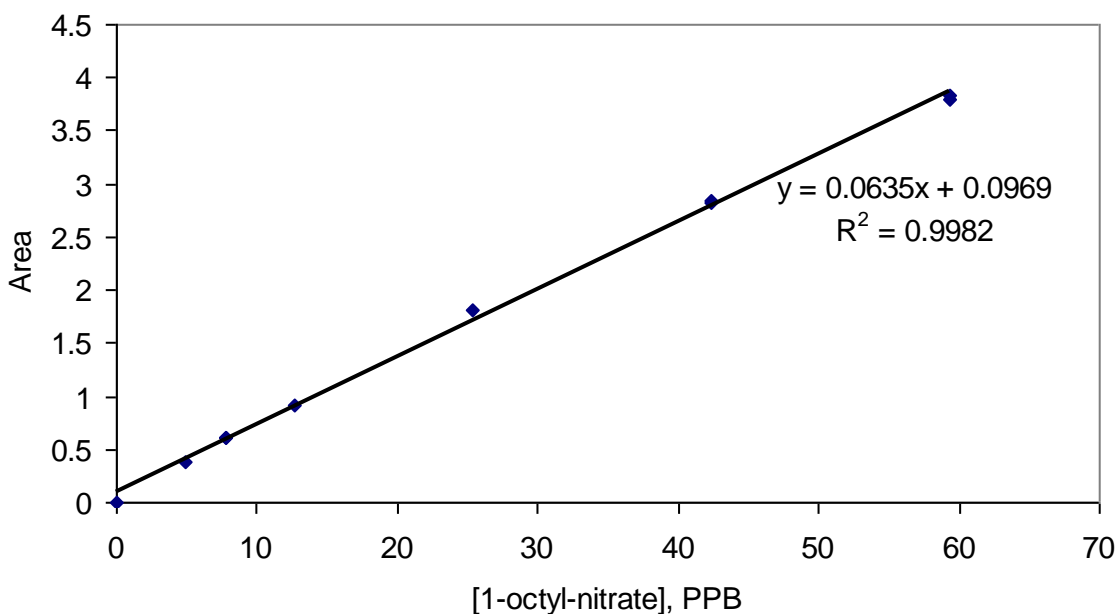
Figure 2.14: Sample calibration curve of 1-octyl-nitrate standard.

Use of 1-octyl-nitrate as a substitute calibration standard for the synthesized α-pinene hydroxynitrates required an additional step in which the relative response of the isoprene nitrate with 1-octyl-nitrate was determined. The results of this analysis were compared with the GC-ECD response to 1-octyl-nitrate and the ratio between the two responses was then used to correct the experimental data to adjust for the substitute calibration standard's relative response in the instrument. This step is discussed in greater detail in Section 3.3.1.

CHAPTER III

α-Pinene Nitrates: Experiment, Yields, and Branching Ratios

3.1 Introduction

Monoterpenes are emitted into the atmosphere at an estimated rate of 127 Tg yr^{-1} [Guenther et al., 1995, 2000]. This constitutes about 11% of the total non-methane biogenic volatile organic compounds (BVOC) emitted annually [Guenther et al.,1995] and can be regionally dominant in mid-latitude regions including areas of North America. While many monoterpenes have been identified, α-pinene is the most studied species because it is observed to have the highest emission rates and global abundance [Rinne et al., 2000]. α-Pinene is emitted by vegetation including the eponymous coniferous tree and many other tree and plant species. With high overall high emission rates and fast chemical reactivity, α-pinene is an important participant in the atmosphere's NO_x and HO_x cycles that impact tropospheric ozone generation. The reaction rate constants of α-pinene with atmospheric hydroxyl radical (OH), nitrate radical (NO_3), and ozone (O_3) are shown in Table 3.1 below.

Species	Rate Constant [cm^3 molecules^{-1} s^{-1}]	Reference
OH	$(6.1\pm0.3)\times10^{-11}$	Davis and Stevens, 2005
NO_3	$(5.8\pm0.8)10^{-12}$	Atkinson, 1984
O_3	$(8.4\pm1.9)\times10^{-17}$	Atkinson, 1990

Table 3.1: Reaction rate constants of OH, NO_3, and O_3 with α-pinene.

The OH reaction pathway is the fastest and often dominates during the daytime but during nighttime the NO_3 and O_3 pathways become more significant [Arey and

Atkinson, 2003]. The fast OH pathway can contribute to tropospheric ozone, increased secondary organic aerosol (SOA) generation [Grosjean et al., 1993], and its oxidation products can act as a sink or reservoir for NO_x.

Calculations using the Kwok and Atkinson structure-reactivity relationship method [Kwok and Atkinson, 1995] show that the OH oxidation pathway of α-pinene is expected to add across the carbon double bond producing β-hydroxyperoxy radicals 95% of the time with the remaining 5% resulting in hydrogen abstraction on other sites of the α-pinene molecule (calculation shown in Appendix A). Figure 3.1 schematically shows the OH addition and hydrogen abstraction process of the initial OH attack on α-pinene.
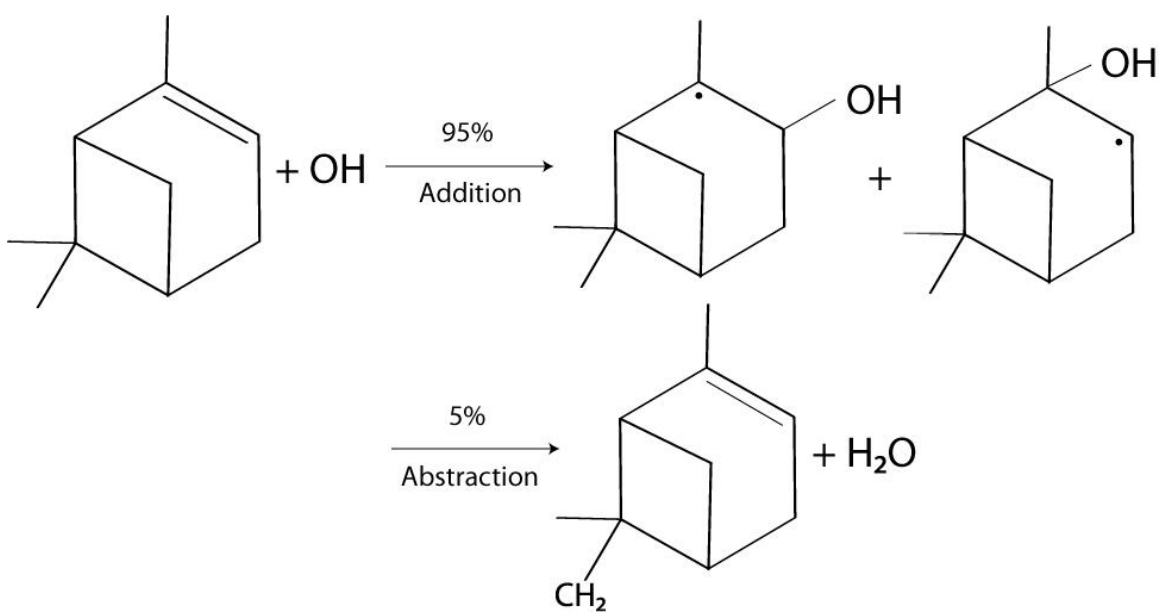
Figure 3.1: Schematic showing the results of initial OH attack on α-pinene. OH addition can occur on either side of the C=C double bond while OH abstraction can happen at any hydrogen site on the molecule.

After addition of O_2, the resulting peroxy radical reacts with NO to form an intermediate peroxy nitrite ROONO in Reaction (R) 3.1a.The unstable intermediate quickly rearranges to form a hydroxynitrate in R3.1c or dissociates into an alkoxy radical RO and NO_2 in R3.1b.

$$RO_2\cdot + NO + M \rightarrow \quad ROONO + M \qquad\qquad (3.1a)$$

$$ROONO \qquad \rightarrow \quad RO\cdot + NO_2 \qquad\qquad (3.1b)$$

$$ROONO \quad + M \rightarrow \quad RONO_2 + M \qquad\qquad (3.1c)$$

The branching ratio of R3.1b and R3.1c ($k_{3.1c}/(k_{3.1b}+k_{3.1c})$) is a particularly relevant measurement as hydroxynitrates are stable oxidation products that act as a sink for the α-pinene peroxy radicals and NO_x. The hydroxyl group present in these nitrates makes them much more susceptible to wet deposition and as a result have a shorter lifetime than analogous alkyl nitrates in the atmosphere [Shepson et al., 1996]. At T = 293°K the measured Henry's Law constants of hydroxyl alkyl nitrates let an estiamted 20-50% of these nitrates to partition into cloudwater in the atmosphere [Treves et al., 2000].

However, the branching ratio of RO_2 + NO in R3.1b and R3.1c has not been measured for many organic nitrates due to the difficulty in obtaining authentic calibration standards and the challenges involved in detecting these species. There is evidence that these hydroxynitrates are likely to undergo irreversible adsorption onto the column and injection port surfaces of analytical instruments, making detection and quantification problematic [Muthuramu et al., 1993].

The reported yields for the hydroxynitrates of alkenes from OH-initiated oxidation include ethene [O'Brien et al., 1998], propene [O'Brien et al., 1998], butene [O'Brien et al., 1998], cyclohexene [Espada and Shpeson, 2005], p-xylene [Espada and Shpeson, 2005], isoprene [Chen et al., 1998; Patchen et al., 2007], α-pinene [Aschmann et al., 2002, Nozière et al., 1999], and C_8-C_{17} alkenes [Matsunaga and Ziemann, 2009]. The yield results and associated references are organized in Table 3.2.

Alkene	Nitrate yield [%]	Reference
ethene	0.86	O'Brien et al.,1998
propene	1.5	O'Brien et al.,1998
1-butene	2.5	O'Brien et al.,1998
cis-2-butene	3.4	O'Brien et al.,1998
1-hexene	5.5	O'Brien et al.,1998
cyclohexene	2.5 ± 0.5	Espada and Shepson, 2005
p-xylene	3.2 ± 0.7	Espada and Shepson, 2005
isoprene	4.4 ± 0.8	Chen et al., 1998
isoprene	7.0 ± 3.1	Patchen et al., 2007
α-pinene	1 ± 0.5	Aschmann et al., 2002
α-pinene	18 ± 9	Nozière et al., 1999
C_{14}-C_{17} alkenes	14 ± 0.9	Matsunaga and Ziemann, 2009

Table 3.2: Published total nitrate yields for several alkenes.

There is a general trend of increasing hydroxynitrate yields for increasing alkene carbon number. Quantum chemistry models indicate that β-hydroxynitrate yields are lower for smaller carbon number alkenes due to weakening of the O-O bond of the ROONO intermediate in R3.1a from the effect of hydrogen bonding between the hydroxyl and peroxy groups [O'Brien et al., 1998]. This enhances the formation of the RO and NO_2 instead of $RONO_2$ for smaller alkenes.

Previous studies show that hydroxynitrate yields from alkenes are about half that of corresponding alkyl nitrates with the same carbon numbers (CN) provided that CN ≤ 8 [O'Brien et al., 1998; Atkinson et al., 1995], making the corresponding alkyl nitrate yield an upper limit on alkene hydroxynitrate yields, although this has not been confirmed for larger carbon numbers. Aschmann et al. [2001] reported experimental results showing that n-decane reaction with OH produces an alkyl nitrate yield of 22.6% and hydroxynitrate yields of 2.4%. Another result reported a β-hydroxynitrate yield for a linear C_{10} n-alkene of ~1-2 % [Matsunaga and Ziemann, 2009]. These results do not

match the experimental results predicting that the branching ratio of alkene nitrates would be about half as much as that for the analogous alkyl nitrates.

Reported yields for total α-pinene β-hydroxynitrates (APN) production range from <1% [Aschmann et al., 2002] to 18 ± 9% [Nozière et al., 1999], two conflicting and divergent sets of data with no overlap. Individually identified and speciated yields for individual APNs are reported for the first time in this thesis to add to the currently very limited set of experimental results for α-pinene β-hydroxynitrate yields. The results also include calculations of the RO_2 and NO branching ratios for these α-pinene β-hydroxynitrates.

Aschmann et al. [2002] conducted yield experiments in a 7500L photochemical reaction chamber in which products were detected using an atmospheric pressure ionization tandem mass spectrometer (API-MS) analytical instrument. The API-MS was operated in both positive and negative modes. In the positive mode protonated water hydrates $(H_3O^+(H_2O)_n$, where n=3-6) generated by a needle corona discharge in the chamber gas protonated the analyte for detection [Atkinson et al., 1995]. In negative mode, adducts between molecules and negative ions from the needle discharge created reagent ions that would then deprotonate the analyte for detection. The mass spectrometer supported two MS/MS scanning modes that allowed the examination of the "product ion" or "precursor ion" mass spectrum of any given ion peak observed so one could trace and further break apart ions to examine the constituent fragments to aid in identification or reverse the process and trace the precursors of specific ion fragments. The total APN yield result of < 1% produced in OH-initiated α-pinene oxidation was assumed to include both hydroxynitrates and dihydroxynitrates. While noting that the Aschmann

experimental results differed from the Nozière [1999] result by an order of magnitude, it was hypothesized that these nitrate products may have partitioned into the particle phase or may have been lost to the chamber wall, hence giving artificially low results [Aschmann et al., 2002].

Nozière et al. [1999] used Fourier Transform Infrared Spectroscopy (FTIR) to detect and measure α-pinene OH-oxidation products in the presence of NO_x and calculated a total APN yield of $18 \pm 9\%$. The FTIR measurement passed IR source light through an interferometer then through the sample before it entered the detector where an interferogram was recorded. A Fourier transform was performed on the signal, and the results were then reconstructed to resemble a conventional infrared absorption spectrum profile for data interpretation. The identification of β-hydroxynitrate products was done by comparing the IR spectra with a reference spectrum published in a previous study that reacted NO_3 directly with α-pinene [Wängberg et al., 1997]. The identifying spectrum used is shown in Figure 3.2.
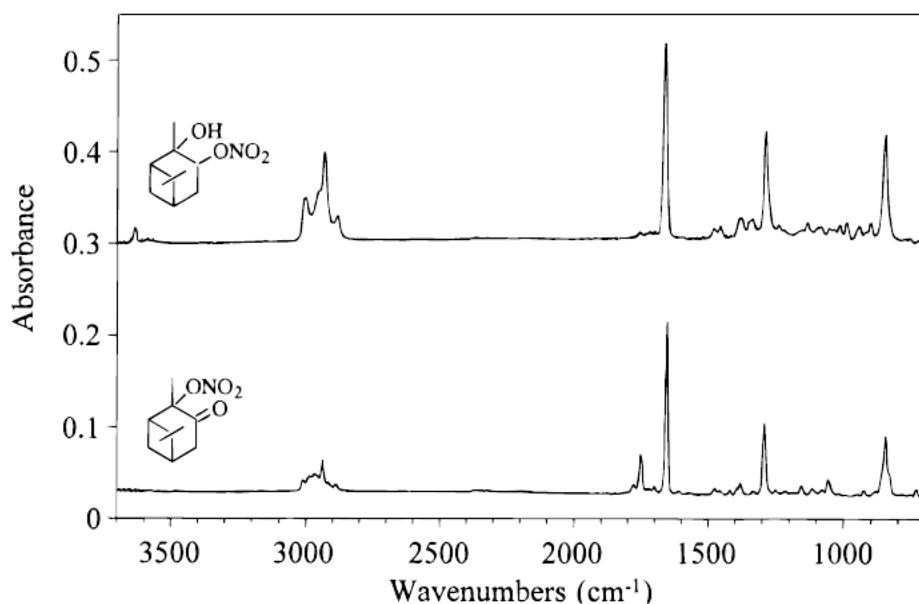
Figure 3.2: FTIR spectra of 2-hydroxypinane-3-nitrate (top) used to identify hydroxynitrate APN-B [From Wängberg et al., 1997].

The Wängberg et al. results [1997] found that reacting NO_3 directly with α-pinene produced a 5% yield of 2-hydroxypinane-3-nitrate. Although the yield from the NO_3 reaction has no direct bearing on this work, it suggests that nitrate production could be a significant pathway for α-pinene oxidation from both OH and NO_3 oxidation.

A possible bias in the FTIR measurements may be due to other products interfering with the absorption band used to quantify nitrate products to inflate the yields artificially. The lack of reference nitrates in the Nozière [1999] experiment likely exacerbated this potential problem by making identification especially difficult.

In studies of hydroxynitrates, the R3.1b rate constant was observed to be generally decreasing with increasing radical size for the available data and a generic reaction rate expression was proposed: 7.5×10^{-12} exp $[-0.17 \cdot (n-1)]$ $cm^3 mol^{-1} sec^{-1}$ [Jenkin et al., 1997] where "n" is the number of carbons in the molecule for $\geq C_3$ alkyl and RO_2 radicals reacting with NO at T = 297°K. For isoprene peroxy radicals, this expression yielded a R3.1b rate constant of 3.80×10^{-12} $cm^3 mol^{-1} sec^{-1}$ rate, which is more than two times slower than that of the only published measured rate constant of 9.4×10^{-12} $cm^3 mol^{-1} sec^{-1}$ [Stevens et al., 2005]. For α-pinene RO_2 radicals, this proposed expression yielded a R3.1b rate constant of 1.62×10^{-12} $cm^3 mol^{-1} sec^{-1}$. However this thesis adopts the Stevens et al. [2005] measured isoprene-based R3.1b rate constant for the branching ratio calculations since it is the only measured result for an isoprene reaction 3.1b rate constant and was more likely to be closer to the true value than the Jenkins et al. [1997] structure-activity relationship-based calculated rate. In the presence of high concentrations of NO_2, the alkoxy radical of α-pinene can react to form a nitrate as shown in R3.2.

$$RO\cdot + NO_2 + M \rightarrow RONO_2 + M \tag{3.2}$$

The production of nitrates via this pathway is not thought to be significant in the atmosphere because NO_2 concentrations are low and RO can react very quickly with O_2 and then decompose by C-C bond scission or isomerize through a 6-membered ring transition state [Atkinson et al., 1997].

3.1.1 α-Pinene nitrate OH-initiated reaction pathway

In this thesis the α-pinene β-hydroxynitrate (APN) isomers are referred to using the nomenclature correlating with the molecular structures presented in Table 3.3. Isomers 3-hydroxypinene-2-nitrate (APN-A), 2-hydroxypinene-3-nitrate (APN-B), and 6-hydroxymenthen-8-nitrate (APN-C). APN-A and APN-B are identical except the sites of the functional groups across the substituted carbon are reversed. A fraction of APN-A's precursor OH + α-pinene adduct, calculated to be 10% [Dibble et al., 2001] or 50% [Vereecken et al., 2007; Vereecken and Peeters, 2000; Peeters et al., 2001], is estimated to undergo breaking of the strained four-membered ring, form an internal double bond and become 6-hydroxymenthen-8-yl before reacting with NO to form APN-C. This mechanism for producing an α-pinene hydroxynitrate has yet to be experimentally confirmed but in quantum chemistry models this pathway was found to be energetically favorable. The calculated barrier height of the APN-C precursor peroxy radical formation is 12.2 ± 0.5 kcal mol^{-1} compared to C-H bond strengths of 95-100 kcal mol^{-1} [Vereecken and Peeters, 2000]. The nitrate formation branching ratio of the APN-C precursor peroxy radical is calculated to be 0.17 from modeling results [Vereecken and Peeters, 2000], meaning that 17% of the APN-C precursor peroxy radical RO_2 reacting with NO results in APN-C.
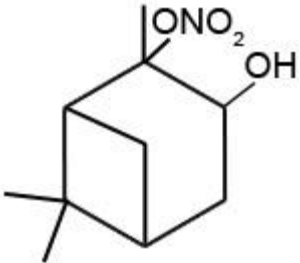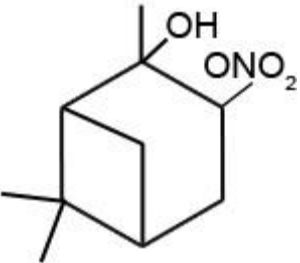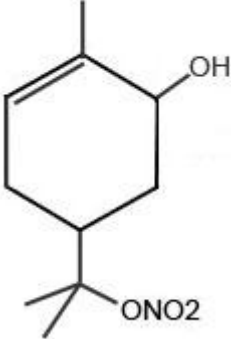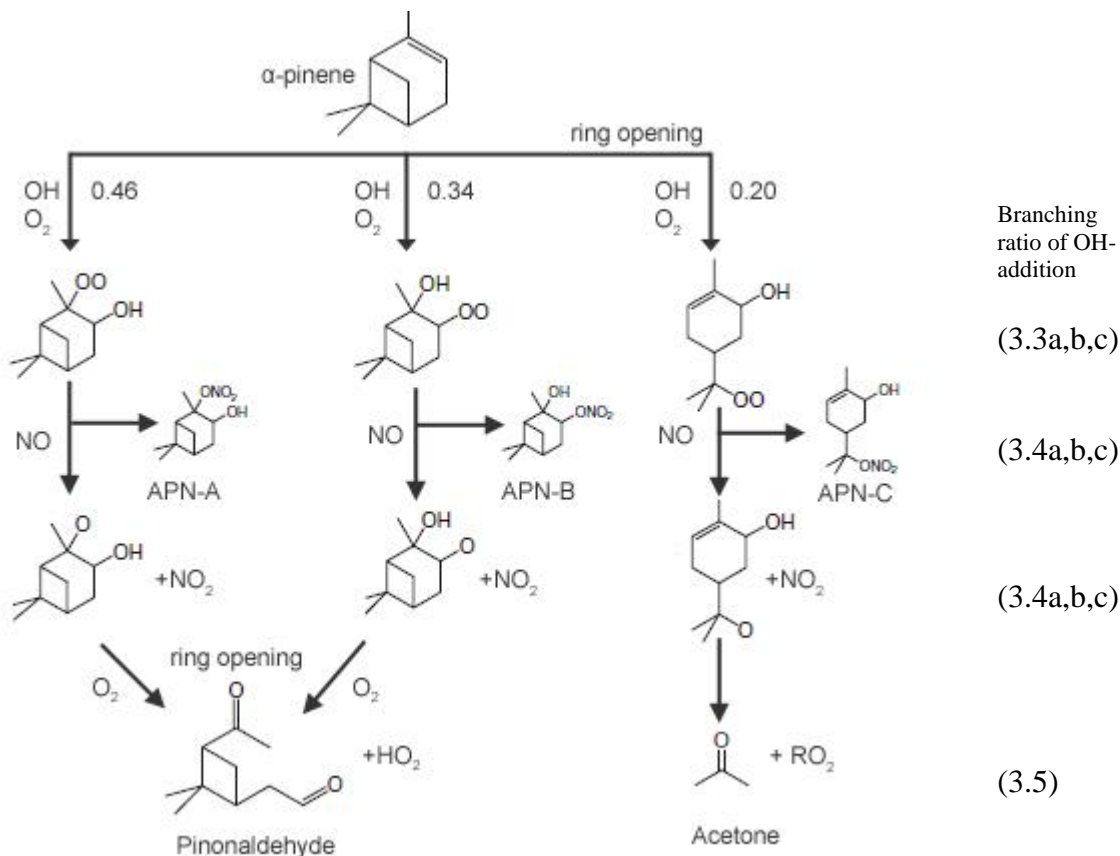
APN-A	APN-B	APN-C
3-hydroxypinene-2-nitrate	2-hydroxypinene-3-nitrate	6-hydroxymenthen-8-nitrate

Table 3.3: Three α-pinene nitrates produced from OH-initiated oxidation. APN-C has not been experimentally confirmed.

An OH-initiated α-pinene oxidation mechanism is presented in R3.3 - R3.8. In R3.3 the OH radical adds across the carbon double bond and the intermediate adduct quickly reacts with O_2 to form a hydroxyperoxy radical. The hydroxyperoxy radical RO_2 can react with NO to create APN through R3.4b or decompose to form an alkoxy radical RO and NO_2. A percentage of the OH + α-pinene adduct precursor of APN-A will rearrange itself and undergo ring-opening [Dibble et al., 2001; Vereecken and Peeters, 2000] forming a new α-pinene and OH adduct that eventually leads to the production of APN-C or decomposes into acetone and another RO_2. For the APN-A precursor, RO_2 calculations using structure-activity relationships calculated in Appendix A show that 66% of OH + α-pinene additions form an APN-A RO_2 precursor and 34% goes to form the APN-B RO_2 precursor. According to Vereecken and Peeters [2000] some 50% of the APN-A RO_2 precursors rearrange to form the APN-C RO_2 precursor while Dibble et al. [2001] estimates this occurs 10% of the time. This thesis uses the average of the two, or 30%, for calculation purposes. Taking 30% of the production of APN-A precursor and

attributing it to the APN-C precursor this translates to a 0.46, 0.34, and 0.20 branching

ratio respectively for the three APN precursors resulting from OH-addition to α-pinene.

$$HO_2 + NO \qquad \rightarrow OH + NO_2 \qquad\qquad (3.6)$$

$$NO_2 + h\upsilon \qquad \rightarrow O(^3P) + NO \qquad\qquad (3.7)$$

$$O(^3P) \; + \; O_2 + M \quad \rightarrow O_3 + M \qquad\qquad (3.8)$$

Due to the generation of NO_2 and HO_2 from the oxidation of α-pinene and the

photolysis of NO_2 leading to O_3 production, it is possible to create 2(1-α) O_3 molecules

per α-pinene oxidation reaction in R3.4a,b,c and R3.6 (where α is the branching ratio

$k_{3.1c}/(k_{3.1b}+k_{3.1c})$). When APNs are produced in R3.4a,b,c, the reaction is considered

terminated except for attrition through wall-loss and OH scavenging. The production of

the APNs and other oxidants lead to more stable products than the parent alkene due to

the saturation of the double bonds. With greater Henry's Law constants and overall de-volitilization of the α-pinene, APNs are a factor in the regional transport and sequestration of NO_x [Shepson et al., 1996].

3.1.2   Atmospheric chemistry impact

The current published APN yields are very divergent and indicate more experimental studies are needed. The experiments presented in this thesis attempt to identify and quantify individual α-pinene hydroxynitrates and compare them with the calculated theoretical yields and previously published results. These experiments will also produce a calculated $RO_2 + NO$ branching ratio α that determines the formation of α-pinene hydroxynitrates. These results are important for regions where ozone production is NO_x-limited, such as large urban centers in Northern America. According to measured reaction rates shown in Table 3.1, in normal atmospheric conditions 93% of α-pinene is oxidized by OH during the daytime making it an important driver of tropospheric ozone production and NO_x sequestration in the troposphere.

3.2 Description of Experimental Methods

The APN yield experiments presented here were conducted using a 5500L volume all-Teflon photochemical reaction chamber located at Purdue University in West Lafayette, Indiana. Starting reactants of α-pinene (Sigma-Aldrich, 99.5%), NO (Matheson, 1.0), and humidified air bubbled through purified water (Millipore) were introduced into the chamber and diluted in ultra-high purity zero air (Praxair, UHP ZAIR 5.0) to reach initial concentrations of 0.5 to 1 ppmv of α-pinene, 200 to 400 ppbv of NO, 20 to 50 ppbv of NO_2, and 30-40% relative humidity (%RH) prior to chamber irradiation.

70

Synthesized 1-octyl-nitrate ($CH_3(CH_2)_7 ONO_2$) was used as an internal standard, unless otherwise stated, for the gas chromatography electron capture detector (GC-ECD) instrument, which detected and measured the growth of APNs. Several supporting instruments were used to monitor the experimental conditions including an UV Photometric Ozone Analyzer (Model 49C, Thermo Environmental Instruments Inc, Franklin, MA) for O_3, a chemiluminescence $NO-NO_2-NO_x$ Analyzer (NO_x Analyzer, Model 42C, Thermo Environmental Instruments Inc, Franklin, MA) for NO/NO_2, an HP 5890 II series gas chromatograph flame ionization detector (GC-FID) for α-pinene consumption, and a humidity instrument (LI-COR LI-7000 CO_2/H_2O Analyzer).

The water vapor introduced into the chamber reacted with NO_2 through surface heterogeneous reactions [Lammel and Cape, 1996], forming nitrous acid (HONO) and nitric acid (HNO_3). HONO quickly photolyzed into OH and NO to start the OH oxidation of α-pinene in the chamber experiments. The reactions leading to OH radical generation are shown in R3.9 and R3.10 below:

$$2NO_2 + H_2O \xrightarrow{surface} HNO_3 + HONO \qquad (3.9)$$

$$HONO + h\upsilon \rightarrow OH + NO \qquad (3.10)$$

After the starting material was introduced into the chamber and the pre-experiment "blank" measurements of each instrument were taken, UV lamps were turned on and the experiment began. Measurements from the supporting instruments (for O_3, NO/NO_y, Δα-pinene, %RH) were conducted synchronously every 15 minutes, while the GC-ECD produced one complete measurement every hour. The experiment normally continued until all the initial α-pinene was consumed, although a few experiments continued in darkness with no dilution flow for wall-loss measurements. During the

experiment when NO levels dropped to less than 20 ppbv, another in-line injection of NO was introduced into the chamber to suppress O_3 growth and allow the experiment to continue. Otherwise the experiment would be terminated to ensure that no O_3 chemistry interfered with the OH oxidation products. The individual instrumental components of the experiment are discussed further below. Detailed step-by-step procedures used in operating the photochemical chamber for this experiment are included in Appendix D.

3.2.1 Photochemical reaction chamber

The experiments were conducted at T = 297 ± 4°K ambient temperature, 1 atm pressure inside the photochemical reaction chamber. The chamber is a cylinder with 1.8m diameter end plates set 1.85m apart and lined with a fluorinated ethylene/propylene copolymer (FEP Teflon) film. A bank of twelve solar simulator UV lamps (Sylvania 48″) are mounted on the inside of the chamber walls providing actinic radiation (λ_{max} = 370nm) for photolysis experiments. A Teflon-coated fan mounted to the top plate promoted even mixing of the reactants during experiments. Starting materials were introduced through the total of twelve ¼″ diameter Teflon lines that were attached via Teflon ports on either side of the chamber end plates. Samples from the photochemical reaction chamber could be drawn through the Teflon lines with pumps for analysis during the experiment. A photograph of the reaction chamber used in these experiments is shown in Figure 3.3 with the blackout outer walls opened to expose the Teflon chamber.

The primary target compounds in these experiments were multifunctional α-pinene hydroxynitrates, which are low in volatility and high in adsorptivity [Muthuramu et al., 1993], making it necessary to have short, heated sampling lines connected from the chamber into the GC-ECD sampling port to reduce line loss. For this purpose, the GC-

ECD was placed within 2m of the closest port opening and the connecting Teflon tubing was heated to 100°C by thermal heating tape controlled by a temperature controller (Omega Corp.).

Figure 3.3: The photochemical reaction chamber.

Before every experiment, air from a clean air generator (Whatman model 74-5041NA), followed by a tank of ultra-high purity zero air, was flushed through the chamber at a rate of ~9L min^{-1} to purge residual products from previous experiments and room contaminants. Reactants were added to the chamber by syringe injection inside a glass tee stopped with a high-temperature septum and volatilized with a heat gun. The vaporized reactant was transported into the chamber with zero air gas flow (Praxair, UHP 5.0) set to 10 L min^{-1} for initial injections and reduced to 2.2 L min^{-1} for dilution flow during the experiment to replenish the chamber air volume lost to the sampling volume drawn from each analytical instrument. While zero air was used as the carrier gas during injection most of the time, during NO injections a tank of N_2 (Praxair, UHP 5.0) was used

instead to prevent the rapid oxidation of NO to NO_2 due to R3.11. The NO to NO_2 oxidation reaction R3.11 is second order in NO so O_2 was minimized during NO injection in order to reduce the starting NO_2 concentration.

$$2NO + O_2 \rightarrow 2NO_2 \hspace{4cm} (3.11)$$

The chamber was purged with air from the clean air generator continuously between experiments to flush out previously generated products, keep out room contaminants and maintain a slightly positive chamber pressure that was monitored with a pressure gauge. At least two full days of flushing the chamber with clean air was needed before a new experiment could be attempted. The cleanliness of the chamber could be ascertained with online instrumentation measurements as well as with a GC-ECD baseline measurement.

3.2.2   Materials and storage notes

The chemicals used in the experiment are listed in Table 3.4 and are used without further purification unless otherwise noted. The synthesis and purification of the organic nitrate and the 1-octyl-nitrate was discussed in Chapter 2. The organic nitrates and the 1-octyl-nitrate were stored in brown amber bottles and placed in a freezer to reduce sample photolysis, degradation, and evaporation.

Chemical	Source	Concentration	Notes
α-pinene	Sigma-Aldrich	98%	
α-pinene oxide	Sigma-Aldrich	97%	Epoxide
1-bromooctane	Sigma-Aldrich	99%	
silver nitrate	Sigma-Aldrich	>99%	
nitric acid	Fisher Scientific	>92%	Fuming
nitrous oxide	Matheson	>99%	
cyclohexane	Sigma-Aldrich	99%	Anhydrous

Table 3.4: Chemicals and their corresponding sources and concentration

3.2.3 GC-FID instrument

The consumption of α-pinene during the photochemical reaction chamber experiments was measured using an HP 5890 Series II gas chromatography - flame ionization detector (GC-FID) instrument. A diaphragm pump pulled sample from the photochemical reaction chamber through a 3m length of Teflon tubing that was heated with a series of silicone rubber fiberglass heater strips (Omega Corp. Omegalux heaters) wound around the Teflon tubing. The heater controllers were set to maintain a constant temperature of 100°C to minimize surface adsorption during sampling. The Teflon tubing terminated at a stainless steel six-port valve (Valco) heated to 100°C where it entered a 1.5 cm^3 ¼″ o.d. stainless steel sample loop where a valve position switch allowed sample loading or injection into the 30m, 0.53mmID Rtx-1 column (Restek) with He (Praxair, UHP 5.0) carrier gas flowing at 10mL min^{-1}. The GC oven temperature was isothermal and set to 155°C while the detector temperature was set to 300°C. A schematic of the instrument is shown in Figure 3.4.
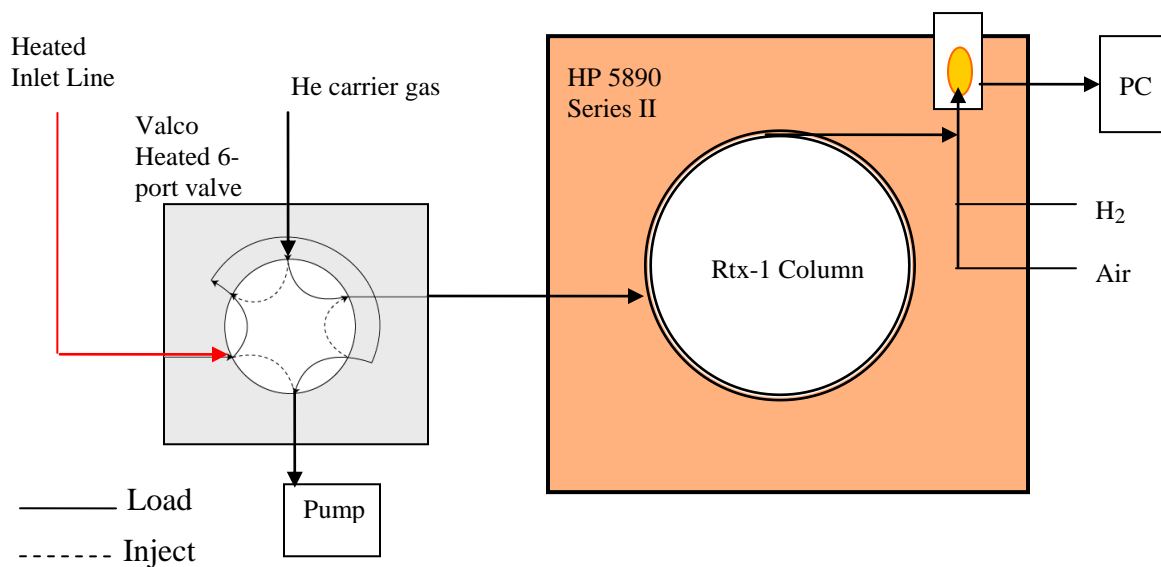
Figure 3.4: Schematic of the HP 5890 Series II GC-FID.

α-Pinene was separated with a retention time of ~4 minutes under these chromatography conditions. The FID flame was operated using a mix of hydrocarbon-free compressed air (Praxair 1.0) and purified hydrogen (Praxair UHP 5.0) with a flow ratio of Air:H_2 of 300:30 mL min^{-1}. A schematic of the FID detector assembly is shown in Figure 3.4b. Analyte exiting the end of the column and entering the bottom of the detector cell is ionized by the hydrogen-air flame.
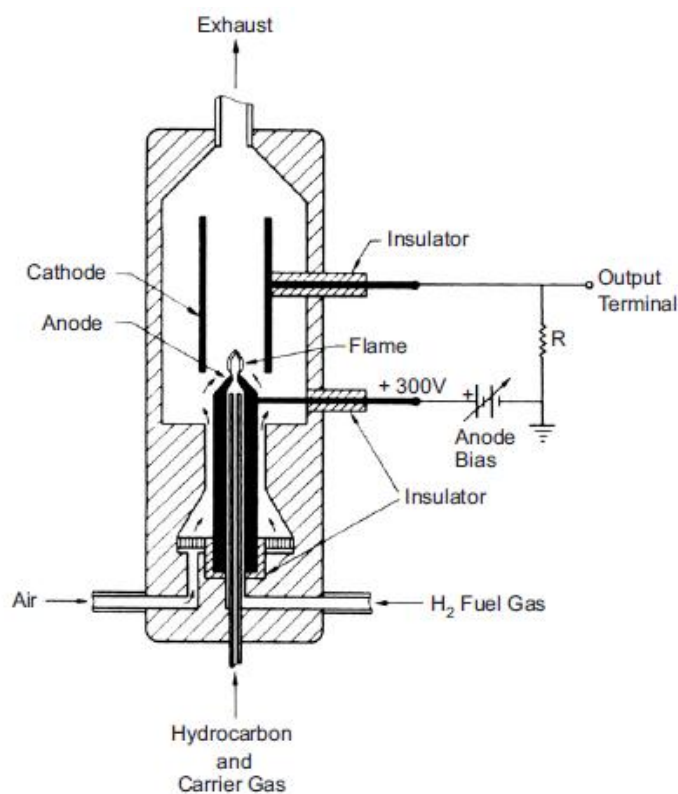
Figure 3.4(b): Schematic of a FID detector assembly [Scholfield, 2007].

The chemi-ionization step is shown in R3.12 [Schofield, 2008].

$$CH + O \rightarrow HCO^+ + e^- \tag{3.12}$$

The negative electrical gradient applied between the flame tip and a collector electrode accelerates the positively charged ions towards the negatively charged collector. The resulting induced current in the collector is detected by an electrometer that amplifies the signal and converts it into an analog voltage signal that can be sent to an

external computer logger program. The amplitude of the signal is proportionate to the amount of electrons generated from the analyte. The GC-FID is excellent at detecting hydrocarbons and other carbon-containing compounds while allowing water, inert gases, and oxygenated carbon species to pass through undetected [Colket et al., 1974].

3.2.4   GC-ECD instrument

APNs were detected using a gas chromatograph – electron capture detector (GC-ECD) analytical instrument. The GC-ECD is a custom benchtop instrument that differs from its commercial counterparts most noticeably by lacking a massive and energy-intensive oven to heat the analytical column. A schematic of the benchtop instrument is shown below in Figure 3.5.
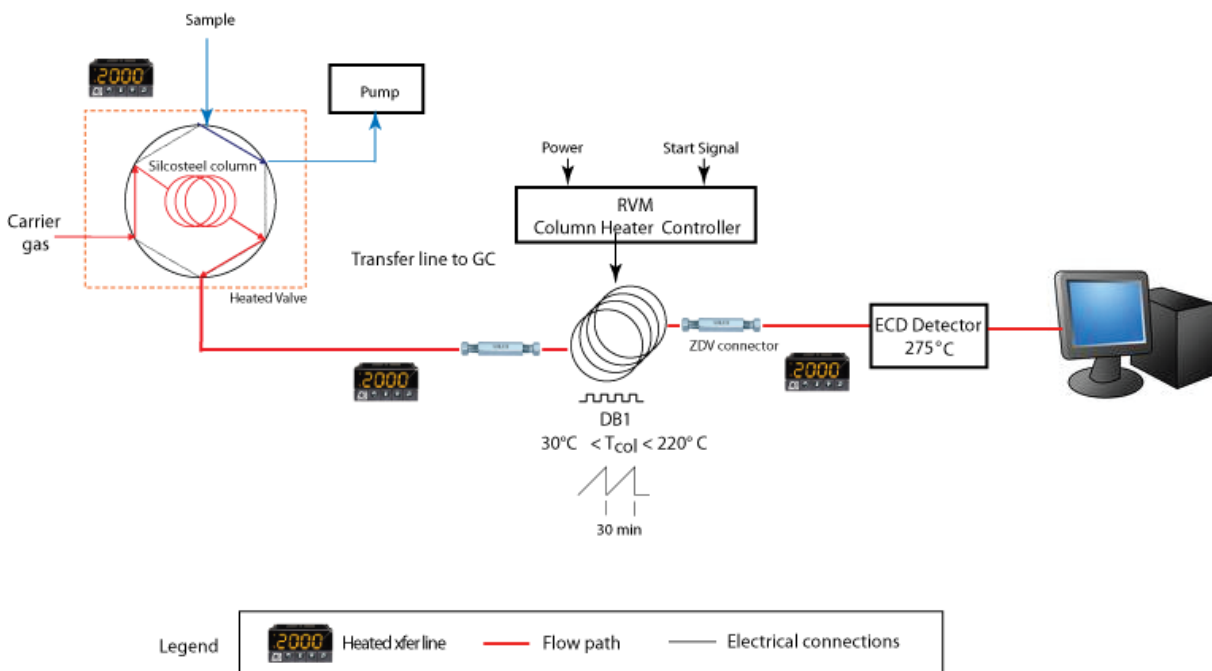
Figure 3.5: Schematic of the GC-ECD instrument. The 6-port inlet valve connects to a 30m Rtx-1 column that separates analytes before carrier gas sweeps them into the ECD detector cell whose signals are recorded by a computer logging program.

77

The inlet port of the GC-ECD is a 6-port valve (Valco) that was heated to 120°C. The valve switched between two positions, one that purged the 1.8 cm^3 1/16″ o.d. stainless steel sample loop with helium carrier gas (Praxair, UHP 5.0), and one that flowed helium carrier gas at a flow rate of 9mL min^{-1} to load sample onto the analytical column.

The analytical column used in the GC-ECD was a 30m 0.25mmID Rtx-1 (Restek) 7.6cm diameter coiled column insulated with fiberglass wool, covered with aluminum sheathing, and heated with intertwining heating wire controlled by a temperature controller (LTM A68 RVM Scientific, now Agilent Technologies). The analytical column was connected to the electron capture detector (SRI Instruments, mounted in a Model 110 GC chassis) via transfer lines heated to 100°C. The detector output was recorded by a USB data acquisition device (Measurement Computing Corporation USB-1408FS) with a custom Labview 8.0 logger program. A photograph of the analytical column unit mounted on the instrument is shown in Figure 3.6a. A top-down view of the column module with the wrapped column coil is shown in Figure 3.6b.
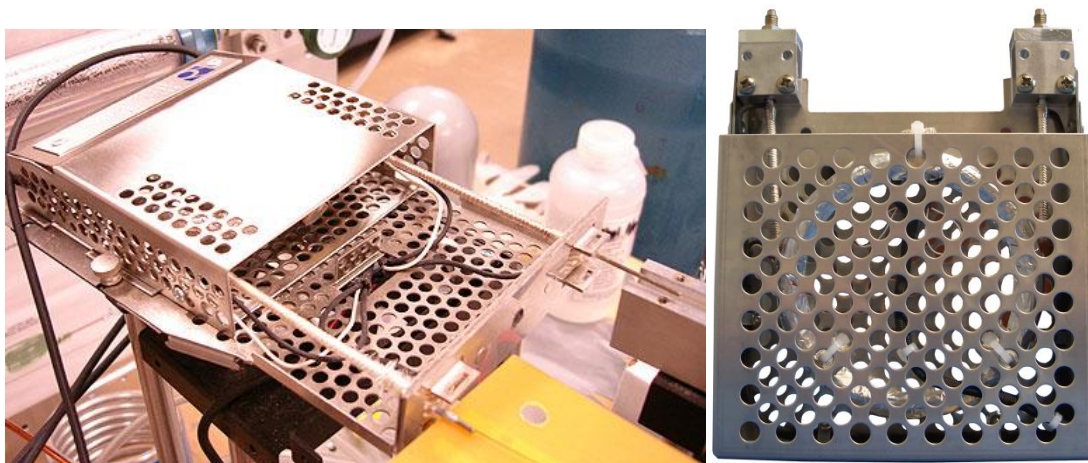
Figure 3.6: (a) A 30m long coiled Rtx-1 wrapped analytical column module.
(b) Top-down view of column module.

A fan mounted beneath the aluminum casing allowed for rapid cooling of the column unit. Because the columns were not enclosed in a conventional GC oven, the post-analysis cooling step was much more rapid and did not require the use of cryogenic consumables. During analysis a temperature ramp was applied to the analytical column. The ramp started by holding the column temperature for 4 minutes at 30°C after the inlet valve had been switched to inject the sample onto the column. Since the target APNs did not elute at 30°C, no further cryocooling was needed to pre-focus or trap the analyte. Four minutes was sufficient to purge the 1.8mL volume sampling loop and load analyte onto the analytical column. After 4 minutes the temperature increased at a rate of 20°C/min to 105°C. Then the temperature program slowed the ramp to 1°C/min to 125°C. Finally the temperature program concluded with a 45°C/min ramp to 250°C and held for 5 minutes to bake out the column in preparation for the next analysis. Using this program, the proxy calibration standard 1-octyl-nitrate eluted at 700s in the GC-ECD and APN-A, APN-B, APN-C eluted at 1055s, 1117s, and 1204s respectively.

The electron capture detector has a radioactive Nickel 63 source. The unstable isotope continuously emitted beta particles, fast electron equivalents that originated from the atomic nucleus. These fast particles collide and ionize the highly purified nitrogen (Praxair Research 6.0) make-up gas molecules. Hydrocarbon and oxygen traps (Restek) were placed in-line with the nitrogen tank to further purify the nitrogen before entering into the detector with a 35mL min^{-1} flow rate. The ratio of make-up gas to column carrier gas flow rate was kept at 6:1 to ensure a short analyte residence time in the ECD.

The Ni 63 source ionizes the nitrogen make-up gas, creating a stable cloud of N_2^- inside the detector cell when bombarded with beta radiation. The N_2^- is attracted to the

positive anode inside the detector, creating a stable baseline standing current. When electronegative compounds such as nitrates or halogenated species are introduced into the detector cell they quickly scavenge some of the electrons, producing a less mobile product, which then is more likely to be swept out of the ECD without being detected, thus reducing the standing current. The decrease of the standing current by the anode is proportional in amplitude to the analyte concentration. The detector electronics were designed to compensate for the change in the standing current by pulsing more current. This signal was then amplified and converted to an output as an analog voltage. The ECD detector cell is shown in Figure 3.7.
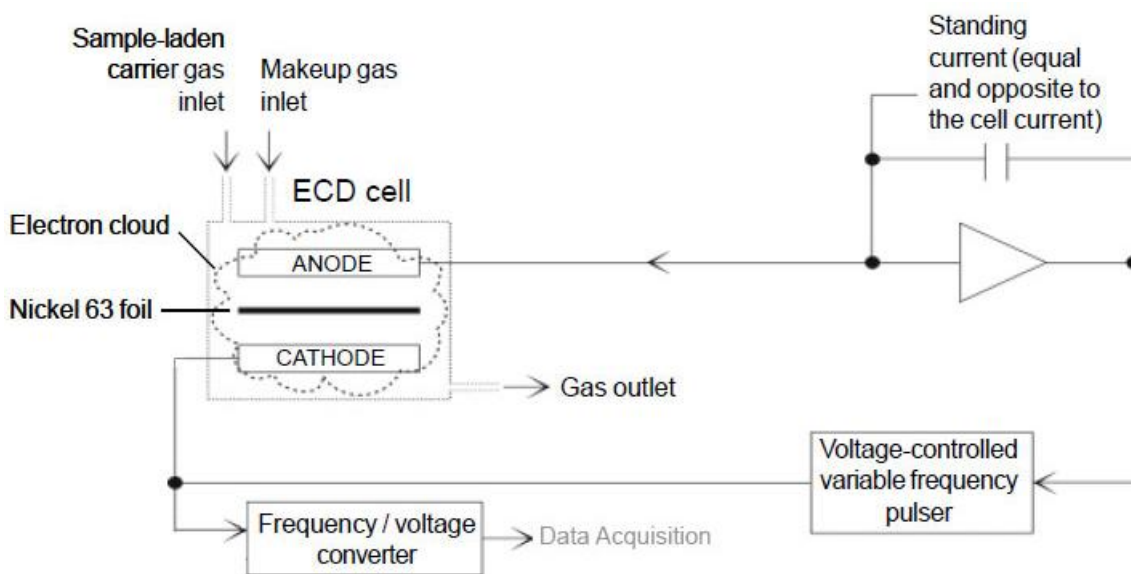
Figure 3.7: Schematic of an ECD detector cell [SRI Instruments].

3.2.5   GC-ECD/GC-FID Calibration

Calibrations for the GC-ECD and the GC-FID were performed before each experiment. A diagram of the injection setup used during calibration sample-making process is shown in Figure 3.8. The mean room temperature (which was air-conditioned) was $22 \pm 2°C$ according to temperature readings taken during experiments. Since the

mass flow controller is sensitive to room temperature, fluctuations during calibrations the temperature was recorded before, during, and after each experiment.
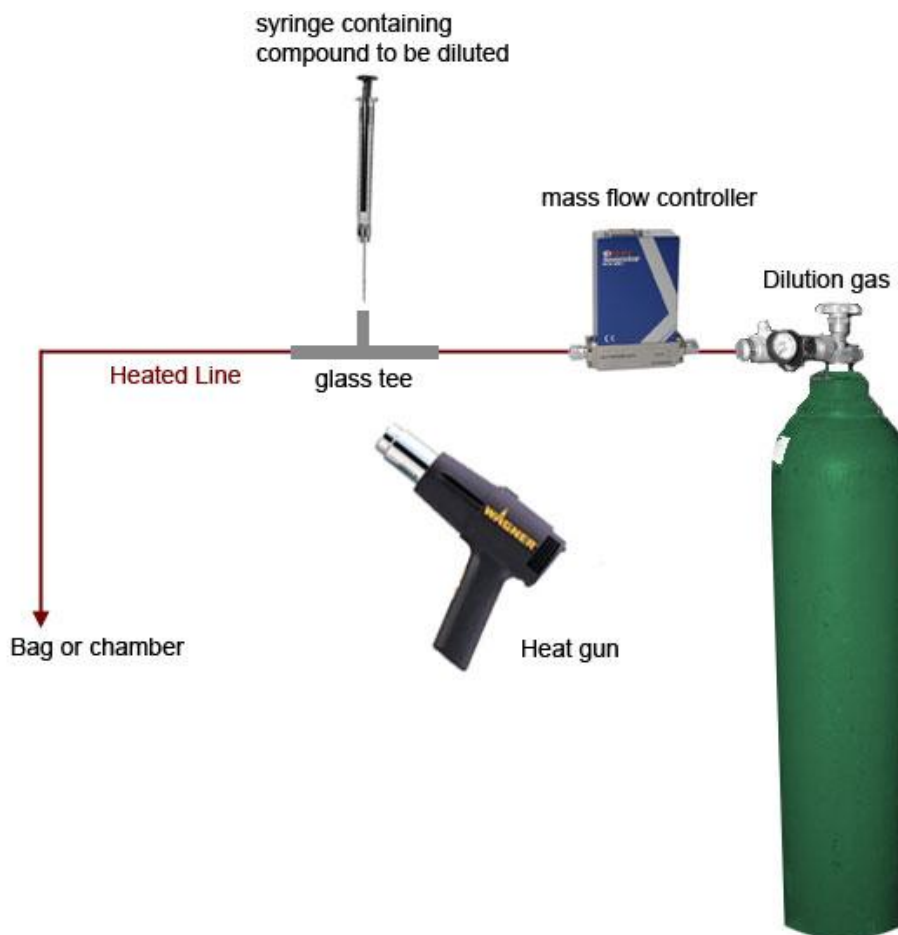
Figure 3.8: Injection setup schematic for calibration or chamber injection.

Calibration gases were prepared using Teflon bags filled with evaporated samples of either the α-pinene or synthesized 1-octyl-nitrate diluted in zero air. The liquid phase samples were injected using precision μL syringes (Hamilton Company Microliter syringe series) into the glass tee flowing with clean air controlled by a mass flow controller at 10L min^{-1}. A heat gun held underneath the glass tee helped vaporize the liquid sample and minimized adsorption onto the glass surface. Heated Teflon tubing connected to the glass tee carried the vaporized sample into a calibration bag or the

photochemical reaction chamber. Varying the injection sample volume allowed different

calibration concentrations to be created to determine detector linearity to the samples.

Figure 3.9 shows a sample calibration of 1-octyl-nitrate in the GC-ECD.
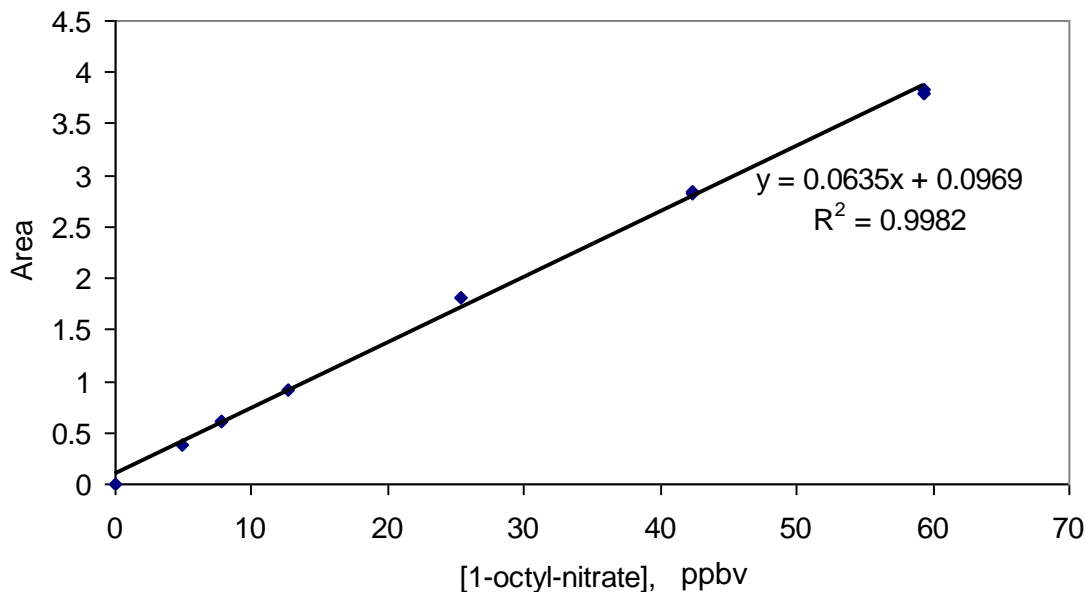
Figure 3.9: GC-ECD calibration curve using 1-octyl-nitrate diluted in cyclohexane.

The concentration of the calibration sample was calculated by dividing the

number of moles of analyte by the total moles of air in the calibration bag using the Ideal

Gas Law relationship and is shown in Equation 3.1.

$$ppbv = \frac{vol(ml) \times density(g/mL) \times purity \times R \times T(K)}{molecular\ weight(g/mol) \times chamber\ vol(L)} \times 10^9 \qquad \text{(Eqn 3.1)}$$

In Equation 3.1 the syringe uptake of liquid sample determined the volume of the

injection. The purity was determined by the manufacturer-stated purity of the standard or

by the NMR-determined purity of the 1-octyl-nitrate synthesized standard. The chamber

(or bag) volume was determined by the stopwatch used to time the flow meter controlled

dilution flow into a bag or chamber. The α-pinene calibration concentrations typically

ranged from 0-800ppbv, while 1-octyl-nitrate calibration concentrations ranged from

0- 50ppbv. The limit of detection for the GC-FID was 15ppbv as determined by calculating the quantity of 3 times the standard deviation of the baseline noise. Calibration plots for the GC-ECD and the GC-FID are shown in Figures 3.9, 3.10 respectively.

$$y = 5.6201x + 19.759$$
$$R^2 = 0.9958$$
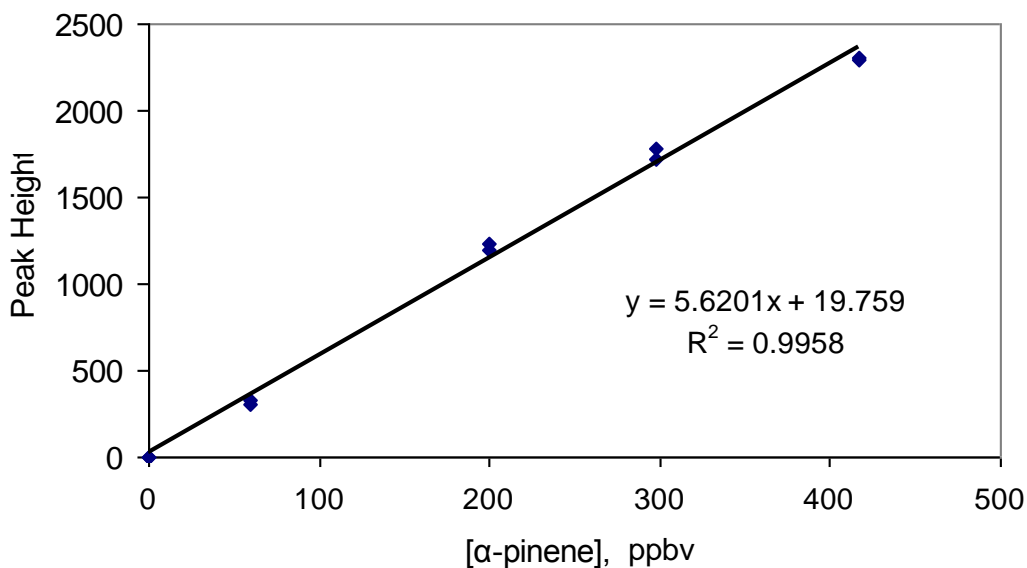
Figure 3.10: GC-FID calibration curve using α-pinene diluted in cyclohexane.

3.2.6 NO$_x$ analyzer

The NO$_x$ concentrations inside the photochemical reaction chamber were measured with a Thermo Environmental Instruments Model 42C NO-NO$_2$-NO$_x$ Analyzer. This instrument determined NO concentrations by reacting NO with O$_3$ in the reaction cell through the R3.9 and R3.10. During the reaction, photons were emitted and the chemiluminescence was monitored by the photomultiplier tube and converted to a ppbv reading.

$$NO + O_3 \rightarrow O_2 + NO_2^{\cdot} \tag{3.13}$$

$$NO_2^{\cdot} \rightarrow NO_2 + h\upsilon \ (590nm < \lambda < 3000nm) \tag{3.14}$$
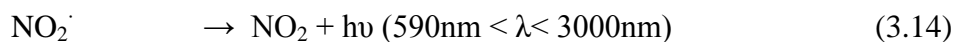
The sample drawn into the inlet line was passed through a molybdenum converter heated to 350°C. By reducing NO_2 and other oxygenated nitrogen species to NO and adding the NO concentration, the analyzer could measure a form of NO_y. Early in the irradiation NO_2 is estimated as NO_y-NO. NO_2 concentration was obtained by the subtraction of NO from NO_x. The analyzer alternated measurements of NO and NO_x every 10 seconds during operation. While the initial NO_2 measurement were valid, the rise of nitroxy compounds such as $RONO_2$ and HNO_3 in the experiment likely interfered with the NO_2 readings due to the molybdenum converter's efficiency at reducing these compounds to NO. The NO_2 concentrations measured from this instrument is therefore not reliable past the first hour during a photochemical chamber experiment and is only used as a reference for comparing against NO concentrations.

The detection range of this analyzer was 0.5ppbv to 100ppmv with a limit of detection of 0.4ppbv as determined from a calibration performed with NO_x concentrations flowed into the analyzer with a calibrated mass-flow controller. A schematic of the analyzer is shown in Figure 3.11.
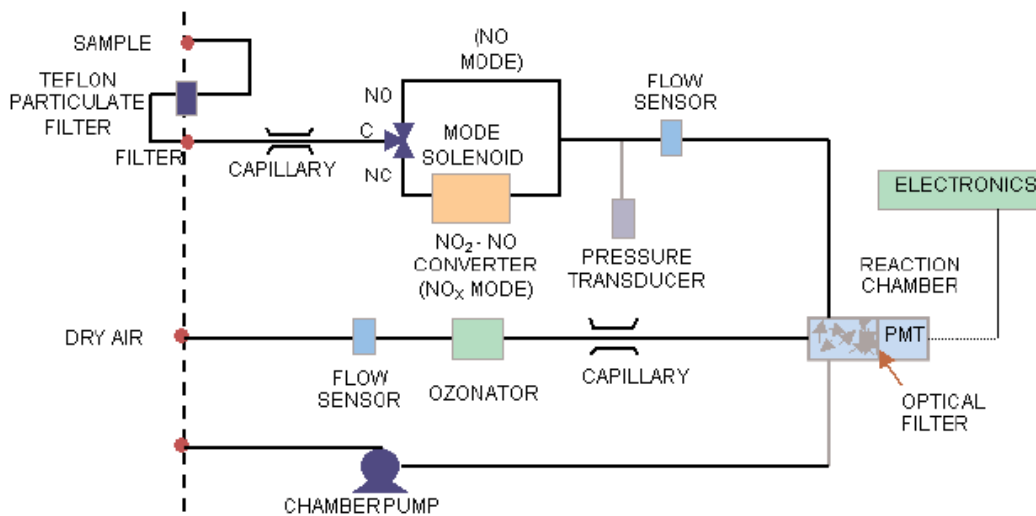
Figure 3.11: Schematic of the Model 42C NO$_x$ analyzer [Thermo Environmental Instruments].

3.2.7   O$_3$ analyzer

The Thermo Environmental Instruments Model 49C Ozone Analyzer measured ozone by utilizing a two-cell system where one cell was purged with reference air scrubbed of ozone while the other cell flowed sample air. When both cells were exposed to UV light the difference in UV absorption in the cells was interpreted as the ozone measurement. The spectral output of the UV lamp was centered at the wavelength (λ=254nm), which is strongly absorbed by O$_3$.

The detection range of the analyzer was 1 ppbv to 200 ppmv with a 0.5ppbv measurement precision as determined by a recent calibration performed on the analyzer by an external laboratory specializing in NIST calibrations. The shortcoming of this analyzer is that it can measure any other compound that absorbs at the same wavelength as ozone, so it was important to take into account whether or not there could be other compounds that may have been inadvertently included as an ozone measurement by this analyzer. A schematic of the analyzer is shown below in Figure 3.12.
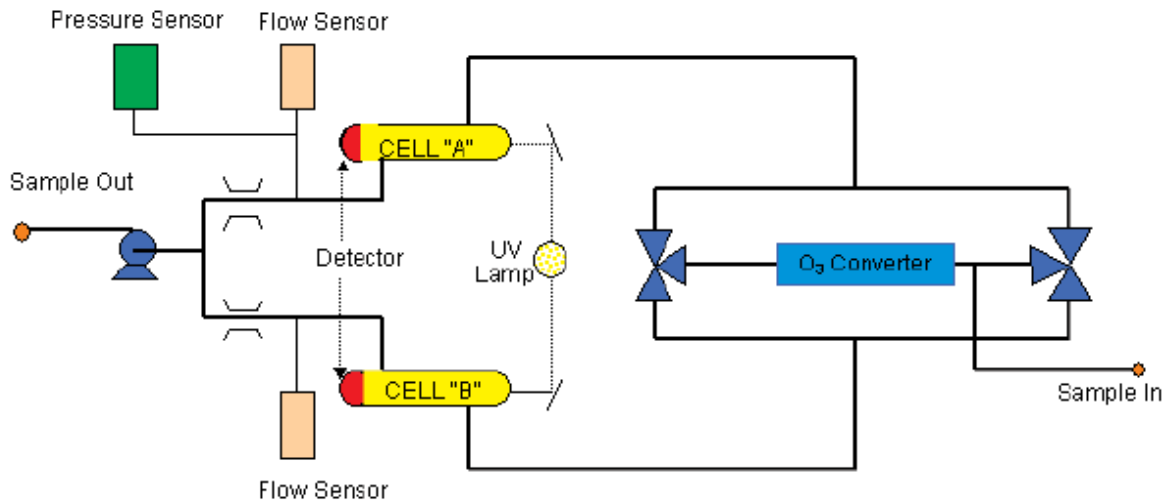
Figure 3.12: Schematic of the Model 49C ozone analyzer [Thermo Environmental Instruments].

3.3 Results

3.3.1 Wall-loss experiment

APNs are low in volatility and highly adsorptive, making chamber wall loss a potentially significant non-photochemical depletion process for the hydroxynitrates during chamber experiments. To correct for this loss process during data analysis, first-order chamber wall loss rates were determined for each APN. 40mL of synthesized APN solution was injected into the chamber and the gradual decrease in the peak areas was monitored in darkness, with no dilution flow for 8 hours to determine the loss rate for the three synthesized APNs. The time-dependent relation of the APN wall loss can be written:

$$k_{loss}[APN] = \frac{-d[APN]}{dt} \tag{Eqn 3.2}$$

Rearranging and then integrating from t = 0 to time t, we arrive at Equation 3.3.

$$\int \frac{-d[APN]}{[APN]} = \int \frac{k_{loss}}{dt} \tag{Eqn 3.3}$$

The integration of Equation 3.3 gives the relationship between the rate constant and the concentration of the APN in Equation 3.4.

$$\ln \frac{[APN]}{[APN]_0} = -k_{loss}t \tag{Eqn 3.4}$$

In order to measure the first order rate constant for the wall loss reaction, the linear plot of $\ln[(APN_t)/(APN_0)]$ with respect to time yields a slope that corresponds to the rate constant k_{loss}. Figure 3.13 shows this applied to a wall loss experimental result. The wall loss first order rate constant of APN-A is $1.1 \pm 0.6 \times 10^{-5}$ s^{-1}, APN-B is 4.3 ± 2.2

x10^{-5} s^{-1}, and APN-C is 3.7 ± 1.9 x10^{-5} s^{-1}. The error represents total experimental

uncertainty discussed in Section 3.3.4. From the results it can be seen that the wall loss

rate constant of APN-B was fastest, at 4.3x10^{-5} s^{-1} followed by APN-C at 3.0x10^{-5} s^{-1}, and

APN-A was slowest at 1.1 x10^{-5} s^{-1}.
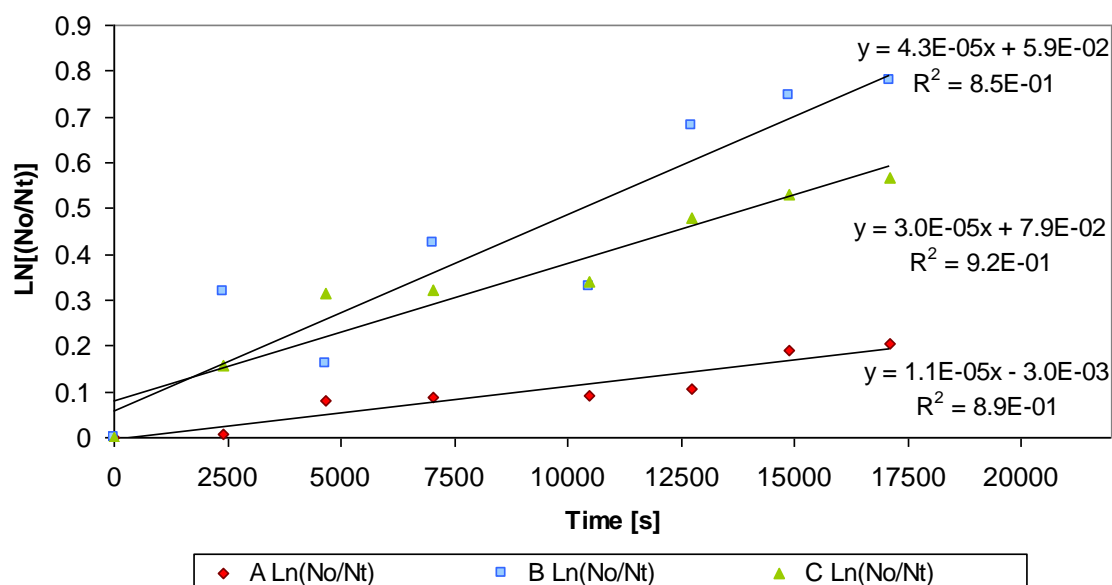
Figure 3.13: α-Pinene nitrate wall loss experiment results. The regression slopes represent the first order wall loss rate constants of the nitrate isomers.

3.3.2 Relative response experiment

While the ECD is very sensitive to electronegative compounds such as organic

nitrates, it responds differently to each class of compounds [Muthuramu et al., 1993]. In

order to make quantitative GC-ECD calibrations possible without the availability of pure

single-compound authentic standards, it was necessary to bridge the gap between the

substitute calibration compound - in this case 1-octyl-nitrate and APN. Using the GC-

ECD in conjunction with an independent analytical instrument, the absolute

concentrations of both the substitute standard and the organic nitrates were measured to

yield the relative response of the GC-ECD to both compounds. Determination of relative

response allowed calibration of the GC-ECD using only the substitute proxy standard.

The ideal methodology would be to use high performance liquid chromatography (HPLC) to individually separate and concentrate a single APN isomer, concentrating enough hydroxynitrate for injection via the glass tee into a Teflon bag as described for the calibration of the GC-ECD. However, insufficient individual APNs were created to separate and create a purified single α-pinene nitrate sample. Instead a previously separated isoprene nitrate (ISPN) prepared by Amanda Lockwood for her isoprene nitrate studies [2008 dissertation] was used.

The purified ISPN used in this experiment was (1,2)-ISPN shown in Figure 3.14. The (1,2) nomenclature terminology following established terminology referring to where the OH and ONO_2 functional groups are located in the molecular structure.
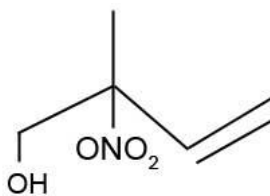
Figure 3.14: (1,2)-Isoprene nitrate used in the relative response experiment.

The independent analytical instrument used to determine the relative response was the Total Reactive Nitrogen Instrument (TRENI). TRENI thermally decomposes isoprene nitrates into NO_2, which is then photolyzed followed by measurement of the photon emitted when an excited NO_2 molecule, created when NO reacts with O_3, decays to its ground state. The reaction steps needed to convert $RONO_2$ to NO are shown in R3.15 and R3.16.

$$RONO_2 \quad \rightarrow \quad RO\cdot + NO_2 \tag{3.15}$$

$$NO_2 + h\upsilon \quad \rightarrow \quad NO + O \tag{3.16}$$

The quartz inlet tube of TRENI was heated to 400°C, which selectively energized and broke the relatively weak O-N bond releasing NO_2 from $RONO_2$. NO_2 was then

photolytically converted to NO and reacted with ozone through R3.7 and R3.8 and the emitted photons were detected with a photomultiplier tube.

A sample of the (1,2)-ISPN was vaporized by heating a 20uL liquid sample injected in the glass tee into a 35L Teflon bag flowing clean air using the same technique as calibrating the GC-ECD described previously. Due to the photosensitivity of ISPN, a large black opaque plastic bag covered the clear Teflon sampling bag so as to not allow ambient light to affect the sample. The Teflon bag and μL volume syringe used for this application were reserved exclusively for nitrate injections due to the irreversible adsorptivity of the organic nitrates and difficulty of cleaning all the interior surfaces.

The GC-ECD analyzed dilute gas samples of (1,2)-ISPN three separate times at different concentrations and coordinated with TRENI to sample as closely together as possible. Absolute ISPN concentrations as measured from TRENI were plotted against the chromatographic peak area from the GC-ECD to obtain a response calibration for the nitrate (Figure 3.15). The GC-ECD was then calibrated three times with isobutyl nitrate (IBN) over a concentration range of 0-40ppbv. The use of IBN rather than 1-octyl-nitrate in the relative response experiment was due in part to the measurement predating the 1-octyl-nitrate synthesis. It was also due to the Muthuramu et al. [1993] results that showed the relative response of 1-propyl, 1-butyl, and 1-pentyl nitrate in a GC-ECD was 0.83 ± 0.03, 0.78 ± 0.02, and 0.78 ± 0.02 respectively - all within 5% of each other and falling within the experimental uncertainty. From these n-alkyl nitrate results it was expected that 1-octyl-nitrate would respond similarly to 1-isobutyl-nitrate in the GC-ECD.

The relative response (RR) can be written as shown in Equation 3.5:

$$RR = \frac{S_{ISPN}}{S_{IBN}}$$
(Eqn 3.5)

The ratio of the slope of the linear fit of the ISPN calibration to the slope of the

linear fit of IBN calibration relates the instrument's response to an alkyl nitrate relative to

an alkene hydroxynitrate. With the assumption that the GC's response to 1-octly-nitrate is

the same as its response to IBN, the ratio could be used to correct the quantitative

concentration data from the GC-ECD when calibrating with the 1-octyl-nitrate standard.

Figure 3.15 shows a plot of the slope of both the IBN calibration and the ISPN

calibration. The S_{ISPN}/S_{IBN} ratio of the GC-ECD was calculated to be 1.44 ± 0.26. The

uncertainty for the relative response experiment is discussed in detail in Section 3.3.4.
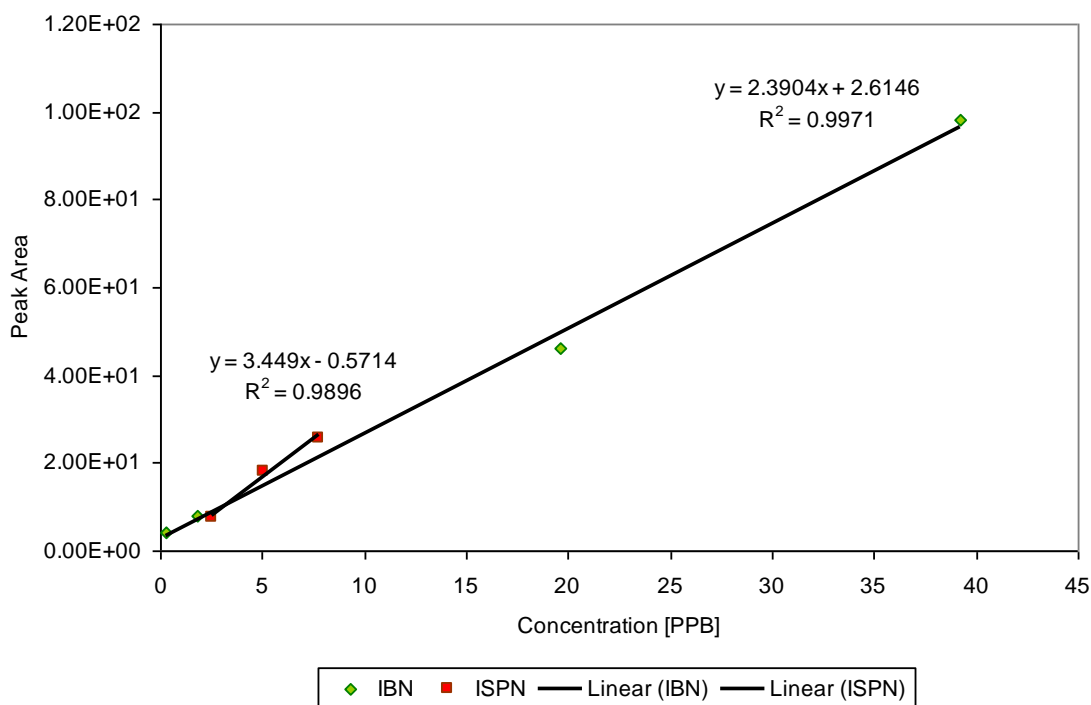
Figure 3.15: Relative response of the GC-ECD for IBN (green) and ISPN (red).

Muthuramu et al. [1993] previously measured the relative response to IBN for

several hydroxynitrates, with an ensemble average relative response of 1.19 ± 0.45 for a

95% (or 2σ) confidence interval. This result overlapped within the uncertainty of the

measured relative response of the GC-ECD in this thesis. In this thesis the relative

response of 1.44 was used for APN data correction during data analysis.

3.3.3 α-Pinene nitrate yields

Experiments involving the oxidation of α-pinene by reaction with OH in the presence of NO_x were conducted in the photochemical reaction chamber according to the procedures outlined in Appendix C. A series of five experiments are analyzed in this thesis. Appendix F presents the individual experimental results and calibrations of all five experiments in detail.

During each experiment, samples from the chamber were drawn by the GC-ECD to track APN growth, the GC-FID for α-pinene decay, along with NO and O_3 changes to gauge the photochemical processes that were present in the experiment. The change in the chromatographic peaks of APN and α-pinene over time provided evidence for the creation and destruction processes of the photochemical products. Using Equation 3.7 as the basis of chromatogram analysis, the degradation of α-pinene was plotted with increase in nitrate concentrations to calculate the yield of APNs. Figure 3.16 shows the change in chamber concentrations of key species α-pinene, NO, and O_3 for one experiment performed in May 15, 2009. The "NO_y" measurement is a measurement of NO_2 and any other nitroxy compound that can be reduced to NO for detection. In the first hour the NO_y is a good indicator of NO_2 but later on it is not usable as an NO_2 measurement. The NO_2 concentration is not used in the analysis except as an indicator of the NO to NO_2 ratio at the beginning of the experiment.
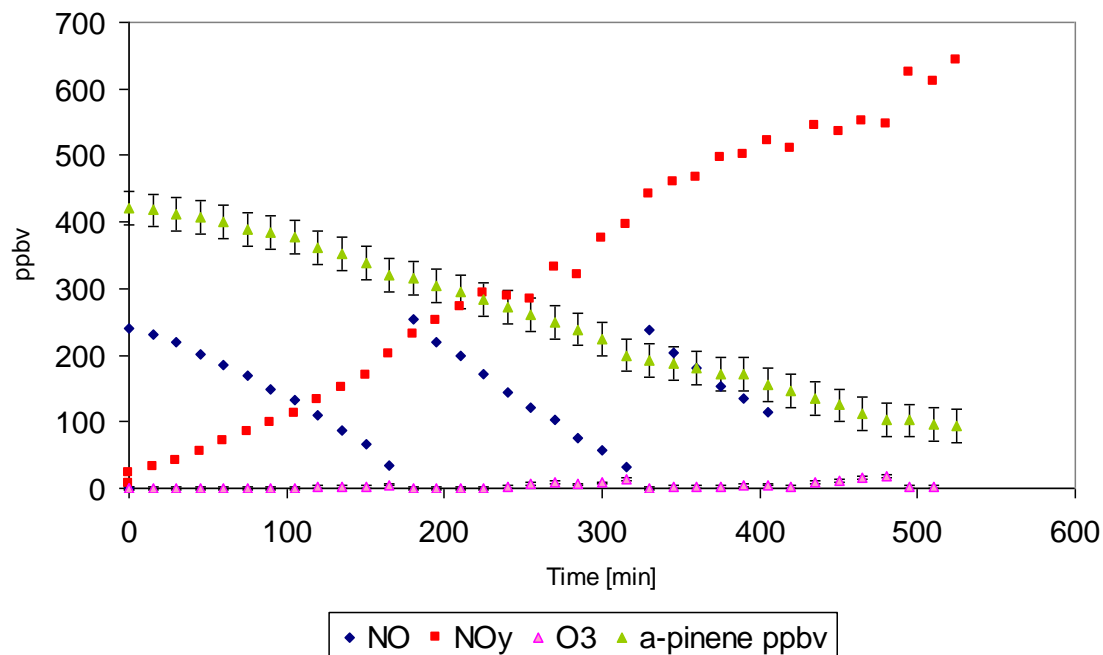
Figure 3.16: Chamber conditions during an experiment showing change in concentrations of NO, NO_y, O_3, and α-pinene over time.

Each data point in Figure 3.16 was collected in 15 minute increments and with error bars corresponding to the uncertainty in the associated analysis instrument. The NO concentrations were measured using the $NO/NO_2/NO_y$ analyzer, the α-pinene consumption by the GC-FID, and O_3 by the ozone analyzer. The initial $NO:NO_2$ ratio was kept as high as possible by minimizing NO_2 formation during NO injection into the chamber. As the NO concentration dropped during the experiment, the "NO_y" rose correspondingly. This indicated that NO was being converted by reaction with peroxy radicals generated via R3.1b and it was also being consumed in the OH oxidation of α-pinene to make APNs along with other nitroxy products.

The GC-ECD produced hourly chromatograms. Figure 3.17 shows the first chromatogram taken prior to chamber irradiation but after all the reactants were injected and is a "blank" used for baseline subtraction in the data analysis.
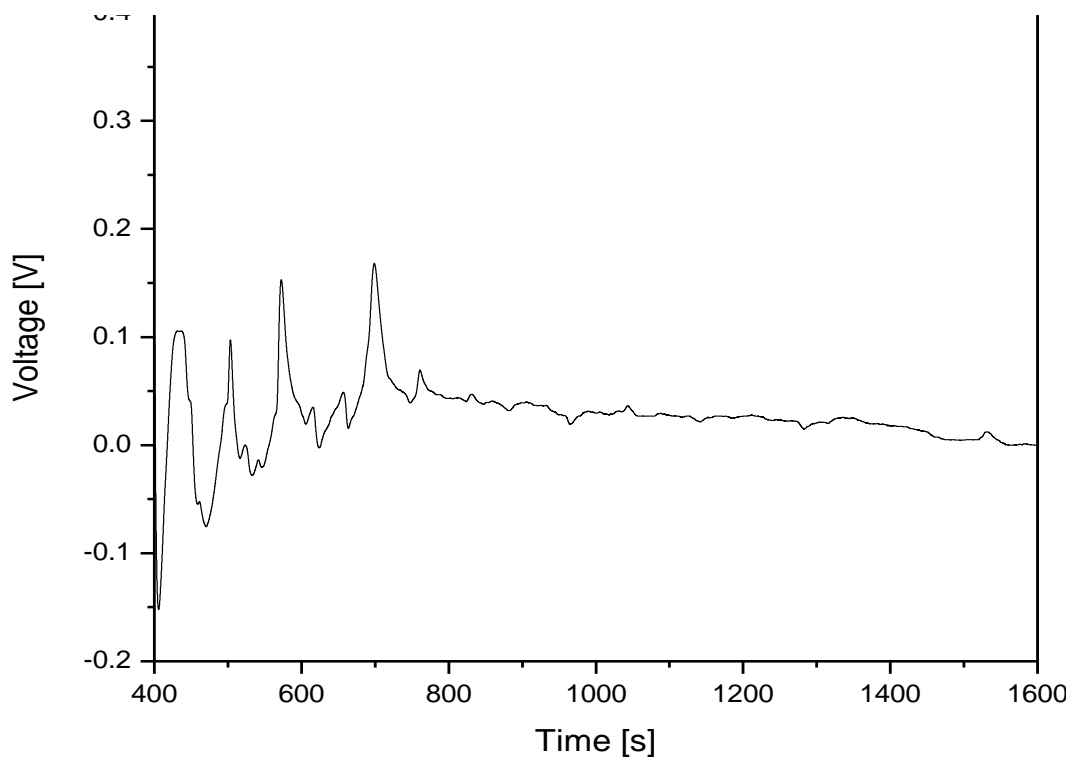
Figure 3.17: GC-ECD chromatogram from a chamber experiment with all reactants injected but prior to irradiation.

The 0-800s eluting peaks are attributable to volatile compounds already present in the chamber prior to the experiment. The chromatographic conditions were tuned to optimize the separation of analytes eluting between 112-120°C, which is a temperature range that was previously determined to correspond to the range of temperatures optimized for APN products from separating the synthesis mixture. This temperature range corresponded to 885s-1365s retention time in the GC-ECD chromatograms. Figure 3.19 shows the temperature ramp used in all of the GC-ECD analyses.
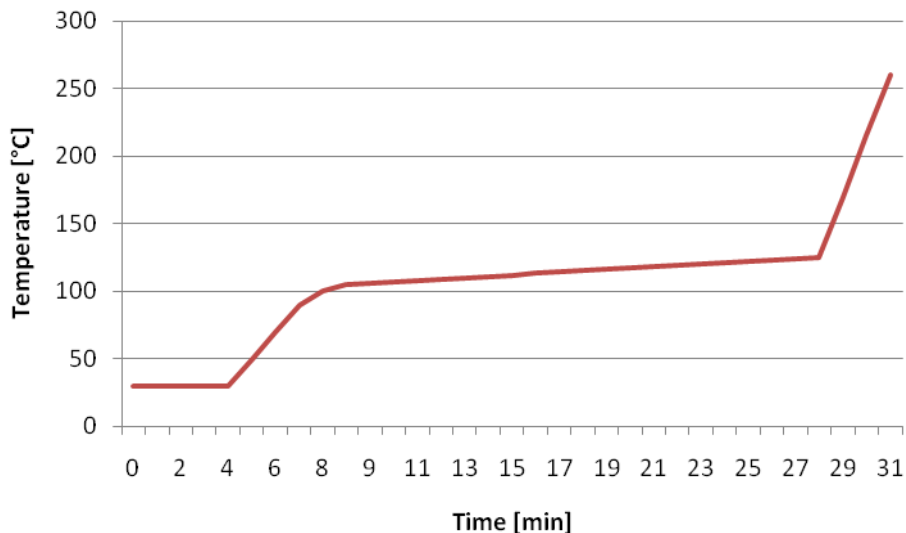
Figure 3.18: Temperature ramp applied to analytical column during a GC-ECD analysis.

A total of 8 to 12 GC-ECD chromatograms were obtained over the length of each successful experiment, which reflects the 8 to16 hour average experiment time. To prolong experiments, extra injections of NO were introduced into the chamber to keep O_3 below 10 ppbv at all times. This ensured that the observed products in the experiment were overwhelmingly the result of OH oxidation rather than ozonolysis.

Figure 3.19 shows a chromatogram typical of those near the end of the chamber irradiation experiments (in the 8th-12th hour of the experiment) in red trace overlaid with the synthesized APN chromatogram (black trace) to identify APN peaks. From the GC-MS results these three peaks were tentatively identified as three α-pinene nitrates. While the GC-MS mass fragmentation information lends a strong case for Peaks A and B to be identified as two α-pinene β-hydroxynitrate isomers, the identification of Peak C is much less certain, although it is likely some type of related nitrate. The corresponding peaks present in both the chamber experiment and in the synthesis are labeled as A, B, and C.
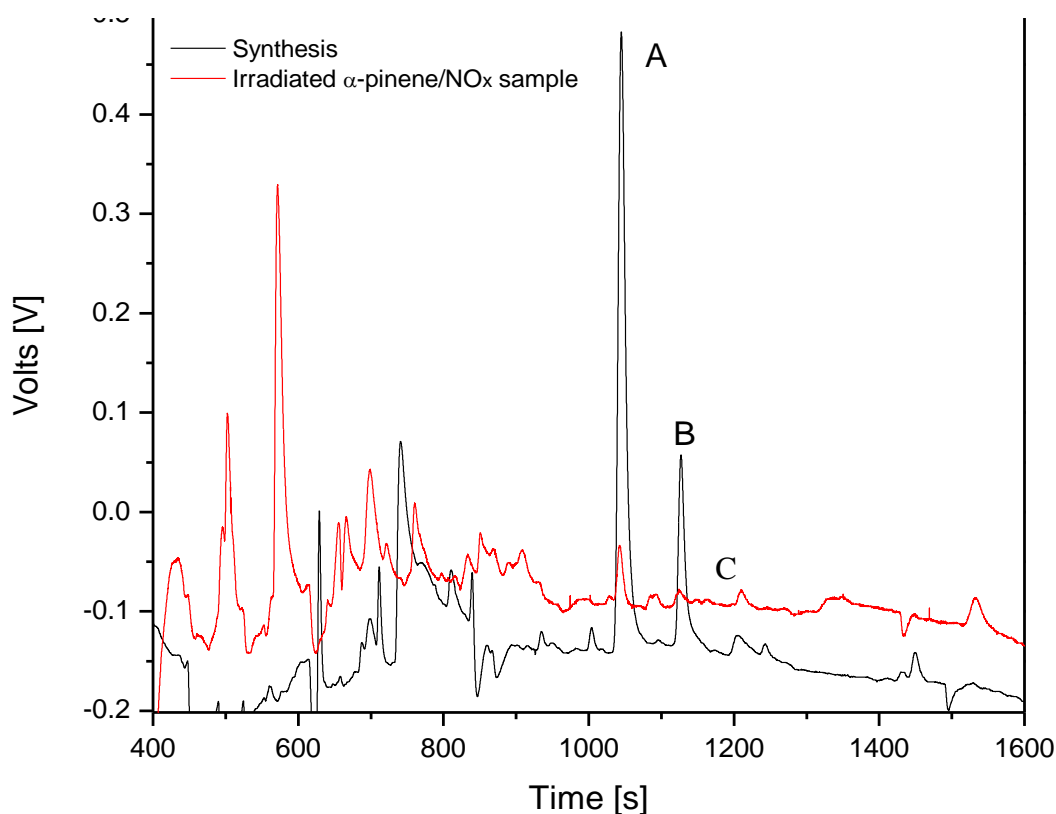
Figure 3.19: Chromatograph no.12 (12 hour) from a chamber experiment series overlaid with the synthesis mixture to identify overlapping nitrate peaks.

The identification of APNs in the chamber experiments was performed using a combination of information from the GC-MS analysis of fragmentation patterns in the α-pinene nitrate standard correlating to GC-ECD peak retention times and model results predicting the formation yields as discussed in Chapter 2. APN-A and APN-B have been detected previously as molecular weight 215 amu hydroxynitrate species [Aschmann et al., 2002]. APN-C may be a hydroxynitrate formed from isomerization of the APN-A OH + α-pinene adduct precursor, however its identification is uncertain and requires further experimental study.
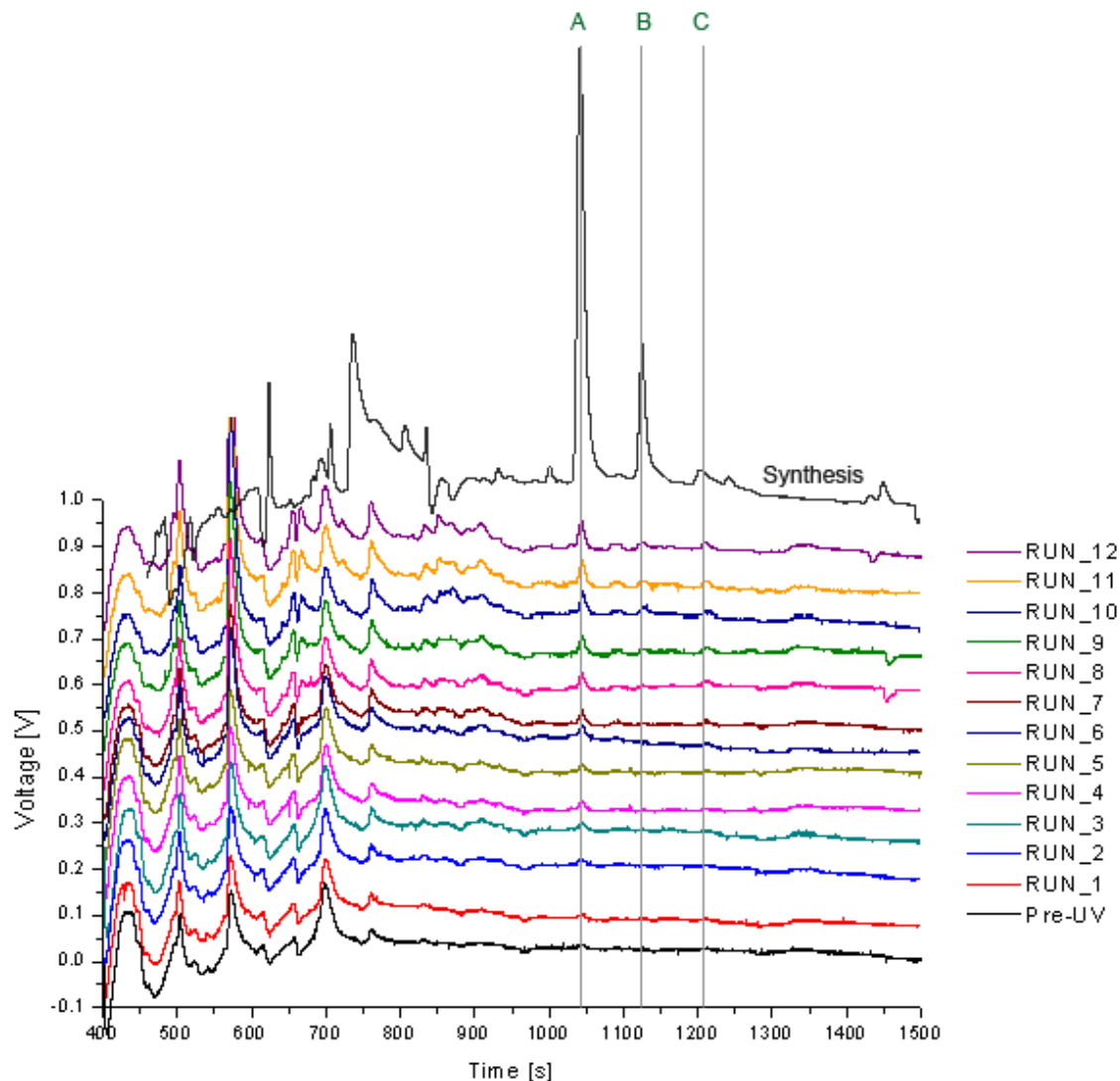
Figure 3.20: Growth of peaks over time in a full set of chromatograms from a single chamber experiment and an APN standard for comparison.

Figure 3.20 shows a complete set of GC-ECD chromatograms from one chamber experiment (May 15th, 2009) ordered by time starting from the pre-irradiation baseline chromatogram at the bottom to the final chromatogram at the top. An APN synthesis chromatogram (black trace, top chromatogram) was overlaid with the chromatogram sequence to aid in identification of the APN peaks. The chromatograms were processed individually for all three APN peaks by integrating and using the substitute calibration standard 1-octyl-nitrate to quantify the concentration in each chromatograph. The ECD

response is assumed to be identical for all three, and the relative response factor

(S_{APN}/S_{IBN}) of 1.44 was used in each case to correct for the APN concentrations.

The production rate of APNs can be written as a time-dependent equation

(Equation 3.6) where γ_i represents the fraction of time where the RO_2 precursor of each

APN is produced and α_i is the branching ratio ($k_{3.1c}/(k_{3.1b}+k_{3.1c})$) governing each APN

production. When APN production is simplified, it results in the relationship Equation

3.7 showing that the governing parameters in determining individual APN yields are the

probability of OH reacting with α-pinene to form the RO_2 precursor radical and the

branching ratio to form nitrates when reacting with NO.

$$-\frac{dRONO_2}{dt} = k_{OH} \cdot \gamma_i \cdot [OH] \cdot [\alpha - pinene] \cdot \alpha_i \qquad \text{(Eqn 3.6)}$$

$$APN_i \; Yield = \frac{d/dt[RONO_2]}{d/dt[\alpha - pinene]} = \frac{k_{OH} \cdot \gamma_i \cdot [OH] \cdot [\alpha - pinene] \cdot \alpha_i}{k_{OH} \cdot [OH] \cdot [\alpha - pinene]} = \gamma_i \cdot \alpha_i \quad \text{(Eqn 3.7)}$$
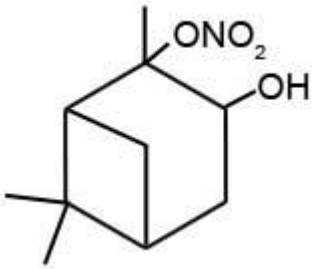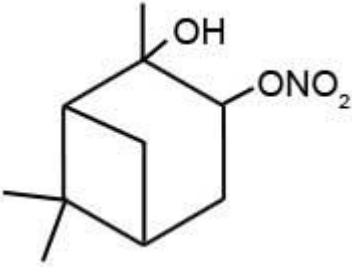
Each APN concentration was corrected for the relative response factor, dilution

air flow during the experiment, and OH consumption using the method described by

Atkinson et al. [1982]. Following the Atkinson method, a correction factor F for each

nitrate was determined using Equation 3.8. The correction factor F was necessary to

account for OH scavenging of nitrate species, which lowers the APN concentration in the

experimental data.

$$F = \left(\frac{k_{\alpha-pinene} - k_{APN}}{k_{\alpha-pinene}}\right) \left\{ \frac{1 - \left(\frac{[\alpha - pinene]_t}{[\alpha - pinene]_0}\right)}{\left(\frac{[\alpha - pinene]_t}{[\alpha - pinene]_0}\right)^{\frac{k_{APN}}{k_{\alpha-pinene}}} - \left(\frac{[\alpha - pinene]_t}{[\alpha - pinene]_0}\right)} \right\} \qquad \text{(Eqn 3.8)}$$

Here $k_{\alpha\text{-pinene}}$ is the OH + α-pinene rate constant and k_{APN} is the OH+APN calculated rate

constant, [α-pinene]$_0$ is the initial concentration of α-pinene, and [α-pinene]$_t$ is the

concentration at time t. Atkinson et al. [1982] estimated the uncertainty of the F factor correction to be between ±15-20% for n-butane through n-hexane. That is adopted for the relative error of the F-factor correction.

The OH rate constant for each APN was calculated using the structure-reactivity relationship of Kwok and Atkinson [1995] (see Appendix A), which gives estimated site-specific OH rate constants for gas phase organic compounds based on the addition or abstraction of functional groups. The calculated reaction rate constants were found to agree within a factor of 2 when compared to available experimental values [Kwok and Atkinson, 1995]. The calculated OH + APN rate constant for each APN is listed in Table 3.5. From Table 3.5. The estimated reaction rate constants for OH+APN-A is 2.6 times faster than that for OH + APN-B and a little more than 1.5 times faster than that for OH+APN-C.

APN	*OH reaction rate constant*
A	$1.63\ (\pm 1.63)\ \times 10^{-11}\ cm^3\ molecules^{-1}\ s^{-1}$
B	$6.19\ (\pm 6.19)\ \times 10^{-12}\ cm^3\ molecules^{-1}\ s^{-1}$
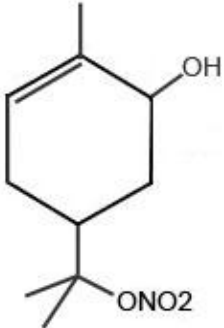
C (chemical structure)	$2.47\ (\pm 2.47) \times 10^{-11}\ \mathrm{cm^3\ molecules^{-1}\ s^{-1}}$

Table 3.5: Calculated APN + OH reaction rate constants.

Using the calculated OH+APN rate constants from Table 3.5, an average correction factor F would be 1.048 as indicated in Equation 3.9, using k_{OH} for α-pinene from Table 3.1 and OH+APN-A from Table 3.5.

$$F = \left(\frac{6.09 \times 10^{-11} - 1.63 \times 10^{-11}}{6.09 \times 10^{-11}}\right)\left\{\frac{1 - \left(\frac{501}{760}\right)}{\left(\frac{501}{760}\right)^{\frac{1.63 \times 10^{-11}}{6.09 \times 10^{-11}}} - \left(\frac{501}{760}\right)}\right\} = 1.048 \qquad \text{(Eqn 3.9)}$$

This correction factor F was calculated during analysis to correct for APN concentrations due to OH scavenging. (Appendix F shows all the F factor corrections for each experiment.) All the individual nitrate concentrations were multiplied by F to correct for loss through further OH reactions. The F factor rapidly increased with time, particularly for APN-A whose OH rate constants are larger. Toward the end of longer-running experiments the F factor was as large as 1.4, which represents a 40% depletion of the nitrate from OH scavenging.

According to Equation 3.2 the slope of total APN concentration plotted vs. the consumption of α-pinene represents the total APN yield for the experiment. The results from the set of experiments included in this work are listed in Table 3.6. The uncertainty of the measurement is ±51% as discussed in Section 3.3.4.

Date	APN-A [%]	APN-B [%]	APN-C [%]	Total Yield [%]
4/25/2009	6.2 ± 3.2	0.8 ± 0.4	2.2 ± 1.1	9.2 ± 4.7
4/29/2009	9.8 ± 5.0	3.1 ± 1.6	4.6 ± 2.3	18 ± 9.2
5/9/2009	6.7 ± 3.4	4.5 ± 2.3	4.8 ± 2.4	16 ± 8.2
5/12/2009	6.9 ± 3.5	4.0 ± 2.0	4.2 ± 2.1	15 ± 7.7
5/15/2009	6.6 ± 3.4	4.4 ± 2.2	4.9 ± 2.5	16 ± 8.2

Table 3.6 Individual Yields Of APNs from the yield experiments in this work.

The plot of the individual isomers along with the total APN yield is shown in

Figure 3.21 which combines all the data sets used in this work in one plot.
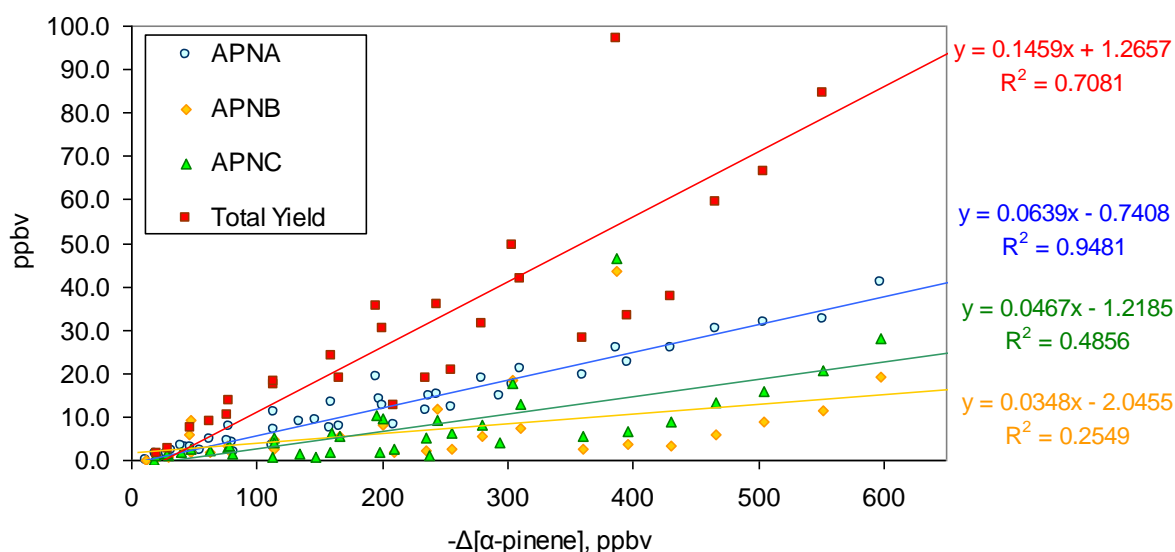
Figure 3.21: Individual and total α-pinene hydroxynitrate yields.

The linear regressions of the APN plots in Figure 3.20 give the yield of the APN

and the total nitrate yield listed in Table 3.7.

APN	Yield%	Propagated Error %
A	6.4	3.3
B	3.5	1.8
C	4.6	2.3
TOTAL	**15**	**7.7**

Table 3.7: Individual Yields of APNs.

The propagated error in Table 3.7 was calculated using Equation 3.12 and represents experimental uncertainties. The total yield for α-pinene hydroxynitrates is 15 ± 7.7%, in agreement with the Nozière et al [1999] results within the uncertainties. Although the exact identity of APN-C remains uncertain, the mass fragmentation information and APN-C's close elution temperature to the other α-pinene hydroxynitrate species indicate that it is likely to be a hydroxynitrate. Thus, its yield is included in the total yield calculation so that the results of these experiments may be compared with the the Nozière et al. [1999] result for total hydroxynitrates.

3.3.4   Error analysis

A 1σ standard deviation is equivalent to a 68% confidence interval shown in Equation 3.10 and is found by calculating the Student t-value test for 68% confidence interval with n-2 degrees of freedom (t_{n-2}) multiplied by the standard deviation of the APN slope (s_b). The uncertainties in this thesis are 1σ unless otherwise stated.

$$1\sigma \quad stdev = 68\% CI = t_{0.68,n-2} \times s_b \qquad \text{(Eqn. 3.10)}$$

The formula used to calculate APN concentrations from a 1-octyl-nitrate calibration curve as shown in Equation 3.11:

$$[APN], ppbv = \left[\frac{Area_S - Area_{blank}}{c} * RR \right] \qquad \text{(Eqn. 3.11)}$$

where $Area_s$ is the peak area from the chromatogram for the α-pinene nitrate sample compound, $Area_{blank}$ is the peak area from the blank measurement used for baseline subtraction, c is the calibration slope relating sample concentration to peak area (see Equation 3.1), and RR is the relative response between the (1,2) isoprene nitrate (1,2-ISPN) standard and the isobutyl nitrate (IBN) for the GC-ECD. The expression for the

propagated error (σ is one standard deviation) for organic nitrate concentration calculations is shown in Equation 3.12.

$$\frac{\sigma_{[APN]}}{[APN]} = \sqrt{\left[\frac{\left(\sigma_{Area\_s}^2 + \sigma_{Area\_blank}^2\right)^{1/2}}{\left(Area_s - Area_b\right)}\right]^2 + \left[\frac{\sigma_c}{c}\right]^2 + \left[\frac{\sigma_{RR}}{RR}\right]^2} \qquad \text{(Eqn. 3.12)}$$

The 1σ standard deviation of the uncertainty in the analyte peak area σ_{Area_s} was found by repeating integrations for a fixed concentration and finding the standard error (due to the fixed sample concentration used) of the integrations. Table 3.8 shows the results of one such experiment, which yields a standard error of 0.0164 for five repeated analyses from a 3.8ppbv sample 1-octyl-nitrate, yielding a standard error of 13.2%.

1-octyl-nitrate concentration	Peak Area
3.8	0.1194
3.8	0.1186
3.8	0.1263
3.8	0.1282
3.8	0.1272
Mean	0.1239
STDERR	0.0164

Table 3.8: Results from repeated sampling of a single concentration of 1-octyl-nitrate with the GC-ECD.

The uncertainty in blank peak areas σ_{Area_blank} was found similarly by statistically analyzing the standard error of the peak areas of five blank samples during calibrations and found to be 0.011. The uncertainty in the calibration sensitivity σ_c was calculated by taking five calibration curves (see Table 3.9 and Appendix F) and finding the standard deviation. The standard deviation of the calibration slopes is 0.010 with a mean slope of 0.056, resulting in an uncertainty of 18%.

Date	1-octyl-nitrate calibration	Slope (c)
4/25/2009	y = 0.0394x + 0.1365	0.0394
4/29/2009	y = 0.0511x + 0.0854	0.0511

5/9/2009	y = 0.0606x + 0.2519	0.0606
5/12/2009	y = 0.0629x + 0.3962	0.0629
5/15/2009	y = 0.0635x + 0.0969	0.0635

Table 3.9: Calibration curves from the five experimental data sets.

The uncertainty of the GC-ECD relative response (RR) to different alkene nitrates can be written in Equation 3.13.

$$\frac{\sigma_{[RR]}}{[RR]} = \sqrt{\left[\frac{\sigma_{ISPN}}{ISPN}\right]^2 + \left[\frac{\sigma_{IBN}}{IBN}\right]^2} \qquad \text{(Eqn. 3.13)}$$

In Equation 3.13 σ_{ISPN} is the standard deviation of the isoprene nitrate concentration, while σ_{IBN} is the standard deviation of the isobutyl nitrate concentration. These two uncertainties are determined by the calibration uncertainties, which are in turn determined by the injection and dilution procedures.

During the relative response experiment, the concentrations of both ISPN and IBN were measured by TRENI, which breaks the weak O-N bond in the nitrate functional group to release NO_2, which is further photolyzed to form NO. The uncertainty of IBN and ISPN are therefore linked directly to the 1σ confidence interval of their respective calibration slopes. The IBN calibration slope standard deviation is 0.091 while the slope is 2.39. The 1σ confidence interval for IBN is then calculated using Equation 3.10 and found to be 0.050 for a relative error of 2.1%. The calibration slope error for ISBN is 0.353 while the slope is 3.449. The 1σ confidence interval is thus 0.194 for a relative error in ISPN of 5.6%.

The 1σ uncertainty of the relative response can then be found in Eqn 3.15

$$\frac{\sigma_{[RR]}}{[RR]} = \sqrt{\left[\frac{\sigma_{ISPN}}{ISPN}\right]^2 + \left[\frac{\sigma_{IBN}}{IBN}\right]^2} = \sqrt{[0.056]^2 + [0.021]^2} = 0.06 \qquad \text{(Eqn. 3.15)}$$

However the uncertainty of the RR in Eqn 3.15 is not the total uncertainty since it is missing the accuracy error component. Making calibration samples of IBN and ISPN involve the use of a high purity standard solution, a precision needle syringe, a calibrated flow meter, and a stopwatch. The syringe volume is accurate to 0.1µL out of 10µL, for a 1% error. The manufacturer of the isobutyl nitrate did not provide a certificate of analysis for the uncertainty in the purity of the sample. However based on certificates of other nitro-compounds from Sigma-Aldrich with the same stated purity, the uncertainty is ±0.5%, which is used here. The chamber volume is dependent on the stopwatch, which is accurate to 0.01sec however the actual human timescale of operating with accuracy is 1s, which out of 5 minutes of operation is 0.3%. The dilution flow meter is reliable to 10% of the maximum flow rate of 100 L min^{-1}, or 1 L min^{-1}, which for an average flow rate of 10 L min^{-1} during dilutions presents a 10% source of error. The chamber volume is determined by the timer and the flow meter volume accuracy. These values give an accuracy error of 1% + 0.5% + 0.3% + 10%= 12%. When the accuracy error is added to the precision error for the relative response, the total RR uncertainty is 18%.

With the values for errors known, Equation 3.12 can be written as Equation 3.16 and when the accuracy error is added, the total error for [APN] is calculated to be 26%+18% = 44%.

$$\frac{\sigma_{[APN]}}{[APN]} = \sqrt{\left[\frac{\left(0.0164^2 + 0.011^2\right)^{1/2}}{\left(0.1094 - 0.003\right)}\right]^2 + \left[\frac{0.010}{0.056}\right]^2 + \left[\frac{0.06}{1.44}\right]^2} = 0.26 \quad \text{(Eqn. 3.16)}$$

The yield of APN can be written as Eqn. 3.15.

$$\frac{\sigma_{yield}}{[APN\_yield]} = \frac{[APN]}{\Delta[\alpha - pinene]} = \sqrt{\left[\frac{\sigma_{APN}}{APN}\right]^2 + \left[\frac{\sigma_{\alpha-pinene}}{\alpha - pinene}\right]^2} \quad \text{(Eqn. 3.17)}$$

The 1σ uncertainty of α-pinene measurements is obtained from the calibration curve, which follows the arguments for 1-octyl-nitrate uncertainty. Table 3.10 shows the calibration slopes for each of the experimental data sets analyzed in this thesis. The standard deviation of the slopes is 1.31, the mean is 6.19, and the relative error is 21%.

Date	α-pinene calibration	Slope (c)
4/25/2009	y = 6.9855x + 9.2381	6.9855
4/29/2009	y = 8.1068x -38.714	8.1068
5/9/2009	y = 5.0985x + 81.9	5.0985
5/12/2009	y = 5.1686x + 57.007	5.1686
5/15/2009	y = 5.6201x + 19.759	5.6201

Table 3.10: Calibration curves from the five experimental data sets.

The propagated precision error of the yield of APN is $\sigma_{yield/Yield} = [(0.26)^2+(0.21)^2]^{1/2} = \pm 0.33$. The total error for APN yields with the accuracy component added is

$$\sigma_{GC-ECD[APN\_yield]} = 33\% + 18\% = 51\% \qquad \text{(Eqn. 3.18)}$$

The GC-ECD uncertainty is 51% and used throughout this thesis as the cited error for APN yield calculations.

3.3.5 RO$_2$+NO Branching Ratio

The branching ratio α =$k_{3.1c}$/($k_{3.1b}$+$k_{3.1c}$), used to determine how often the reaction of RO$_2$ with NO results in organic nitrate production has been measured for several alkyl and alkene peroxy radical species [O'Brien et al., 1998; Arey et al., 2001; Aschmann et al., 2001]. Previous experimental work by O'Brien et al. [1998] and Arey et al. [2001] have shown that the branching ratio increased with increasing carbon number for both alkyl and alkene peroxy radicals. In an empirical mechanistic model Zhang et al. [2004] found a linear dependence between the branching ratio and carbon number with α = 0.0174 * CN + 0.0088 of the for C$_1$ to C$_7$ systems (Figure 3.22). If projecting this linear

relation forward to include C_{10} species, the branching ratio of α-pinene would be 0.18.

This is a reasonable forward projection based on the linear nature of the model results

with the addition of successive -CH_2- groups. However, it does ignore the impact of the

β-hydroxyl group and thus may overestimate the branching ratio by as much as 2x.
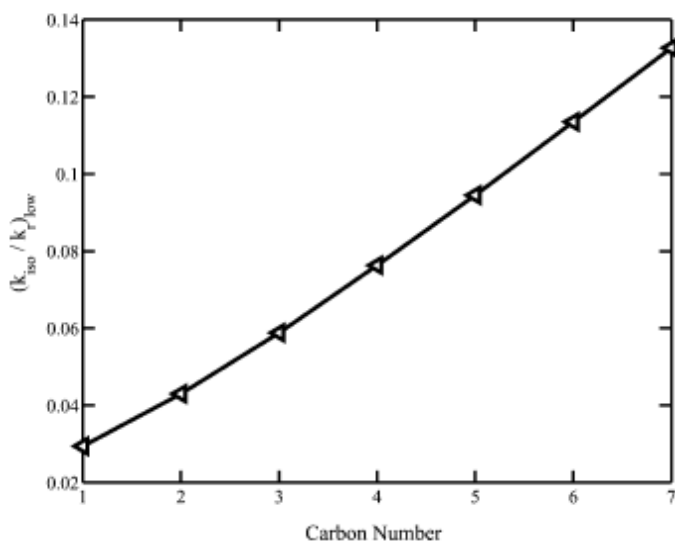

**Figure 3.22: Branching ratio α versus carbon number showing a linear increase
with carbon number [Zhang et al., 2004].**

Aschmann et al. [2001] performed experiments to determine three different C_{10}

alkyl nitrate branching ratios and reported 0.184±0.034, 0.244±0.044, 0.252± 0.052,

0.24±0.040 for n-decane with an average branching ratio of 0.233 ±0.040. This is ~30%

higher than estimated from the Zhang et al. [2004] linear relationship for a C_{10}

compound. This result is relevant to α-pinene nitrate branching ratios since n-decane is a

C_{10} compound like α-pinene, although it is not an alkene and does not have the β-

hydroxyl group.
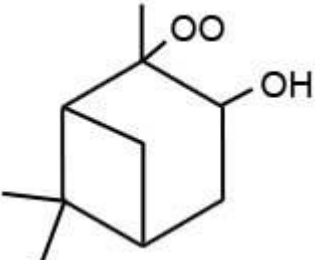
α-Pinene reacting with OH produces an RO_2 radical 95% of the time (Appendix

A). When the peroxy radical reacts with NO and forms an APN, its branching ratio is a

function of the initial RO_2 precursor. The production of the APN from its precursor RO_2

106

formation can then be written as Equation 3.19 and rearranged as shown in Equation 3.20.

$$\frac{d[APN_i]}{dt} = \frac{k_{3.1c}}{k_{3.1c} + k_{3.1b}} \frac{d[RO_2]_i}{dt} \qquad \text{(Eqn 3.19)}$$

$$\frac{d[RO_2]_i}{dt} = \frac{1}{\alpha_i} \frac{d[APN_i]}{dt} \qquad \text{(Eqn 3.20)}$$

Here APN_i is the species of APN and $[RO_2]_i$ is the precursor peroxy radical. To form a precursor RO_2 radical the initial hydroxyl radical must add across the double bond rather than abstract hydrogen, calculated to be 95% of the time. After this step the OH must add to one of the two carbon sites on either side of the double bond. The structure-activity relationship described by Peeters et al. [2001, 2007] was used to find the site-specific OH-addition ratio across the 1- and 2-carbons of 65:35 (see Appendix A). Since it was estimated that some 30% of the APN-A precursor OH+α-pinene adduct rearranges to form the APN-C precursor, APN-C is estimated to have an OH-addition adduct probability of 0.65*0.3 = 0.20. The RO_2+NO branching ratio is found by dividing the yield of individual APNs by the fraction of the time the precursor RO_2 radical is formed in OH-addition, shown in Table 3.11.

APN	RO_2 precursor	OH addition across double bond	OH addition site ratio	Yield From Table 4.3	Branching ratio $k_{3.1c}/(k_{3.1b}+k_{3.1c})$
A		0.95	0.46	0.064	0.15±0.09
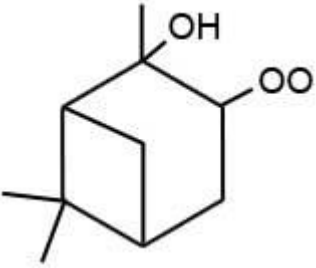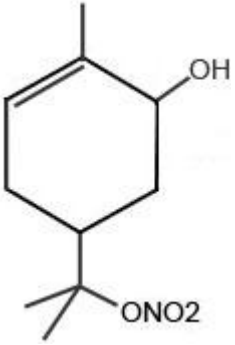
B		0.95	0.34	0.035	0.11±0.06
C		0.95	0.20	0.046	0.24±0.14
A+B+C	**Overall**	0.95	1.0	0.145	0.15±0.09

Table 3.11: Listing the branching ratios of each APN. The column "OH addition across double bond" refers to the fraction of time OH adds instead of abstracts hydrogen. "Branching ratio for OH site addition" refers to the site-specific OH addition to either side of the carbon double bond. "Yields" were taken from the results of Table 4.3 and the last column is the branching ratio for the $RO_2 + NO$ reaction resulting in the formation of the specific APN.

The branching ratios for APN-A, APN-B, and APN-C calculated from the results in this thesis are $0.064/(0.95*0.46) = 0.15±0.09$, $0.035/(0.95*0.35) = 0.11±0.06$, and $0.046/(0.95*0.20) = 0.24±0.14$ respectively. The overall branching ratio for the APN-RO_2+NO is $0.145/(0.95*1) = 0.15±0.09$. Since the branching ratio is determined by APN/([APN-RO_2]) the uncertainty is the error propagation of [APN] and [APN-RO_2]. Since the peroxy precursor radical is not measured directly, the uncertainty in [APN-RO_2] is tied to the error in the Kwok and Atkinson structure-activity relationship [1995], estimated to be 30%. Thus the 1σ uncertainty in the branching ratio is $[(0.51)^2 + (0.3)^2]^{1/2}$ $= 0.59$, which is used to calculate the uncertainty of in the branching ratio in Table 3.11.

The overall branching ratio is smaller but of similar magnitude to the Zhang et al. [2004] calculated branching ratio linear relation extended to a C_{10} system. The branching ratio of the APNs is smaller than for the C_{10} alkyl nitrate branching ratio of 0.23 in Aschmann et al. [2001]. This experimental result is consistent with the O'Brien et al. [1998] and Arey et al. [2001] observations that hydroxynitrate branching ratios are lower than the analogous alkyl nitrate counterpart.

In Table 3.11 the branching ratio of APN-C is significantly higher than that of APN-A and APN-B. This could indicate that APN-C is structurally different from the other two hydroxynitrates due to the presence of an internal double bond. The double bond of APN-C should allow the hydroxynitrate to react more quickly with radicals compared to the other two nitrates, which do not have an internal double bond. Experiments reacting APN-C with OH or ozone could cause it to dissipate faster than APN-A and APN-B, confirming the structural disparity between the C and the A and B nitrates.

In a series of C_2-C_6 alkene and OH reaction experiments O'Brien et al. [1998] found that the hydroxynitrate yields were substantially lower than their alkyl nitrate analogues. Molecular modeling gave evidence that the presence of the β-hydroxyl group interfered with hydroxynitrate formation [O'Brien et al., 1998]. This negative effect of the β-hydroxyl group could make the alkyl nitrate branching ratio an effective upper limit to the associated hydroxynitrate branching yields. However when this rule was applied to experimental results the evidence has been mixed. Isoprene nitrate yields have been reported to be between 4-15% [Chen et al., 1998; Tuazon and Atkinson, 1990] compared to the associated alkyl peroxy radical branching ratio of about 11% [Arey e al., 2001].

Chuong and Stevens [2002] measured a branching ratio of 0.15 ± 0.10 for nitrate formation from the reaction of NO + isoprene precursor RO_2 radicals. The Chuong and Stevens [2002] branching ratio is the same as the branching ratio reported in this thesis for α-pinene nitrates, although it should theoretically be less due to isoprene being a hydrocarbon with a smaller carbon number. Espada and Shepson [2005] reported cyclohexene nitrates branching ratios that were 15% that of cyclohexane nitrate branching ratios. This contrast in the branching ratio was attributed to the OH group having a similar effect as increasing the total number of methylene groups in a precursor radical because of inductive effects of the oxygen atom [Espada and Shepson, 2005]. Espada and Shepson [2005] also suggested that the presence of a cyclic aromatic structure in a β-hydroxy peroxy radical substantially decreases the branching ratio compared to a linear β-hydroxy peroxy radical.

Further relative branching ratio experimental studies should be pursued for α-pinene and other monoterpenes to compare against this set of results. Additional studies of alkyl and alkenes nitrates with $CN \geq 10$ should be studied to expand the branching ratio information beyond the lighter alkyl and alkenes. The experimental alkyl nitrate data can then be compared to monoterpene and sesquiterpene hydroxynitrate branching ratios when they become available.

3.4 Discussion

3.4.1 Nitrate yields and branching ratios

The total α-pinene nitrate yield was found to be $15 \pm 7.7\%$, which is consistent with the results of $18 \pm 9\%$ reported by Nozière et al [1999] and in contrast to the <1% yield by Aschmann and Arey [2000]. The individual APN yields were determined for

first generation α-pinene β-hydroxynitrates: APN-A is 6.4 ±3.3 %, APN-B is 3.5 ±1.8 %, and APN-C is 4.6 ±2.3 %. Although APN-C's exact identification is still in question it is likely a related hydroxynitrate and is included in comparison with published experiments detailing total nitrate yields.

The experimental data indicated that the most abundant APN isomer in the experiment was APN-A. This was largely due to OH adding preferentially to the less substituted site of α-pinene compared to the unsubstituted carbon. APN-B and APN-C were of similar abundance. The ratio of APN-A to APN-B and APN-C is 1.8:1:1.3. If APN-A and APN-C were lumped together due to their sharing the same OH + α-pinene adduct, the ratio of the 1-carbon to 2-carbon site addition in the initial OH-addition step is 3.1:1, which is larger than the results from the Peeters et al. [2001] structure-activity relationship, which predicted that the site addition ratio was 1.8:1.

The branching ratio of RO_2+NO was calculated to be 0.15±0.09 for APN-A, 0.11±0.06 for APN-B, and 0.24±0.10 for APN-C. The overall branching ratio of 0.15±0.09 is consistent with the estimated 0.18 branching ratio from the mechanistic model of Zhang et al. [2004]. It is also smaller than the alkyl nitrate branching ratio of 0.23 observed by Aschmann et al. [2001] for three C_{10} decane compounds.

3.4.2 α-Pinene nitrate atmospheric lifetime

The lifetimes of the APNs in the atmosphere undergoing OH reactions during the daytime (τ) can be expressed as Equation 3.16.

$$\tau = \frac{1}{k_{OH}[OH]} \qquad \text{(Equation 3.16)}$$

Since the OH reaction rate constant is much faster than O_3 and NO_3 is not important during the daytime, this is a good representative of the atmospheric residence time for the APNs. [OH] was assumed to be 1×10^6 molecules cm^{-3}, a typical daytime atmospheric mixing ratio [Prinn et al., 1992]. The k_{OH} used was the estimated OH+APN in Table 3.4 using Kwok and Atkinson [1995] structure-activity relationship methodology. Using Equation 3.16 the average lifetime time for APN in the presence of OH was calculated and listed in Table 3.12.

APN	OH reaction rate constant [cm^3 molecules^{-1} s^{-1}]	T daytime [hours]
A	1.63×10^{-11}	17
B	6.19×10^{-12}	45
C	2.47×10^{-11}	11

Table 3.12: OH reaction rate and calculated lifetime time of α-pinene nitrates.

The lifetime of all the APNs last a full daytime cycle or longer indicating the OH reaction acts on APN over a longer time period than α-pinene, which has a residence time of 11 minutes to a few hours [Atkinson and Arey, 2003]. The OH loss channel scavenging the APN is fairly restricted making APNs a reservoir for NO_x.

The relatively long lifetime of APN produced in the daytime obscures the fact that their higher Henry's Law constants (due to de-volatilization in the oxidation process [Shepson et al., 1996]) make them susceptible to wet and dry deposition. This causes the nitrates to terminate from atmospheric reaction processing and shorten their atmospheric lifetime. α-Pinene is a prolific source of SOA [Hatekeyama et al., 1989; Griffin et al., 1999a; Winterhalter et al., 2003; Bonn et al., 2007]. Yu et al. [2008] showed some evidence of organic nitrates being present in the secondary organic aerosols generated

from α-pinene OH reactions, although it was not certain what the source of the nitrate was and unclear whether it was organic or inorganic.

3.5 Conclusion

The reactivity of α-pinene nitrates in the presence of OH can sequester NO_x and transport it in the regional troposphere. The relatively long residence time of individual APNs in the atmosphere makes it appropriate to include this chemistry in regional and global atmospheric chemistry models. Giacopelli et al. [2005] reported calculated branching ratios of 0.058 and 0.15 for isoprene nitrates, while this work calculated a branching ratio of 0.11-0.24 with an overall branching ratio of 0.15 ± 0.09 for α-pinene hydroxynitrates. This is consistent with O'Brien et al. [1998] and Arey et al. [2001] observations that increased carbon numbers correspond to increased branching ratios. It also is consistent with previous observations that hydroxynitrate branching ratios are smaller than their unsubstituted analogues.

The total yield of APNs was found to be $15 \pm 7.7\%$. The individual nitrate yields for APN-A is 6.4 ± 3.3 %, APN-B is 3.5 ± 1.8 %, and APN-C is 4.6 ± 2.3 %. This result is consistent with the results of Nozière et al. [1999] and in contrast to the Aschmann et al. [2002] results of <1%. The atmospheric lifetime of these nitrates are on the order of 1-2 days, making it possible for them to influence regional atmospheres and participating in transport processes.

CHAPTER IV

Chemical Modeling of α-Pinene Nitrate Experiments

4.1 Introduction

The oxidation of monoterpenes can lead to the formation of organic nitrates that act as a NO_x reservoir and terminate the oxidation pathways leading to ozone formation as demonstrated in Reaction (R) 4.1 through R4.5.

$$C_{10}H_{16} + OH \quad \rightarrow HOC_{10}H_{16}\cdot \text{ (intermediate)} \tag{4.1}$$

$$HOC_{10}H_{16}\cdot + O_2 \quad \rightarrow HOC_{10}H_{16}OO\cdot \text{ (peroxy radical)} \tag{4.2}$$

$$HOC_{10}H_{16}OO\cdot + NO \rightarrow HOC_{10}H_{16}O\cdot \text{ (alkoxy radical)} + NO_2 \tag{4.3a}$$

$$HOC_{10}H_{16}OO\cdot + NO \rightarrow HOC_{10}H_{16}ONO_2 \text{ (α-pinene hydroxynitrate)} \tag{4.3b}$$

$$NO_2 + h\nu \rightarrow NO + O(^3P) \tag{4.4}$$

$$O(^3P) + O_2 \rightarrow O_3 \tag{4.5}$$
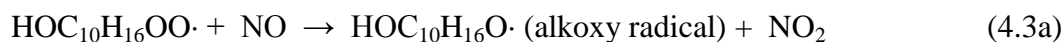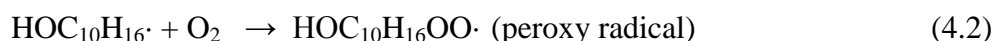
The photochemical chamber experiments discussed in Chapter 3 were simulated by a chemical model that takes into account the known rate constants for α-pinene OH reactions and combines it with mechanism protocols as suggested by the work of Jenkin et al. [1997]. The goals of this chapter include modeling the first-generation α-pinene hydroxynitrate yields from the reaction of α-pinene with OH in the presence of NO_x, assessing the sensitivity of the APNs to NO_2 concentrations, and suggesting future improvements of the model.

4.1.1   Previous α-pinene OH-oxidation mechanisms

Notable published models of α-pinene OH-oxidation chemistry include Peeters et al. [2001], Capouet et al. [2004], and Pinho et al. [2007]. There are others that

tangentially include the formation of α-pinene nitrates in the mechanism as a means to produce secondary organic aerosols, but these generally estimate a total nitrate production yield without explicitly calculating it from individual reaction pathways [Barthelmie et al., 1999; Chen et al., 2005].

The total α-pinene first generation nitrate yields determined by the Peeters et al. [2001], Capouet et al. [2004], and Pinho et al. [2007] models are tabulated in Table 4.1 with RO_2 + NO branching ratios. In the table "‡" indicates that the branching ratio is estimated from Eqn. 4.2 [Arey et al., 2001] for alkyl nitrates and "†" indicates the branching ratio is assigned by MCM v.3.1 [Saunders et al., 2002] based on the Peeters et al. [2001] structure-activity relationship.

Model	*Total Nitrate Yield (%)*	*RO_2+NO branching*
Peeters et al. [2001]	19±6	0.31‡
Capouet et al. [2004]	16.3±0.5	0.31‡
Pinho et al. [2007]	~22%	0.24†

Table 4.1: Comparison of model results of total nitrate yield from α-pinene oxidation in OH in the presence of NOx. Errors are standard deviations around the means.

Capouet et al. [2004] presented a near-explicit mechanism of 1500 reactions for α-pinene oxidation using the Nozière et al. [1999] results as a test case for the large mechanism. The mechanism lumped together classes of oxidants past the first generation products to simplify the reaction mechanism, making it a near-explicit mechanism and not a fully explicit mechanism. Only the main pathway of OH-addition via the 1-carbon or 2-carbon positions were included to the exclusion of the hydrogen-abstraction channels. Assumptions important to the model included the RO_2+NO reaction rate

coefficients, which were theoretical estimates based on the generalized temperature dependent expression recommended by Saunders et al [2003] for the C>2 peroxy radicals:

$$k = 2.54 \times 10^{-12} e^{\frac{360}{T}} \text{ cm}^3 \text{ molecule}^{-1} \text{ s-1} \qquad \text{(Eqn. 4.1)}$$

The branching ratio $\alpha = k_{4.3b}/(k_{4.3b}+k_{4.3c})$ of the RO_2 + NO reaction was based on Arey et al. [2001] expression shown in Equation 4.2, which is a function of only the carbon number "n" of the starting alkane.

$$k_{4.3b}/(k_{4.3b}+k_{4.3c}) = (0.0381 \pm 0.0031)n - (0.073 \pm 0.0178) \qquad \text{(Eqn 4.2)}$$

The branching ratio relation of Equation 4.2 was not a good fit for α-pinene, an alkene. Capouet et al.'s work predated the empirical alkene branching relationship shown in Zhang et al. [2004] and should be altered in the future to update the branching ratio. $RO_2 + NO_2$ reactions were ignored in the mechanism due to the negligible laboratory production as reported by Atkinson et al. [2003]. Wall loss rates were assumed to be the same as that of pinonaldehyde measured in Nozière et al. [1999] with a first order rate constant of 4.3×10^{-5} s^{-1} for all stable products.

Detailed permutations of various self-reaction and cross-reaction of RO, RO_2 and RO_3 species were included based on the recommendations of Atkinson et al. [2003]. The effects of these self- and cross-reactions in the presence of high NO would be expected to be limited based on the slow reaction rate constants (a geometric average of the self-reaction rates of the two species' undergoing reaction) and small relative concentrations. In laboratory experiments of Nozière et al. [1999], the NO concentrations were high, on the order of $(1-10) \times 10^{14}$ molecules cm^3, making RO_2+NO first order reactions rates on the order of 1000-10000 s^{-1}, overwhelming those of RO_2+HO_2 and RO_2+RO_2 channels.

The concentrations of ~600 species were reported and a few key species compared with the Nozière laboratory experimental results in Figure 4.1. The total nitrate yield from this model was 16.3±0.5%, somewhat lower than the experimental yield of 19±8% measured by Nozière et al. [1999].
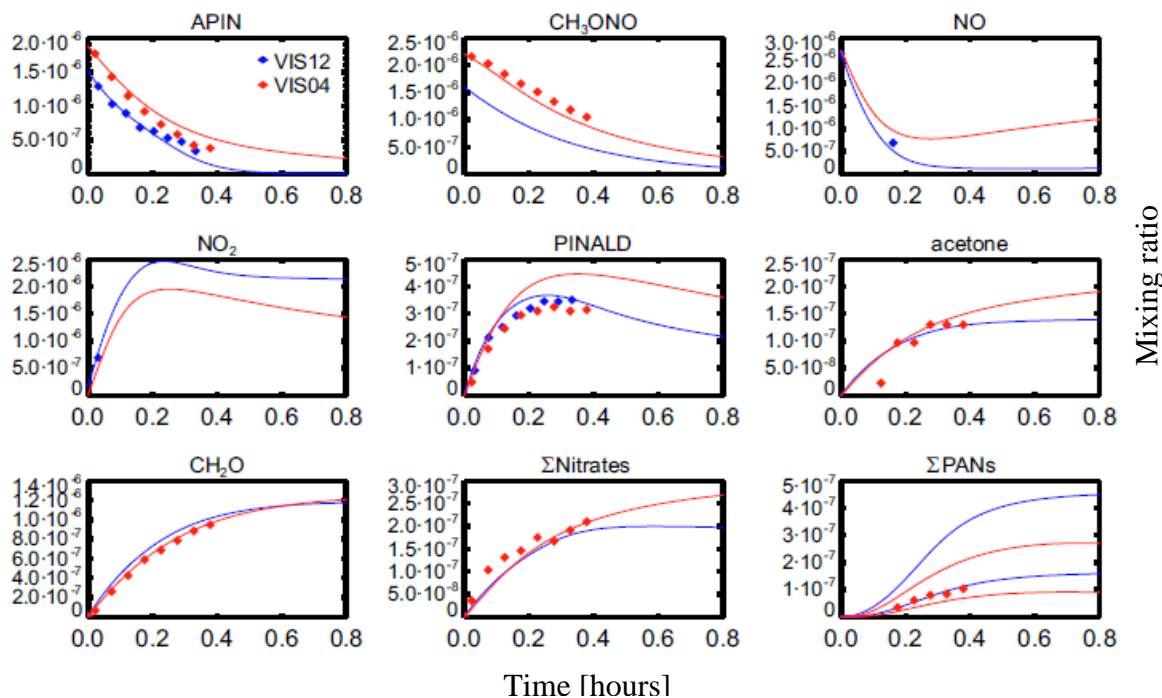
Figure 4.1 : Results from Capouet et al. [2004] model of Noziere et al. [1999] experiments. Experimental data (diamonds) is plotted vs. simulated (curves) concentrations as a function of time.

Peeters et al. [2001] developed a detailed mechanism for the OH-initiated atmospheric oxidation of α-pinene in the presence of NO_x based on quantitative structure-activity relationships and quantum chemistry methods. Rate constants were calculated from quantum chemical rovibrational data using RRKM theory and thermal rate constants were calculated using transition state theory to find a spatially and energy-optimized mechanism. In this model the OH-addition channel accounted for ~90% of the reactions between α-pinene and OH. The model assigned a 44% yield to both OH + α-pinene adducts across the double bond. As much as 50±15% of the OH-adduct precursor

of APN-A was estimated to isomerize into 6-hydroxymenthen-8-yl [Vereecken and Peeters, 2000], discussed in Chapter 3 as an APN-C OH-adduct precursor, something that has not been experimentally verified but predicted in Dibble et al. [2001], Vereecken and Peeters [2000, 2007], and included in the mechanism of Peeters et al. [2001] and the Leeds University Master Chemical Mechanism v3.1. This isomerization step to rearrange the OH-adduct was predicted to account for a significant yield of acetone, whose formation mechanism due to monoterpene oxidation is important to its presence as a trace gas in the atmosphere [Reissell et al., 1999; Wisthaler et al., 2001]. The isomerization of the APN-A precursor to the APN-C precursor is constrained by acetone yields reported in literature [Wisthaler et al., 2001]. In the Peeters et al. [2001] mechanism the branching ratio (Equation 4.2) largely adopted the Arey et al. [2001] expression for alkanes and the total organic nitrate yield was estimated to be 19±6%.

Pinho et al. [2007] presented an evaluation of the Master Chemical Mechanism v3.1 (MCM) as it pertains to α- and β-pinene degradation. The MCM is a near-explicit chemical mechanism that describes the degradation of 135 primary VOCs with a total of 13,500 reactions of 5,900 species [Saunders et al., 2003]. The mechanism assumes that the kinetics and products of a large number of as-yet-unstudied chemical reactions can be based on the results from mechanistically similar studied species from use of available structure-activity relationships [Kwok and Atkinson, 1995; Peeters et al., 2001] and generalized reaction rates [Jenkin et al., 1997; Arey et al., 2001; Zhang et al., 2004; Saunders et al., 2003].

The α-pinene mechanism in the MCM was compared with the chamber experiment results to evaluate the accuracy of the MCM for describing α-pinene/NO_x

118

photooxidation, The mechanism adopted a quantity $D(O_3-NO)$ (Equation 4.3) as a main criterion to evaluate its performance.

$$D(O_3-NO)_t = [O_3]t-[NO]_t-([O_3]_0-[NO]_0) \hspace{3cm} \text{(Eqn. 4.3)}$$

In Equation 4.3 subscript "t" indicates the concentration at time t after the experiment begins and subscript "0" indicates the start of the experiment. The quantity $D(O_3-NO)$ is an indicator of the ozone production in the reaction mechanism, giving a measure of the reaction development even in the presence of O_3-quenching NO [Carter and Lurmann, 1991; Pinho et al., 2005]. The $D(O_3-NO)$ parameter and the α-pinene consumption rate were generally found to be overestimated by the MCM simulations, ranging from an overestimation of 11% in the highest VOC/NO_x experiment to 60% in the lowest VOC/NO_x experiment. The average $D(O_3-NO)$ formation rate generated by the MCM mechanism was 27% larger than observed in the chamber data. This indicated incompleteness of the MCM mechanism and Pinho et al. suggested several strategies to refine the mechanism and bring the $D(O_3-NO)$ parameter more in-line with observation. Some suggested modifications include increasing the yield in the organic nitrate production by using the Ruppert et al. [1999] FTIR product study data, which reported a 24±1.3% total nitrate yield, the highest known result to date. Other suggestions included adding more variation (such as the ring-breaking isomerization of an OH-adduct precursor) to the radical propagation pathways in first-generation products, reducing OH yield from the ozonolysis of α-pinene, increasing the positional-shift isomerization of first-generation peroxy radicals, and decomposing peroxy radicals through CH_3 ejection (as postulated first by Nozière 1999) to form formaldehyde. These refinements were

utilized in the Pinho et al. [2007] mechanism to bring the D(O_3-NO) parameter and α-pinene consumption within 3% agreement of the Pinho et al. [2007] chamber study.

4.2   Chemical mechanism description

An explicit chemical model was created to simulate the formation of α-pinene β-hydroxynitrates from the photo-oxidation reactions of α-pinene with OH in the presence of NO_x. The model simulates photochemical reaction chamber conditions and implements an α-pinene OH-oxidation reaction mechanism that terminates one chemical reaction step past the formation of hydroxynitrates to include sinks such as OH scavenging, wall loss, and thermal decomposition. The chemical model used the partial differential equation solver KINTECUS v. 3.1, a 0-D box model software package as described in Ianni [Kintecus Manual, 2009] to calculate the time-dependent concentrations of key species in the mechanism. A total of 84 reactions were included in the mechanism, 42 inorganic and 42 organic. The individual reactions are listed in Appendix D Table 1. The chemical structures and descriptions of the species involved in the reactions are listed in Appendix D Table 2.

The reaction mechanism was initiated with OH arising from HONO photolysis. HONO was assumed to be formed by second order surface heterogeneous reaction of H_2O and NO_2 [Pitts et al., 1984] as shown in R4.6.

$$2NO_2 + H_2O \xrightarrow{\;surface\;} HONO + HNO_3 \qquad\qquad (4.6)$$
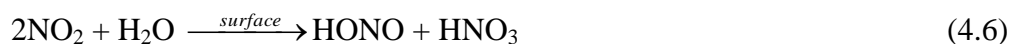
HONO then photolyzed quickly to form OH and NO. Since HONO was not directly measured in the chamber experiments and wall-desorption of HONO was not measured, the initial HONO concentration and production rates were adjusted in the model to match the α-pinene consumption rate. Monitoring NO to estimate HONO

production was not feasible because the initial NO concentration in the experiment was so high (>200ppb) compared to the amount created from HONO photolysis that it could not be used as a gauge for OH or HONO production.

The OH radical added to α-pinene across the C=C double bond and the adduct radical quickly reacted with O_2 to form an organic radical RO_2. Hydrogen abstraction was not considered as the calculated reaction probability of OH abstracting of alkyl hydrogens was less than 5% [Kwok and Atkinson, 1995; Appendix A]. The RO_2 radical reacted with NO, and depending on the $RO_2 + NO$ branching ratio a hydroxynitrate could be produced in R4.3b.

The values used for the individual RO_2 radical formation yields were based on the estimated OH-reaction rate constants using a combination of the Kwok and Atkinson [1995] structure-reactivity relationship and Peeters et al. [2001] OH-addition to polyalkene structure-activity relationship. The Kwok and Atkinson [1995] method gave the estimated percentage of OH-addition (95%) versus hydrogen abstraction (5%) of the α-pinene OH-oxidation reaction pathway. However it did not differentiate between the 1-carbon or 2-carbon site for the OH-addition process. The Peeters et al. [2001] methodology gave an estimated 55:30 ratio of α-pinene adding across the 1-carbon versus the 2-carbon site (Appendix A). Combining the information from the two structure-reactivity relationships gave estimated APN-A peroxy radical precursor (APN-AO$_2$) yield of 0.66 and APN-B peroxy radical precursor (APN-BO$_2$) yield of 0.34. Due to the isomerization of a fraction of APN-A peroxy radical precursors to form APN-C precursors (APN-CO$_2$), the yield of APN-A peroxy radical precursor was adjusted to 0.46 and the APN-C peroxy radical precursor was adjusted to 0.20 in the mechanism.

The branching ratios of RO_2+NO were found by using the APN-A, APN-B, and APN-C nitrate yields found in the experimental result described in Chapter 3. These yields were divided by their respective RO_2 precursor yields to find the branching ratios of APN-AO_2 + NO, APN-BO_2 + NO, and APN-CO_2 + NO. The reaction rate constant for RO_2+NO forming NO_2 and an alkoxy radical RO in the model used the experimentally measured isoprene-RO_2 + NO reaction rate constant of 9.4×10^{-12} cm^3 molecule^{-1} s^{-1} from Chuong and Stevens [2002]. This reaction rate constant is the only experimental measurement available for a BVOC alkene with a $C_{5x}C_{8x}$ composition and is used here in lieu of a reaction rate constant for α-pinene peroxy radical + NO. The reaction rate constant is a less important parameter in the model than the branching ratios since it does not alter the total nitrate yields. Error in the reaction rate constant itself manifests as a time shift in the production of these nitrates during the simulation. Using the Chuong and Stevens [2002] reaction rate constant and the branching ratio from this work gives the reaction rate constant of APN-AO_2 + NO forming a nitrate (APN-ANO_3) of 1.7×10^{-12} cm^3 molecule^{-1} s^{-1}, APN-BO_2 + NO forming a nitrate (APN-BNO_3) reaction rate constant of 1.2×10^{-12} cm^3 molecule^{-1} s^{-1}, and APN-CO_2 + NO reaction rate constant of 3.0×10^{-12} cm^3 molecule^{-1} s^{-1}.

Once a hydroxynitrate was formed in the mechanism, the loss processes eroding the concentrations included: 1) OH reaction; and 2) Wall-loss processes to the Teflon wall of the photochemical reaction chamber. The APN reaction with OH could generate another alkoxy radical RO and NO_2 that could participate in the oxidation chemistry again. The reaction rate constants of the APN reacting with OH were estimated using the Kwok and Atkinson [1995] methodology. The wall-loss rates of the individual

hydroxynitrates inside the reaction chamber were measured and discussed in Chapter 3. The α-pinene oxidation mechanism did not include pathways developed past the first generation products of the hydroxynitrate formation, so the model terminated after the APN underwent one of the two loss processes.

The main goal of the model mechanism is to attempt to reproduce the chamber experiment results by modeling the α-pinene OH oxidation reactions and plotting the concentration versus time of key species in the experiment. The comparison of the model and the experiment concentrations helps to test the current understanding of the α-pinene OH-oxidation mechanism. No ozone or NO_3 reaction pathways were included although O_3 concentrations were produced and compared against the experiment. Figure 4.2 shows a schematic of the mechanisms included in this model.
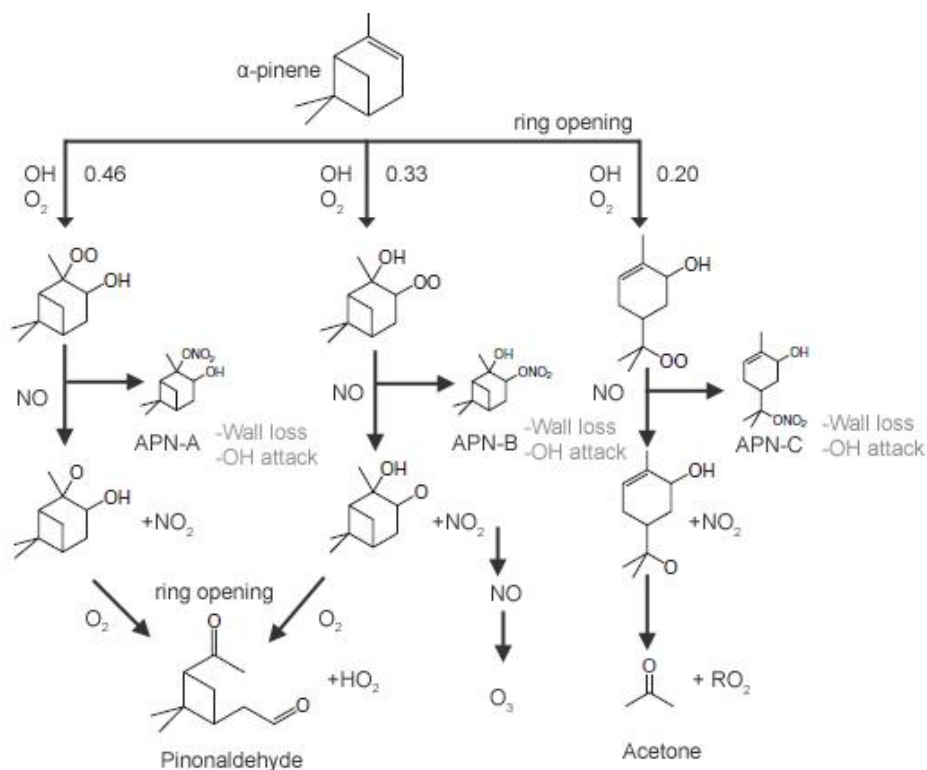
Figure 4.2: The reactions incorporated in the α-pinene OH-oxidation model.

This model produced concentration information for all the species undergoing reaction at each time-step (1s). Effects of chamber air dilution were simulated with a first-order rate constant. Similarly the wall-loss effects were simulated with a first-order rate constant measured in a wall-loss experiment. The model adapted reaction rate constants from Atkinson et al. [2003], JPL Chemical Kinetics and Photochemical Data Evaluation No. 15 [2006], the MCM v 3.1 [Saunders et al., 2002], and this work.

4.3 Results and Discussion

The experimental data from the May 15th, 2009 chamber experiment is used in this discussion. The initial starting material concentrations in the chemical model included 6×10^{12} molecules·cm^{-3} of NO, 1×10^{13} molecules·cm^{-3} of α-pinene, 5.88×10^{11} molecules·cm^{-3} of NO_2, and 4×10^{17} molecules cm^{-3} water vapor. At just before Hour 3, Hour 6, and Hour 8, additional injections of NO were introduced into the chamber to dampen the growth of O_3 to prevent ozonolysis reactions. These events were modeled in the mechanism by introducing concentrations of NO at times that correspond to the experimental injection concentrations.

The indicator species α-pinene, NO, NO_2, and ozone from the simulation results were overlaid with experimental data and plotted together in Figure 4.3. The solid lines correspond to simulation results and the discrete points correspond to the experimental data. Time 0 is the start of irradiation from the solar lamps during the experiment.
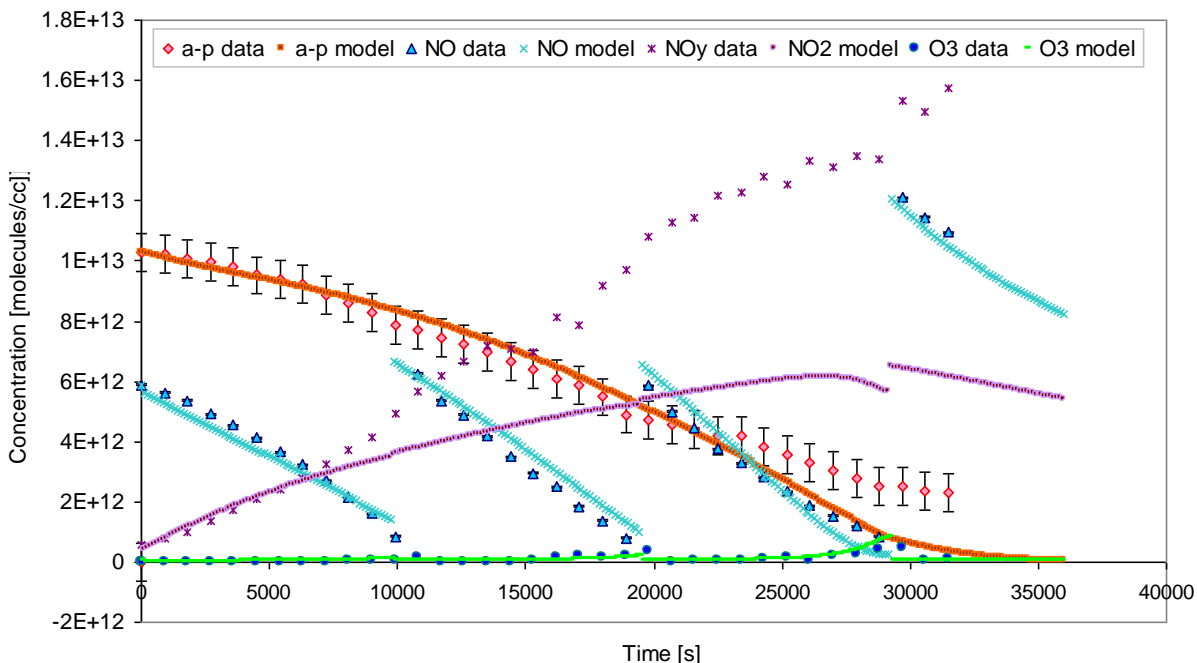
Figure 4.3: Model results veresus experimental conditions. Solid lines are model results. Discrete symbols are experimental results.

During the experiment α-pinene concentrations dropped steadily as it was attacked by OH to form peroxy radicals. NO concentrations dropped also as it reacted with RO_2 and HO_2, producing NO_2 when RO_2+NO or RO_2+HO_2 did not produce a nitrate and recycled NO_x back into the experiment. NO quenching of ozone was seen in both the experiment and the model during NO injection events.

A key indicator of chamber reactivity is ozone production in the mechanism [Pinho et al., 2007]. When plotting ozone experimental data with model results in Figure 4.4 the growth and quenching of ozone with NO injections were reproduced by the mechanism almost exactly. The fit at each point including the discontinuities due to NO injections were in very good agreement.
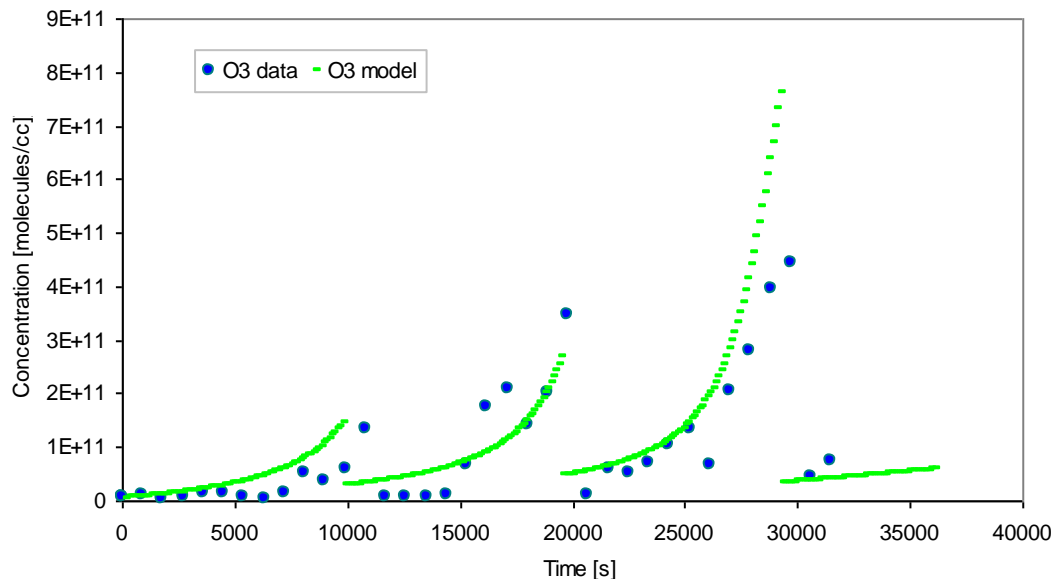
Figure 4.4: Comparison of simulated ozone results with experimental ozone data.

The decrease in α-pinene produced by the model remained within 20% of the measured concentration at every point except past the 7.5h mark when its consumption was accelerated. This indicated an overproduction of OH in the mechanism due to a large surge of ozone at t=7.5h (seen in Figure 4.4), which increased the concentration of OH late in the simulation. The NO_2 concentrations started out with good correlation to the experimental data. At the 3 hour mark, however, the NO_2 concentrations began to show underproduction compared to experimental data, eventually reaching a maximum of 50% difference at the end of the experiment. This underproduction could be due to the contribution from peroxy radicals other than the three nitrate precursor RO_2 radicals reacting with NO and producing NO_2.

The modeled APN-A, APN-B, and APN-C concentrations are plotted along with experimental results in Figure 4.5. As expected APN-A is the dominant isomer with APN-B and APN-C at about half as abundant. The ratio of APN-A:APN-B:APN-C in the model at the 3 hour mark was 2:1:1.

126
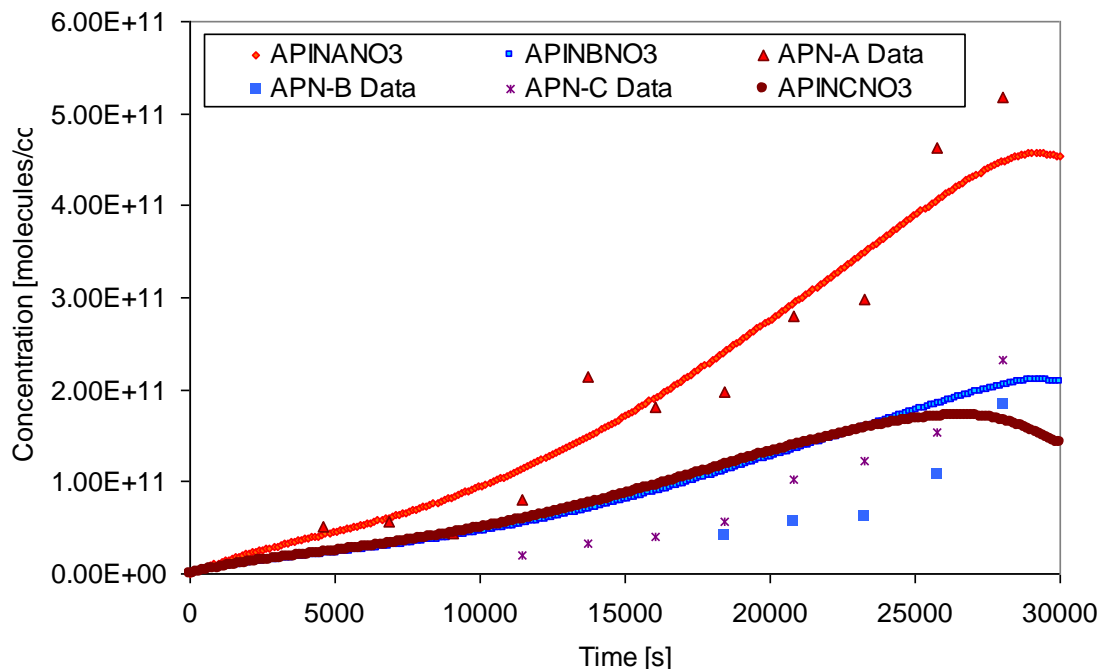
Figure 4.5: α-pinene nitrate experimental data plotted with model data.

The model predicted the concentration of APN-A isomer with great accuracy, while APN-B was somewhat over-predicted along with APN-C although the general agreement is reasonably good. The under-prediction of APN-B and APN-C is most noticeable at the beginning. This could be attributed to APN-B and APN-C having a slower reaction rate constant than APN-A. The two nitrates are therefore produced less quickly, making them more difficult to detect early in the experiment. The overall shape of the model's nitrate concentration growth follows the experimental result well, although at the end of the experiment when the α-pinene and NO are exhausted the model shows a leveling off of the nitrate after the experiment ended.

The quantity $D(O_3\text{-}NO)$ was calculated and plotted for both the experimental results and the model data. Shown in Figure 4.6, the $D(O_3\text{-}NO)$ "nitrogen reactivity" index were consistent to each other for the duration of the experiment except in the

beginning where there were some fluctuations in the data. This is an indicator of the

mechanism's ability to appropriately model the $RO_2 + NO$ to $NO_2 + RO$ reaction.
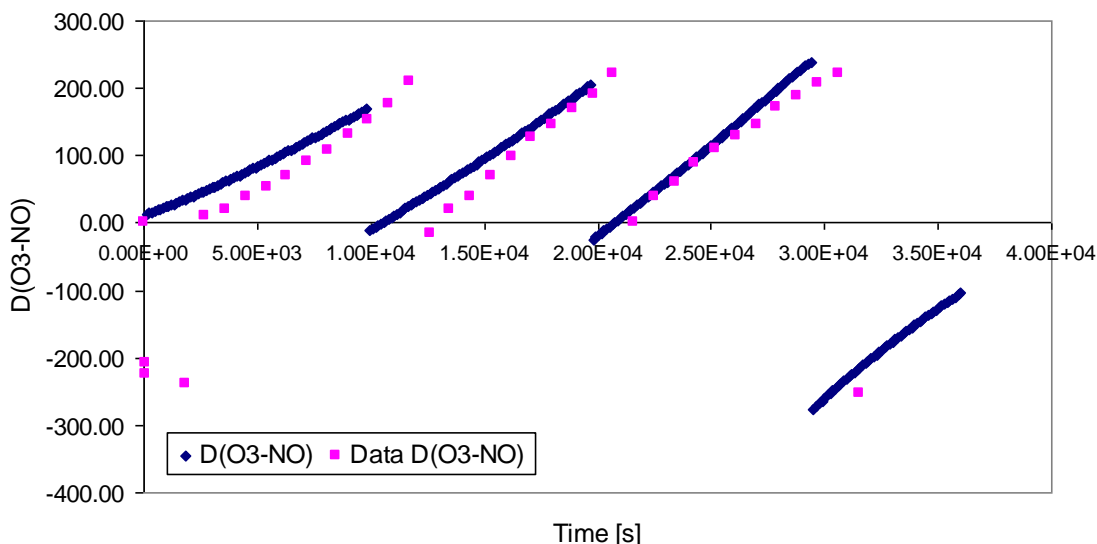
Figure 4.6: $D(O_3\text{-NO})$ for the model and the chamber data.

4.3.1 Recommendations for improvement

The overall agreement of the model with the experimental data is good. The only

species that shows discrepancy of ~50% is the production of NO_2. A study of the

sensitivity of k_{OH} to the concentration of NO_2 produced would reveal whether it is related

to the first order reaction rate constant rather than missing chemistry.

4.4 Conclusions

A mechanism for describing α-pinene OH-initiated photo-oxidation in NO_x has

been created to simulate the reaction chamber experimental results of Chapter 3. From

the results of the model the α-pinene consumption, NO decay, NO_2 growth, and APN

concentrations are within 50% of the experimental data. Past hour 3 NO_2 was

underpredicted in the mechanism, however the other key species, ozone, α-pinene

degradation, and APN generation matched the experimental data quite well.

CHAPTER V

Evaluation of GCxGC and Solid-State Thermal Modulator

5.1 The Method of GCxGC Chromatography

Introduced in the latter part of the 20th century, the basic operation of the conventional one-dimensional GC (1D-GC) remains the same – a sample mixture is introduced in a column and separated via physical and chemical characteristics as dictated by the stationary phase that can be customized to target specific attributes, such as volatility or polarity. The separated sample compounds are swept along by carrier gas flow and arrive at a detector array, which ionizes and detects the analyte concentration in a linear response [McNair and Miller, 2009].

The 1D-GC has been the reliable workhorse of chemical analytical instruments but its well-known limitations in low peak capacity, defined as the number of peak-to-peak signals with a 90% separation, and resultant overlapping peaks make compound identification and integration of complex mixtures very difficult [Panic and Górecki 2006]. For a complex random sample it has been estimated that the probability that any one analyte is completely separated in a 1D-GC is only 19-37% [Davis and Giddings, 1983]. Although this has been sufficient for a large number of applications in the past, increasingly complex mixtures demand correspondingly higher peak capacity and separation power. One proven way to increase peak capacity in the 1D-GC has been to lengthen the analytical column used in the separation, but even the longest column cannot

separate the compounds in commercial gasoline and pesticides, and the corresponding increase in analysis time makes this solution unattractive [McNair and Miller, 2009].

Multidimensional chromatography was introduced as a method to solve the problem of low separation power in the 1D-GC. There are two classes of multidimensional chromatography mechanisms: 1) Fractional introduction of effluent into the second column; 2) Comprehensive introduction of effluent into the second dimension [Cortes et al., 2009]. The most commonly-applied form of comprehensive multidimensional chromatography is GCxGC (otherwise known as two-dimensional GC). Introduced in the 1990s by Philips and Liu [1999], GCxGC sought to improve upon the 1D-GC methodology by using two columns in series for separations, typically one long column for volatility and one short column for polarity. Choosing column stationary phases that have separation mechanisms independent of each other can be understood as column "orthogonality" [Marriott, 2002; Ryan et al., 2005]. The vast majority of GCxGC instruments use volatility stationary phase in the first dimension because the elution behavior of compounds is predictable [Cortes et al., 2009]. A short polar second dimension column separates narrow analyte plugs from the first dimension in isothermal conditions independent of the influence of the first column to yield orthogonal separations that maximize analyte separation [Ryan et al., 2005].

A key component of the GCxGC is the thermal modulator located between the first and second column. The thermal modulator traps, then releases effluent from the first column into the second column in small plugs to prevent peak switching order problems and to preserve the separation information from the first column analysis. To do this the thermal modulator fulfills three primary functions: 1) Continuously accumulate

small fractions of effluent off of the first column prior to injection into the second

column; 2) Cryofocus the trapped effluent prior to injection; and 3) Inject into the second

column in narrow focused pulses at a frequency of 0.1-1.0 Hz. The pulses are empirically

determined to optimize two competing timing demands on the thermal modulator: it must

be fast enough to modulate an analyte peak (Figure 5.1a) at least 3-4 times before the

peak passes through the first column completely but it must be slow enough to allow a

full modulation cycle of rapid heating and cooling to be completed before continuing.

This results in multiple modulated peaks per analyte different from the continuous single

peak from as shown in Figure 5.1.
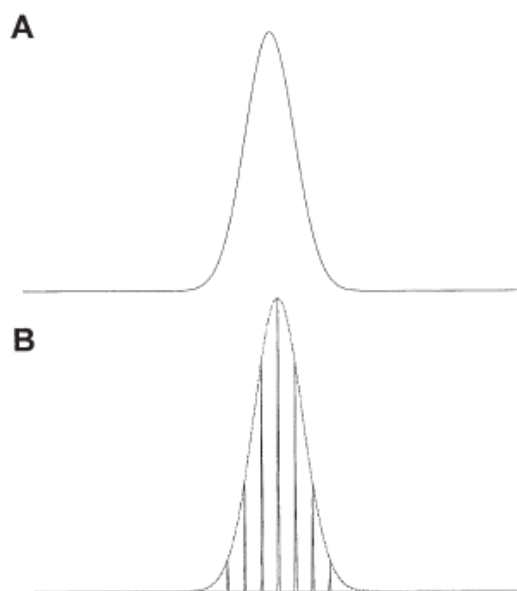
Figure 5.1: Peaks from a 1D-GC (A) and a GCxGC (B) [Ong and Marriott, 2002].

There are many different designs of thermal modulators. Lee et al. [1999] and Pursch et

al. [2002] have reviewed several published thermal modulator designs but new designs

continue to be proposed [Libardoni et al., 2005; Seeley et al., 2006; Mohler et al., 2006;

Wang, 2008; Pizzutti et al., 2009; Poliak et al., 2009]. Figure 5.2 shows a schematic of a

GCxGC with several different types of thermal modulator designs. The different designs

are mostly thermal trapping but Modulator E is valve-based. While temperature trapping

is popular, valve-based flow control offers the ability to prevent any premature analyte

injections from occurring. In Figure 5.2 the instrument injector port introduces effluent

into a long first dimension column, which performs an initial separation of analyte, which

then enters into a thermal modulator. After separation by the short second dimension

column, the effluent goes into the detector array.
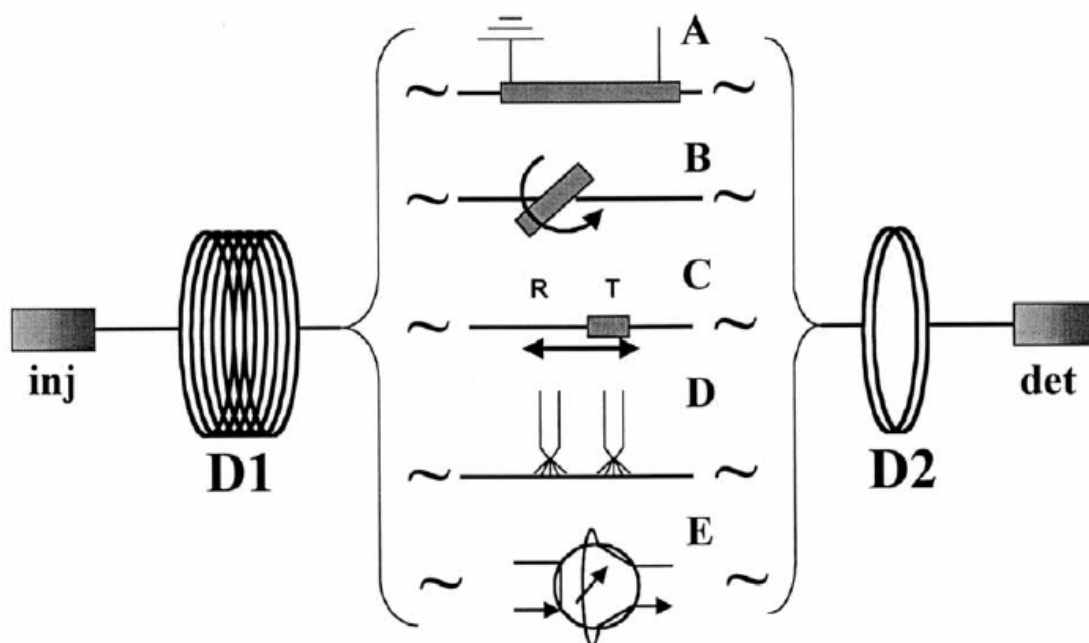
Figure 5.2: Schematic of various thermal modulators used in a GCxGC instrument: A) A heating tube encasing the capillary column and heated resistively. B) A thermal sweeper rotates over the column to heat and sweep effluent to the next column C) An oscillating cryotrap traps the solute and then release it as it moves back and forward D) Two high speed jets one is cryogen the other is hot air E) A valve that fills a loop before flushing it onto the second column [Ong et al., 2002].

In Figure 5.2 thermal modulator A is a metal-coated length of column that is

resistively heated by a high current load supplied from an external power source. The

modulator is thermally cycled. However the metal paint coating has proven to be

unreliable [Cortes et al., 2009]. Modulator B is also known as a thermal sweeper and uses a slotted heater to sweep the solute into the second column when it is over the column. The high heat of the slotted heater relative to the column needed to remobilize the solute trapped in the column is a serious limitation. Modulator C is a longitudinal modulator that collects and concentrates a segment of effluent that enters the trapping region by moving the modulator along the column. Cryocooling the moving modulator unit makes it difficult to continuously cool inside a GC oven with a ramping temperature program. Modulator D is a two jet system that blows cold and hot air on-column to trap and remobilize effluent. Modulator E is a stop-flow valve system that collects solute from the primary column in a sampling loop then rapidly switches the valve to flush the sampling loop into the second column. Each of these designs has its own particular benefits and challenges, and is often chosen to fit a specific application [Ong and Marriott, 2002].

In a GCxGC, the modulation produces a planar chromatograph very different from the one-dimensional trace in 1D-GC. Figure 5.3 shows the data collecting process from a typical GCxGC run. A three component co-eluting peak is modulated in step 1. The modulation step produces many modulation peaks that are injected into the second column and undergo a second separation. The chromatograph is transformed via computer deconvolution software that picks out the second dimension separation information and refactors the data such that it can be plotted on a 2D plane with the first dimension separation on the x-axis and the second dimension separation on the second axis. The resulting peaks are no longer 1-D traces but 2-D shapes that can be visualized by colors, shading, or topographical 3-D plot using concentration in the z-axis.
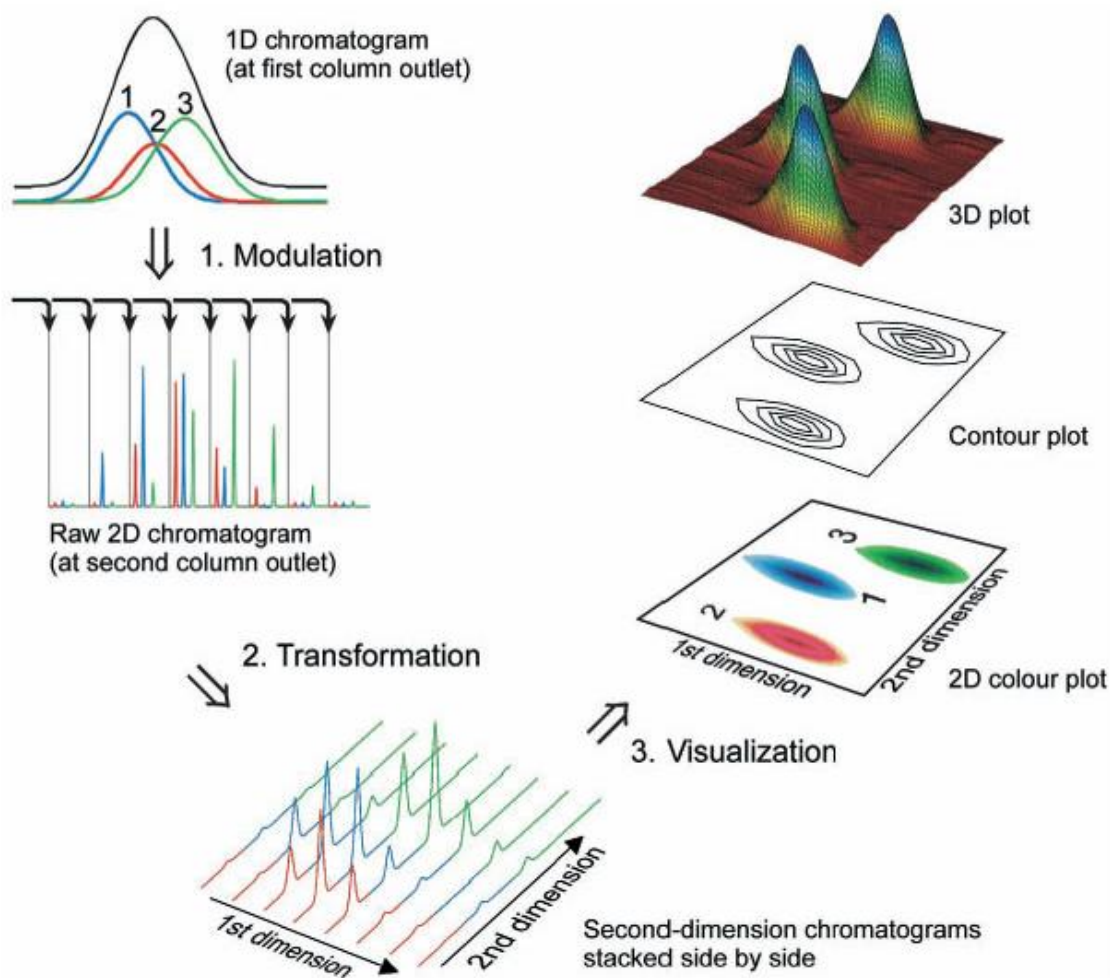
Figure 5.3: The process of GCxGC peak generation and chromatogram visualization [Dallüge et al., 2006].

A side-by-side comparison of the chromatographs resulting from the GCxGC technique vs. the 1D-GC technique for the same mixture is shown in Figure 5.4. An urban air sample is separated using cryogenic modulation using both 1D-GC and GCxGC. The 1-D retention times are still present in the GCxGC data but polarity data is now present with aromatic compounds separated from the non-polar compounds on the baseline. One unique property of GCxGC chromatograms are the "clustering" of similar analytes, which can be seen in the grouping of aliphatics, carbonys, and aromatics in the GCxGC chromatograms in Figure 5.4.
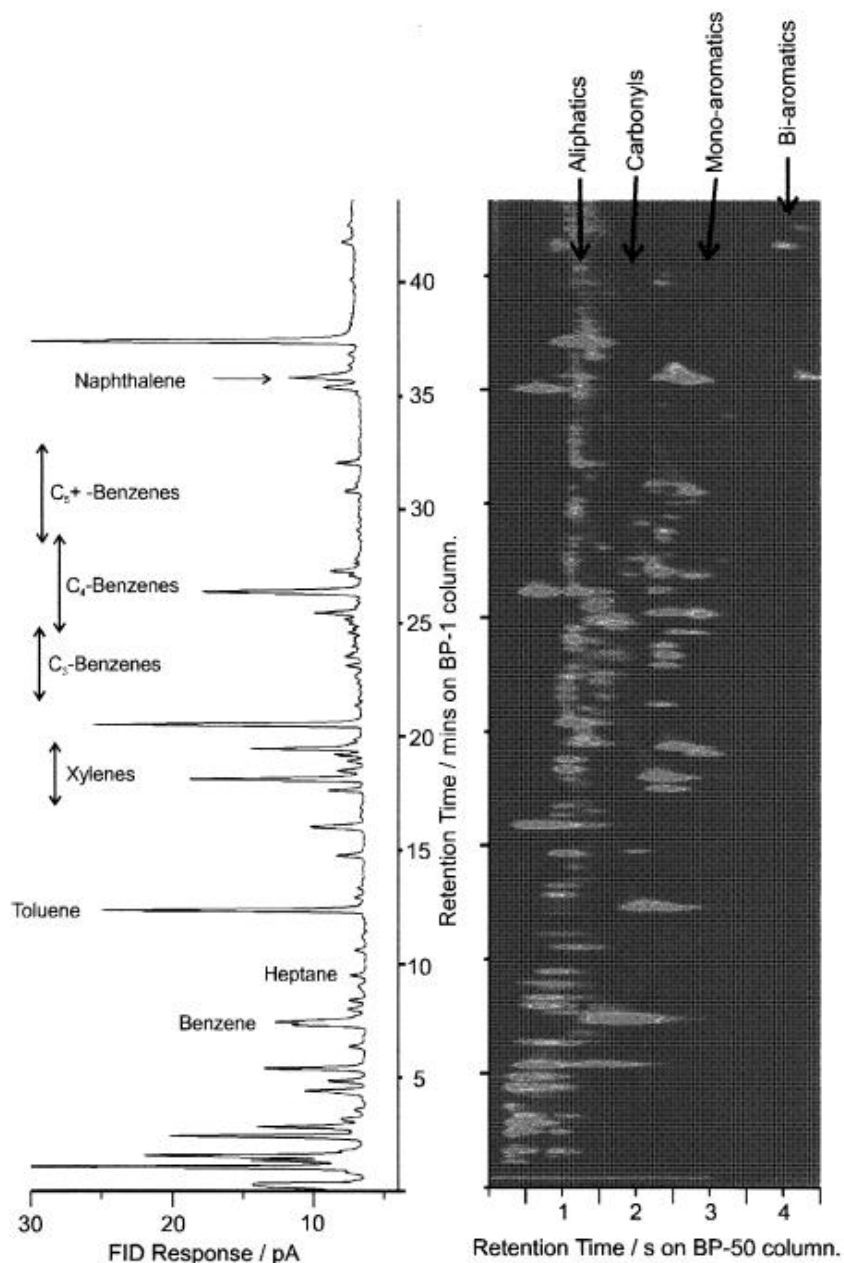
Figure 5.4: 1D-GC and GCxGC chromatograms compared side-by-side [Lee et al. 1999].

The peak capacity of the GCxGC, as the name suggests, is the multiplication of

the peak capacities (or total number of peaks that can be 90% separated at full-width-

half-maximum) of both orthogonal separation columns. The GCxGC separation power is

also improved due to the nature of the two-dimensional retention plane, which increases

135

the probability of full peak separation (also defined as 90% separation at FWHM). The second column is both an asset and a problem, as the secondary separation can yield more information about the compound, but it could also potentially destroy or erase the work performed by the first column separation. The thermal modulator prevents the loss of information from the first column separation because its operation is timed such that the time between injections into the second column is spaced wide enough apart to allow the second separation to be completed, typically on the order of a few seconds, which is shorter than the time it takes for the thermal modulator to complete one full cryocooling and injection cycle. The minimum number of modulations per analyte peak should be 3 so that it can be deconvoluted successfully on the separation plane.

The GCxGC does have its detractions - it requires much more complicated electronics and operational considerations than a 1D-GC. The thermal modulator design presents significant mechanical challenges as it must satisfy conflicting requirements of rapid, reproducible heating and cool-down to be delivered to a chromatography column, usually a very small diameter silica or steel tube. The design of a compact, low-resource (referring to the lack of cryogens or circulating heat exchange fluids), and robust thermal modulator is still an area of active research. A solid-state cooled thermal modulator was designed to require no cryogen for operation, no consumables, and no outside heat-transfer agent. The module was designed to be "plug-and-play" requiring only a power supply to operate the thermoelectric chillers. This solid-state thermal modulator assembly is robust and portable with no moving parts to maintain, making it attractive for future field work and remote sites with few operators. An evaluation of the thermal performance of this solid state thermal modulator is presented in this chapter.

5.2 Benchtop GCxGC Instrument

A benchtop oven-less GCxGC shown schematically in Figure 5.5 was designed and built to evaluate a two-stage solid-state cooling thermal modulator. A cryofocusing inlet preconcentrated samples before introduction into the first column, a 30m RTX-1 column (Restek 0.25um i.d.). The two-stage solid-state thermal modulator (TM) was located between the first and second column to modulate injection into the second column, a 1m Rtx-1701 column (Restek, 0.1μm i.d.). No oven was used in this instrument to house and heat the chromatography columns. Instead the analytical columns were wrapped with heating wire and fiberglass insulation controlled by an on-board microcontroller set with a temperature ramping program. This decreased the amount of extra cooling needed to counter oven heating and keep the thermal modulator cool enough to trap effluent efficiently. The instrument detector was an electron capture detector (ECD) with a beta-particle emitting NI 63 source highly sensitive to electronegative species such as compounds with nitrate and halogen functional groups.
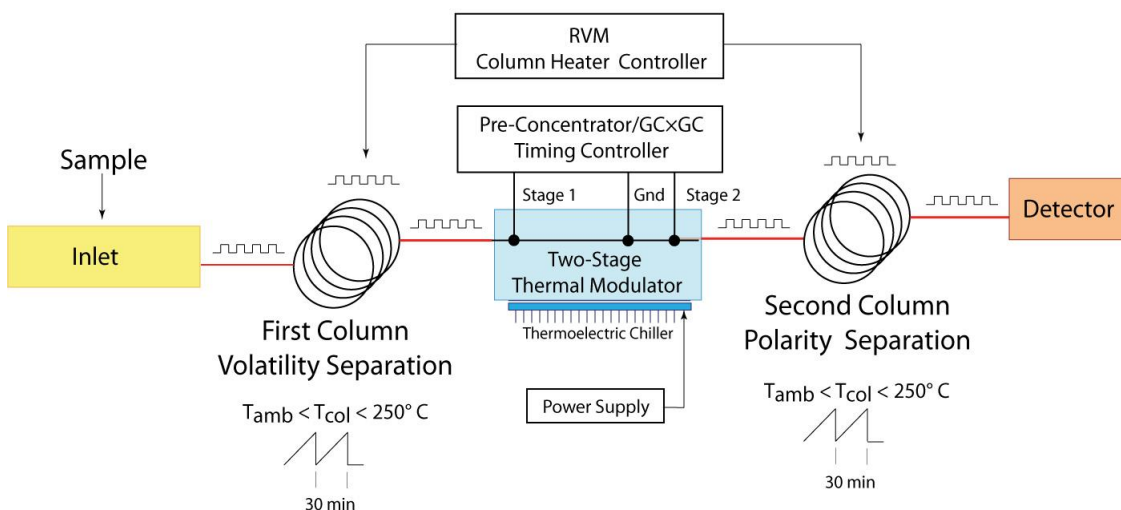
Figure 5.5: Schematic of benchtop GCxGC with solid-state thermal modulator.

5.2.1 Sample inlet and cryofocuser

The sample inlet and cryofocuser unit used to collect and preconcentrate sample was designed to be compact and consumable-free. For the inlet, a loop of 1/8" stainless steel tubing 10 ft in length was attached to a 6-port 2-position Valco switching valve that collected and then injected sample as shown in figure 5.6a and figure 5.6b respectively. Valve position 1 (Figure 5.6a) pulled sample through the inlet and purged the sample loop. Valve position 2 (Figure 5.6b) switched to connect the loop to He carrier gas pushing the sample into the cryofocuser to begin the preconcentration step.
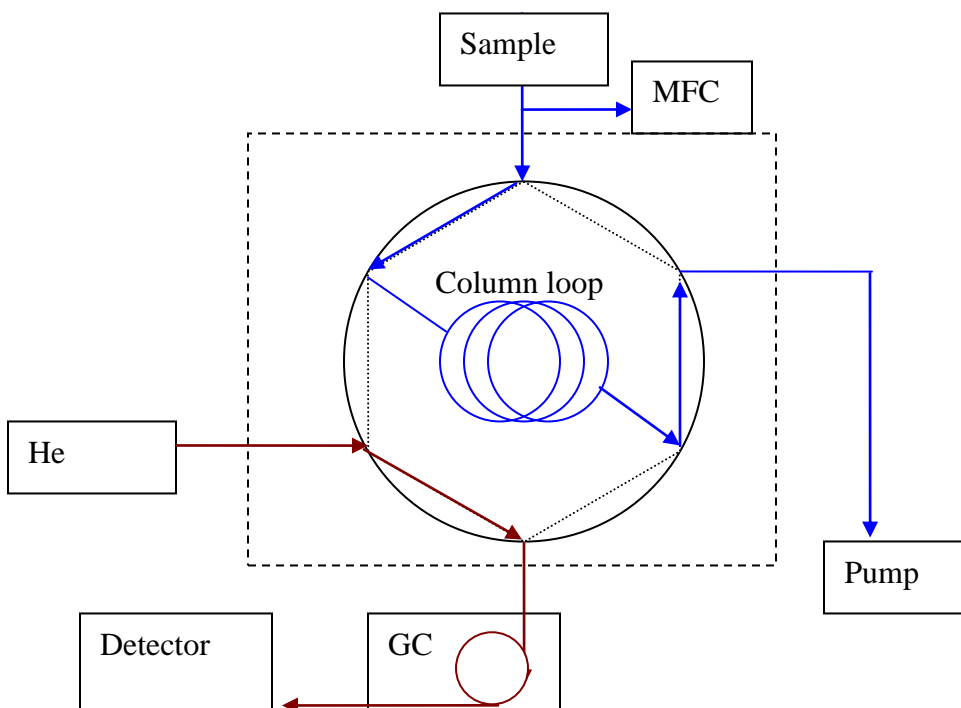
Figure 5.6a: During sample loading the 6 port valve switches so that sample is trapped in a column loop pulled by a pump. Meanwhile helium flows through the GC system.
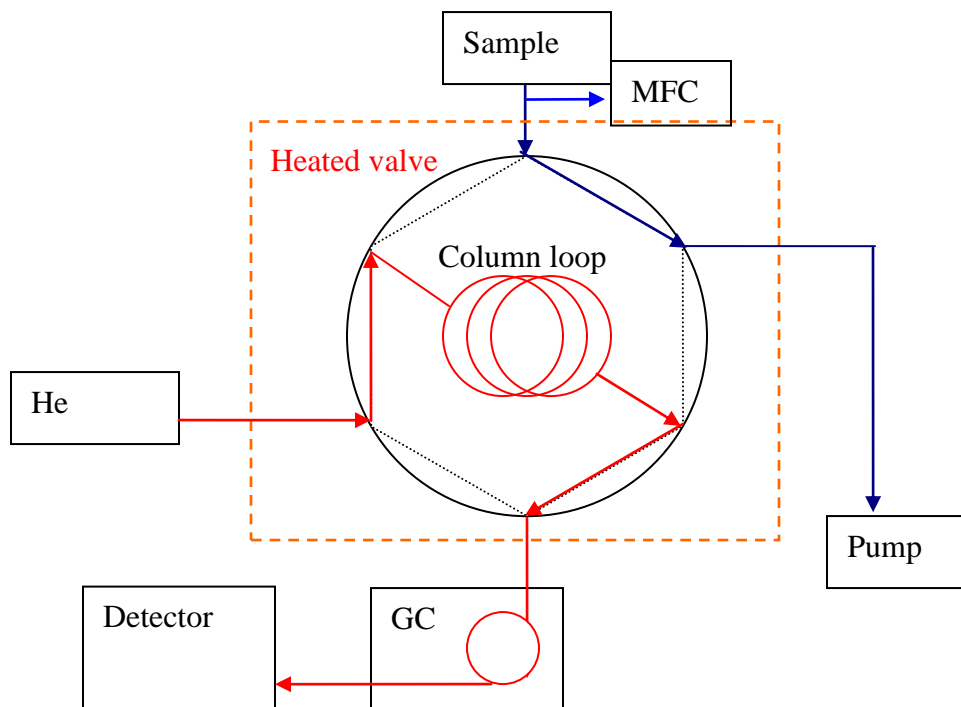
Figure 5.6b: During sample injection the valve switches so that the carrier gas sweeps the sample inside the column loop onto the GC column.

Shown schematically in Figure 5.7 the inlet sample cryofocuser was a 1-meter length of DB-1701 megabore column (Restek, 0.53μm i.d.) wound inside a custom aluminum housing unit with dual TEC chillers and fans on the top and bottom of the column housing. Cooling down to 0°C was achieved with solid-state chillers starting from room temperature conditions (22°C). At 0°C water vapor could pass through the short cryofocuser successfully without being trapped while the target nitrates were able to be trapped and preconcentrated during the cryofocusing step. During sample injection, a tubular heater with 835W of heating power (Omega Corp.) rapidly heated the cryofocuser temperature to 160°C and injected the sample into the first column of the GCxGC.
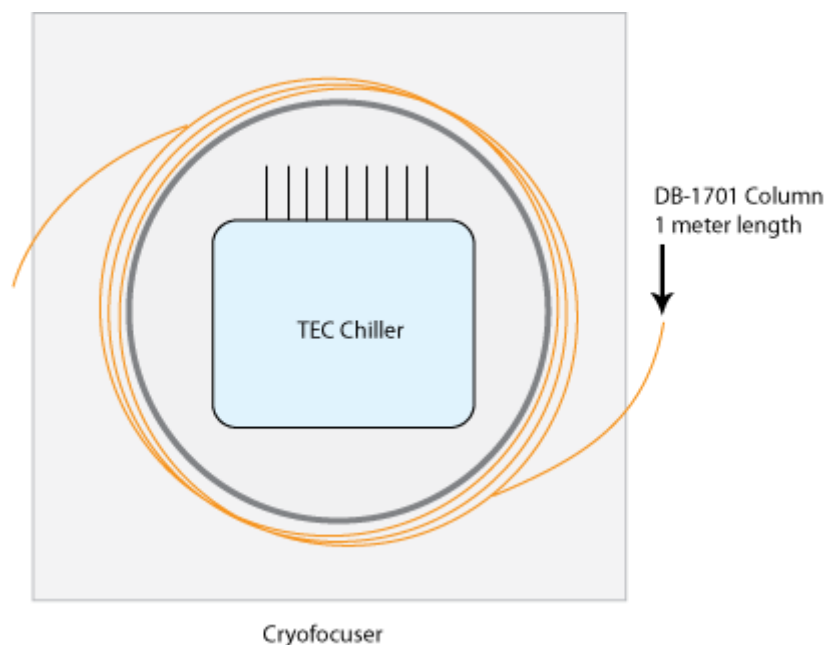
Figure 5.7: The cryofocuser attached to the sample inlet unit. Twin TEC chillers cool a 1 meter length of DB-1701 column that is then heated with a heater rod to reach mobilization temperature of 100°C.

5.2.2 Two-stage solid-state thermal modulator

After the inlet and cryofocuser unit pushed sample effluent onto the first column, the effluent was separated and swept into a solid-state two-stage TM. Discussed by Libardoni et al. [2005] this thermal modulator design used on-column electrical resistive heating to produce rapid heating to remobilize sample trapped in the column during the cryofocusing step. The two stages of this TM design refer to the two separate heating and cooling cycles that occur in sequence before each effluent plug is injected into the secondary column. This extra step in the TM modulation cycle prevents analyte plugs from breaking through the cryotrapping and prematurely entering the second column during the heating and cooling cycle. The heatup and cooldown steps take a finite amount of time during which effluent can migrate and produce this "breakthrough" effect observed in the peak fronting of the resulting chromatography data, where the leading

140

edge of a chromatography peak is front-loaded and the overall shape is distorted and non-Gaussian. Figure 5.8a shows a 3-D schematic of the aluminum housing and copper sleeve that surrounds the thermal modulator. Silicone seals (orange colored pieces) help keep the assembly water tight and the aluminum construction helps to dissipate heat.
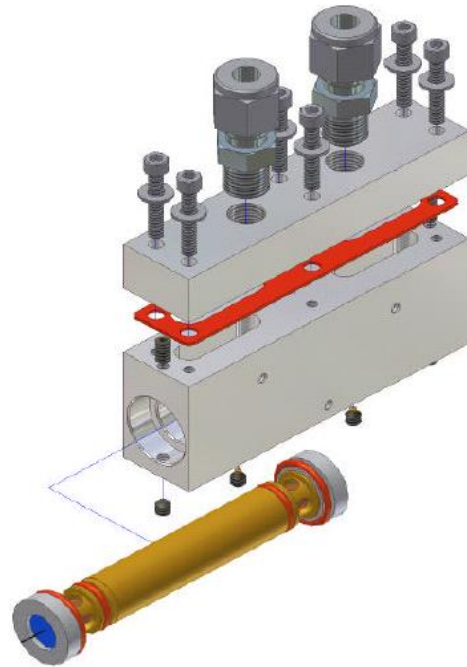
Figure 5.8a: The 2-stage thermal modulator inside aluminum housing.
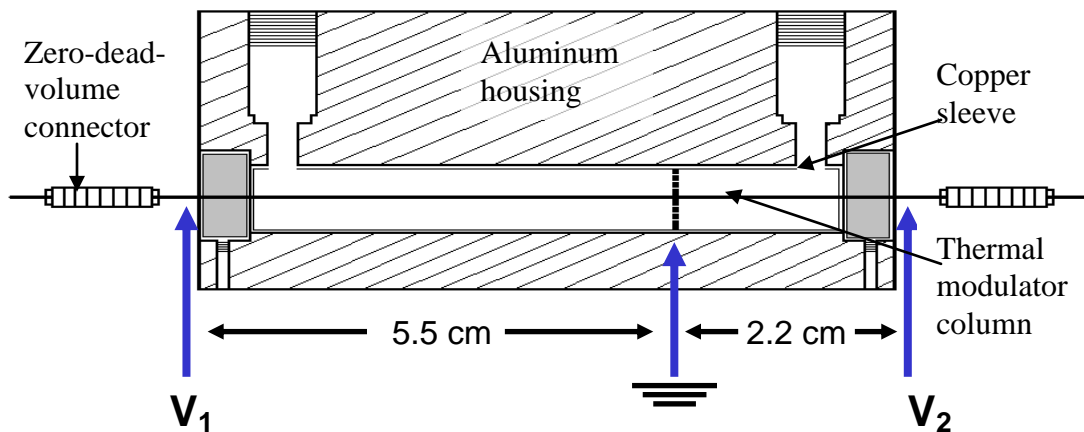
Figure 5.8b: The electrical nodes of the two-stage thermal modulator.

Figure 5.8b shows the electrical nodes where two power supplies are connected to the silcosteel column inside the copper sleeve and power is transferred to the column in

the form of resistive heat. The addition of the solid-state cooling with Peltier coolers to replace the previous external circulating coolant heat exchanger was a new modification of the two-stage thermal modulator assembly intended to shrink the TM form factor and power requirements of the GCxGC instrument so it would be easier for future field deployment. The solid-state cooled TM relied on the thermal transfer properties of a methanol/water bath mixture and thermoelectric coolers affixed to the thermal modulator housing to rapidly transfer heat after a modulator firing cycle to cool down the thermal modulator column.

In the two-stage modulator, the heating and trapping cycle occurs twice as shown schematically in Figure 5.8c. The triangular, rectangular, and circular dots inside the columns represent three different analytes undergoing separation. During step A, a plug of effluent from the first column is stopped at the head of the two-stage modulator due to the large temperature difference between the first column and the temperature of the modulator, usually set at -20°C or lower. In step B the first stage of the modulator heats up and a small effluent plug is allowed to migrate through to the head of the second stage due to the higher temperature. In step C the analyte plug is stopped again at the end of the first stage because the second stage is cold compared to the first stage. In step D the first stage of the modulator is cooled down again, preventing other analyte plugs from migrating through while the second stage is heated to remobilize the plug at the head of the second stage through to the second dimension column. In step E the second dimension column successfully separates the previously co-eluting analyte plug by another physical or chemical property before it enters the detector.
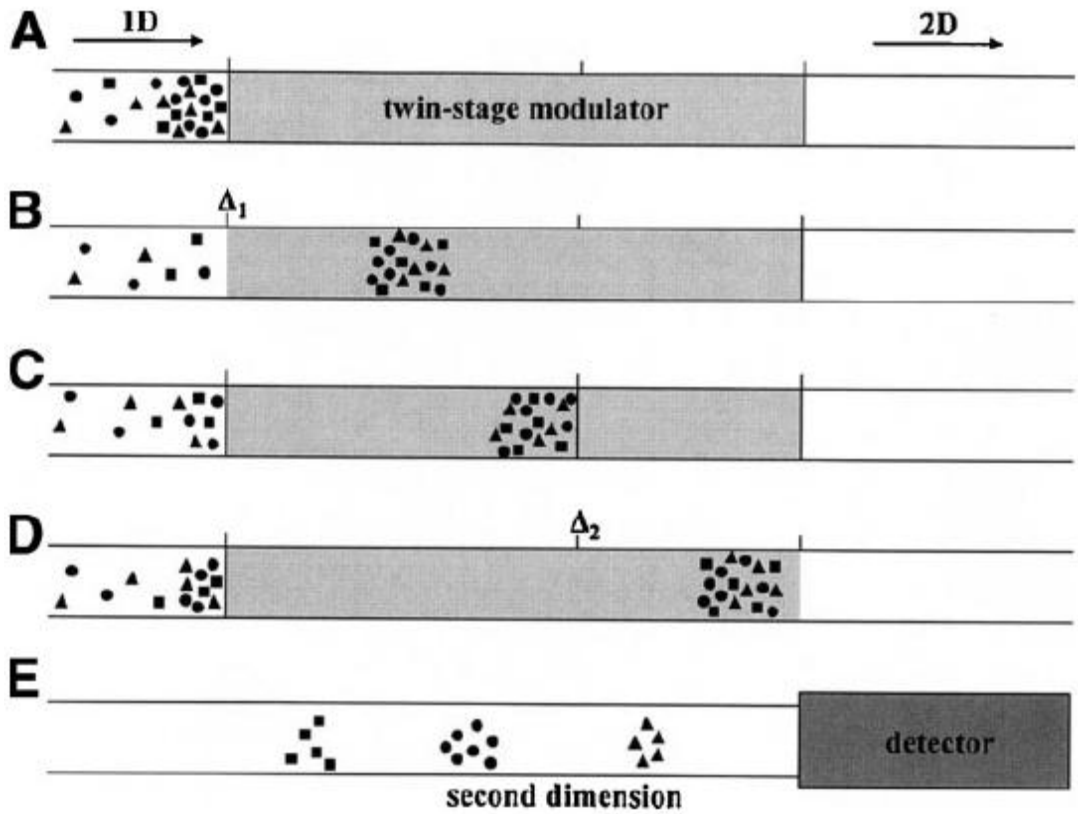
Figure 5.8c: Illustration of the thermal modulation process [Mondello et al., 2008].

Figure 5.9 shows a component view of the two-stage thermal modulator inside a solid-state cooling assembly. Two thermoelectric Peltier chillers (Marlow Industries SP5162-01AC) were attached on either side of the flat rectangular surfaces of the thermal modulator aluminum housing. The Peltier chillers were mated with large heat sinks with radiating fins to dissipate the heat from the hot side of the chiller plate, aided with motorized fans. The Peltier cooler and thermal modulator assembly was insulated with foam to isolate it from ambient temperatures while it was operating.

143
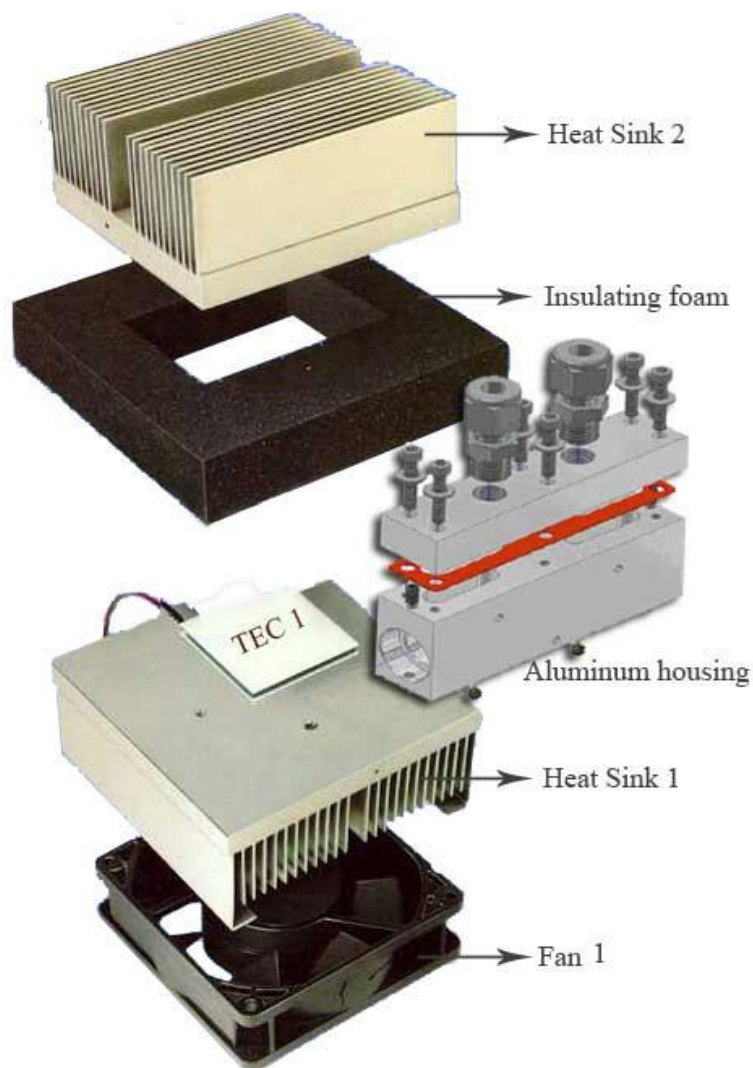
Figure 5.9: View of the solid-state chilling assembly around the two-stage thermal modulator aluminum housing.

A bath of methanol (Fischer Scientific, 99%) and water mixed at a ratio of 60:40

was added inside the water-tight aluminum TM housing to facilitate faster heat exchange

between the heated silcosteel thermal modulator columns and the thermoelectric Peltier

coolers. The methanol/water mix was chosen due to its low freezing point and ease of

evaporation, which absorbs significant heat from the source to form vapor [Hopkins and

Reid, 2006]. The lowest temperature achieved using this solid-state thermal modulator

assembly with the methanol/water bath was -26.2°C as measured by a J-thermocouple

144

(Omega) inserted inside the copper sleeve of the thermal modulator aluminum housing. The pulses used for the two-stage modulation firing cycles were 3.28V and 3.56V respectively.

Figure 5.10 shows the pulsing profile of the thermal modulator through two complete cycles of modulation. The twin pulses correspond to voltage drops across nodes V1 and V2 (Figure 5.8b) across the silcosteel column inside the thermal modulator aluminum housing. Given the resistance of the silcosteel column was measured to be $0.015(\pm0.005)$ Ω, the voltage drop corresponded to a current load of ~4-5Amps heating the column per modulation, corresponding to the power supply current display of the current drop during modulation. The power transferred onto the column per modulation is 0.3-0.4 Watts.
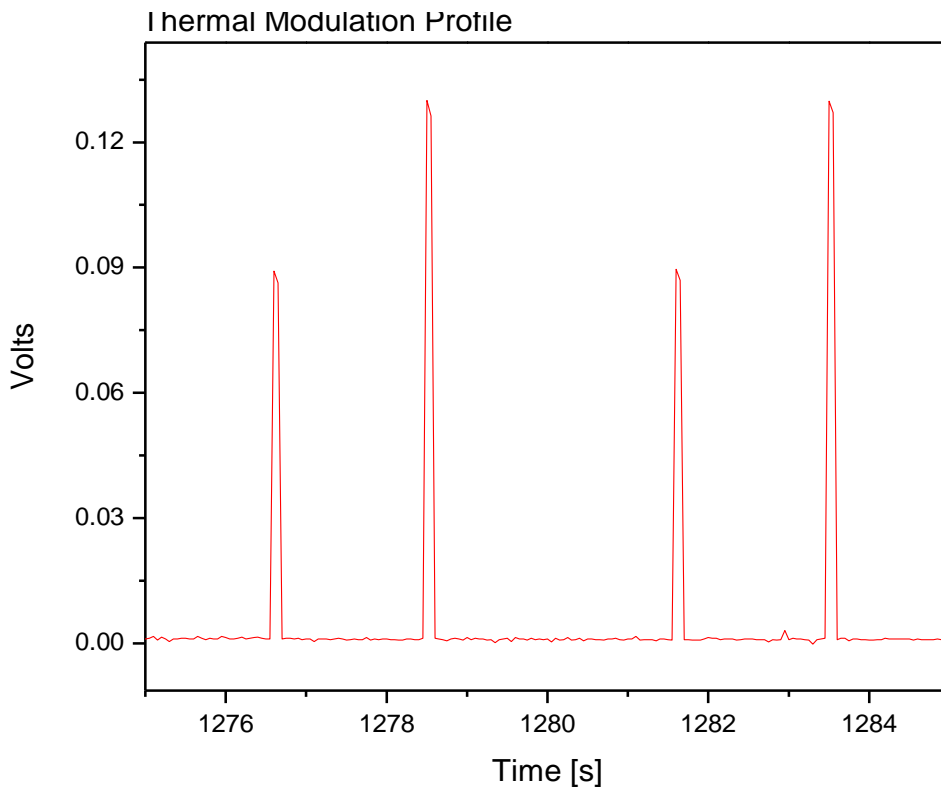
Figure 5.10: Thermal modulation profile with two cycles of modulation.

A problematic aspect of GCxGC thermal modulator development has been the inability to know the instantaneous temperature on-column of the thermal modulator region undergoing rapid heating. The small diameter of the silcosteel column embedded inside the insulated thermal modulator assembly makes it impossible to seat a thermocouple directly on the column to measure temperature. Instead a new methodology of gauging thermal modulator temperature instantaneously is shown here.

Adapted from work developed to monitor the bridgewire temperature used to detonate an electroexplosive device [Neyer, 1997; Mei et al., 2008], the temperature across a wire heated resistively can be written as a function (eqn 5.1) dependent only on the current across the wire and the initial temperature of the wire (or, in this case, silcosteel column) T_0:

$$T = T_0 + \frac{I^2 R l^2}{m C_p 8D} = T_0 + CI^2 \qquad\qquad \text{(Eqn 5.1)}$$

where I is the current across the column, R is the resistance of the silcosteel column, m is the mass of the column, l is the length of the column, D is the thermal diffusivity constant, and Cp is the specific heat of the column. All but one of these quantities (temperature) are material properties of the silcosteel column inside the thermal modulator and can be combined into one constant C.

To measure the current across each stage of the silcosteel column inside the thermal modulator, a shunt resistor with $1m\Omega$ resistance is placed in series to the column grounding wire. Since the voltage is known to $\pm0.1V$, the voltage across the shunt resistor can be used to obtain the current across the silcosteel column, enabling the temperature to be calculated via Equation 5.1.

Figure 5.11a shows the measured voltage drop of the first stage of the thermal

146

modulator (black trace) and the shunt resistor voltage (red trace) overlaid to compare the electrical waveforms. The shunt resistor shows significantly more line noise due to its small resistivity, which is sensitive to small temperature fluctuations. A heat sink was affixed to one side of the resistor to stabilize the temperature of the resistor during measurements. The TM waveform resembles an approximate square wave, but the shunt resistor measurements show an underdamped shape for the voltage readings - a gradual increase reaching the maximum value rather than a sharp leading edge. This is indicative of the resistive heating that occurred in the TM between the first stage and the shunt resistor.
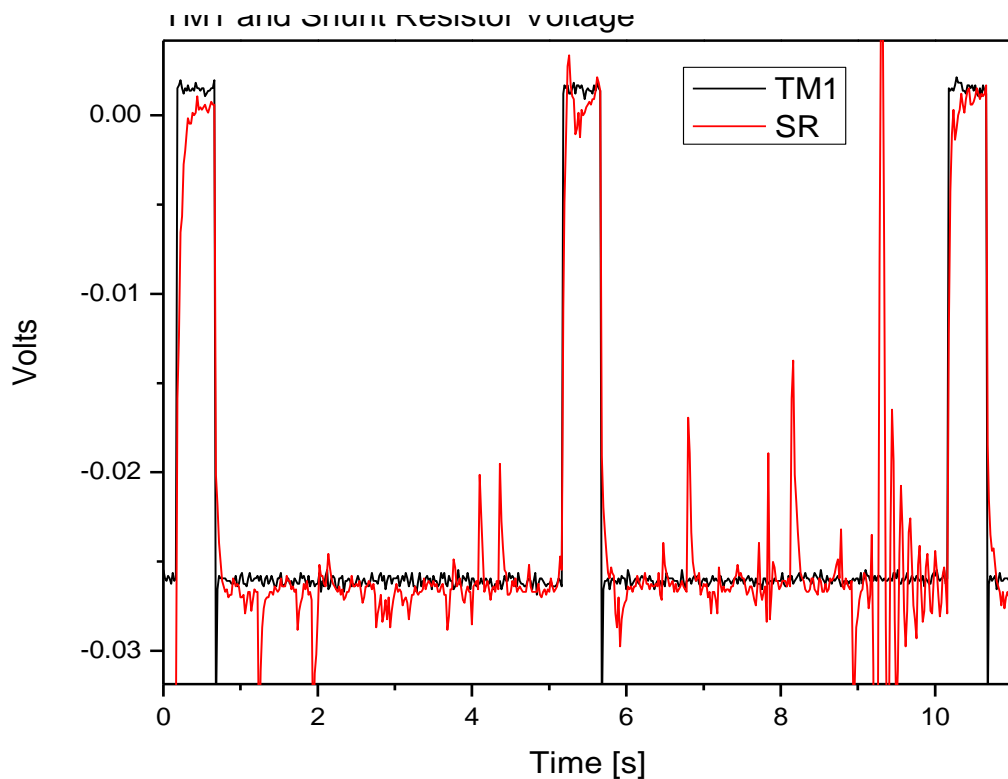
Figure 5.11(a): Thermal pulsing profile of the TM. Trace "TM1" is the voltage drop across the first stage of the modulator and Trace "SR" is the voltage drop across the shunt resistor.

The temperature of the silcosteel column embedded in the thermal modulator during the modulation cycles can be immediately determined from the shunt resistor

147

voltage drop. The noise in the small resistance shunt resistor can be reduced by isolating the resistor from room fluctuations and fitting a large heat sink to the resistor to minimize heat fluctuations, which affect resistivity. Using the parameters for stainless steel, the temperature profile of the thermal modulation of Figure 5.11a can be calculated and displayed as shown in Figure 5.11b. The modulator voltage in Figure 5.11a baseline was shifted to 0V for the calculation.
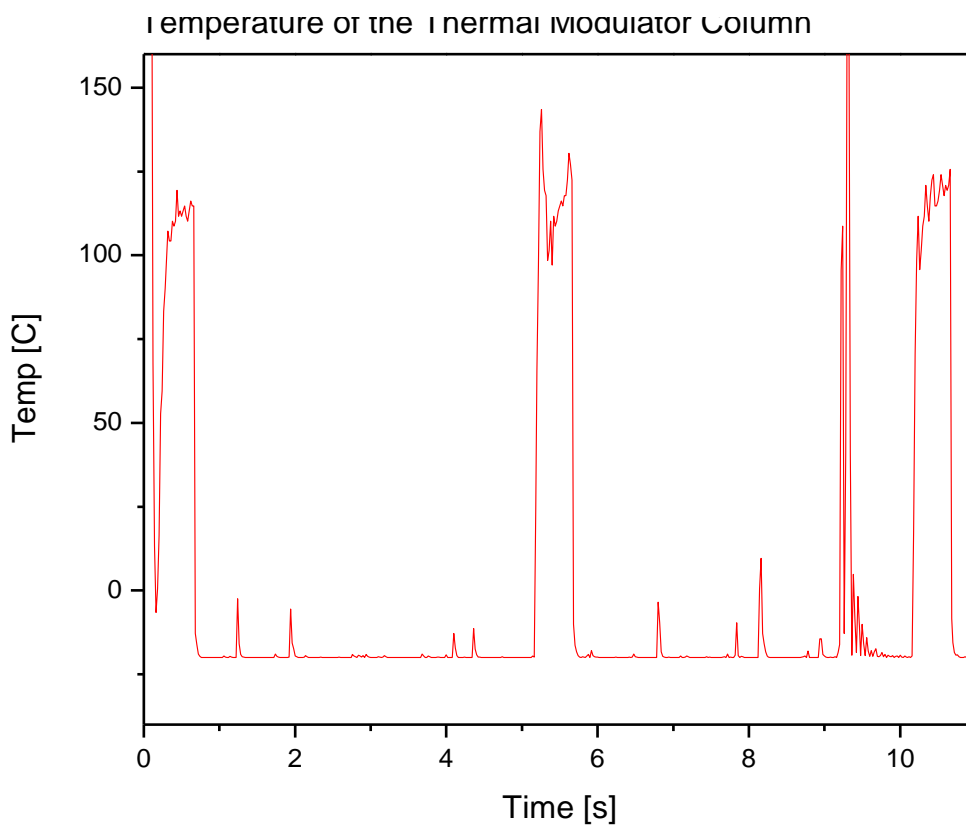

Figure 5.11(b): Temperature of the thermal modulator column over three cycles.

This solid-state cooling thermal modulator assembly was used as part of the GCxGC system with a 30-m Rtx-1 and a 1-m Rtx-1701 column connected to an ECD to examine its effectiveness at separating organic nitrate species, specifically α-pinene hydroxynitrates. An α-pinene OH-oxidation experiment in the presence of NOx was conducted in the interior of a large Teflon bag. The Teflon bag was injected with α-

pinene and isobutyl nitrite (OH source) and examined prior to irradiation and every hour during the start of the photooxidation experiment to check for products using the GCxGC with the solid-state cooling thermal modulator. Figure 5.12a shows the mixture prior to irradiation. There are few products, and some analyte species that were unretained in the second dimension shoed up as a vertical streak with no boundaries. Figure 5.12b shows the mixture in hour 4 after the UV lamps were turned on. Many new oxidation products were generated during the experiment. Both low molecular weight unretained products that co-elute with the air peak and less-volatile high boiling point products that elute later are more numerous in Figure 5.12b. There is also greater density and concentrations of compounds in the chromatograph and separation of compounds along the polar separation axis.
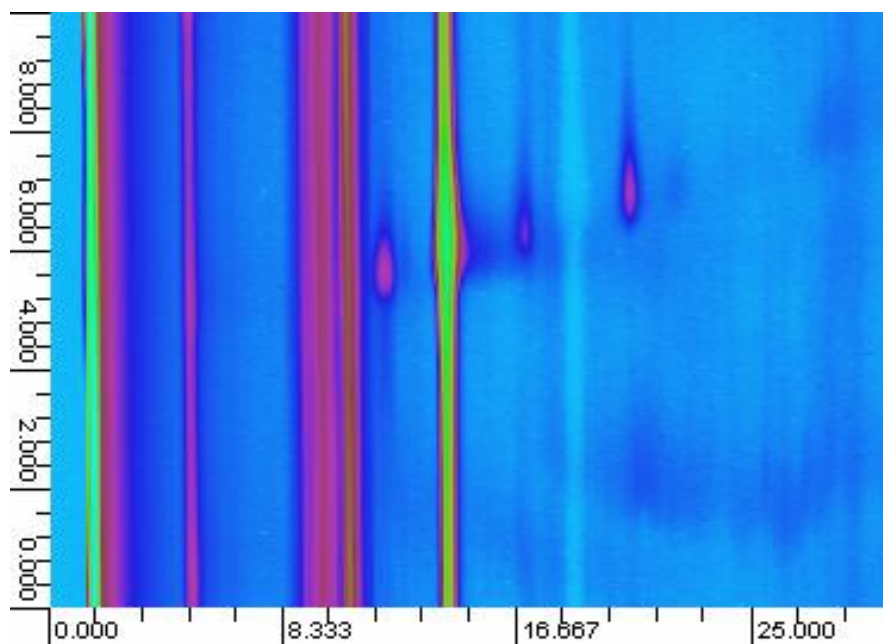
Figure 5.12(a): GCxGC chromatogram of α-pinene and NO$_x$ before irradiation.
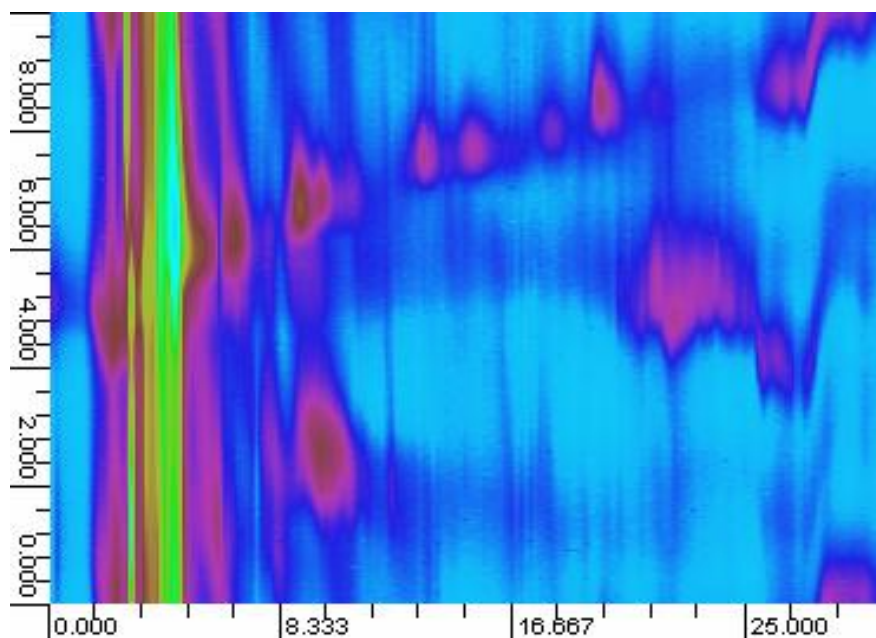
Figure 5.12(b): GCxGC chromatogram of α-pinene photo-oxidation reaction products.

Figure 5.12(c) is another way to visualize the GCxGC chromatograph by plotting the concentration as the third axis. The 3-dimensional visualization generates a topography that is useful for highlighting different groupings of compounds and seeing the relative concentrations. The green and yellow coloring in the first five minutes of the first dimension separation in the three figures represents high concentrations of unretained starting material along with the air peak. The pink oblong peak areas are oxidation products from the photo-oxidation of α-pinene. The z-axis height is much smaller but the vertical extent in Figure 5.12(c) makes the multiple peaks in the 18-25 minute first dimension elution block can be easier to detect.
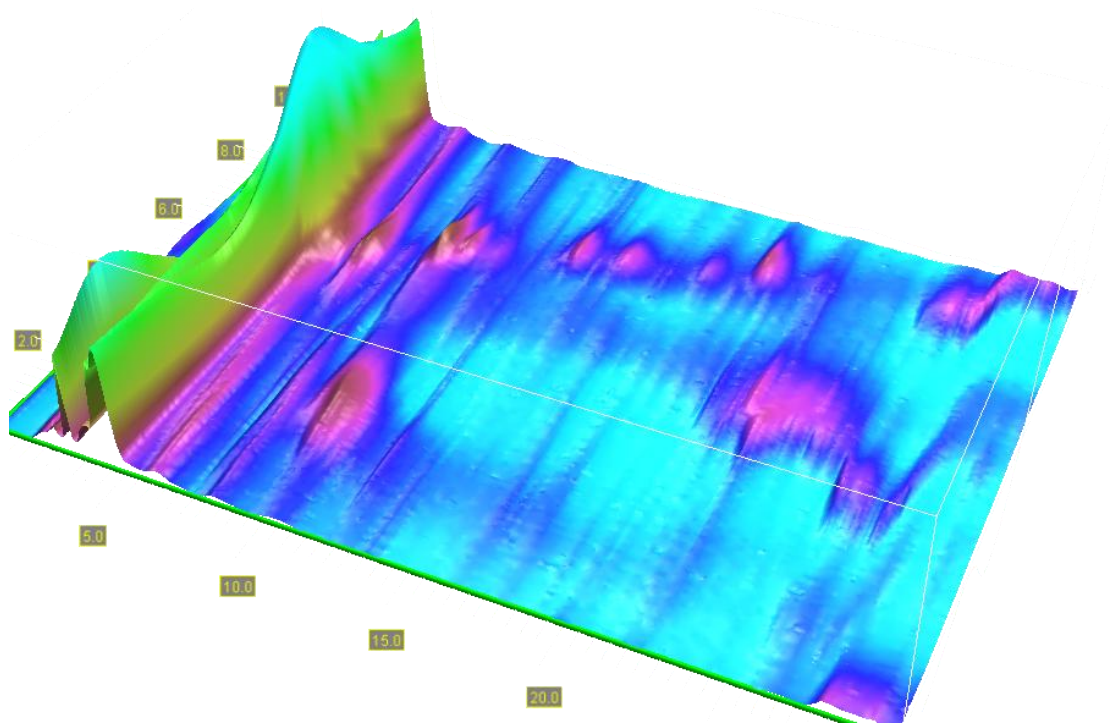
Figure 5.12(c): 3-dimensional representation of a GCxGC chromatogram.

The success in detecting oxidants and polar separation in the second dimension indicate that the GCxGC could be a useful analytical method for analyzing gas phase samples with known polar compounds such as aromatics and nitrates. However, the lack of good definition in the second dimension is an indicator that the cryofocusing step of the thermal modulator is not sufficient to trap all the effluents and the temperature of the thermal modulator needs to be even colder to fully trap and release the effluent plugs without the breakthrough that appears as "echoes" in the second dimension separation as slightly elevated background noise.
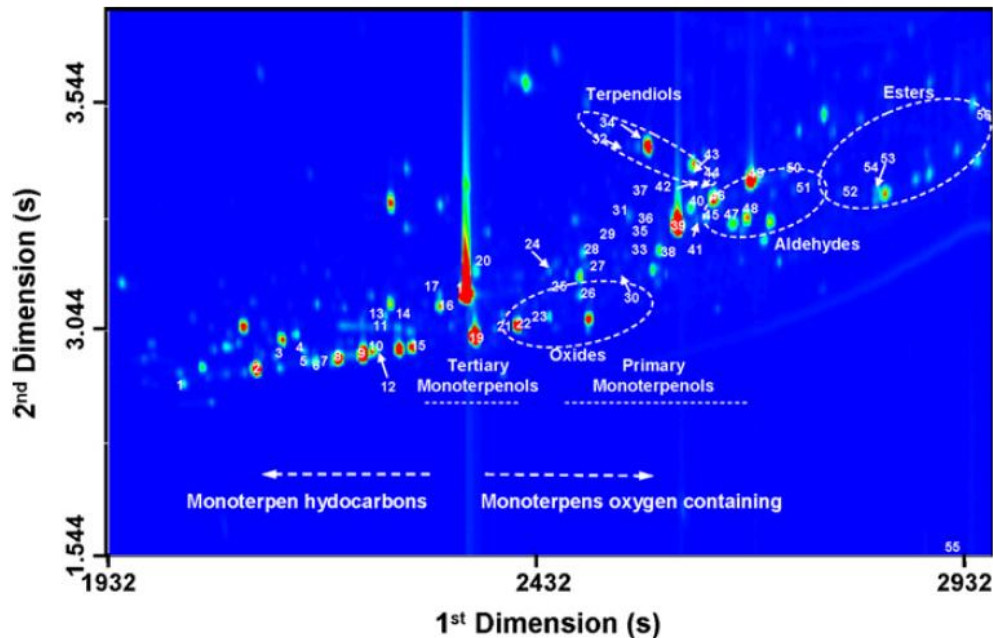
Fig. 5.13: GC×GC extracted chromatogram contour plot of m/z 93, 121 and 136. Bands or clusters formed by structurally related compounds are indicated [Rocha et al., 2007].

Rocha et al. [2007] analyzed monoterpenoids (monoterpene, monoterpenols, monoterpendiols, and cyclic monoterpenes) of white grapes with GCxGC and found significant increase in polarization of oxygenated products in the second dimension (Figure 5.13). From the Rocha et al. [2007] results and the preliminary results reported here, the potential of refining this technique in future analysis of BVOC nitrate species could be significant with a more efficient thermal modulator.

5.3 Thermal Modulator Model

The α-pinene oxidation experiment using a methanol/water mixture as a heat transfer fluid in the thermal modulator of the GCxGC instrument showed that separation of the monoterpene oxidant species was possible. However the cryofocusing step in the thermal modulator was not efficient during the modulation steps causing the

152

deconvoluted chromatograph to display streaky noise signals wrapping around the peaks in the second dimension. This is the GCxGC's equivalent of peak fronting from analyte breakthrough.

To improve the heat transfer efficiency of the thermal modulator a new heat transfer compound around the silcosteel column with better heat transfer properties was considered. Indium (In) is a soft and malleable post-transition metal similar to aluminum and gallium. With a melting point of 429.7°K, atomic weight of 114.82 amu and a specific heat capacity of 26.74 J mol^{-1} K^{-1} and 29.36 J mol^{-1} K^{-1} in the solid phase and liquid phase respectively, indium has high energy storage density due to a large difference in specific heat capacity between liquid and solid phases and a relatively low melting point [Gronvold, F., 1978]. During thermal modulation a portion of the indium undergoes phase change into liquid indium. The extent of the phase change and where the maximum radius of liquid indium can be expected during a typical modulation cycle were simulated in a model to evaluate the feasibility of using indium as a heat transfer agent.

A finite-element computational model for isothermal phase change of phase change material surrounding a thermal modulator column was created in Matlab [Appendix C]. The solid-state model predicted the heating and cooling profiles of the indium and the amount of liquid phase transition from the column center outwards. The model is time-dependent and one dimensional, assuming radial homogeneity in the phase change and heat transfer. The grid is fixed and each time step is uniform. Future versions could be done in cylindrical coordinates and use a variable time step size to maintain stability in each iteration [Furenes and Lie, 2006]. The discretization method was

suggested to be able to extend into a 2-dimensional case but the time step must be restricted such that the boundary movement in each direction lies within one element grid, making the improvement only incrementally better than the 1-dimensional case [Chun and Park, 2000].

The major components of the model include resolving the moving boundary between the liquid and solid phases and locating the radial distance of the maximum liquid phase change during modulation cycling. The most commonly used method for numerical solutions to this moving boundary problem is the enthalpy method as it does not require explicit tracking of the phase change boundary throughout the model domain [Furenes and Lie, 2006; Kovacevic et al, 2003]. However some drawbacks include the resulting non-linear equations due to the discretization of the domain space. Figure 5.14 shows the setup of the model that is one dimensional where z=0 is the heating source of the indium phase change corresponding to the location of the thermal modulator column and z=L is the radius of the copper housing that is the extent of the indium shell.
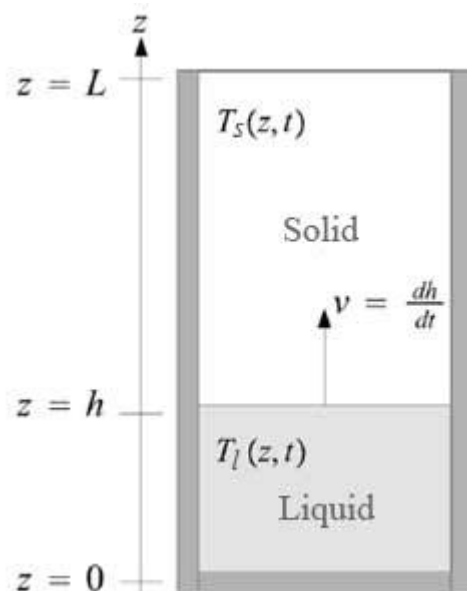
z

$z = L$ ┼

$T_s(z,t)$

Solid

$v = \frac{dh}{dt}$

$z = h$

$T_l(z,t)$

Liquid

$z = 0$ ┼

Figure 5.14: Schematic of the setup of the model with a moving boundary layer between the solid and liquid phase. The temperature at each point is

monitored to find the location of the phase boundary layer [Adapted from Furenes and Lie, 2006].

Initially, the model has a rectangular grid with *n* individual elements. The number of elements *n* determines the resolution of the model, but increasing the elements also increases computation time. The number of elements defined in the model domain was arbitrarily set at 100x1 elements and the run-time set at 1000 time steps (of 1ms each). Assuming the cylindrical space around the TM to be homogeneous and heat transfer to be uniform the one-dimensional z-axis slice will suffice to understand the propagation of the phase change boundary. The z = 0 origin was set to be the TM heat source, and for simplification, the TM source temperature were set at 400°K, a typical thermal modulation temperature according to Figure 5.11b. The boundary condition at z=L was set at 300°K. This simplification of the TM temperature could be improved by simulating the heating and cooling ramp times of the TM to gain a more realistic phase change instead of a step function temperature increase. The original configuration of the temperature and model nodes is shown in Figure 5.15. The first two nodes of the grid were held at the source temperature, while the rest was held at ambient levels. This eliminated the issue of discontinuous nodes at either extreme when processing the linearized calculations since the solution used the temperatures of the node before and after the current node.
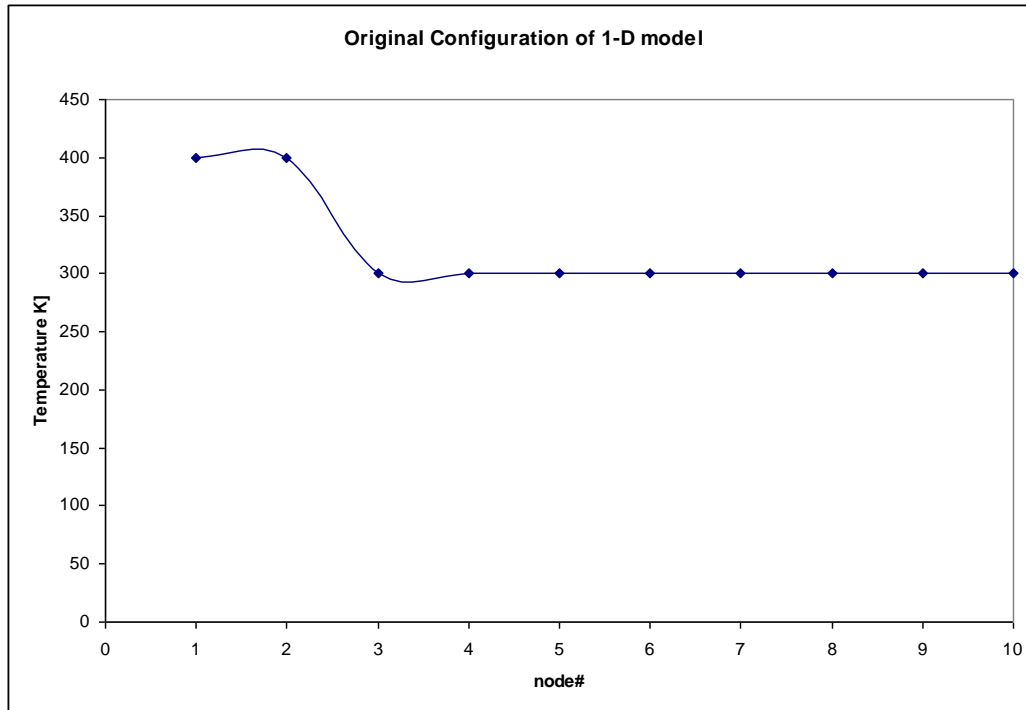
Figure 5.15: Original t=0s configuration of the 1-D model domain with first 10 nodes of 100 shown.

A series of assumptions were made regarding the thermal modulator in the model, including [Adapted from Zivkovic et al, 2002]:

a) Thermal conductivity parallel to the heat transfer fluid direction is ignored

b) Effects of convection is ignored (although it may be added in the future)

c) The material undergoing phase change is assumed to be ideal

d) The material undergoing phase change is assumed to have a definite melting point.

e) The material undergoing phase change is isotropic and homogeneous

f) Thermal resistance across the wall of the container is ignored

g) The sides of the container are insulated and heat transfer only occurs at the site of the finite elements in the model.

With these assumptions in place, the enthalpy formulation can be written as eqn 5.2:

$$\frac{\partial H}{\partial t} = \nabla \cdot \left(\frac{k}{\rho} \nabla T \right) \qquad \text{(Eqn 5.2)}$$

where $H = h + L \cdot f_1$ is the enthalpy split into sensible (h) and latent heat components (L*f1). The sensible component h is an integral of the temperature from the melting point temperature to end temperature in Eqn 5.3.

$$h = \int_{T_m}^{T} c \, dT \qquad \text{(Eqn 5.3)}$$

f_1, the liquid fraction, is defined to be Eqn 5.4:

$$f_1 = \begin{cases} 1 & T > T_m \\ 0 & T < T_m \end{cases} \qquad \text{(Eqn 5.4)}$$

The latent heat component enters the enthalpy equation whenever f_1 is 1. To find temperature, the sensible enthalpy component is deconvolved from the total enthalpy and differentiating.

This formulation breaks the model into two components, one which is undergoing phase change, and one which is not. When undergoing phase change, the ordinary heat diffusion equation solved by the model is Eqn 5.5:

$$\frac{\partial T_i}{\partial t} = \frac{k}{\rho c \Delta x^2} \left(T_{i-1} - 2T_i + T_{i+1} \right) \qquad \text{(Eqn 5.5)}$$

where ρ is the mass density of the medium and c is the specific heat of the phase, k is the thermal conductivity of the medium.

The heat diffusion equation 5.5 can be numerically solved by applying the backward differencing technique, which after rearranging gives a fully implicit finite difference equation Eqn 5.6 that updates the temperature in each grid element by looking at the two adjacent element temperatures:

$$a_{i-1} \cdot T_{i-1} + a_i \cdot T_i + a_{i+1} \cdot T_{i+1} = T_i^{old} \qquad \text{(Eqn 5.6)}$$

Where coefficients $a_{i-1}=a_{i+1}$ = the Fourier number F_0 and $a_i = 1+2*F_0$. F_0 is Eqn 5.7:

$$F_0 = \frac{k}{\rho c \Delta x^2} \qquad \text{(Eqn. 5.7)}$$

. Using this solution the temperature at each grid could be examined at each time step. The other quantity needed is the liquid fractionation of the grid to determine the location of the phase boundary. In a phase change regime, the heat diffusion equation becomes Eqn 5.8:

$$L\frac{\partial f_i}{\partial t} = \frac{k}{\rho c \Delta x^2}\left(T_{i-1} - 2T_m + T_{i+1}\right) \qquad \text{(Eqn 5.8)}$$

The liquid fraction is updated using backward differencing of the left hand term, yielding:

$$f_{li} = f_{li}^o + \frac{k\Delta t}{\rho L \Delta x^2}\left(T_{i-1} - 2T_m + T_{i+1}\right) \qquad \text{(Eqn 5.9)}$$

This f_i quantity was monitored at each time step. When the value of f_i reaches 1, the element that most recently showed unity liquid fraction was the location of the phase change boundary. During computation, the start and end of the phase change boundary was noted to observe how far beyond the TM column the boundary expands.

5.4 Model Results

The thermal modulator heat source at the beginning of the simulation was pulsed to a temperature of 497°K, or 200°C, and the rest of the grid elements were kept at ambient temperature 300°K. After 1000 time steps of 0.1ms intervals were processed according to the backward difference technique to numerically solve the heat diffusion partial differential equations the results of the temperature in the first 8 nodes that are elements with increments of 0.1cm in the z-axis are shown in Figure 5.16a. The figure

shows the moving phase boundary propagates from node to node, starting with node 1

and terminating at node 4 when the system reaches steady state, which occurs at ~500ms.

From these dimensions, this corresponds to a liquid phase maximum boundary location

of approximately 0.3cm outside of the TM column. This demonstrates that the liquid

phase boundary will not reach the outer walls housing the TM and indium, and can be

contained within a TM housing of reasonable size, less than 1cm in diameter.

For comparison, the same model was run with a lower thermal modulator heat

source temperature set at 400°K. The result shown in Figure 5.16b shows no phase

change in the heating profile of the first 8 nodes, and correspondingly no moving phase

change boundary. Instead a smooth diffusion of temperature across the nodes was seen

for each node.
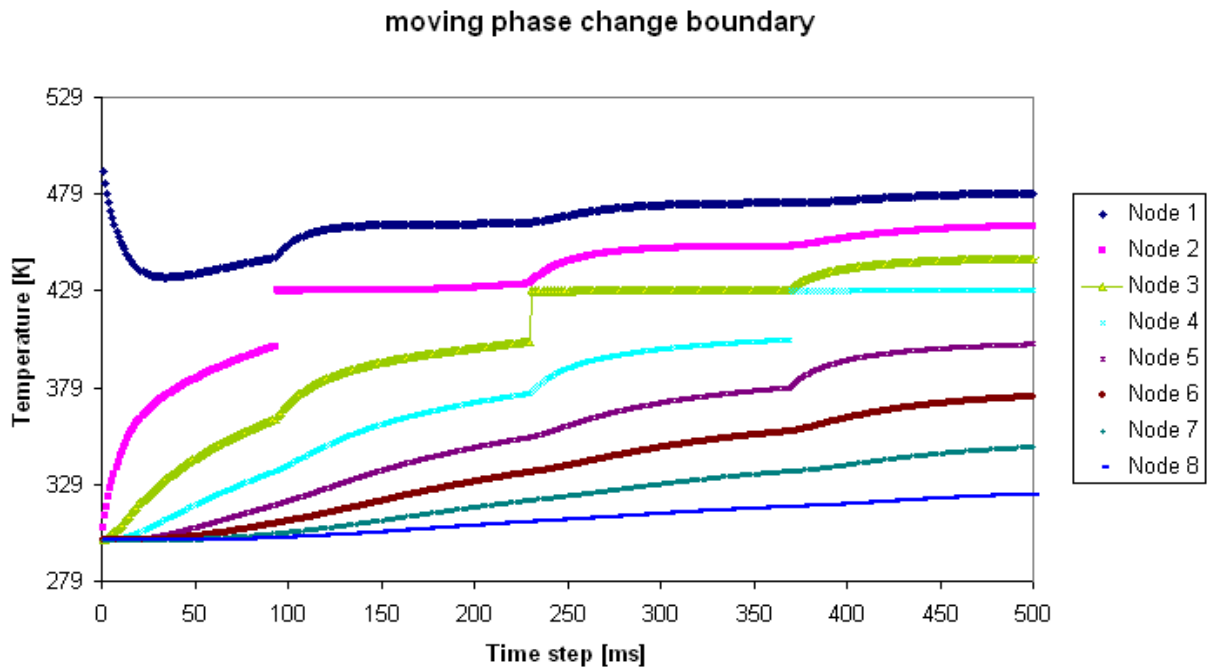
Figure 5.16(a): The moving phase change boundary with applied 497K heat source at origin. This shows that the phase change stops at node 4.

low origin heat source
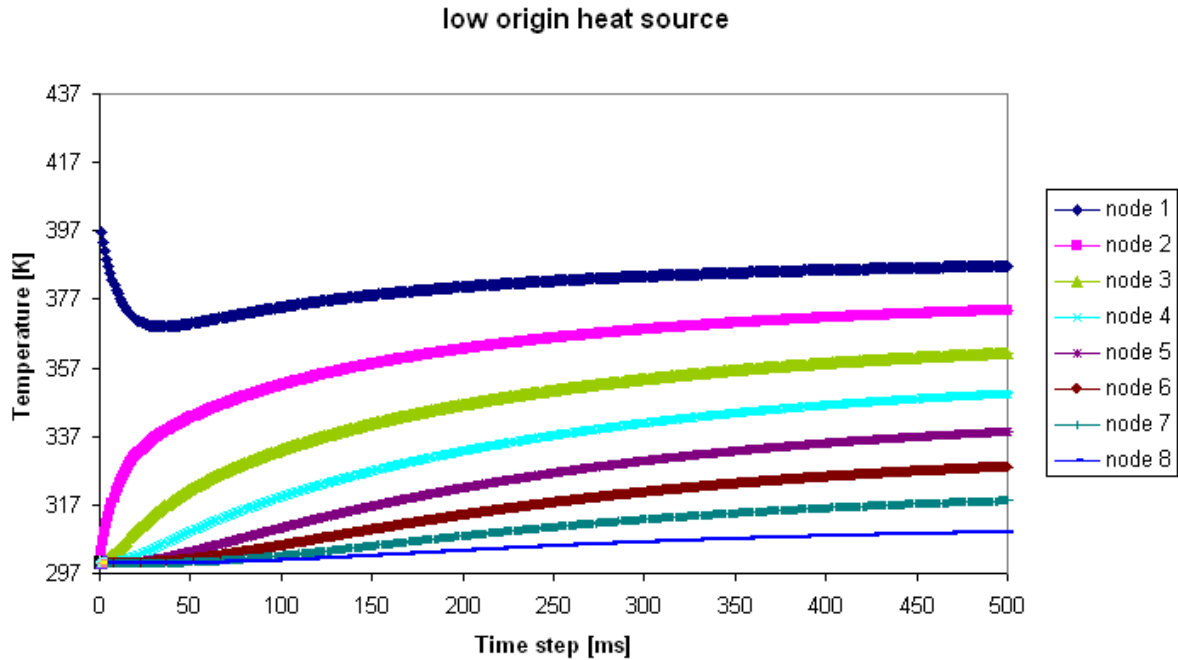
Figure 5.16(b): With a TM heat source (400K) less than the boiling point of indium, showing no phase change in the nodes.

5.5 Conclusions

The indium thermal modulator model can give a time and space prediction of where the boundary phase transition occurs. It gives a theoretical basis for a modification of the solid-state TM design replacing the methanol/water heat transfer fluid with indium and places constraints regarding the size and heating profile of a new indium solid-state TM. The main limitation of this model is that it applies a constant heating temperature at the origin and that is not reflective of the actual heating profile the TM undergoes. However this is a good first-order representation of the maximum heating load the TM would experience and dissipate into the heat transfer material. In future modeling attempts, a variable heating source should be implemented to ascertain the temperature change response.

The evaluation of GCxGC in the context of α-pinene hydroxynitrate detection remains to be pursued. The first attempts to integrate a two-stage solid-state modulator with a methanol/water heat transfer fluid produced temperatures of -20°C inside the thermal modulator, but was found to be inefficient at stopping peak breakthrough. A lower modulator operating temperature could be achieved with a more efficient heat transfer interface. The integration of indium as the heat-transfer interface in the two-stage solid-state thermal modulator could be pursued based on the temperature and phase change profile presented here.

CHAPTER VI

Conclusions and Future Work

6.1 Evaluation of Results

Individual isomers of α-pinene β-hydroxynitrates (APNs) were synthesized and identified for the first time. Two APN isomers, APN-A and APN-B, were identified during analysis of the synthesized organic nitrate standard and detected in the photochemical chamber experimental results. A third isomer, APN-C, is tentatively identified as a related hydroxynitrate but more experiments are necessary to explore its molecular structure, including whether or not it does indeed have an internal double bond as suggested by quantum chemistry models [Vereecken and Peeters, 2000].

A series of photochemical reaction chamber experiments measured the total yield of all three APNs to be 15 ± 7.7 %. Speciated nitrate yields of APN-A = 6.4 ± 3.3 %, APN-B = 3.5 ± 1.8 %, and APN-C = 4.6 ± 2.3 % were determined for the first time. The total hydroxynitrate yield result is consistent with the 18 ± 9 % result of Nozière et al. [1999] and in contrast to the Aschmann et al. [2002] results of <1%. The atmospheric lifetime of these APNs are calculated to be on the order of 1-2 days, making it possible for these nitrates to influence regional atmospheres and participating in transport processes. Despite the ~50% uncertainty in the total nitrate yield, it is clear that the nitrates generated are well above the <1% reported by Aschmann and Arey [2002].

The branching ratio of RO_2+NO ($k_{3.1c}/(k_{3.1b}+k_{3.1c})$) for each APN was calculated to be 0.15 ± 0.09 for APN-A, 0.11 ± 0.06 for APN-B, and 0.24 ± 0.10 APN-C with an overall branching ratio (for total hydroxynitrates) of 0.15 ± 0.09. This result is similar to the quantum chemical model predicting a branching ratio of 0.18 by Zhang et al. [2004] for alkenes and smaller than the analogous C_{10} alkyl nitrate branching ratio of 0.23 measured by Aschmann et al. [2001]. This result is consistent with O'Brien et al. [1998] and Arey et al. [2001] observations that RO_2 radicals with a β-hydroxyl functional group have a branching ratio less than their unsubstituted analogues. However, the branching ratio for α-pinene hydroxynitrates is not higher than the experimentally measured branching ratio of 0.15 ± 0.10 for isoprene nitrates by Chuong and Stevens [2002] as had been theoretically predicted. This could possibly be attributed to the cyclic aromatic structure of α-pinene, which Espada and Shepson [2005] have suggested could substantially decrease the nitrate branching ratio compared to a linear analogue. Experiments measuring the branching ratio of a linear C_{10} alkene hydroxynitrates would allow a useful comparison.

A chemical model created to explore the α-pinene OH reaction mechanism showed good agreement with chamber conditions for important chamber reactivity markers such as NO decay, O_3 growth, and α-pinene degradation. The mechanism predicted the concentration of APN-A very well while over-predicting APN-B and APN-C, most notably in the first two to three hours of the experiment where the model predicted 2x higher concentrations of APN-B and APN-C than was measured. This could indicate that the GC-ECD instrument may have had difficulties detecting both APN-B

and APN-C during the early stages of the experiment when the B and C nitrates were produced in smaller quantities.

GCxGC ("two-dimensional" gas chromatography) was explored as a potential new methodology to analyze gas-phase BVOC mixtures with a large amount of aromatic and nitrate functional groups. A bench-top GCxGC-ECD was used to test a two-stage solid-state thermal modulator assembly for an α-pinene OH-oxidation experiment. The experiment blank response and the post-irradiation chromatograms showed that many new species were produced from the reaction of α-pinene with OH along with the successful separation of compounds along the second dimension. A finite-element model was created to evaluate the use of indium as a possible heat transfer material in the next iteration of the solid state thermal modulator.

6.2 Laboratory Experience ("Lessons Learned")

A set of five α-pinene OH-oxidation photochemical reaction chamber experiments was presented in this thesis. Approximately 40 completed experiments were discarded from further consideration due to numerous shortcomings, including insufficient peak separation, calibration anomalies, one or more instrument malfunctions, and lack of data convergence in the analysis, which pointed to chromatography or experimental conditioning problems.

The experience gained from learning how to work with low-volatility and highly-adsorptive organic nitrate compounds in a photochemical chamber environment could be useful to other researchers. Important laboratory experience is presented here for the edification of other intrepid researchers aiming to extend or repeat the experiments.

Major concerns during the photochemical reaction chamber experiments were: 1) Transfer line adsorption; 2) Chamber initial conditions; 3) Initial NO_x ratio; 4) Column temperature programming; and 5) Instrument conditioning. The low volatility and high adsorptivity of alkene nitrates lead to irreversible adsorption on chamber walls and instrument surfaces [Muthuramu et al., 1993]. The temperature of all inlet and outlet lines leading from the chamber to each analytical instrument must be held to at least 100°C but no more than 140°C to prevent significant sample loss. The heating tape, heating wire, cartridge heaters used to heat all the transfer lines during the experiment were monitored with a thermocouple so that all the temperatures were within 5°C of each other to prevent cold spots from forming in the system during sample transfer.

The condition of the chamber prior to commencing the irradiation experiment was highly important to the repeatability of experimental results. Many photochemical chamber walls are a significant source of HONO and HNO_3, which can photolyze to provide OH, NO, and NO_2. The increased OH production speeds up the consumption of the starting alkene material, which is typically undesirable since the GC-ECD requires 45 minutes per run time and a faster reaction time means fewer data points per experiment, detrimental to experiment statistics. The NO_2 produced from the photolysis of HNO_3 increased the amount of ozone generated in the chamber and depleted NO too quickly, resulting in slower nitrate growth. Experience has shown that the cleaner the chamber prior to experiment the more reproducible the reaction products. A chamber cleaning procedure that has yielded good and repeatable results begins with a full 24 hour purge of high flow rate (10L min^{-1}) flushing of the chamber with a clean air source and the UV lamps turned on to offgas HNO_3. Ozone can react with compounds that are adsorbed onto

165

the walls and remove them, which, when combined with the high flow air can help clean the chamber. Performing this cleaning operation once a month helps keep the "blank" baseline sample analysis of the chamber as noise-free as possible. 24 hours before each chamber experiment, a tank of ultra-high purity zero air is used to flush the chamber thoroughly just before injection of starting material. The zero air is much more reliably contaminant-free than lab air from a clean air generator and helps dilute contaminants already present inside the chamber. A tank of ultra-high purity zero air was also used for the dilution flow during a chamber experiment for the same reasons. Over a typical 8-16 hour long oxidation experiment contamination from a dilution flow source that is unreliable can wreak considerable havoc on the experimental data, introducing contaminant hydrocarbons to participate in the reactions or unknown contaminants that can change the conditions of the reaction.

The starting compounds (α-pinene, NO/NO_2, water vapor) were injected into the chamber with ultra-high purity zero air or ultra-high purity nitrogen (for NO injections) to minimize the starting NO_2 concentration. High NO_2:NO ratios suppress nitrate formation since a high NO_2 results in lower initial NO concentrations, dramatically slowing the production of α-pinene nitrates. Holding the NO_2:NO to a 1:30 ratio or lower from experience appeared to be optimal in the initial starting NO_x injections.

Lastly, tuning the temperature ramp of the GC-ECD was extremely important in isolating and maximizing the column separation for α-pinene nitrates. Balancing fast analysis time and sufficient separation of the nitrates required many iterations of testing to develop a final temperature program for the analytical column. The α-pinene nitrates eluted at 114-116°C in the GC-ECD system as well as the GC-MS, so a quick ramp from

the starting temperature to 105°C, just below the target elution temperature, was slowed to a ramp of 1°C min^{-1} until 125°C followed by a final ramp to 250°C to clear the column for the next analysis. This fast, slow, fast temperature ramp centering around the 105-125°C elution temperature proved to be the best strategy for optimizing the temperature programming of the GC analytical column. This temperature ramping allowed one full GC-ECD analysis to be performed every 60 minutes allowing for a 45 minute analysis followed by a 15 minute cool-down and sampling for the next run.

Muthuramu et al. [1993] found that the first few injections of mixtures containing organic nitrates registered very low response in a detector. When the same solution was re-injected 30 times in succession and the peak area was plotted versus injection number the detected concentration stabilized after about the 4th or 5th consecutive injection. From their experience it was expected that before repeatable results were possible an instrument must be "conditioned" by repeated injections of high concentrations of target organic nitrates. This conditioning coated the columns, interfaces and instrument surfaces to decrease the inadvertent and largely irreversible adsorption of sample during analysis. indicating that hydroxynitrate and dinitrate concentrations do not stabilize in a GC until several consecutive injections of sample material have been introduced in the instrument.

Daily injections of α-pinene synthesized nitrates helped to keep the GC-ECD instrument in the best conditioning for nitrate separation when performing photochemical experiments. Prior to each experiment at least 3 successive sampling from a Teflon bag containing a high-concentration gas phase organic nitrates mixture were sufficient to condition the instrument prior to the experiment. Three successive samples of concentrated organic nitrate standards showed growth in nitrate peaks that leveled off by

the third analysis. This instrument conditioning step was important in helping to ensure reproducibility of results and should not be skipped.

6.3 Suggested Future Work

There are many possible directions to extend the work presented in this thesis. Some suggestions for future work include isolation of individual α-pinene nitrates in the synthesized nitrate mixture for ^{1}H NMR analysis to examine the structure of the isolated compound. Past experience has shown this method to be unsuccessful for an isolated isoprene nitrate but it could be re-examined for each HPLC-separable peak in the synthesized mixture.

The synthesized mixture as separated by the HPLC show 3 products in Figure 2.4, but according to dipole moment calculations, more than a dozen APN conformers could have been produced in the synthesis process. While only a few of the possible conformers would be energetically favorable for formation, it is likely that with better separation in the HPLC analysis would allow identification of additional synthesis products than has been shown in this work. A stationary phase that is tuned for organic nitrate separation would be useful to distinguish between alkyl nitrate, hydroxynitrates and dinitrate synthesis products such as one produced by Kastler et al. [1998]. Due to the large permutations of nitrate functional group location on the alkene molecule, there could be many trace nitrate species that were not detectable with the current all-purpose HPLC column.

Additional identification analysis of the synthesized compounds could be carried out using GC-MS directly on-line with the photochemical reaction chamber during experiments. Currently a GC-ECD, which does not produce mass fragmentation

information unlike the GC-MS is connected to the photochemical chamber. The chromatography peaks detected in the GC-ECD were compared to a GC-MS of the synthesized nitrate samples and that identification was then transferred to the experimental results. This identification through intercomparison of the GC-MS and GC-ECD instrument data introduces uncertainties that would be eliminated if a GC-MS or similar mass information producing instrument were placed on-line with the chamber during experiments.

The RO_2+NO reaction rate constants calculated in this work and used in the model were based on isoprene-RO2 + NO reaction rate constants reported by Stevens et al. [1999]. It would be useful to have a reaction rate constant experimentally determined for α-pinene peroxy radicals, which would affect the rate of nitrate formation in both the model.

Investigation into GCxGC or some other comprehensive multidimensional separations could be invaluable for improving the separation of the gas phase air mixture inside the chamber experiment and should be pursued in the future. The complex mixture present during the chamber oxidation experiments could benefit greatly from the improved separation power and peak capacity of a multidimensional chromatography method. The preliminary results from the GCxGC evaluation of an α-pinene oxidation experiment discussed in Chapter 5 show that a comprehensive multidimensional chromatography method tuned for nitrate analysis could be promising, particularly if a detector producing mass identification information could be added to the instrument, such as a time-of-flight or quadrupole mass spectrometer. Improvement of the solid-state thermal modulator with a better heat transfer medium than a methanol/water mixture such

as indium would be the next logical step to improve the second dimension separation in the GCxGC analysis. The model used to evaluate the efficacy of indium as a heat transfer medium for the solid-state thermal modulator could be expanded to cylindrical coordinates with a variable grid and step size to enhance the resolution and stability of the solution.

Lastly, ozone reaction rate experiments could be carried out for each individual α-pinene nitrate. While OH reactions with α-pinene are dominant, the ozonolysis of α-pinene is the most efficient pathway to generating SOAs, with a branching ratio as high as 0.67 [Pathak et al., 2007].

APPENDIX A. Structure-Activity Relationship Calculations

Kwok and Atkinson [1995] provided a structure-activity relationship for estimating the reaction rate of OH and α-pinene. The total reaction is $k_{OH} = k_{abstraction} + k_{addition}$ and the percentage of reactions resulting in hydrogen-abstraction rather than OH-addition is $k_{abstraction}/k_{OH}$.
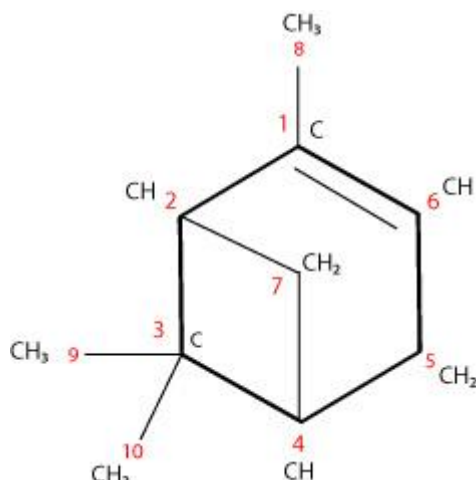
Figure A.1 Structure of α-pinene with labeled molecular sites where OH can react.

Site	Reaction on site	Group rate constants	$k_{OH} \times 10^{12}$ cm^3 $molecule^{-1}$ s^{-1}
8,9,10	$3 \, k_{prim}F(CH_3))$	3(0.136)(1.23)	0.501
2	$k_{tert}F(C)F(CH_2)F(C)F_6 \, F_4F_6$	(1.94)(1.23)(1.23)(0.28)	0.822
7	$k_{sec}F(CH)F(CH)F_4F_6$	(0.934)(1.23)(1.23)(0.28)	0.396
4	$k_{tert}F(C)F(CH_2)F(CH_2)F_6F_4F_6$	(1.94)(1.23)(1.23)(0.28)	0.822
5	$k_{sec}F(CH)F(CH_2)F_6F_6$	(0.934)(1.23)(1.23)	1.41
6	$k_{addition}(>C=CH-)$	86.9	86.9
6	$k_{sec}F(CH_2)F(>C=CH-)F_6F_6$	(0.934)(1)	0.934

Table A.1 Site-specific OH abstraction and addition rate constants.

The total hydrogen abstraction is 4.89×10^{12} cm^3 $molecule^{-1}$ s^{-1}. OH addition across the double bond has k_{OH} of 86.9×10^{12} cm^3 $molecule^{-1}$ s^{-1}. $k_{OH \, addition} / k_{total} \sim 95\%$ and $k_{OH \, abstraction} / k_{total} \sim 5\%$.

Peeters et al. [2001, 2007] developed another structure-activity relationship for the addition of OH to polyalkenes. This SAR discriminates between the two sides of a double bond OH addition. The reaction rate is based on the environment of either carbon of the double bond. Assigning C_a as one carbon and C_b as the other carbon of the double bond, for k_{OH} in α-pinene, the OH addition reaction is calculated as $k_{OH\ addition} = k_{Ca} + k_{Cb}$.
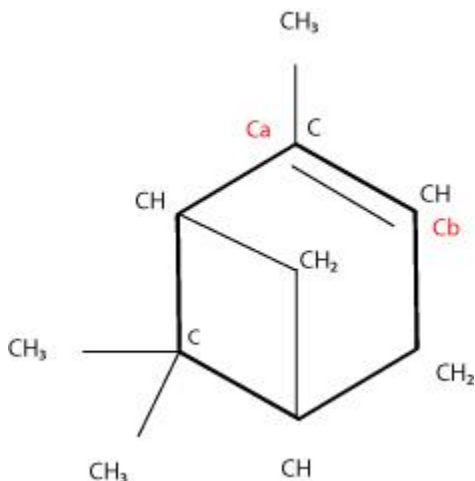
Figure A.2 The two carbon sites undergoing OH addition in α-pinene reactions
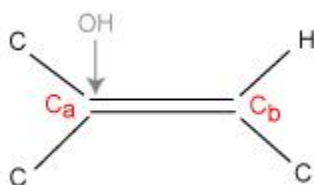
Figure A.3(a) C_a reaction site   **Figure A.3(b) C_b reaction site**
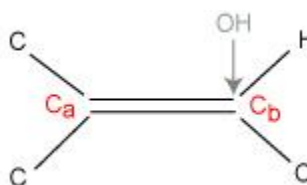
Carbon "C_a" is a tertiary product radical due to it having no hydrogens in its immediate neighbors as shown in Figure A.3(a). Carbon "C_b" as the site of the addition produces a secondary product radical due to it having one hydrogen and one non-hydrogen in its immediate vicinity as shown in A.3(b). The calculated reaction rate for the C_a carbon site addition of OH is 5.5×10^{-11} cm^3 molecule^{-1} s^{-1}, for C_b it is 3.0×10^{-11} cm^3 molecule^{-1} s^{-1}. The ratio of OH addition between the two carbon sites, which correspond to APN-A and APN-B precursors is approximately 2:1.
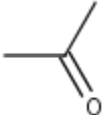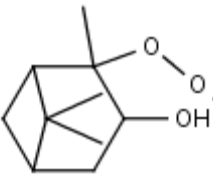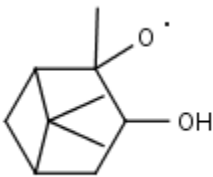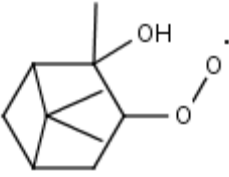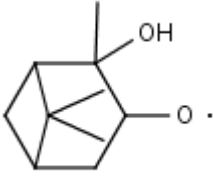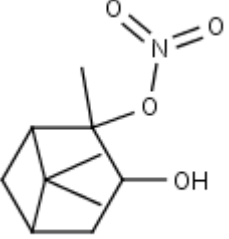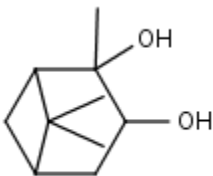
APPENDIX B. α-Pinene OH-oxidation Reaction Mechanism Tables

k	Reaction	Source
2.80E-11	APINENE + OH ==> APINAO2	Peeters et al. 2001
1.70E-12	APINAO2 + NO==>APINANO3	this work
9.40E-12	APINAO2 + NO==>APINAO + NO2	Chuong and Stevens, 2002
1.63E-12	APINANO3+OH==>PINAL+NO2	Kwok and Atkinson 1995
6.44E-14	2APINAO2==>2APINAO+O2	MCM
2.76E-14	2APINAO2==>2APINAOH	MCM
1.00E-03	APINAO ==> PINAL + HO2	MCM
2.09E-11	APINAO2+HO2==>APINAOOH	MCM
1.83E-11	APINAOOH+OH==>APINAO2	Kwok and Atkinson 1995
5.79E-06	APINAOOH==>APINAO+OH	MCM
2.50E-12	APINAO2+NO3==>APINAO+NO2	Stockwell 1997
1.49E-11	APINAOH+OH==>APINACO+HO2	MCM
1.1E-05	APINANO3==>WallLoss1	this work
2.13E-11	APINENE + OH ==> APINBO2	Peeters et al. 2001
1.40E-12	APINBO2+NO==>APINBNO3	this work
9.40E-12	APINBO2+NO==>APINBO+NO2	Chuong and Stevens, 2002
6.19E-12	APINBNO3+OH==>APINBCO+NO2	Kwok and Atkinson 1995
8.80E-13	2APINBO2==>2APINBO+O2	MCM
8.80E-13	2APINBO2==>2APINBOH	MCM
1.49E-11	APBINBOH+OH==>APINBCO+HO2	Kwok and Atkinson 1995
1.00E-04	APINBO ==> PINAL + HO2	MCM
2.09E-11	APINBO2 + HO2 ==> APINBOOH	MCM
5.79E-06	APINBOOH+hv==>APINBO+OH	MCM
3.28E-11	APINBOOH+OH==>APINBCO+OH	Jenkin 1997
8.18E-12	APINBCO+OH==>carbonyls	MCM
2.50E-12	APINBO2+NO3==>APINBO+NO2	Stockwell 1997
4.3E-05	APINBNO3==>WallLoss2	this work
1.22E-11	APINENE + OH ==> APINCO2	Peeters 2007
2.96E-12	APINCO2+NO==>APINCNO3	this work
9.40E-12	APINCO2+NO==>APINCO+NO2	Chuong and Stephens, 2002
4.69E-15	2APINCO2==>2APINCO+O2	MCM
2.47E-11	APINCNO3+OH==> CH3COCH3+carbonyl+NO2	MCM
1.00E-05	APINCO ==> CH3COCH3 + otherRO2	MCM
2.36E-12	otherRO2+NO==>otherNO3	MCM
7.44E-12	APINCO2 + HO2 ==> APINCO + NO2	MCM
2.09E-11	APINCO2+HO2==>APINCOOH	MCM
5.79E-06	APINCOOH+hv==>APINCO+OH	MCM
1.30E-10	APINCOOH+OH==>APINCO2	MCM
2.50E-12	APINCO2+NO3==>APINCO+NO2	MCM
3.0E-5	APINCNO3==> WallLoss3	Loss -empirical
3.29E-35	NO2+NO2+H2O==>HONO+HNO3	Estimated
3.96E-04	HONO==>OH+NO	JPL
2.89E-10	HNO3==>OH+NO2	JPL
3.50E-12	HO2 + NO==>OH + NO2	JPL

5.00E-16	HO2 + NO2 ==>HONO + O2	JPL
1.50E-12	2HO2==>H2O2+O2	JPL
8.10E-12	HO2+NO==>NO2+OH	JPL
1.39E-12	HO2+NO2==>HNO4	JPL
1.05E-12	HO2+NO3==>HNO2+O2	JPL
2.45E-12	HO2+NO3==>NO2+OH+O2	JPL
1.29E-08	H2O2==>2OH	JPL
1.70E-12	H2O2+OH==>HO2+H2O	JPL
1.93E-30	OH + NO2 +M ==>HNO3 + M	JPL
4.50E-12	OH+HONO==>NO2+H2O	JPL
1.15E-13	OH+HNO3==>NO2+H2O	JPL
4.60E-12	OH+HNO4==>NO2+O2+H2O	JPL
4.87E-12	OH+NO==>HONO	JPL
2.20E-11	OH+NO3==>NO2+HO2	JPL
6.69E-15	OH+H2==>H2O+HO2	JPL
1.11E-10	OH+HO2==>O2+H2O	JPL
6.83E-14	O3+OH==>HO2+O2	JPL
1.90E-15	O3+HO2==>OH+2O2	JPL
1.90E-14	O3+NO==>NO2+O2	JPL
3.23E-17	O3+NO2==>NO3+O2	JPL
2.65E-11	NO3+NO==>2NO2	JPL
2.65E-11	NO2+NO3==>NO+NO2+O2	JPL
2.90E-11	NO2+NO3==>N2O5	JPL
2.30E-16	NO3+NO3==>2NO2+O2	JPL
4.50E-04	NO3==>NO2+O	JPL
4.36E-02	N2O5==>NO2+NO3	JPL
2.29E-16	2NO3==>2NO2+2O	JPL
3.00E-17	O+HNO3==>OH+NO3	JPL
8.00E-15	O+O3==>O2+O2	JPL
6.15E-34	O+O2+M==>O3+M	JPL
1.66E-12	O+NO==>NO2	JPL
1.04E-11	O+NO2==>NO+O2	JPL
1.58E-12	O+NO2==>NO3	JPL
1.00E-11	O+NO3==>O2+NO2	JPL
2.87E-11	O2==>O+O	JPL
7.00E-04	NO2==>NO+O	Measured
8.62E-02	HNO4==>HO2+NO2	JPL
2.40E-13	CO+OH==>HO2+CO2	JPL
3.40E-11	APINENE + OH ==> APINAO2	Peeters et al. 2001
1.70E-12	APINAO2 + NO==>APINANO3	this work
9.40E-12	APINAO2 + NO==>APINAO + NO2	Chuong and Stevens, 2002
5.50E-12	APINANO3+OH==>PINAL+NO2	Kwok and Atkinson 1995
6.44E-14	2APINAO2==>2APINAO+O2	MCM
2.76E-14	2APINAO2==>2APINAOH	MCM
1.00E-03	APINAO ==> PINAL + HO2	MCM
2.09E-11	APINAO2+HO2==>APINAOOH	MCM
1.83E-11	APINAOOH+OH==>APINAO2	Kwok and Atkinson 1995

5.79E-06	APINAOOH==>APINAO+OH	MCM
2.50E-12	APINAO2+NO3==>APINAO+NO2	Stockwell 1997
1.49E-11	APINAOH+OH==>APINACO+HO2	MCM
1.38E-05	APINANO3==>WallLoss1	this work
1.82E-11	APINENE + OH ==> APINBO2	Peeters et al. 2001
1.40E-12	APINBO2+NO==>APINBNO3	this work
9.40E-12	APINBO2+NO==>APINBO+NO2	Chuong and Stevens, 2002
2.50E-12	APINBNO3+OH==>APINBCO+NO2	Kwok and Atkinson 1995
8.80E-13	2APINBO2==>2APINBO+O2	MCM
8.80E-13	2APINBO2==>2APINBOH	MCM
1.49E-11	APBINBOH+OH==>APINBCO+HO2	Kwok and Atkinson 1995
1.00E-04	APINBO ==> PINAL + HO2	MCM

Table B.1 List of Reactions used in the Explicit Chemical Mechanism

Abbreviation	Structure	Abbreviation	Structure
APINENE		CH3COCH3	
APINAO2		APINAO	
APINBO2		APINBO	
APINANO3		APINBOH	
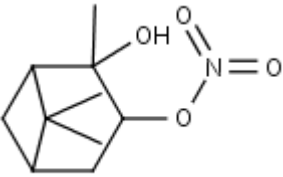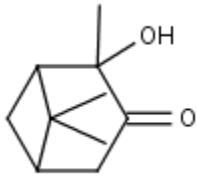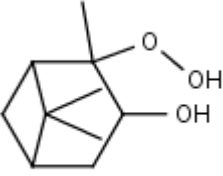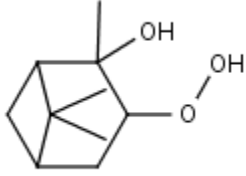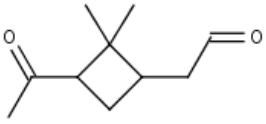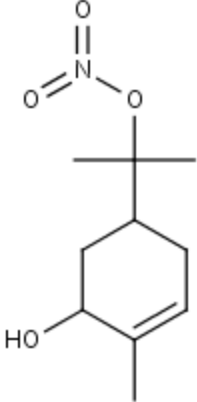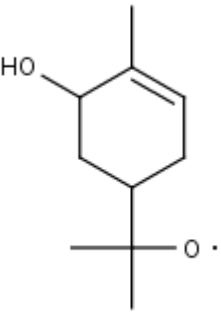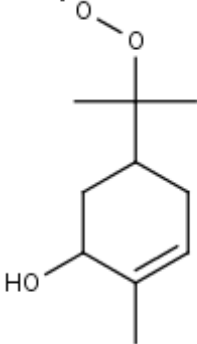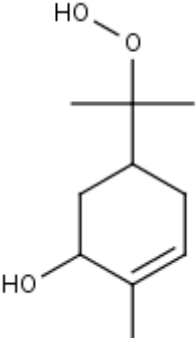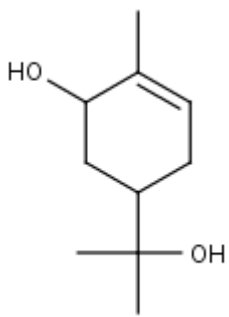
APINBNO3		APINBCO	
APINAOOH		APINBOOH	
PINAL		APINCNO3	
APINCO		APINCO2	
APINCOOH		APINCOH	

Table B.2 Molecular structure of organic species included in the chemical model.

APPENDIX C. Matlab Code for Indium thermal modulator simulation

```matlab
% File: Matlab Code
% Purpose: The purpose of this file is to perform an iterative solution
on the heat transfer properties and phase change boundary of indium in
a thermal modulator

clear all

%%%% Set up the TM parameters %%%%%
radius = 10;                        % radius of TM
k = 81.8;                           % solid In thermal conductivity [W/m*k]
rho_s = 7310;                       % solid In density [kg/m3]
rho_l = 7020;                       % liquid In density at melting point
[kg/m3]
cp = 26.74;                         % solid In heat capacity  [J/mol*k]
Tmp = 429.75;                       % solid In melting point [K]
Tbp = 2345;                         % In boiling point [K]
hof = 28.47;                        % Latent heat of fusion [kJ/kg]
m = 0.1;                            % kg, used to get L = hof*m
L = m*hof;

%%%% parameters %%%%
i=1;
dx = 0.1;                           %./radius;
dt = 0.1;                           % time increments
t = 0;
MaxIters = 1000;                    % Maximum iteration

%%%% setup %%%%
T = zeros(1,radius);                % The interior points all start as 0
F = zeros(1,radius);                % Fill the Liquid fraction matrix with
0
oldF = F;
newF = F;
alpha_s = k / (rho_s * cp);     % thermal diffusivity of solid PCM
alpha_l = k / (rho_l * cp);     % thermal diffusivity of liquid PCM
Fo_s = (alpha_s * 8.77 * dt) / (dx)^2 % Fourier number, set to solid
Indium parameters
Fo_l = (alpha_l * 8.77 * dt) / (dx)^2 % Fourier number, set to liquid
Indium parameters

%%%%  Boundary Conditions %%%%
T(1,:)= 300;                        % 20 C
T(1,1)= 400;                        % heat input
T(1,2)=T(1,1);                      % heat input
newT = T;
oldT = T;
plotT=zeros(MaxIters,radius);
% The numerical scheme
Iters = 1;
originalT = T;

while Iters < MaxIters
```

```matlab
    % solve equation
    for j=2:radius-1
          if F(1,j) < 1 & F(1,j)>0
               newT(1,j) = Tmp;
          else
               newT(1,j) = (Fo_s*(T(1,j-1)+T(1,j+1)) +
oldT(1,j))/(1+2*Fo_s);
          end
          j=j+1;
    end
    T = newT;

    % update liquid fractions
    for j=2:radius-1

newF(1,j)=abs(oldF(1,j)+((k*dt)/(rho_s*L*(dx)^2))*(T(1,j-1)-
2*Tmp+T(1,j+1)));

    end


    % check for start and end of phase change
    for j=2:radius-1
          if (oldT(1,j) < Tmp) & (newT(1,j) >= Tmp)

newF(1,j)=abs(oldF(1,j)+((k*dt)/(rho_l*L*(dx)^2))*(T(1,j-1)-
2*Tmp+T(1,j+1))-(cp/L)*(Tmp-oldT(1,j)));

          elseif newF(1,j+1) >= 1 & oldF(1,j+1) < 1
               newT(1,j) = (Fo_l*(T(1,j-1)+T(1,j+1)) + Tmp-L/(cp*(1-
oldF(1,j))))/(1+2*Fo_l);
          end

          j=j+1;
    end
    newF;

     % solve equation
    for j=2:radius-1
          if F(1,j) < 1 & F(1,j)>0
               newT(1,j) = Tmp;
          else
               newT(1,j) = (Fo_s*(T(1,j-1)+T(1,j+1)) +
oldT(1,j))/(1+2*Fo_s);
          end
          j=j+1;
    end
    T = newT;


    % check for liquid fraction issues
    for j=2:radius-1
         if newF(1,j) < 0
               newF(1,j) = 0;
```

```matlab
            elseif newT(1,j) >= Tmp
                newF(1,j) = 1;
            elseif newF(1,j) > 1
                newF(1,j) = 1;
            end
            j=j+1;
        end
        newF;


        oldT = T;
        T = newT;
        oldF = F;
        F = newF;
        plotT(Iters,:) = newT(1,:);
        Iters = Iters + 1;
    end

% Plots
figure
X = linspace(0,1,size(T,2));
Y = linspace(0,1,size(plotT,1));
plot(plotT);
```

APPENDIX D. Photochemical Reaction Chamber ("BOB") Procedures

DAY BEFORE Experiment

1. Hydrate chamber using bubbler with ZAIR flow Bob. Assume 5% initial RH in BOB. Desire 20-40% humidity. Allow bubbler to operate ~12 hours if using 10L/min flow.

2. Leave all Teflon tube fitting plugs open during humidifying process.

3. Overnight inject NO_2 (0.3mL for 55ppb) – check with NO_x analyzer. When filling with NO_2, turn far bubble tab switch off, then the end closest to the regulator, then detach regulator. Regulator needs to be detached from gas tank after each use. Use silicone septum on bubble glass opening. Discard after use, do not let is remain on glass bubble.

4. Measure Ozone and NOx with analyzers to check concentrations. There should be no ozone or +/-1 ppbv at most. NO_x should be lower than the initial injection concentration. Check initial concentration after injecting NO_2. Let mix and then hook up NOx box and recheck NO2 concentrations after a few minutes.

5. Make α-pinene/cyclohexane mixture (high concentration, higher than injected to BOB) to calibrate Iron Chef with. Integrate using Labview integrator to get peak area/height. 1 bag with Iron Chef of isoprene. 800ppbv or 1ppmvof isoprene. Check concentration more than once. Start Labview program then let pump run for a few seconds and inject.

DAY OF Experiment

6. Take blank of Bob before anything is added. Take blank with Iron Chef, Ozone monitor and NOx box. Keep track of initial values. This is the blank measurement.

7. Let all instruments sit 5 minutes while hooked up to settle and stabilize reading.

8. Iron Chef needs to pull from Bob about 3 minutes or so – enough time to pull air out of Bob. It pulls at ~ 300mL per minute.

9. Inject. Isoprene injection 14uL to get 600ppb of isoprene. Use 10mL syringe. Clean afterwards with methanol, let sit to air dry. Check concentration with Iron Chef. Wait several minutes. Check concentration again after 5 minutes of stabilizing. Do more than twice to make sure. Because of volatility, may want to separately inject less than full amount (5mL per injection) so excess can be pushed out prior to injection to tee.

10. Add NO. 1.2mL of NO. 200ppb pure NO. Gas syringe to inject. When filling with NO, use one stage regulator. No pressure gauge. Make sure there is sufficient flow to clear out NO2, but minimize waste. When injecting, overdraw in the syringe what is needed, push excess before injection. Make sure not to clean the gas tight syringe.

11. Make sure enough NO is present (NOx box). Inject some more if not high enough concentration. Higher is fine.

12. Hook up NOx box. Hook up ozone analyzer. Take Ozone measurements, NOx, Iron Chef, my measurement. Pre-photolysis measurement.

13. Flip lights on. Time master clock. Let lights go until when ozone maxes. Then NO is done, NO2 is maxed. Ozone will max suddenly. Every 15 minutes take data point from all 3. About 3-5 hours analysis time expected.

14. Dilution flow. NOx pulls ~0.7L/min, O3 about 1L/min, 20 minutes for each. Account for Iron chef 300mL/min for 20 mintues. Total flow per hour for three instruments. Add air continuously to make up for lost volume.

15. Flush with everything open.

16. There are 6 lines up top and 6 on the bottom. Make sure each is plugged. Plugs are usually near the lines.

17. Make sure the BOB pressure meter does not exceed 0.2. Unplug one tube if necessary, or hook to a pulling instrument. Only Iron chef does not actively pull flow.

APPENDIX E. Photochemical Reaction Chamber Cleaning Procedures

After several experiments, large amounts of HNO_3 and adsorptive oxidant products coat the Teflon wall lining of the photo reaction chamber and affect the ability to accurately measure products in

1. Take baseline sample of the chamber's current cleanliness with GC-FID and GC-CD and aerosol counter/sizer if available.

2. Flush the chamber with high flow rates of clean air generator air for about 24 hours with the chamber UV lamps turned fully on.

3. After 2-3 days of continuous flushing with the lights on, switch the air from CAG to a tank UHP zero air.

4. Run the zero air through the chamber until the tank is empty.

5. Take another baseline sample from the chamber with GC-FID,GC-ECD, and aerosol counter/sizer to compare against pre-cleaning baseline.

APPENDIX F. Detailed Data Presentation

The five sets of photochemical reaction chamber data used in this thesis are presented here in detail with calibration, chamber conditions, and yield plots.

Date	APN-A [%]	APN-B [%]	APN-C [%]	Total Yield [%]
4/25/2009	6.2	0.8	2.2	9.2
4/29/2009	9.8	3.1	4.6	18
5/9/2009	6.7	4.5	4.8	16
5/12/2009	6.9	4.0	4.2	15
5/15/2009	6.6	4.4	4.9	16

Table F.1: Individual and total yields for α-pinene hydroxynitrates.

Date	α-pinene calibration	1-octyl-nitrate calibration
4/25/2009	y = 6.9855x + 9.2381	y = 0.0394x + 0.1365
4/29/2009	y = 8.1068x -38.714	y = 0.0511x + 0.0854
5/9/2009	y = 5.0985x + 81.9	y = 0.0606x + 0.2519
5/12/2009	y = 5.1686x + 57.007	y = 0.0629x + 0.3962
5/15/2009	y = 5.6201x + 19.759	y = 0.0635x + 0.0969

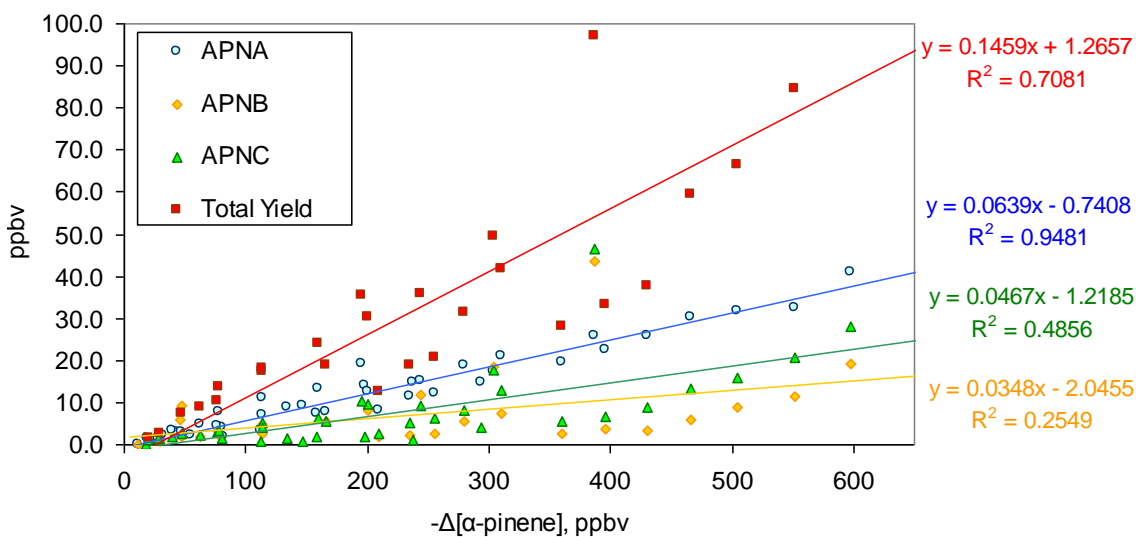**Table F.2: Calibrations for each experiment.**

Figure F.1: Total and speciated APN yields.
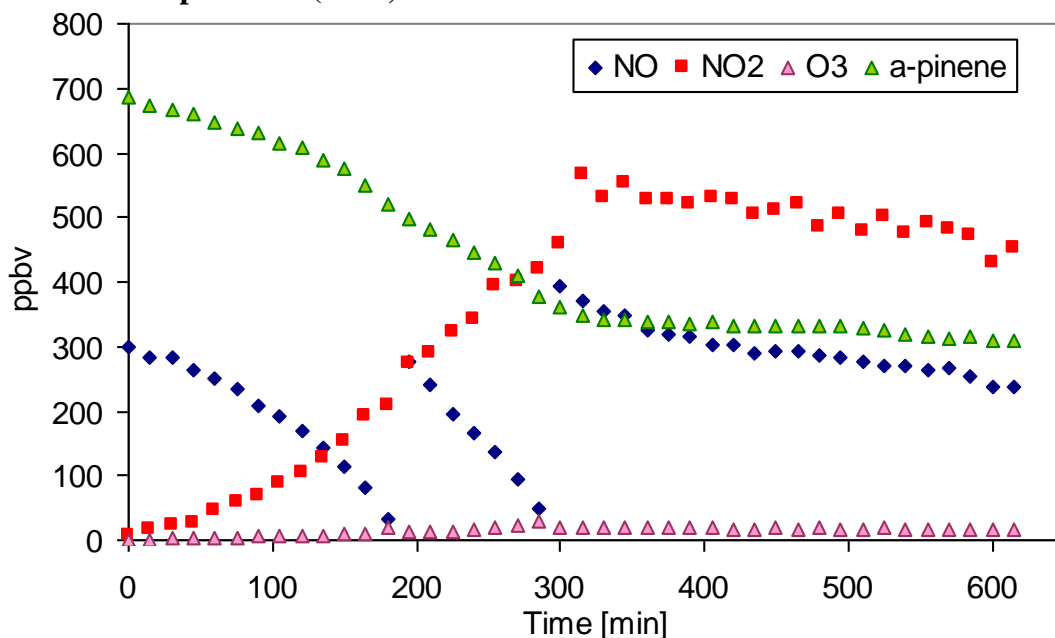
4/25/2009 Experiment (Set 1)

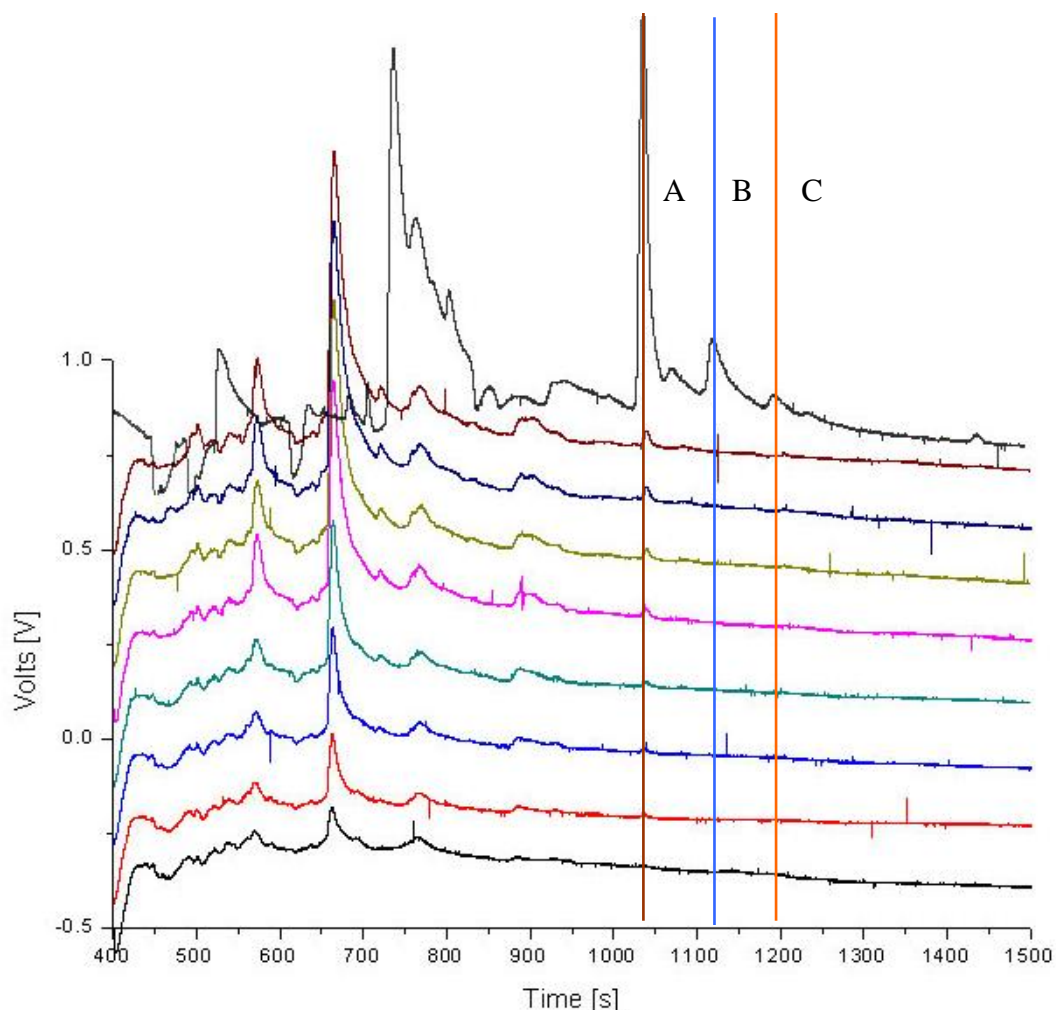**Figure F.1(a): Photochemical reaction chamber NO/NO₂, O₃, and α-pinene conc.**

Figure F.1(b): Total chromatograms for experiment overlaid with synthesis reference.
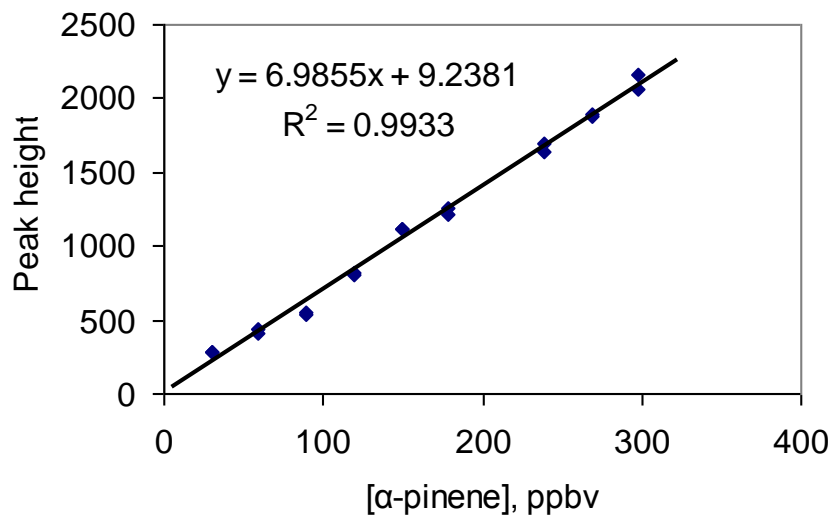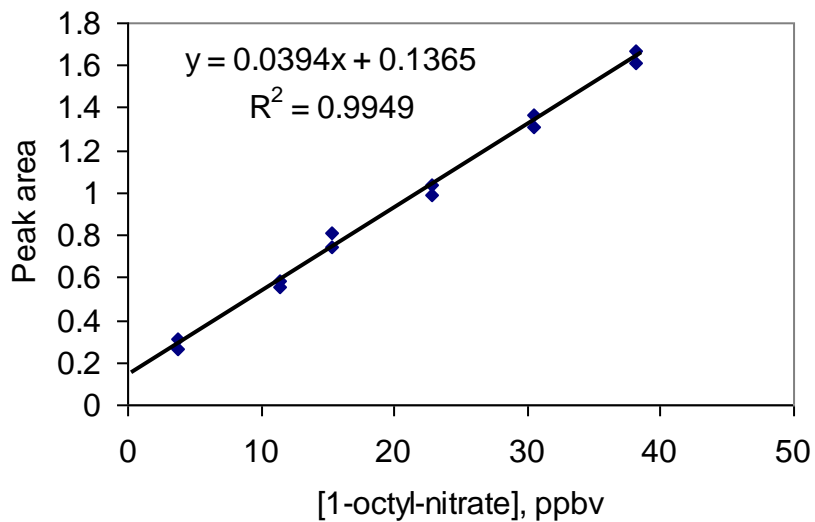
Figure F.1(c): α-Pinene calibration curve of the GC-FID.

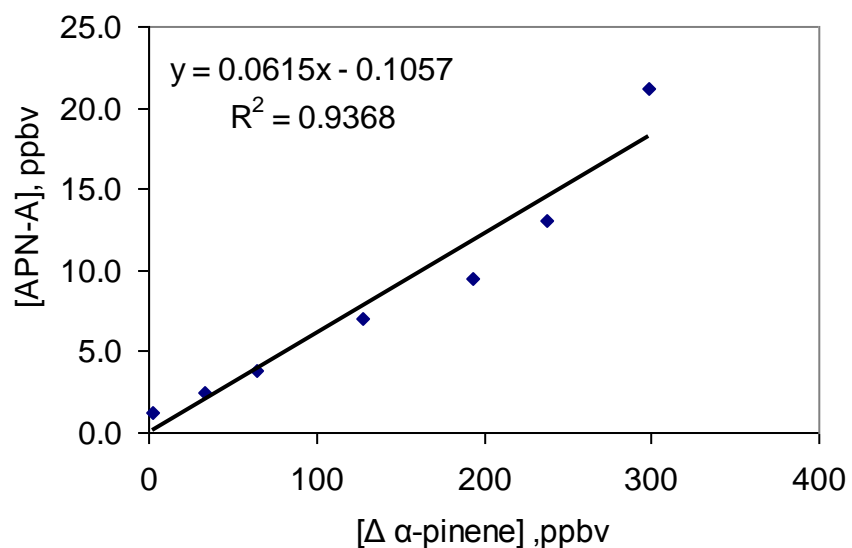**Figure F.1(d): 1-octyl-nitrate calibration curve of the GC-ECD.**

Figure F.1(e): APN-A yield plot.

RUN	Δ α-pinene [ppbv]	APN-A [ppbv]	F-factor	APN-A with F-factor applied [ppbv]
0	0	0	-	-
1	2.8	1.3	1.000546	1.3
2	33	2.4	1.006647	2.4
3	65	3.8	1.013563	3.8
4	128	6.8	1.028773	7.0
5	193	9.0	1.047232	9.4
6	238	12.3	1.062143	13.1
7	298	19.5	1.085635	21.2

Table F.3: APN-A concentration with and without F-factor correction.
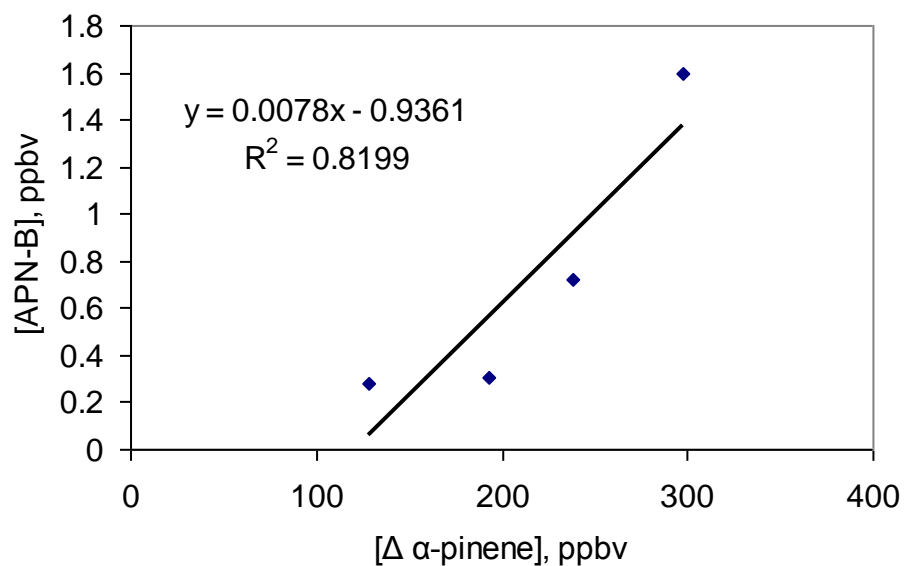
Figure F.1(f): APN-B yield plot.

RUN	Δ α-pinene [ppbv]	APN-B [ppbv]	F-factor	APN-B with F-factor applied [ppbv]
0	0	0	-	-
1	2.8	0	-	-
2	33	0	1.000	-
3	65	0	1.003	-
4	128	0.3	1.005	0.3
5	193	0.3	1.011	0.3
6	238	0.7	1.018	0.7
7	298	1.6	1.023	1.6

Table F.4: APN-B concentration with and without F-factor corrections.
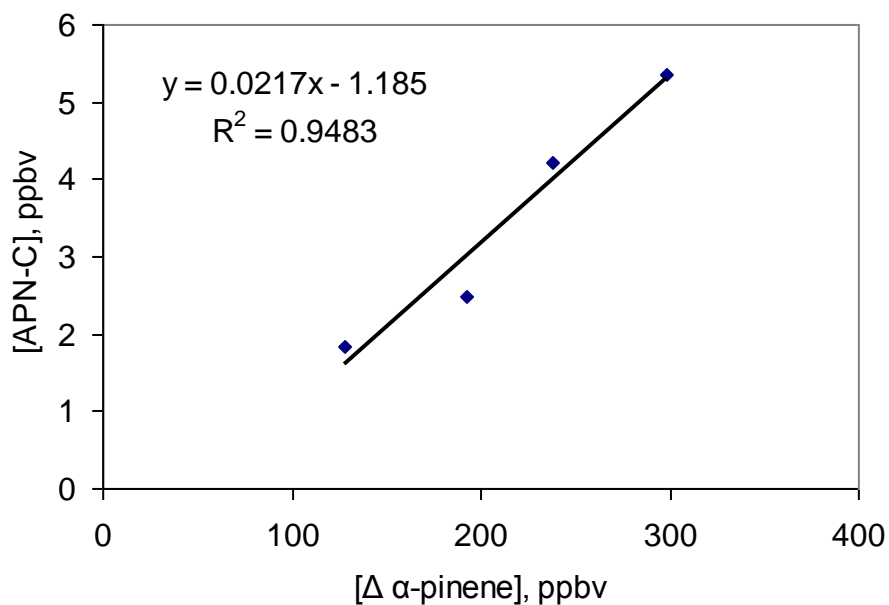
Figure F.1(g): APN-C yield plot.

RUN	Δ α-pinene [ppbv]	APN-C [ppbv]	F-factor	APN-C with F-factor applied [ppbv]
0	0	-	-	-
1	2.8	-	-	-
2	33	-	1.001	-
3	65	-	1.010	-
4	128	1.8	1.021	1.8
5	193	2.4	1.044	2.5
6	238	3.9	1.072	4.2
7	298	4.9	1.095	5.3

Table F.5: APN-C concentration with and without F-factor corrections.

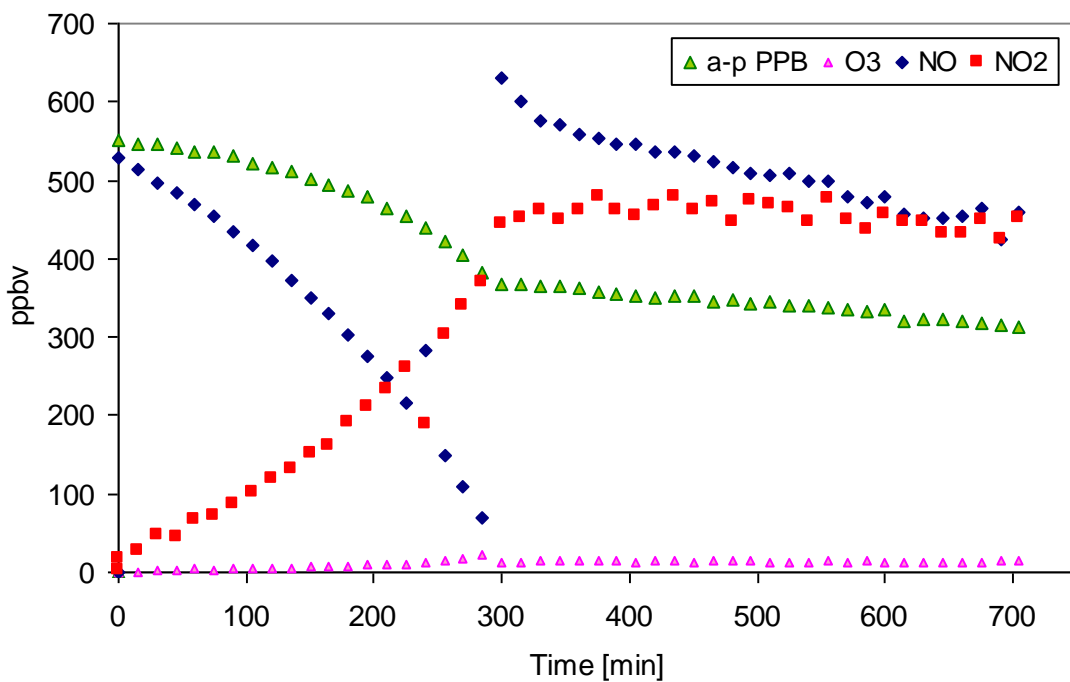**4/29/2009 Experiment (Set 2)**

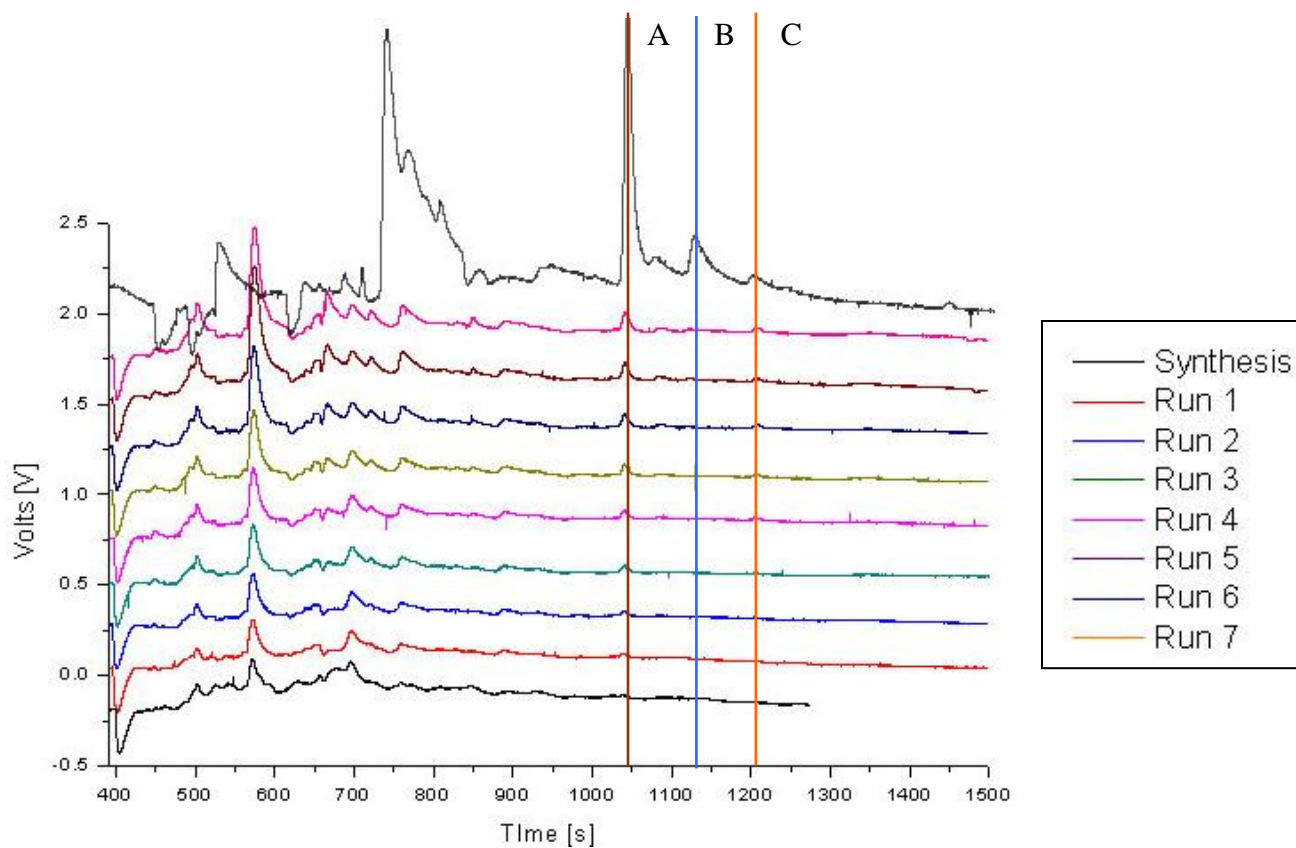Figure F.2(a): NO/NO₂, O₃, and α-pinene concentrations.

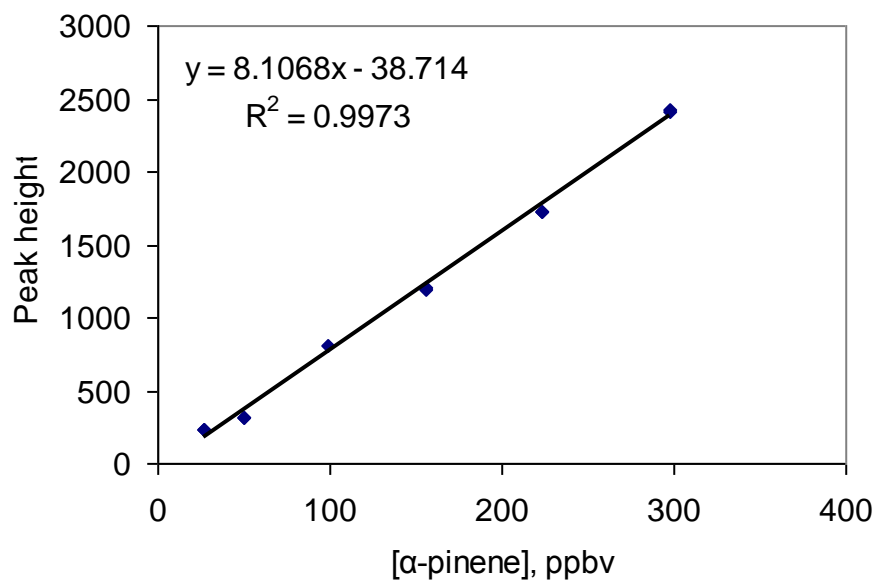Figure F.2(b): All chromatograms from the experiment along with

Figure F.2(c): α-Pinene calibration curve of the GC-FID.
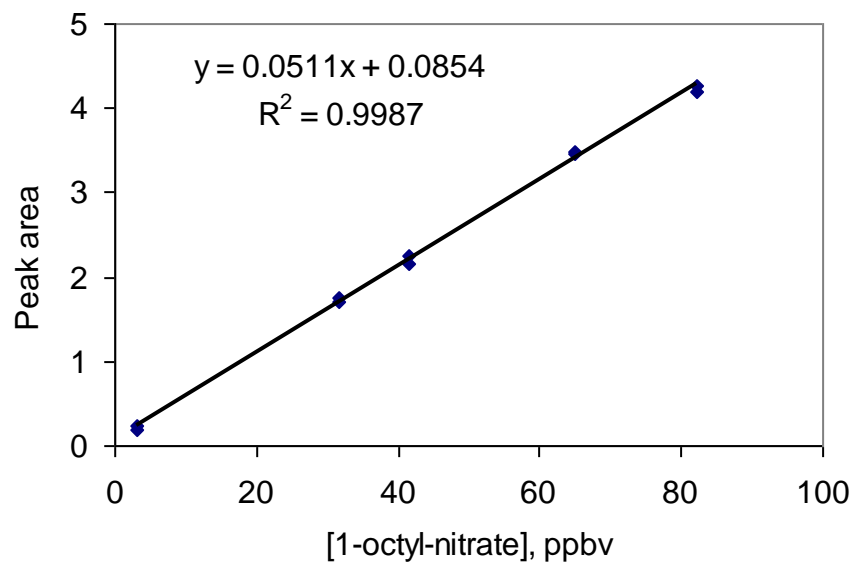
Figure F.2(d): 1-octyl-nitrate calibration curve of the GC-ECD.
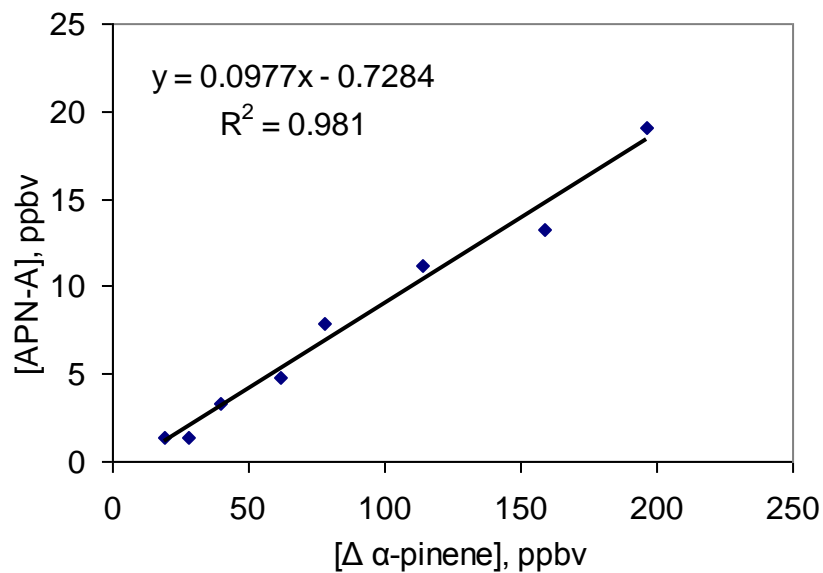
Figure F.2(e): APN-A yield plot.

RUN	Δ α-pinene [ppbv]	APN-B [ppbv]	F factor	APN-B with F factor applied [ppbv]
1	19	1.3	1.0046	1.3
2	28	1.3	1.0069	1.3
3	40	3.3	1.0100	3.3
4	62	4.7	1.0160	4.8
5	78	7.8	1.0206	7.9
6	114	11	1.0317	11.2
7	159	13	1.0475	13.2
8	196	18	1.0625	19.1

Table F.6: APN-A data with F-factor adjustments.
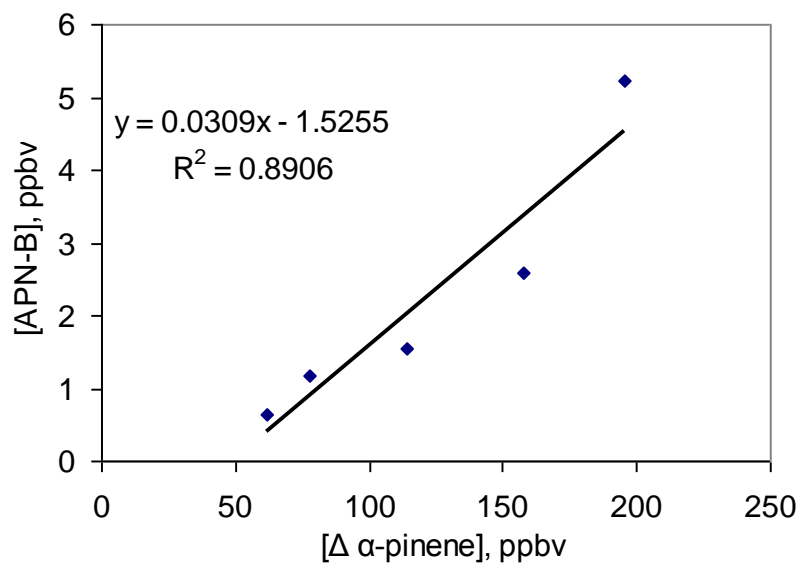
Figure F.2(f): APN-B yield plot.

RUN	Δ α-pinene [ppbv]	APN-B [ppbv]	F factor	APN-B with F factor applied [ppbv]
1	19	-	-	-
2	28	-	-	-
3	40	0.4	1.001317	0.4
4	62	0.3	1.002483	0.3
5	78	0.6	1.004719	0.6
6	114	1.2	1.006431	1.2
7	158	1.5	1.010577	1.5
8	196	2.5	1.016299	2.6

Table F.7: APN-B concentrations with F-factor applied.
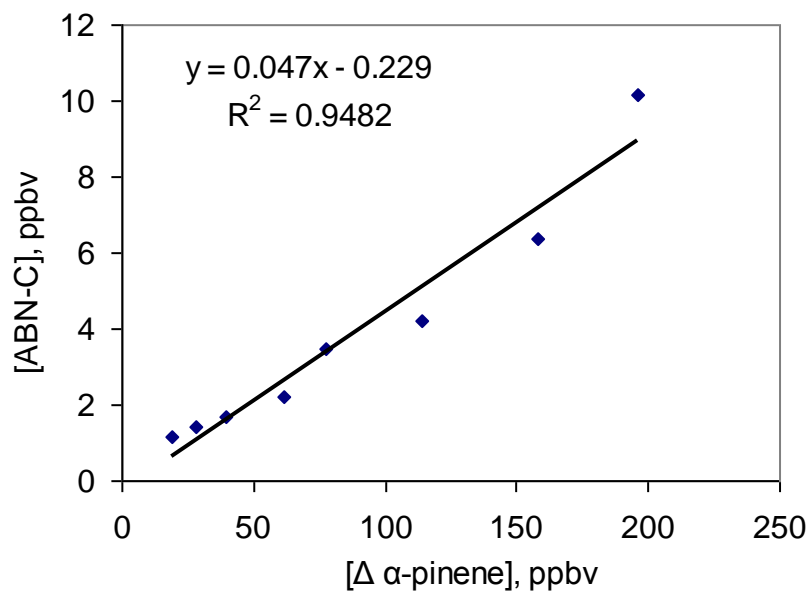
Figure F.2(g): APN-C yield plot.

RUN	Δ α-pinene [ppbv]	APN-C [ppbv]	F factor	APN-C with F factor applied [ppbv]
1	19	0.8	1.00701	0.8
2	28	1.2	1.01045	1.4
3	40	1.3	1.00364	1.7
4	62	1.5	1.00891	2.2
5	78	2.1	1.01518	3.5
6	114	2.3	1.02385	4.3
7	158	2.4	1.04001	5.0
8	196	3.2	1.06026	7.7

Table F.8: APN-C concentrations with F-factor adjustments.

5/9/2009 Data Set
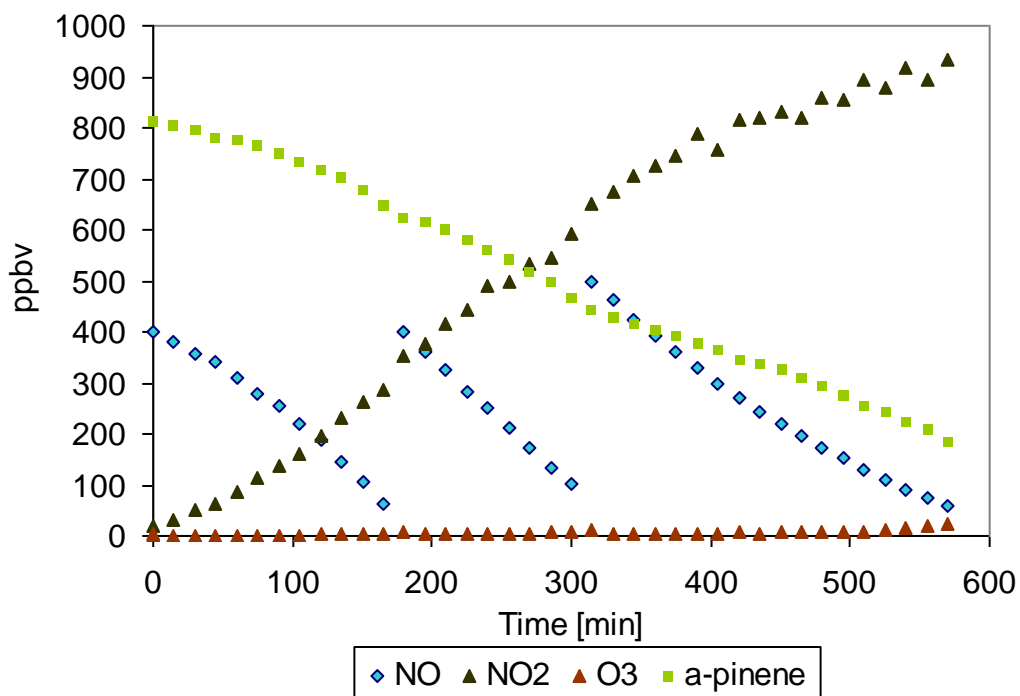
Figure F.3(a) NO,NO₂,O₃,α-pinene conditions.
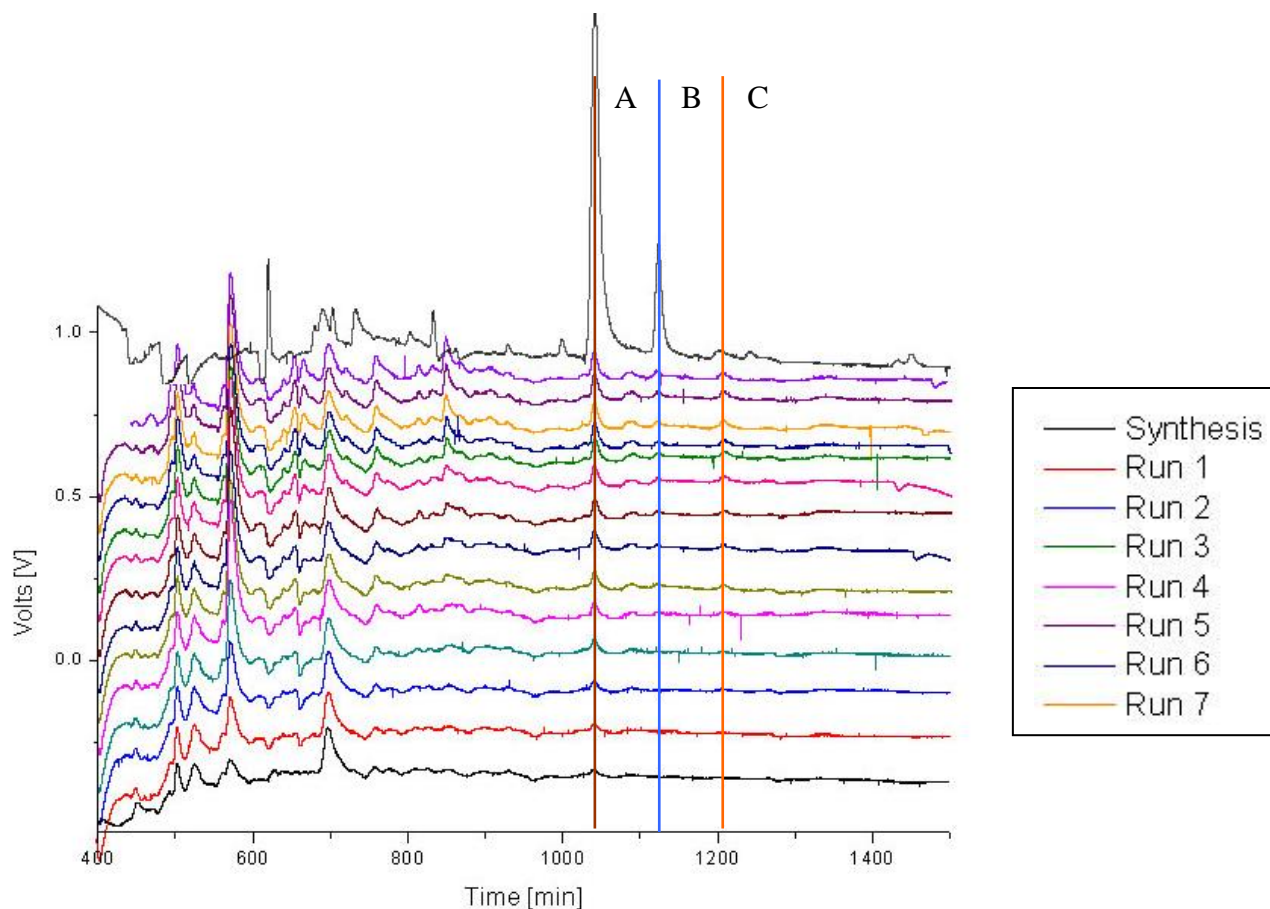
Figure F.3(b) Total chromatograms overlaid with synthesis separation.
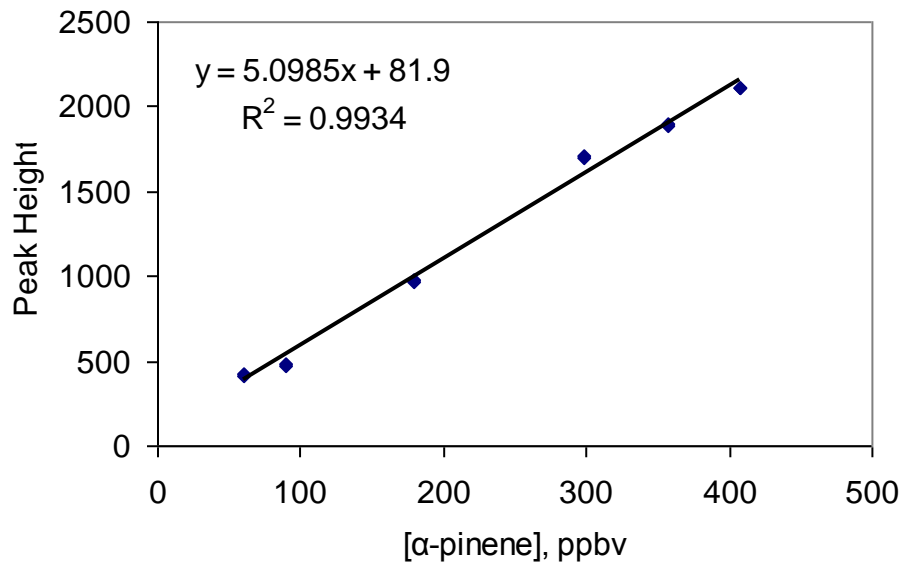
Figure F.3(c) α-pinene calibration curve.
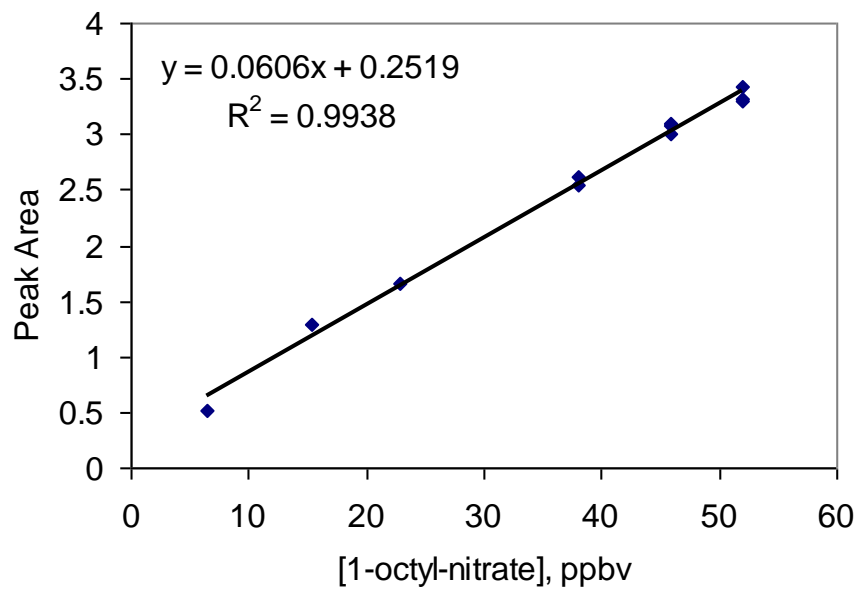
Figure F.3(d) 1-octyl-nitrate calibration curve.
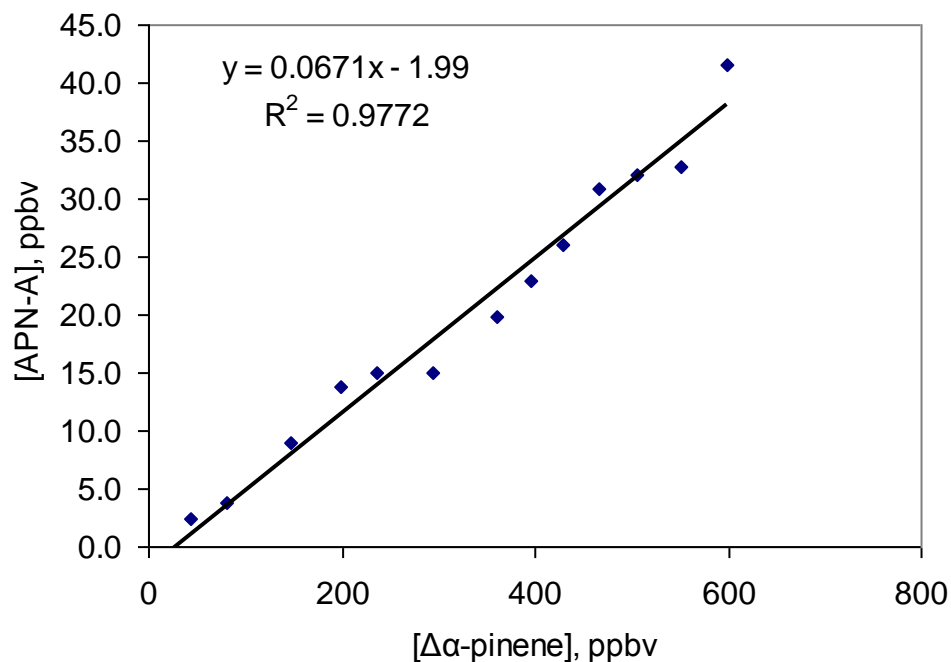
Figure F.3(e) APN-A yield plot.

RUN	Δ α-pinene [ppbv]	APN-A [ppbv]	F-factor	APN-A with F-factor applied [ppbv]
1	11	2.3	1.0018	2.3
2	44	3.1	1.0076	3.2
3	81	4.4	1.0146	4.5
4	147	10	1.0284	10
5	198	14	1.0405	15
6	237	15	1.0508	15
7	294	14	1.0677	15
8	360	18	1.0911	20
9	396	21	1.1060	23
10	430	23	1.1219	26
11	466	27	1.1411	31
12	505	28	1.1655	32
13	552	27	1.2017	33
14	598	34	1.2477	42

Table F.9: APN-A data table.
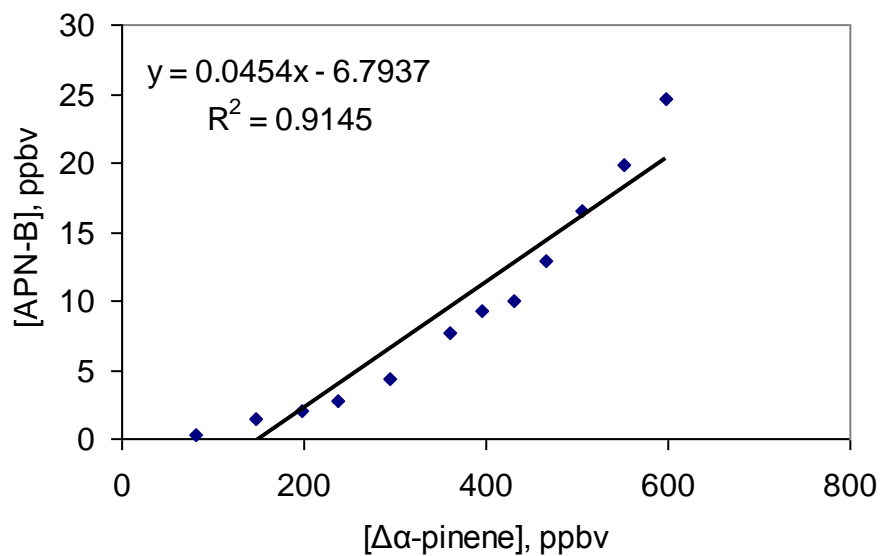
Figure F.3(f): APN-B yield plot.

RUN	Δ α-pinene [ppbv]	APN-B [ppbv]	F factor	APN-B with F-factor applied [ppbv]
1	11	-	-	-
2	44	0	1.0029	0
3	81	0.3	1.0055	0.3
4	147	1.5	1.0107	1.5
5	198	2.0	1.0152	2.1
6	237	2.7	1.0190	2.8
7	294	4.3	1.0253	4.4
8	360	7.4	1.0339	7.7
9	396	8.9	1.0393	9.3
10	430	9.6	1.0450	10
11	466	12	1.0519	13
12	505	16	1.0606	17
13	552	19	1.0732	20
14	598	23	1.0890	25

Table F.10: APN-B data table.

$$y = 0.0484x - 8.1511$$
$$R^2 = 0.8217$$
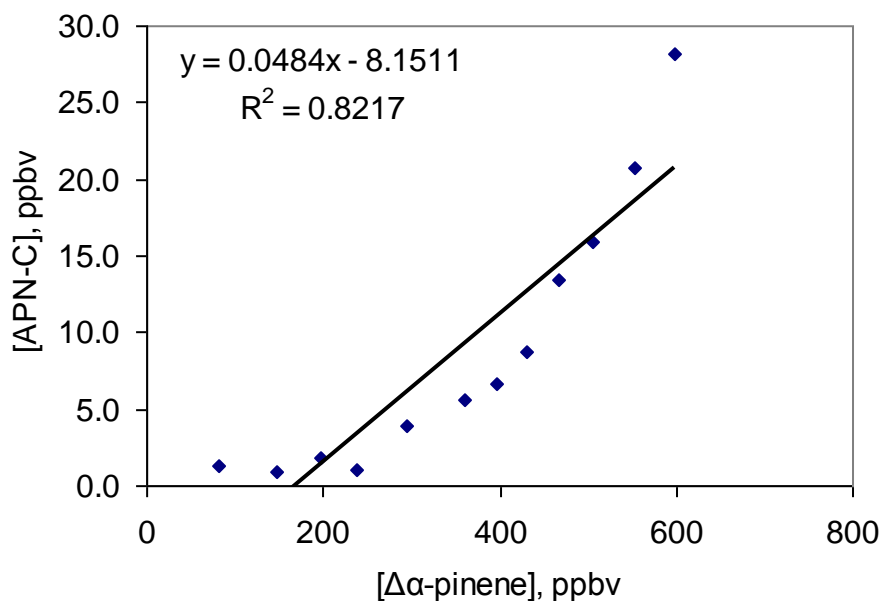
Figure F.3(g): APN-C yield plot.

RUN	Δ α-pinene [ppbv]	APN-C [ppbv]	F-factor	APN-C with F-factor applied [ppbv]
1	11	-	1.0019	-
2	44	-	1.0077	-
3	81	1.3	1.0147	1.3
4	147	0.9	1.0344	0.9
5	198	1.8	1.0405	1.9
6	237	1.0	1.0508	1.0
7	294	3.7	1.0678	4.0
8	360	5.1	1.0911	5.6
9	396	6.0	1.1060	6.7
10	430	7.6	1.1453	8.8
11	466	11	1.1748	13
12	505	13	1.2017	16
13	552	16	1.2863	21
14	598	22	1.2937	28

Table F.11: APN-C data table.

5/12/2009 Data
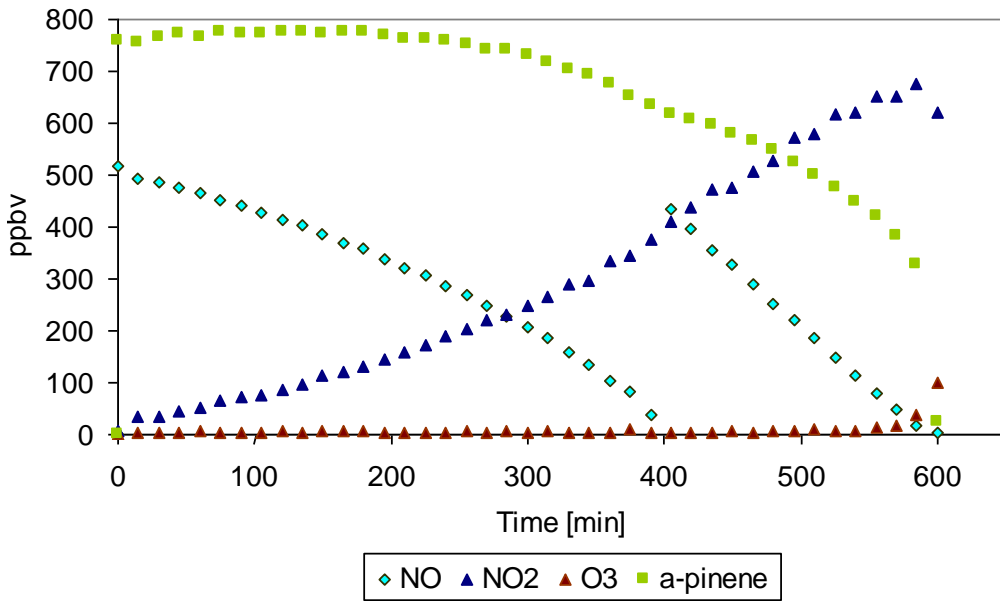
Figure F.4(a): NO,NO₂,O₃,α-pinene conditions.
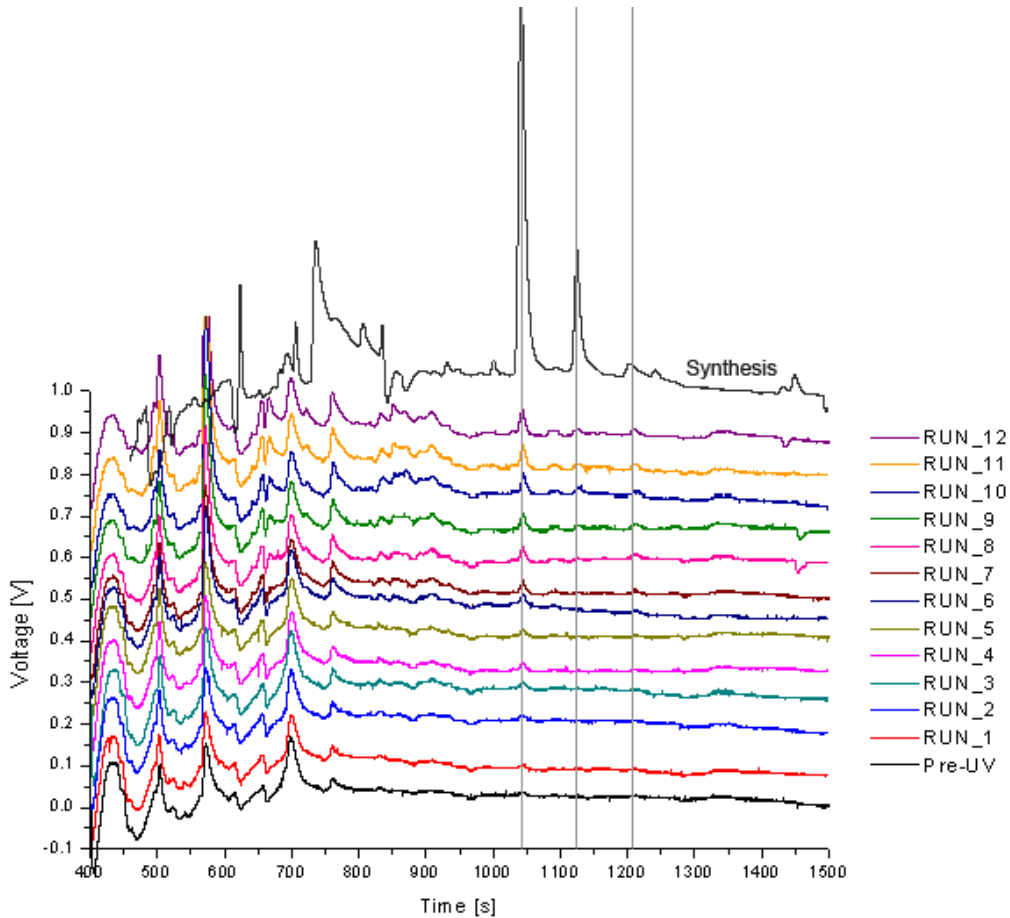
Figure F.4(b): Total chromatograms overlaid with reference synthesis chromatogram.

199

Figure F.4(c): α-pinene calibration curve.

$y = 5.1686x + 57.007$

$R^2 = 0.9978$
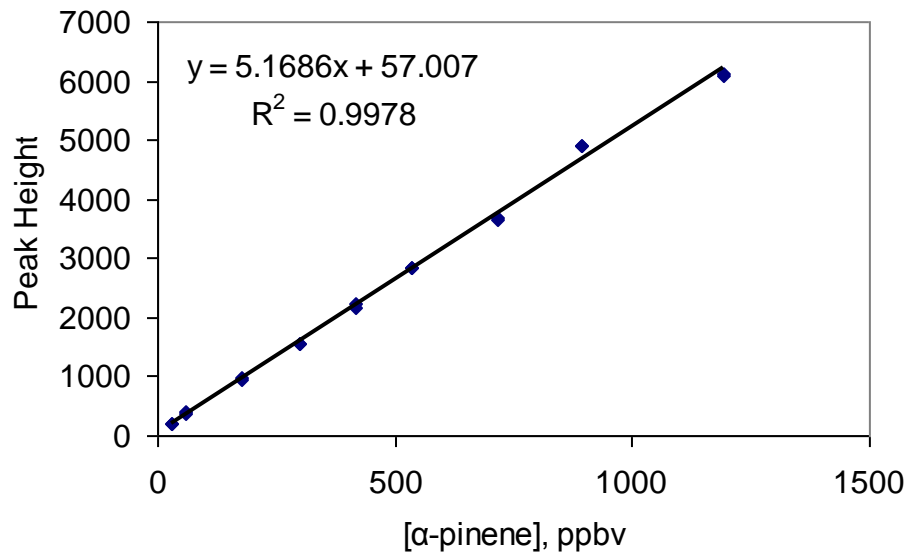
Figure F.4(d): 1-octyl-nitrate calibration curve.

$y = 0.0629x + 0.3962$

$R^2 = 0.9981$
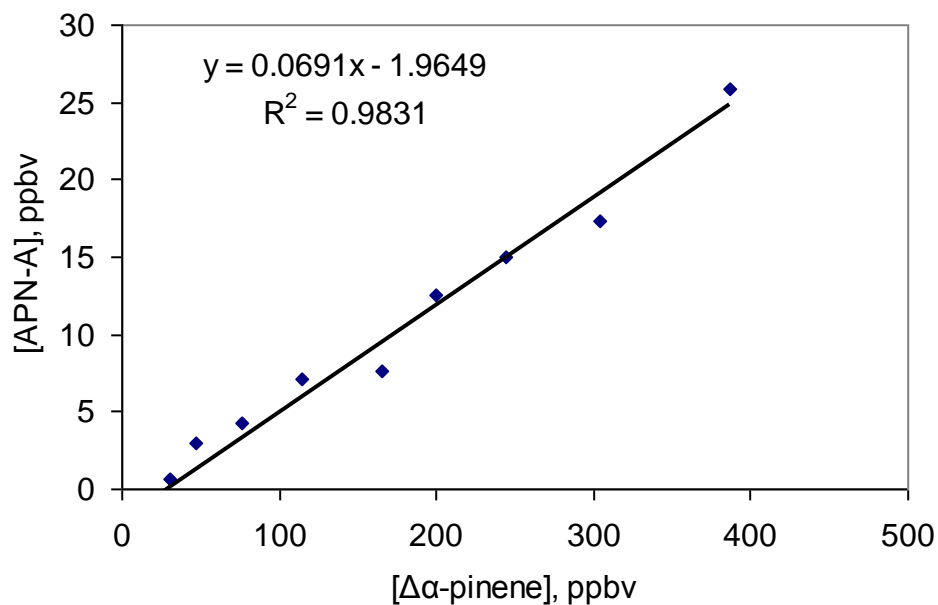
Figure F.4(e): APN-A yield plot.

RUN	Δ α-pinene [ppbv]	APN-A [ppbv]	F-factor	APN-A with F-factor applied [ppbv]
1	2	-	1.0003	-
2	5	-	1.0009	-
3	15	-	1.0026	-
4	18	-	1.0031	-
5	20	-	1.0035	-
6	30	0.6	1.0052	0.625
7	47	3.0	1.0083	2.982
8	76	4.2	1.0139	4.268
9	114	6.9	1.0216	7.083
10	166	7.4	1.0333	7.677
11	200	12.0	1.0417	12.521
12	244	14.3	1.0536	15.031
13	304.5	16.1	1.0725	17.285
14	387	23.4	1.1043	25.818

Table F.12: APN-A data table.

$$y = 0.0396x - 0.6192$$
$$R^2 = 0.9654$$
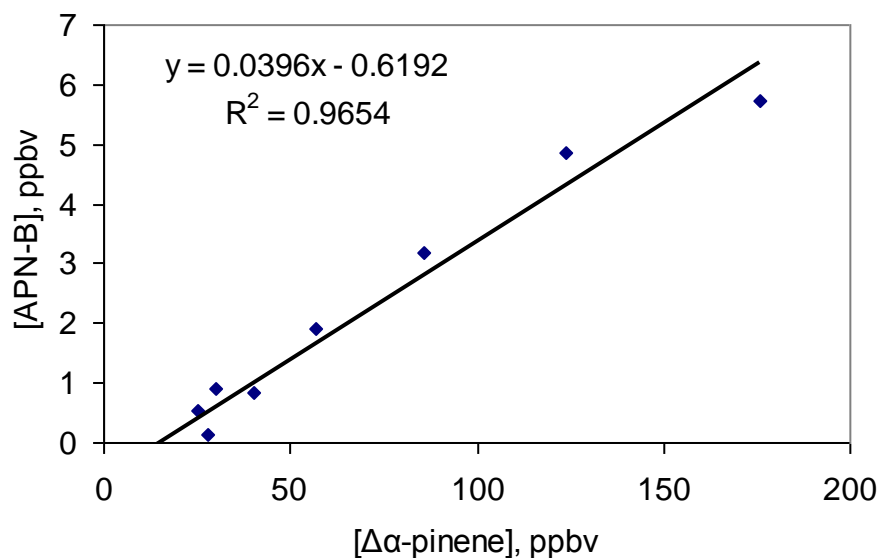
Figure F.4(f): APN-B yield plot.

RUN	Δ α-pinene [ppbv]	APN-B [ppbv]	F-factor	APN-B with F-factor applied [ppbv]
1	2	-	1.0008	-
2	5	-	1.0010	-
3	15	-	1.0016	-
4	18	-	1.0018	-
5	20	-	1.0020	-
6	30	0.6	1.0026	**0.8**
7	47	3.0	1.0038	**1.9**
8	76	4.2	1.0059	**3.2**
9	114	6.9	1.0089	**4.9**
10	166	7.4	1.0132	**5.7**
11	200	12.0	1.0164	**7.9**
12	244	14.3	1.0209	**12**
13	305	16.1	1.0279	**15**
14	387	23.4	1.0395	**34**

Table F.13: APN-B data table.
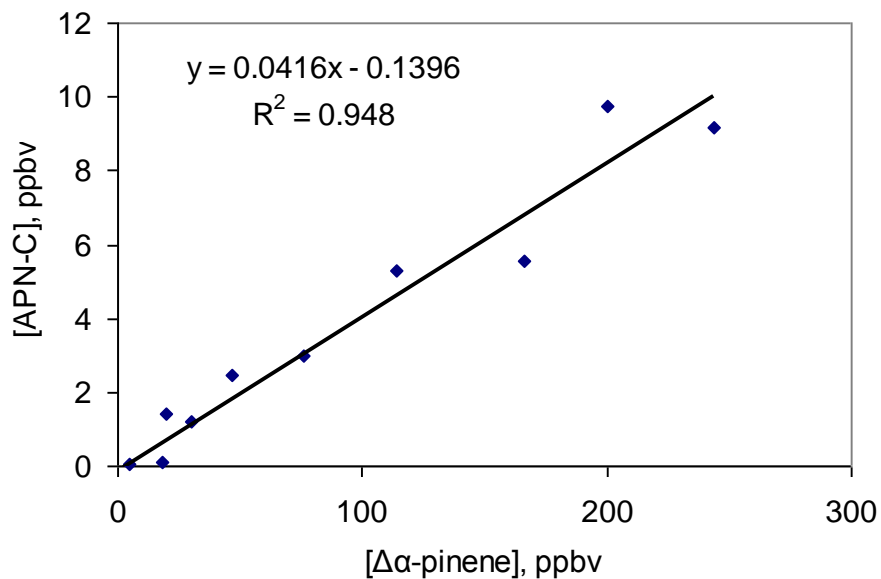
Figure F.4(g): APN-C yield plot.

RUN	Δ α-pinene [ppbv]	APN-C [ppbv]	F-factor	APN-C with F-factor applied [ppbv]
1	2	-	1.0005	-
2	5	-	1.0013	-
3	15	-	1.0039	-
4	18	-	1.0047	-
5	20	-	1.0052	-
6	30	1.2	1.0079	1.2
7	47	2.5	1.0127	2.5
8	76	2.9	1.0211	3.0
9	114	5.1	1.0329	5.3
10	166	5.3	1.0507	5.5
11	200	9.2	1.0636	9.7
12	244	8.5	1.0820	9.2
13	305	16	1.1112	18
14	387	32	1.1609	38

Table F.14: APN-C data table.

5/15/2009 Data Set
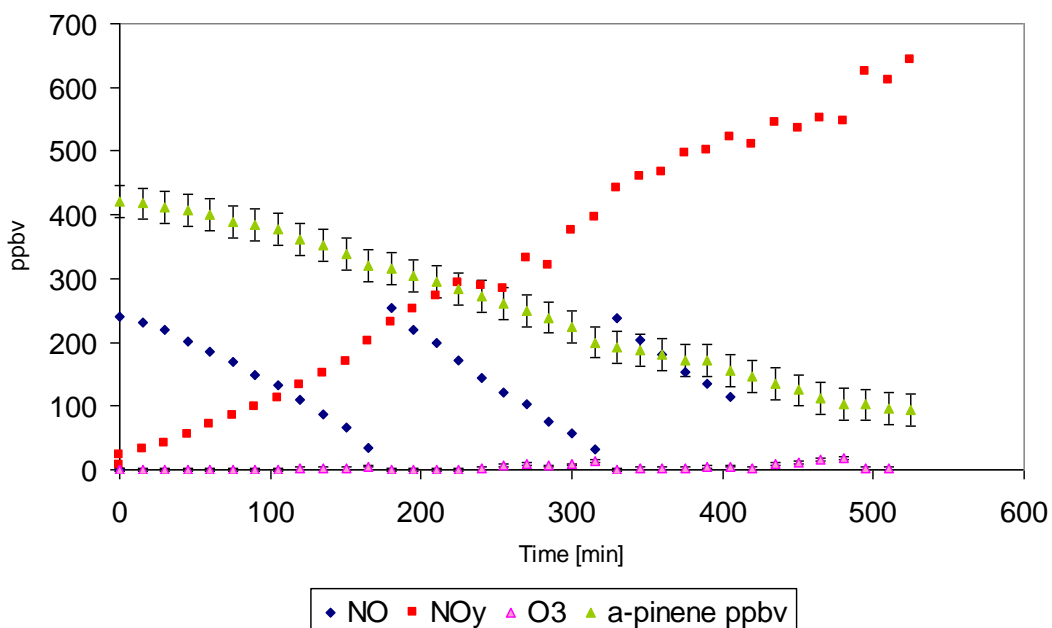
Figure F.5(a): Change in concentrations of NO, NO₂, O₃, and α-pinene.
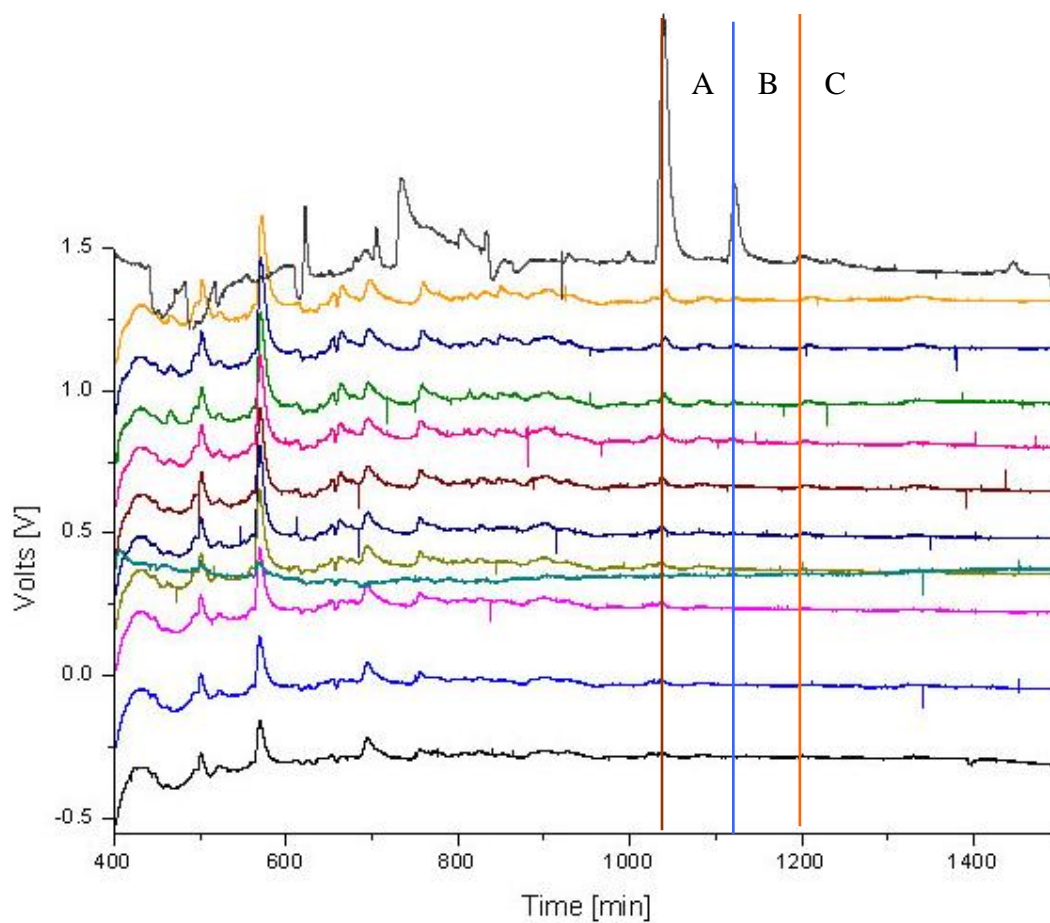
Figure F.5(b): Chromatograms overlaid with reference synthesis chromatogram.
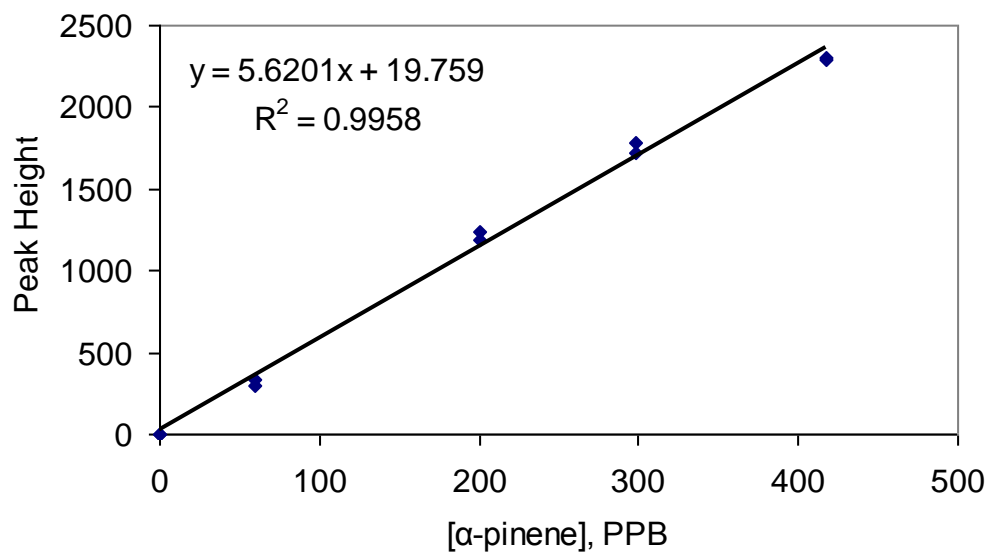
Figure F.5(c): Calibration curve for α-pinene.
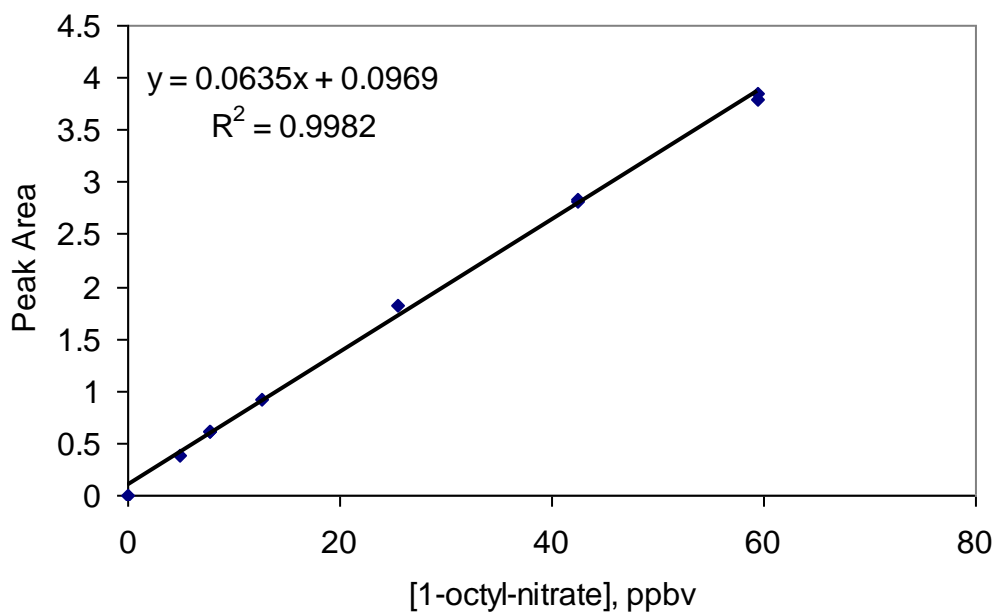
Figure F.5(d): Calibration curve for 1-octyl-nitrate.
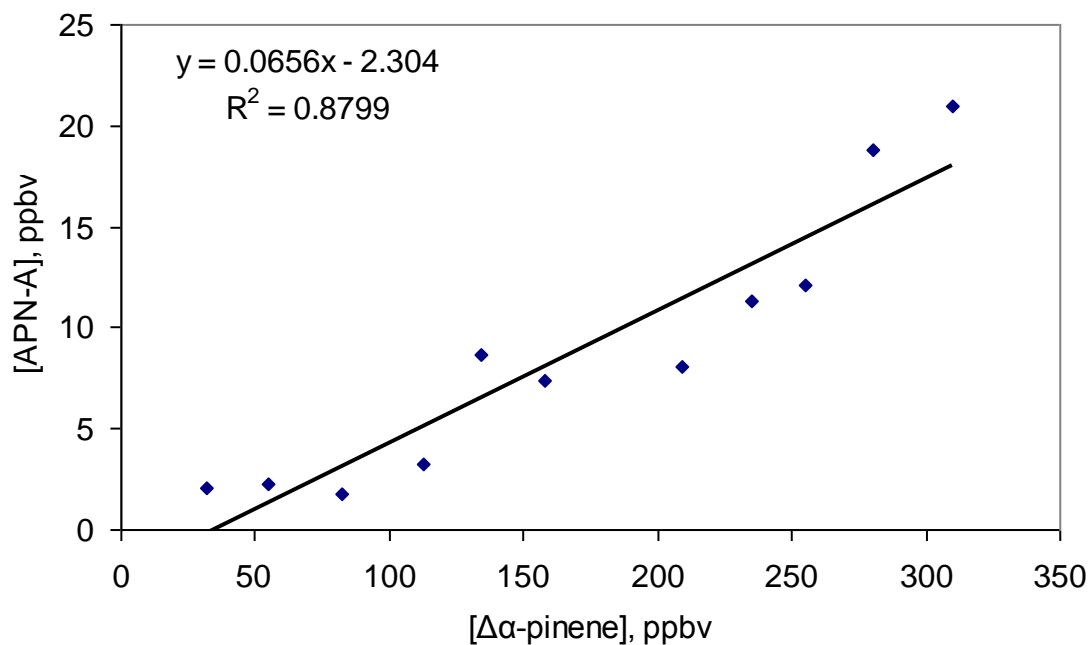
Fig F.5(e): APN-A yield plot.

RUN	Δ α-pinene [ppbv]	APN-A [ppbv]	F-factor	APN-A with F-factor applied [ppbv]
1	10.5	2.6	1.0034	2.6
2	32	2.1	1.0108	2.1
3	55	2.2	1.0193	2.3
4	82	1.8	1.0304	1.8
5	113	3.1	1.0448	3.3
6	134	8.2	1.0558	8.7
7	158	6.9	1.0698	7.4
8	209	7.3	1.1065	8.1
9	235	10.1	1.1304	11.4
10	255	10.5	1.1522	12.2
11	280	15.9	1.1853	18.8
12	310	17.0	1.2376	21.0

Table F.15: APN-A data.
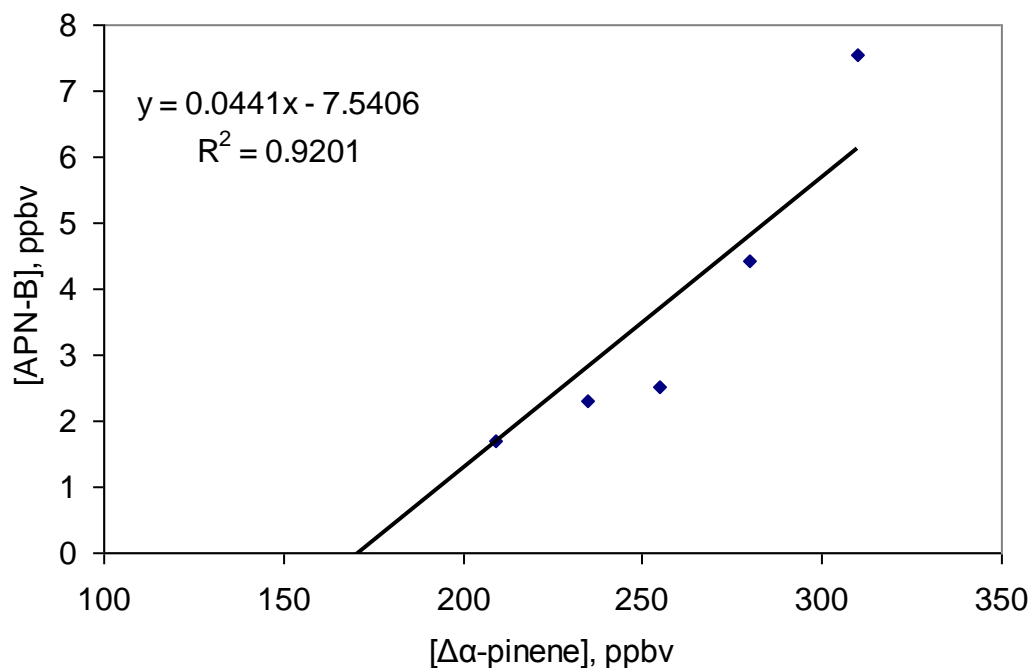
Fig F.5(f): APN-B yield plot.

RUN	Δ α-pinene [ppbv]	APN-B [ppbv]	F-factor	APN-B with F-factor applied [ppbv]
1	10.5	-	1.0013	-
2	32	-	1.0041	-
3	55	-	1.0073	-
4	82	-	1.0115	-
5	113	-	1.0169	-
6	134	-	1.0209	-
7	158	-	1.0261	-
8	209	0.6	1.0395	1.7
9	235	0.7	1.0481	2.3
10	255	0.7	1.0559	2.5
11	280	1.0	1.0675	4.4
12	310	1.6	1.0856	7.5

Table F.16: APN-B data.
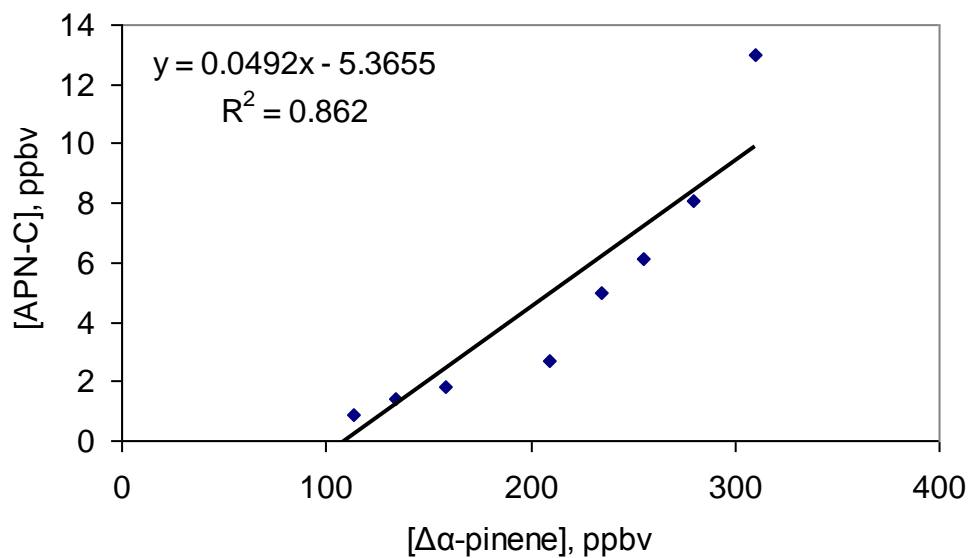
Figure F.5(g): APN-C yield plot.

RUN	Δ α-pinene [ppbv]	APN-C [ppbv]	F-factor	APN-C with F-factor applied [ppbv]
1	10.5	-	1.0052	-
2	32	-	1.0164	-
3	55	-	1.0294	-
4	82	-	1.0464	-
5	113	0.8	1.0684	0.9
6	134	1.3	1.0853	1.4
7	158	1.6	1.1070	1.8
8	209	2.3	1.1645	2.7
9	235	4.1	1.2023	5.0
10	255	5.0	1.2371	6.1
11	280	6.3	1.2903	8.1
12	310	9.4	1.3759	13

Table F.17: APN-C data.

BIBLIOGRAPHY

Amann, M., Bertok, I., Cabala, R., Cofala, J., Heyes, C., Gyarfas, F., Klimont, Z., Scho¨ pp,W., Wagner, F., 2005. Target Setting Approaches for Cost-effective Reductions of Population Exposure to Fine Particulate Matter in Europe. CAFE Report 4. International Institute for Applied Systems Analysis (IIASA), Laxenburg, Austria.

Andreae, M.O., Crutzen, P. J., 1997. Atmospheric aerosols: Biogeochemical sources and role in atmospheric chemistry. Science, vol. 276, 1052.

Andreae, M.O., Rosenfeld, D., 2008. Aerosol–cloud precipitation interactions. Part 1. The nature and sources of cloud active aerosols. Earth Science Revision, vol. 89, 13–41.

Apel, E.C., Riemer, D.D., Hills, A., Baugh, W., Orlando, J., Faloona, I., Tan, D., Brune, W., Lamb, B., Westberg, H., Carroll, M.A., Thornberry, T., Geron, C.D., 2002. Measurement and interpretation of isoprene fluxes and isoprene, methacrolein, and methyl vinyl ketone mixing ratios at the PROPHET site during the 1998 Intensive. Journal of Geophysical Research, vol. 107, 10.1029/2000JD000225.

Arey, J., Atkinson, R., Aschmann, S.M., 1990. Product study of the gas-phase reactions of monoterpenes with the OH radical in the presence of NO_x. Journal of Geophysical Research, vol. 95, 18539–18546.

Arey, J., S. M. Aschmann, E. S. C. Kwok, and R. Atkinson, 2001. Alkyl nitrate, hydroxyalkyl nitrate, and hydroxycarbonyl formation from the NO_x-air photooxidations of C_5–C_8 n-alkanes, J. Phys. Chem. A, vol. 105, 1020–1027.

Aschmann, S.M., Reissell, A., Atkinson, R., Arey, J., 1998. Products of the gas phase reactions of the OH radical with a- and b-pinene in the presence of NO. Journal of Geophysical Research, vol. 103, 25553–25561.

Aschmann, S.M., Arey, J., Atkinson, R., 2000. Formation of β-hydroxycarbonyls from the OH radical-initiated Reactions of Selected Alkenes. Environmental Science and Technology, vol. 34, 1702-1706.

Aschmann, S.M., Arey, J., Atkinson, R., 2001. Atmospheric chemistry of three C_{10} alkanes. J. Phys. Chem., vol. 105, 7598–7606.

Aschmann, S.M., Atkinson, R., Arey, J. 2002. Products of reaction of OH radicals with α-pinene. Journal of Geophysical Research, vol. 107(D14), 4191.

Aschmann, S.M., Arey, J., Atkinson, R., 2002b. OH radical formation from the gas-phase reactions of O_3 with a series of terpenes. Atmospheric Environment, vol. 36, 4347–4355.

Aschmann, S.M., Arey, J., Atkinson, R., 2003. Kinetics and products of the gas-phase reaction of OH radicals with 5-hydroxy-2-pentanone at 296 +/- 2K. Journal of Atmospheric Chemistry, vol. 45(3), 289-299.

Ashmore, M. R., 2005. Assessing the future global impacts of ozone on vegetation. Plant Cell Environ, vol. 28, 949-964.

Atkinson, R., S. M. Aschmann, W. P. L. Carter, A. M. Winer, Pitts Jr., J.N., 1982. Alkyl nitrate formation form the NO_x- air photooxidations of C_2–C_8 n-alkanes. Journal of Physical Chemistry, vol. 86, 4563–4569.

Atkinson, R., Kwok, E.S.C., Arey, J., Aschmann, S.M., 1995. Reactions of alkoxy radicals in the atmosphere. Faraday Discussions, vol. 100(100), 23-37.

Atkinson, R., 1997. Gas-phase tropospheric reactions of volatile organic compounds, 1, Alkanes and alkenes. Journal of Physical Chemistry Ref. Data, vol. 26, 215–290.

Atkinson, R., Arey, J., 1998. Atmospheric chemistry of biogenic organic compounds. Accounts of Chemical Research, vol. 31(9), 574-583.

Atkinson, R., Arey, J., 2003. Gas-phase tropospheric chemistry of biogenic volatile organic compounds: a review. Atmospheric Environment, vol. 37, S197–S219.

Atkinson, R., Baulch, D. L., Cox, R. A., Crowley, J. N., Hampson, R. F., Kerr, J. A., Rossi, M. J., and Troe, J., 2003. Summary of evaluated kinetic and photochemical data for atmospheric chemistry, IUPAC subcommittee on gas kinetic data evaluation for atmospheric chemistry, available on the subcommittee's website at http://www.iupac-kinetic.ch.cam.ac.uk.

Atlas, E., 1988. Evidence For ≥C-3 Alkyl Nitrates In Rural And Remote Atmospheres. Nature, vol. 331, 426-428.

Aunan, K., Bernsten, T.K., Myhre, G., Rypdal, K., Streets, D. G., Woo, J.H., Smith, K. R., 2009. Radiative forcing from household fuel burning in Asia. Atmospheric Environment, Vol 43 (35), 5674-5681.

Barker, J.R.; Lohr, L.L.; Shroll, R.; Reading, S., 2003. Modeling the organic nitrate yields in the reaction of alkyl peroxy radicals with nitric oxide. 2. Reaction simulations, J. Phys. Chem. A, vol. 107, 7434-7444.

Barthelmie, R.J., Pryor, S.C., 1999. A model mechanism to describe oxidation of monoterpenes leading to Secondary Organic Aerosol. Journal of Geophysical Research, vol. 104(D19), 23,657-23,699.

Becke, A. D., 1993. Density-functional thermochemistry. III. The role of exact exchange. Journal of Chemical Physics, vol. 98, 5648-5652.

Beens J, Dalluge J, Adahchour M, 2001. Moving cryogenic modulator for the comprehensive two-dimensional gas chromatography (GC x GC) of surface water contaminants, Journal of Microcolumn Separations, vol. 13(3), 134-140.

Bonn, B., Hirsikko, A., Hakola, H., Kurten, T., Laakso, L., Boy, M., Dal Maso, M., Makela, J.M., Julmala, M., 2007. Ambient sesquiterpene concentration and its link to air ion measurements. Atmospheric Chemistry and Physics, vol. 7(11), 2893-2916.

Cape, J.N., 2008. Surface ozone concentrations and ecosystem health: Past trends and a guide to future projections. Science of the Total Environment, vol. 400, 257-269.

Capouet, M., Peeters, J., Nozière, B., Müller, J.F., 2004. α-Pinene oxidation by OH: Simulations of laboratory experiments. Atmospheric Chemical Physics, vol. 4, 2285–2311.

Carey, F.A., 2008. "Organic Chemistry", McGraw-Hill Science/Engineering/Math. Print.

Carter, W.P.L., Atkinson, R., 1989. Alkyl nitrate formation from the atmospheric photooxidation of alkanes – A revised estimation method. Journal of Atmospheric Chemistry, vol. 8(2), 165-173.

Carter, W.P.L., Lurmann, F.W., 1991. Evaluation of a detailed gas-phase atmospheric reaction-mechanism using environmental chamber data. Atmospheric Environment Part A – General Topics, vol. 25(12), 2771-2806.

Chan, M.N., Chan, A.W.H., Chabra, P.S., Surratt, J.D., Seinfeld, J.H., 2009. Modeling of secondary organic aerosol yields from laboratory chamber data. Atmospheric Chemistry and Physics, vol. 9(15), 5669-5680.

Chapman, S., 1930. On ozone and atomic oxygen in the upper atmosphere. Philosophical Magazine, vol. 10(64), 369-383.

Chen, J., Griffin, R.J., 2005. Modeling Secondary Organic Aerosol Formation from Oxidation of α-pinene, β-pinene, and δ-limonene. Atmospheric Environment, vol. 39, 7731-7744.

Chen, J., Cao, K., 2005. Plant VOCs emission: a new strategy of thermotolerance. Journal of Forestry Research, vol. 16(4) 323-326.

Chun, C. K., Park, S. O., 2000. A Fixed-Grid Finite-Difference Method for Phase-Change Problems. Numerical Heat Transfer B, vol. 38, pp. 59–73.

Chuong, B., Davis, M., Edwards, M., Stevens, P.S., 2002. Measurements of the kinetics of the OH-initiated oxidation of isoprene. Journal of Geophysical Research – Atmospheres, vol. 107(D13), 4162.

Colket, M.B., Naegeli, D.W., Dryer, F.L., Glassman, I., 1974. Flame ionization detection of carbon oxides and hydrocarbon oxygenates. Environmental Science Technologies, vol. 8(1), 43-46.

Cortes, H.J., Winniford, B., Luong, J., Pursch, M., 2009.Comprehensive two dimensional gas chromatography review. Journal of Separation Science, vol. 32, 883-904.

Crutzen, P.J., 1995. Overview of Tropospheric Chemistry: Developments during he Past Quarter Century and a Look Ahead. Faraday Discussions, vol. 100, 1-21.

Dallüge, J, Beens, J, Brinkman, U.A.T., 2003. Comprehensive two-dimensional gas chromatography: a powerful and versatile analytical tool, Journal of Chromatography A, vol.1000(1-2), 69-108.

Darbeau, R.W., 2006. Nuclear Magnetic Resonance (NMR) Spectroscopy: A review and a Look at its Use as a Probative Tool in Deamination Chemistry. Applied Spectroscopy Reviews, vol. 41(4), 401-425.

Davis, J. M., Giddings, J.C., 1983. Statistical-theory of component overlap in multicomponent chromatograms. Analytical Chemistry, vol. 55(3), 418 – 424.

Dawson, J.P., Adams, P.J., Pandis, S.N., 2007. Sensitivity of ozone to summertime climate in the eastern USA: A modeling case study. Atmospheric Environment, vol. 41(7), 1494-1511.

Day, D.A., Dillon, M.B., Wooldridge, P.J., Thornton, J.A., Rosen, R.S., Wood, E.C., Cohen, R.C., 2003. On alkyl nitrates, O_3, and the "missin NO_y". Journal of Geophysical Research, vol. 108(D16), 4501.

Di Carlo, P., Brune, W.H., Martinez, M., Harder, H., Lesher, R., Ren, X., Thornberry, T., Carroll, M.A., Young, V., Shepson, P., Riemer, D., Apel, E., Campbell, C., 2004, Missing OH Reactivity in a Forest: Evidence for Unknown Reactive Biogenic VOCs. Science, vol. 304, 722-725.

Dibble, T.S., 2008. Failures and limitations of quantum chemistry for two key problems in the atmospheric chemistry of peroxy radicals. Atmospheric Environment, vol. 42, 5837-5848.

Espada, C., Grossenbacher, J., Ford, K., Couch, T., Shepson, P. B., 2005. The Production of Organic Nitrates from Various Anthropogenic Volatile Organic Compounds, Int. J. Chem. Kinet, vol. 37, 675-685.

Fahey, D., Hübler, G., Parrish, D., Williams, E., Norton, R., Ridley, B., Singh, H., Liu, S., Fehsenfeld, F., 1986. Reactive Nitrogen Species in the Troposphere: Measurements of NO, NO_2, HNO_3, Particulate Nitrate, Peroxyacetyl Nitrate (PAN), O_3, and Total Reactive Odd Nitrogen (NO_y) at Niwot Ridge, Colorado. Journal of Geophysical Research - Atmospheres, vol. 91(D9), 9781-9793.

Faloona, I., Tan, D., Brune, W., Hurst, J., Barket Jr., D., Couch, T.L., Shepson, P., Apel, E., Riemer, D., Thronberry, T., Carroll, M.A., Sillman, S., Keeler, G.J., Sagady, J., Hooper, D., Paterson, K., 2001. Nighttime observations of anomalously high levels of hydroxyl radicals above a deciduous forest canopy. Journal of Geophysical Research, vol. 106(D20), 24,315- 24,333.

Fiore, A. M., L. W. Horowitz, D. W. Purves, H. Levy II, M. J. Evans, Y. Wang, Q. Li, and R. M. Yantosca (2005), Evaluating the contribution of changes in isoprene emissions to surface ozone trends over the eastern United States, J. Geophys. Res., vol. 110, D12303, doi:10.1029/ 2004JD005485.

Forster, P., Ramaswamy, V., Artaxo, P., et al., 2007. The Fourth Assessment Report of the Intergovernmental Panel on Climate Change, edited by: Solomon, S., Qin, D., Manning, M., et al., Cambridge Univ. Press, Cambridge.

Fuentes, J. D., et al., 2000. Biogenic hydrocarbons in the atmospheric boundary layer: A review, Bulletin of the American Meteorological Society, vol. 81, 1537– 1575.

Furenes, B., Lie, B., 2006. Using event localization in finite-difference methods for phase-change problems. Numerical Heat Transfer Part B-Fundamentals, vol. 50(2), 143-155.

Fuhrer, J., Skarby, L., Ashmore, M.R., 1997. Critical levels for ozone effects on vegetation in Europe. Environmental Pollution, vol. 97, 91–106.

Fuzzi, S., Andreae, M., Huebert, B.J., Kulmula, M., Bind, T.C., Doherty, S.J., Guenther, A., Kanakidou, M., Kawamura, K., Kerminen, V.-M., Lohmann, U., Pöschl, U., Russell, L.M., 2006. Critical assessment of the current state of scientific knowledge, terminology, and research needs concerning the role of organic aerosols in the atmosphere, climate, and global change. Atmospheric Chemistry and Physics, vol. 6, 2017–2038.

Giacopelli, P., Ford, K., Espada, C., Shepson, P.B., 2005, Comparison of the measured and simulated isoprene nitrate distributions above a forest canopy. Journal of Geophysical Research, vol. 110, D01304, D01304, doi:10.1029/2004JD005123.

Goldstein, A.H., Galbally, I.E., 2007. Known and unexplored organic constituents in the Earth's atmosphere. Environmental Science and Technology, vol. 41(5), 1514-1521.

Graetzel, M., Infelta, P., 2002. The Bases of Chemical Thermodynamics, Vol. 2.

Griffin, R.J., Cocker III, D.R., Flagan, R.C., Seinfeld, J.H., 1999a. Organic aerosol formation from the oxidation of biogenic hydrocarbons. Journal of Geophysical Research, vol. 104, 3555–3567.

Griffin, R.J., Cocker III, D.R., Seinfeld, J.H., Dabdub, D., 1999b. Estimate of global atmospheric organic aerosol from oxidation of biogenic hydrocarbons. Geophysical Research Letters, vol. 26, 2721–2724.

Gronvold, F., 1978. Heat Capacity of Indium from 300 to 1000K. Journal of Thermal Analysis, vol. 13, 419-428.

Grosjean, D., Williams II, E. L., Seinfeld, J. H., 1992. Atmospheric oxidation of selected terpenes and related carbonyls: Gas-phase carbonyl products, Environmental Science & Technology., vol. 26, 1526– 1533.

Grosjean, E., Grosjean, D., 1994. Rate constants for the gas phase reactions of ozone with unsaturated aliphatic alcohols. International Journal of Chemical Kinetics, vol. 26, 1185–1191.

Grossenbacher, J.W., Couch, T., Shepson, P.B., Thronberry, T., Witmer-Rich, M., Carroll, M.A., Faloona, I., Tan, D., Brune, W., Ostling, K., Bertman, S., 2001. Measurements of isoprene nitrates above a forest canopy. Journal of Geophysical Research, vol. 106(d20), 24,429-24,438.

Guenther, A., Hewitt, C.N., Ericson, D., Fall, R., Geron, C., Graedel, T., Harley, P., Klinger, L., Lerdau, M., 1995. A global model of natural volatile organic compound emissions. Journal of Geophysical Research, vol. 100, 8873–8892.

Guenther, A., Geron, C., Pierce, T., Lamb, B., Harley, P., Fall, R., 2000. Natural emissions of non-methane volatile organic compounds; carbon monoxide, and oxides of nitrogen from North America. Atmospheric Environment, vol. 34(12-14), 2205-2230.

Guenther, A.B., Zimmerman, P.R., Harley, P.C., Monson, R.K., Fall, R., 2003. Isoprene and monoterpene emission ratevariability-model evaluations and sensitivity analyses. Journal Geophysical Research 9, 12609–12617.

Guenther, A.B., Karl, T., Harley, P., Wiedinmyer, C., Palmer, P.I., Geron, C., 2006. Estimates of global terrestrial isoprene emissions using MEGAN (Model of Emissions of Gases and Aerosols from Nature). Atmospheric Chemistry and Physics, vol. 6, 3181-3210.

Hallquist, M., Wängberg, I., Ljungström, E., 1997. Atmospheric fate of carbonyl oxidation products originating from α-pinene and 3-carene: Determination of rate of reaction with OH and NO_3 radicals, UV absorption cross sections, and vapor pressures, Environ. Sci. Technol., vol. 31, 3166–3172.

Hansen, J., Sato, M., Kharecha, P., Russell, G., Lea, D. W., and Siddall, M.: Climate change and trace gases, Philos. T. Roy. Soc. A, 365, 1925–1954, doi:10.1098/rsta.2007. 2052, 2007.

Hakola, H., Arey, J., Aschmann, S.M., Atkinson, R. 1994, Product formation from the gas-phase reactions of OH radicals and O_3 with a series of monoterpenes. Journal of Atmospheric Chemistry, vol. 18(1), 75-102

Hatakeyama, S., Izumi, K., Fukuyama, T., Akimoto, H., Washida, N., 1991. Reaction of OH with α-pinene and β-pinene in air: estimate of global CO production from the atmospheric oxidation of terpenes. Journal of Geophysical Research, vol. 96, 947–958.

Heald, C.L., Heald, C.L., Henze, D.K., Horowitz, L.W., Feddema, J., Lamarque, J.-F., Guenther, A., Hess, P.G., Vitt, F., Seinfeld, J.H., Goldstein, A.H., Fung, I., 2008. Predicted change in global secondary organic aerosol concentrations in response to future climate, emissions, and land use change. Journal of Geophysical Research, vol. 113, D05211.

Hochbruck, M., Ostermann, A., Schweitzer, J., Exponential Rosenbrock-Type Methods Siam J. Numerical Analysis, 2009 Society for Industrial and Applied Mathematics, vol. 47(1), pp. 786–803

Hoffmann, T., Odum, J.R., Bowman, F., Collins, D., Klockow, D., Flagan, R.C., Seinfeld, J.H., 1997. Formation of Organic Aerosols from the Oxidation of Biogenic Hydrocarbons. Journal of Atmospheric Chemistry, vol. 26(2), 189-222.

Hogrefe, C., Lynn, B., Civerolo, K., Ku, J.Y., Rosenthal, J., Rosenzweig, C., Goldberg, R., Gaffin, S., Knowlton, K., Kinney, P.L., 2004. Simulating changes in regional air pollution over the eastern United States due to changes in global and regional climate and emissions. Journal of Geophysical Research - Atmospheres, vol. 109(D22), D22301.

Hopkins, R.J., Reid, J.P., 2006. A Comparative Study of the Mass and Heat Transfer Dynamics of Evaporating Ethanol/Water, Methanol/Water, and 1-Propanol/Water Aerosol Droplets, J. Phys. Chem. B, vo.110, 3239-3249.

Horii, C.V., Munger, J.W., Wofsy, S.C., Zahniser, M., Nelson, D., McManus, J.B., 2006. Atmospheric reactive nitrogen concentration and flux budgets at a Northeaster U.S. forest site. Agricultural and Forest Meteorology, vol. 136, 159-174.

Horowitz, L.W., 2006. Past, present, and future concentrations of tropospheric ozone and aerosols: methodology, ozone evaluation, and sensitivity to aerosol wet removal. Journal of Geophysical Resarch - Atmospheres, vol. 111, D22211.

Horowitz, L. W., Fiore, A.M., Milly, G.P., Cohen, R.C., Perring, A., Wooldridge, P.J., Hess, P.G., Emmons, L.K., Lamarque, JF., 2007. Observational constraints on the chemistry of isoprene nitrates over the eastern United States. Journal of Geophysical Research, vol. 12, D12S08.

Howard, J.N., King, J.I.F., Gast, P.R., 1960. Thermal Radiation, Handbook of Geophysics, Chap. 16, Macmillan, New York. Print.

Ianni, J.C. Kintecus Manual, 2009. http://kintecus.org

Iinuma, Y., Böge, O., Gnauk, T., Herrmann, H., 2004. Aerosol-chamber study of the a-pinene/O_3 reaction: influence of particle acidity on aerosol yields and products. Atmospheric Environment, vol. 38, 761-773.

IPCC, 2007. The Physical Science Basis. Contribution of Working Group I to the Fourth Assessment Report of the Intergovernmental Panel on Climate Change. Cambridge University Press, New York, USA. Available at: http://www.ipcc.ch.

Isaksen, I.S.A., and O. Hov. 1987. Calculation of trends in the tropospheric concentration of ozone, hydroxyl, carbon monoxide, methane, and nitrogen oxides. Tellus vol. 39B, 271-285.

Ito, A., Sillman, S., Penner, J.E., 2009. Global chemical transport model study of ozone response to changes in chemical kinetics and biogenic volatile organic compounds emissions due to increasing temperatures: sensitivities to isoprene nitrate chemistry and grid resolution, vol. 114, D09301.

Jaffe, D., Price, H., Parrish, H., 2003. Increasing background ozone during spring on the west coast of North America. Geophysical Research Letters, vol. 30(12), 1613.

Jaffe, D., Ray, J., 2007. Increase in surface ozone at rural sites in the western US. Atmospheric Environment , vol. 41 (26), 5452–5463.

Jang, M., Kamens, R.M., 1998. A thermodynamic approach for modeling partitioning of semivolatile organic compounds on atmospheric particulate matter: Humidity effects. Environmental Science & Technology, vol. 32(9), 1237-1243.

Jenkin, M., Saunders, S.M., Pilling, M.J., 1997. The tropospheric degradation of volatile organic compounds: a protocol for mechanism development. Atmospheric Environment, vol. 31(1), 81-104.

Joos, F., Spahni R., 2008. Rates of change in natural and anthropogenic radiative forcing over the past 20000 years. Proceedings of the National Academy of Sciences USA, vol. 105(5), 1425–1430.

Kalabokas, P., Bartzis, J. G., Bomboi, T., Ciccioli, P., Cieslik, S., Dlugi, R., Foster, P., Kotzias, D., and Steinbrecher, R., 1997. Ambient atmospheric trace gas concentrations and meteorological parameters during the first BEMA measuring campaign on May 1994 at Castelporziano, Italy, Atmos. Environ., vol. 31, Supplement 1, 67-77.

Kanakidou, M., Tsigaridis, K., Dentener, F.J., Crutzen, P., 2000. Human-activity enhanced formation of organic aerosols by biogenic hydrocarbon oxidation. Journal of Geophysical Research, vol. 105, 9243–9254.

Karnosky D.F., Skelly JM, Percy KE, Chappelka, A.H., 2007. Perspectives regarding 50 years of research on effects of tropospheric ozone air pollution on US forests. Environmental Pollution, vol.147, 489–506.

Kavouras, I.G., Mihalopoulos, N., Stephanou, E.G., 1998. Formation of atmospheric particles from organic acids produced by forests. Nature, vol. 395(6703), 683-686.

Kerminen, V.-M., Lihavainen, H., Komppula, M., Viisanen, Y., Kulmala, M., 2005. Direct observational evidence linking atmospheric aerosol formation and cloud droplet activation. Geophysical Research Letters, vol. 32, L14803.

Kesselmeier, J., Schäfer, L., Ciccioli, P., Brancaleoni, E., Cecinato, A., Frattoni,M., Foster, P., Jacob, V., Denis, J., Fugit, J.-L., Dutaur, L., and Torres, L., 1996. Emission of monoterpenes and isoprene from a Mediterranean oak species Quercus ilex L. measured within the BEMA (Biogenic Emissions in the Mediterranean Area) project, Atmos. Environ. 30, 1841–1850.

Kesselmeier, J., Staudt, M.,1999. Biogenic Volatile Organic Compounds (VOC): An Overview on Emission, Physiology and Ecology, Journal of Atmospheric Chemistry vol 33, 23-88.

Kesselmeier, J., Kuhn, U., Wolf, A., Andreae, M. O., Ciccioli, P. Brancaleoni, E., Frattoni, M., Guenther, A., Greenberg, J., Vasconcellos, P. D., de Oliva, T., Tavares, T., Artaxo, P., 2000, Atmos.Environ., vol. 34, 4063–4072

Kley, D., Kleinmann, M., Sanderman, H., Krupa, S., 1999. Photochemical oxidants: State of the science. Environ Pollution, vol. 100, 19–142.

Kovacevic, I., Poredos, A., Sarler, B., 2003. Solving the Stefan Problem with the Radial Basis Function Collocation Method, Numer. Heat Transfer B, vol. 44, 575–599.

Kwok, E.S.C., Atkinson, R., 1995. Estimation of hydroxyl radical reaction rate constants for gas-phase organic compounds using a structure-reactivity relationship: an update. Atmospheric Environment, vol. 29(14), 1685-1695.

Kwok, E.S.C., Atkinson, R., Arey, J., 1995. Observation of hydroxycarbonyls from the OH radical-initiated reaction of isoprene. Environmental Science and Technology, vol. 29, 2467–2469.

Lamarque, J.F., Hess, P., Emmons, L., Buja, L., Washington, W., Granier, C., 2005. Tropospheric ozone evolution between 1890 and 1990. Journal of Geophysical Research – Atmospheres, vol. 110(D8), D08304.

Larsen, B.R., Di Bella, D., Glasius, M., Winterhalter, R., Jensen, N.R., Hjorth, J., 2001. Gas-phase OH oxidation of monoterpenes: gaseous and particulate products. Journal of Atmospheric Chemistry, vol. 38, 231–276.

Lathiere, J., Hauglustaine, D.A., Friend, A., Noblet-Ducoudre, N.D., Viovy, N., Folberth, G., 2005. Impact of climate variability and land use changes on global biogenic volatile organic compound emissions. Atmospheric Chemistry and Physics - Discussion 5, 10613–10656.

Lee, A.L., Lewis, A., Bartle, K.D., McQuaid, J.B., Marriott, P.J., 2000. A Comparison of Modulating Interface Technologies in Comprehensive Two-Dimensional Gas Chromatography (GCxGC), J. Microcolumn Separations, Vol. 12(4), 187-193.

Lei, W., Zhang, R., McGivern, W.S., Dereckskei-Kovacs, A., North, S.W., 2001. Theoretical Study of OH-O2-Isoprene Peroxy Radicals. Journal of Physical Chemistry A, vol. 105, 471-477.

Li, S., Matthews, J., Sinha, A., 2008. Atmospheric hydroxyl radical production from electronically excited NO_2 and H_2O. Science 319, 1657–1660.

Liao, H., Zhang, Y., Chen, W.T., 2009. Effect of chemistry-aerosol-climate coupling on predictions of future climate and future levels of tropospheric ozone and aerosols. Journal of Geophysical Research - Atmospheres, vol. 114, D10306.

Libardoni, M., Waite, J.H., Sacks, R., 2005. Electrically Heated, Air-Cooled Thermal Modulator and at-Column Heating for Comprehensive Two-Dimensional Gas Chromatography, Analytical Chemistry, vol. 77, 2786-2794

Librando, V., Tringali, G., 2005. Atmospheric fate of OH initiated oxidation of terpenes. Reaction mechanism of α-pinene degradation and secondary organic aerosol formation. Journal of Environmental Management, vol. 75, 275-282.

Lihavainen, H., Kerminen, V.-M., Komppula, M., Hatakka, J., Aaltonen, V., Kulmala, M., Viisanen, Y., 2003. Production of ''potential'' cloud condensation nuclei

associated with atmospheric new particle formation in northern Finland. Journal of Geophysical Research, vol. 108, 4782.

Lin, C.Y.C., Jacob, D.J., Munger, J.W., Fiore, A.M., 2000. Increasing background ozone in surface air over the United States. Geophysical Research Letters 27 (21), 3456–3468.

Lui, Z., Phillips, J.B., 1991. Comprehensive two-dimensional gas chromatography using an on-column thermal modulator interface. Journal of Chromatography Science, vol. 29, 227–31.

Lockwood, A., 2008. Fate or Organic Nitrates - Ph.D. dissertation. Purdue University, West Lafayette, IN, 2008. Print.

Ma, Y., Luciani, T., Porter, R.A., Russell, A.T., Johnson, D., Marston, G., 2007. Organic acid formation in the gas-phase ozonolysis of α-pinene, Physical Chemistry Chemical Physics, vol. 9, 5084-5097.

Ma, Y., Russell, A.T., Marston, G., 2008. Mechanisms for the formation of secondary organic aerosol components from the gas-phase ozonolysis of α-pinene. Physical Chemistry Chemical Physics, vo.10, 4294-4312.

Ma, Y., Porter, R.A., Chappell, D., Russell, A.T., Marson, G., 2009. Mechanisms for the formation of organic acids in the gas-phase ozonolysis of 3-carene. Physical Chemistry Chemical Physics, vol. 11, 4184-4197.

Marriott, P.J., 2002. "Orthogonal GC-GC". In Multidimensional Gas Chromatography. L. Mondello, A.C. Lewis, and K.D. Bartle, Eds. John Wiley & Sons, Ltd., Chichester, U.K. Print.

Matsunaga, A., Docherty, K.S., Lim, Y.B., Ziemann, P.J., 2009. Composition and yields of secondary organic aerosol formed from OH radical-initiated reactions of linear alkenes in the presence of NO_x: Modeling and measurements, vol. 43:1349-1357.

Matsunaga, A., Ziemann, P.J., 2009. Yields of #-Hydroxynitrates and Dihydroxynitrates in Aerosol Formed from OH Radical-Initiated Reactions of Linear Alkenes in the Presence of NO. Journal of Physical Chemistry A, vol. 113(3), 599-606.

Mauzerall, D.L., Wang, X., 2001. Protecting agricultural crops from the effects of tropospheric ozone exposure: reconciling science and standard setting in the United States, Europe and Asia. Annual Review of Energy and the Environment, vol. 26, 237–68.

Mei, S.G., Wang, T., Yin, F., He, J.F., Ruan, C., Wu, L.X., Zhao, T., 2008. Study on the Induced Current Measurement in Bridgewire EED. Microwave and Optical Technology Letters, vol. 501(11), 2833-2835.

Mickley, L.J., Jacob, D.J., Rind, D., 2001. Uncertainty in preindustrial abundance of tropospheric ozone: Implications for radiative forcing calculations. Journal of Geophysical Research – Atmospheres, vol. 106(D4), 3389-3399.

Mohler, R., Prazen, B.J., Synovec, R.E., 2006. Total-transfer, valve-based comprehensive two-dimensional gas chromatography, Analytica Chimica Acta, vol. 555, 68-74.

Mondello, L., Tranchida, P.Q., Dugo, P., Dugo, G., 2008. Comprehensive two-dimensional gas chromatography-mass spectrometry: A review, Mass Spectrometry Reviews, vol. 27(2), 101-124.

Monks, P.S., 2005. Gas-phase radical chemistry in the troposphere. Chemical Society Reviews, vol. 34, 376–395.

Monks, P.S., Granier, C., Fuzzi, S., Stohl, A., Williams, M.L., Akimoto, H., Amann, M., Baklanov, A., Baltensperger, U., Bey, I., Blanke, N., Blake, R.S., Carslaw, K., Cooper, O.R., Dentener, F., Fowler, D., Fragkou, E., Frost, G.J., Generoso, S., Ginoux, P., Grewe, V., Guenther, A., Hansson, H.C., Henne, S., Hjorth, J., Hofzumahaus, A., Huntrieser, H., Isaksen, I.S.A., Jenkin, M.E., Kaiser, J., Kanakidou, M., Klimont, Z., Kulmala, M., Laj, P., Lawrence, M.G., Lee, J.D., Liousse, C., Maione, M., McFiggans, G., Metzger, A., Mieville, A., Moussiopoulos, N., Orlando, J.J., O'Dowd, C.D., Palmer, P.I., Parrish, D.D., Petzold, A., Platt, U., Pöschl, U., Prévôt, A.S.H., Reeves, C.E., Reimann, S., Rudich, Y., Sellegri, K., Steinbrecher, R., Simpson, D., ten Brink, H., Theloke, J., van der Werf, G.R., Vautard, R., Vestreng, V., Vlachokostas, Ch., von Glasow, R., 2009. Atmospheric composition change – global and regional air quality. Atmospheric Environment, vol. 43, 5268-5350.

Muthuramu, K., Shepson, P., & O'Brien, J., 1993, Preparation, analysis, and atmospheric production of multifunctional organic nitrates. Environ. Sci. Technol., vol. 27 1117-1124.

Neyer, B.T., Bridgewire heating, Proceedings of the Sixteenth Symposium on Explosives and Pyrotechnics, Essington, PA, April 1997.

Nichols, P. L., Magnusson, A. B., Ingham, J. D., 1953. Synthesis of nitric esters by the addition of nitric acid o the ethylene oxide ring. Journal of Am. Chem. Soc., vol. 75 4255-4258.

Nozière, B., Barnes, I., Becker, K.H., 1999. Product study and mechanisms of the reactions of α-pinene and pinonaldehyde with OH radicals. Journal of Geophysical Research, vol. 104, 23,645–23,656.

O'Brien, J.M., Czuba, E., Hastie, D.R., Francisco, J.S., Shepson, P.B., 1998. Determination of the hydroxy nitrate yields from the reaction of C_2–C_6 alkenes with OH in the presence of NO. Journal of Physical Chemistry A, vol. 102, 8903–8908.

Olsen, M.A., Schoeberl, M.R., Douglass, A.R., 2004. Stratosphere-troposphere exchange of mass and ozone. Journal of Geophysical Research, vol. 198, D24114.

Olsen, M.A., Schoeberl, M.R., Nielsen, J.E., 2007. Response of stratosphere circulation and stratosphere-troposphere exchange to changing sea surface. Journal of Geophysical Research - Atmospheres, vol. 112(D16), D16104.

Ong, R.C.Y., Marriott, P.J., 2002. A Review of Basic Concepts in Comprehensive Two-Dimensional Gas Chromatography, Journal of Chromatographic Science, vol. 40, 276-291.

Orlando, J.J., Nozière, B., Tyndall, G.S., Orzechowska, G.E., Paulson, S.E., Rudich, Y., 2000. Product studies of OH- and ozone-initiated oxidation of some monoterpenes. Journal of Geophysical Research, vol. 105, 11561–11572.

Owen, S., Boissard, C., Street, R. A., Duckham, S. C., Csiky, O. and Hewitt, N. C., 1997. Screening of 18 Mediterranean plant species for volatile organic compound emissions. Atmos. Environ., vol. 31 Supplement 1, 101-117.

Panic, O., Gorecki, T., 2006. Comprehensive two-dimensional gas chromatography (GCxGC) in environmental analysis and monitoring, Anal Bioanalytical Chemistry, vol. 386, 1013-1023

Pankow, J.F., 1994. An absorption model of the gas/aerosol partitioning involved in the formation of secondary organic aerosol. Atmospheric Environment, vol. 28, 189–193.

Patchen, A.K., Pennino, M.J., Kiep, A.C., Elrod, M.J., 2007. Direct kinetics study of the product-forming channels of the reaction of isoprene-derived hydroxyperoxy radicals with NO. International Journal of Chemical Kinetics, vol. 39, 353–361.

Pathak, R.K., Presto, A.A., Lane, T.E., Stanier, C.O., Donahue, N.M., Pandis., S.N., 2007. Ozonolysis of α-pinene: parameterization of secondary organic aerosol mass fraction. Atmospheric Chemistry and Physics, vol. 7, 3811–3821.

Paulson, S.E., Chung, M., Sen, A.D., Orzechowska, G., 1998. Measurement of OH radical formation from the reaction of ozone with several biogenic alkenes. Journal of Geophysical Research, vol. 103, 25533–25539.

Paulson, S.E., Seinfeld, J.H., 1992. Development and Evaluation of a Photooxidation Mechanism for Isoprene. Journal of Geophysical Research – Atmospheres, vol. 97(D18), 20,703-20715.

Peeters, J., Vereecken, L., Fantechi, G., 2001. The detailed mechanism of the OH initiated atmospheric oxidation of α-pinene: a theoretical study. Physical Chemistry Chemical Physics, vol. 3, 5489–5504.

Perdew, J. P. et al., 1996. Generalized gradient approximation for the exchange-correlation hole of a many-electron system. Phys. Rev. B, vol. 54, 16533-16539.

Philips, J.B., Beens, J., 1999. Comprehensive two-dimensional gas chromatography: a hyphenated method with strong coupling between the two dimensions. Journal of Chromatography A., vol. 856, 331-347.

Pinho, P.G., Pio, C.A., Jenkin, M.E., 2005. Evaluation of isoprene degradation in the detailed tropospheric chemical mechanism, MCM v3, using environmental chamber data. Atmospheric Environment, vol. 39, 1303–1322.

Pinho, P.G., Pio, C.A., Carter, W.P.L., Jenkin, M.E., 2007. Evaluation of α- and β-pinene degradation in the detailed tropospheric chemistry mechanism, MCM v3.1, using environmental chamber data. Journal of Atmospheric Chemistry, vol. 57, 171-202.

Pitts, Jr., J.N., Sanhueza, E.S., Atkinson, R., Cater, W.P.L., Winter, A.M., Harris, G.W., Plum, C.N., 1984. An investigation of the dark formation of nitrous acid in environmental chambers. Int. J. Chem. Kinet., vol. 16, 919.

Poliak, M., Fialkov, Amirav, A., Pulsed flow modulation two-dimensional comprehensive gas chromatography–tandem mass spectrometry with supersonic molecular beams, Journal of Chromatography A., Vol. 1210, Issue 1, 108-114, 2008

Prinn, R., Cunnold, D., Simmonds, P., Alyea, F., Boldi, R., Crawford, A., Fraser, P., Gutzler, D., Hartley, D., Rosen, R., Rasmussen, R., 1992. Global average concentration and trend for hydroxyl radicals deduced from ale gauge tricholoethane (methyl chloroform) data for 1978-1990. Journal of Geophysical Research – Atmospheres, vol. 97(D2), 2445-2461.

Racherla, P.N., Adams, P.J., 2006. Sensitivity of global tropospheric ozone and fine particulate matter concentrations to climate change. Journal of Geophysical Research – Atmospheres, vol. 111(D24), D24103.

Reissell, A., Harry, Ch., Aschmann, S.H., Atkinson, R., Arey, J., 1999. Formation of acetone from the OH radical- and O_3-initiated reactions of a series of monoterpenes. Journal of Geophysical Research, vol. 104(13), 868–13,879.

Review of the National Ambient Air Quality Standards for Ozone; U.S. Environmental Protection Agency; Office of Air Quality Planning and Standards: Research Triangle Park, NC, 2007.

Rinne, J., Hakola, H., Laurila, T., Rannik, U., 2000. Canopy scale monoterpene emissions of Pinus sylvestris dominated forests. Atmospheric Environment, vol. 34(7), 1099-1107.

Rocha, S.M., Coelho, E., Zrostlikova, J., Delgadillo, I., Coimbra, M.A., 2007. Comprehensive two-dimensional gas chromatography with time-of-flight mass spectrometry of monoterpenoids as a powerful tool for grape origin traceability. Journal of Chromatography A., vol. 1161, 292-299.

Ruppert, L., Becker, K.H., Nozière, B., Spittler, M, 1999. Development of monoterpene oxidation mechanisms: results from laboratory and smog chamber studies. Borrell, P.M., Borrell, P. (eds.) Transport and Chemical Transformation in the Troposphere. Proceedings of the EUROTRAC-2 Symposium '98, 63–68.

Ryan, D., Morrison, P., Marriott, P., 2005. Orthogonality considerations in comprehensive two-dimensional gas chromatography. Journal of Chromatography A, vol. 1071(1-2), 47-53.

Sato, K., Tanimoto, H., Imamura, T., 2005. Negative Ion Chemical Ionization Mass Spectra of C_1-C_6 n-Alkyl Nitrates. The Chemical Society of Japan Chemistry Letters, vol. 34(8), 1200-1021.

Saunders, S.M., Jenkin, M.E., Derwent, R.G., Pilling, M.J., 2003. Protocol for the development of the Master Chemical Mechanism, MCM v3, part A: tropospheric degradation of non-aromatic volatile organic compounds. Atmospheric Chemistry and Physics, vol. 3, 161–180.

Seeley, J.V., Micyus, N.J., McCurry, J.D, 2006. Comprehensive two-dimensional gas chromatography with a simple fluidic modulator. American Laboratory, vol. 38(9), 24-26.

Seinfeld, J.H., Pankow, J.F., 2003. Organic atmospheric particulate matter. Annual Review of Physical Chemistry, vol. 54, 121–140.

Seufert, G., Bartzis, J., Bomboi, T., Ciccioli, P., Cieslik, S., Dlugi, R., Foster, P., Hewitt, C. N., Kesselmeier, J., Kotzias, D., Lenz, R., Manes, F., Perez Pastor, R., Steinbrecher, R. Torres, L., Valentin, R. and Versino, B., 1997. An overview of the Castelporziano experiments. Atmos. Environ., vol.31 Supplement 1, 5-17.

Shepson, P. "Organic Nitrates". Volatile Organic Compounds in the Atmosphere. (Hardcover) Wiley-Blackwell; 1 edition. 2007. 269-289. Print.

Shepson, P. B., Mackay, E., Muthuramu, K., 1996. Henry's law constants and removal processes for several atmospheric β-hydroxy alkyl nitrates, Enivronmental Science & Technolology, vol. 30, 3618– 3623.

Shindell, D.T., Faluvegi, G., Bell, N., 2003. Preindustrial-to-present-day radiative forcing by tropospheric ozone from improved simulations with GISS chemistry-climate GCM. Atmospheric Chemistry and Physics, vol. 3(5), 1675-1702.

Singh, H.B., O'Hara, D., Herlth, D., Sachse, W., Blake, D.R., Bradshaw, J.D., Kanakidou, M., Crutzen, P.J., 1994. Acetone in the atmosphere: distribution, sources, and sinks. Journal of Geophysical Research 99, 1805–1819.

Singh, H., Chen, Y., Tabazadeh, A., Fukui, Y., Bey, I., Yantosca, R., Jacob, D., Arnold, F., Wohlfrom, K., Atlas, E., Flocke, F., Blake, D., Blake, N., Heikes, B., Snow, J., Talbot, R., Gregory, G., Sachse, G., Vay, S., Kondo, Y., 2000. Distribution and fate of selected oxygenated organic species in the troposphere and lower stratosphere over the Atlantic. Journal of Geophysical Research, vol. 105, 3795–3805.

Sprengnether, M., Demerjian, K.L., Donahue, N.M., Anderson, J.G., 2002. Product analysis of the OH oxidation of isoprene and 1,3-butadiene in the presence of NO. Journal of Geophysical Research, vol. 107, 4268.

Steinbrecher, R., Smiatek, G., Köble, R., Seufert, Günther, Theloke, Jochen, Hauff, K., Ciccioli, P., Vautard, R., Curci, G., 2009. Intra- and inter-annual variability of VOC emissions from natural and semi-natural vegetation in Europe and neighboring countries. Atmospheric Environment, vol. 43(7), 1380-1391.

Steiner, A. L., Tonse, S., Cohen, R.C., Goldstein, A.H., Harley, R.A., 2006. Influence of future climate and emissions on regional air quality in California. Journal of Geophysical Research – Atmospheres, vol. 111(D18), D18303.

Stevenson, D. S., Johnson, C. E., Collins, W. J., Derwent, R. G., Edwards, J. M., 2000. Future tropospheric ozone radiative forcing and methane turnover - The impact of climate change. Geophysical Research Letters, vol. 27, 2073–2076.

Stevenson, D.S., Dentener, F.J., Schultz, M.G., Ellingsen, K., van Noije, T.P.C., Wild, O., Zeng, G., Amann, M., Atherton, C.S., Bell, N., Bergmann, D.J., Bey, I., Butler, T., Cofala, J., Collins, W.J., Derwent, R.G., Doherty, R.M., Drevet, J., Eskes, H.J., Fiore, A.M., Gauss, M., Hauglustaine, D.A., Horowitz, L.W., Isaksen, I.S.A., Krol, M.C., Lamarque, J.F., Lawrence, M.G., Montanaro, V., Müller, J.F., Pitari, G., Prather, M.J., Pyle, J.A., Rast, S., Rodriguez, J.M., Sanderson, M.G., Savage, N.H., Shindell, D.T., Strahan, S.E., Sudo, K., Szopa, S., 2006. Multimodal ensemble simulations of present-day and near-future tropospheric ozone. Journal of Geophysical Research, vol. 111, D08301.

Tillmann, R., Saathoff, H., Brauers, T., Kiendler-Scharr, A., Mentel, T., 2009, Temperature dependence of the rate coefficient for the α-pinene reaction with ozone in the range between 243K and 303K, Physical Chemistry Chemical Physics, vol. 11, 2323-2328

Trainer, M., Williams, E.J., Parrish, D.D., Buhr, M.P., Allwine, E.J., Westberg, H., Fehsenfeld, F.C., Liu., S.C., 1987. Models and observations of the impact of natural hydrocarbons on rural ozone, Nature, vol. 329, 705– 707.

Trainer, M., Parrish, M., Buhr, M.P., Norton, R.B., Fehsenfeld, F.C, Anlauf, K.G., Bottenheim, J.W., Tang, Y.Z., Wiebe, H.A., Roberts, J.M., Tanner, R.L., Newman, L., Bowersox, V.C., Meagher, J.F., Olszyna, K.J., Rodgers, M.O., Wang, T., Berresheim, H., Demerjian, K.L., Roychowdhury, U.K., 1993. Correlation of Ozone with NO_y in Photochemically Aged Air. Journal of Geophysical Research − Atmospheres, vol. 98(D2), 2917-2925.

Treves, K., Sharinga, L., Rudich, Y., 2000. Henry's law constants of some beta-, gamma-, and delta-hydroxy alkyl nitrates of atmospheric interest. Environmental Science & Technology, vol. 34(7), 1197-1203.

Tsigaridis, K., Krol, M., Dentener, F.J., Balkanski, Y., Lathie` re, J., Metzger, S., Hauglustaine, D.A., Kanakidou, M., 2006. Change in global aerosol composition since preindustrial times. Atmospheric Chemistry and Physics, vol. 6, 5143–5162.

Tsigaridis, K., Kanakidou, M., 2007. Secondary organic aerosol importance in future atmosphere. Atmospheric Environment, vol. 41, 4682–4692.

Tuazon, E.C., Atkinson, R., 1990. A product study of the gas-phase reaction of isoprene with the OH radical in the presence of NO_x. International Journal of Chemical Kinetics, vol. 22, 1221–1235.

Tuazon, E.C., Atkinson, R., 1990b. A product study of the gas phase reaction of methacrolein with the OH radical in the presence of NOx. International Journal of Chemical Kinetics, vol. 22, 591–602.

van den Bergh, V., Vanhees, I., De Boer, R., Compernolle, R., Vinckier, C., 2000. Identification of the oxidation products of the reaction between α-pinene and hydroxyl radicals by gas and high-performance liquid chromatography with mass spectrometric detection. Journal of Chromatography A, vol. 896, 135– 148.

Vaughan, S.,Canosa-Mas ,C.E., Pfrang, C., Shallcross, D.E., Watson, L., Wayne, R.P., 2006. Kinetic studies of reactions of the nitrate radical (NO_3) with peroxy radicals (RO_2): an indirect source of OH at night? Physical Chemistry Chemical Physics, vol. 8, 3749-3760.

Vereecken, L., Peeters, J., 2000. Theoretical study of the formation of acetone in the OH-initiated atmospheric oxidation of α-pinene. Journal of Physical Chemistry A, vol. 104, 11140–11146.

Vereecken, L., Peeters, J., 2004. Nontraditional (per)oxy ring-closure paths in the atmospheric oxidation of isoprene and monoterpenes. The Journal of Physical Chemistry A, vol. 108, 5197–5204.

Vereecken, L., Muller, J.F., Peeters, J., 2007. Low-volatility poly-oxygenates in the OH-initiated atmospheric oxidation of α-pinene: impact of non-traditional peroxyl radical chemistry, Physical Chemistry Chemical Physics, vol. 9, 5241-5248

Vinckier, C., F. Compernolle, A. M. Saleh, N. Van Hoof, and I. Van Hees, 1998. Product yields of the α-pinene reaction with hydroxyl radicals and the implication on the global emission of trace compounds in the atmosphere. Fresenius Environmental Bulletin, vol. 7, 361– 368.

Vingarzan, R., 2004, A review of Surface Ozone Background Levels and Trends, Atmospheric Environment, vol. 38(21), 3431-3442

Voller, V.R., Fast implicit finite-difference method for the analysis of phase change problems. Numerical Heat Transfer, Part B, vol. 17, 155-169.

von Kuhlmann, R., M. G. Lawrence, U. Poschl, and P. J. Crutzen (2004), Sensitivities in global scale modeling of isoprene, Atmos. Chem. Phys., vol. 4, 1 –17.

Wang, F. C. Y., 2008. New valve switching modulator for comprehensive two-dimensional gas chromatography, Journal of Chromatography A., vol. 1188(2), 274-280.

Wängberg, I., Barnes, I., Becker, K.H., 1997. Product and Mechanistic Study of the Reaction of NO_3 Radicals with α-pinene. Environmental Science and Technology, vol. 31, 2130–2135.

Wayne, R. P., Barnes, I., Biggs, P., Burrows, J.P., Canosa-Mas, C.E., Hjorth, J., Le Bras, G., Moortgat, G.K., Perner, D., Poulet, G., Restelli, G., Sidebottom, H. 1991. The Nitrate Radical: Physics, Chemistry, and the Atmosphere, Atmospheric Environment, vol. 25A(1), 1-203.

Weinhold, B., 2008. Ozone Nation: EPA Standard Panned by the People, Environ Health Perspect., vol. 116(7), A302–A305.

Wennberg, P. O., Dabdub, D., 2008 . Rethinking Ozone Production, Science, vol. 319, 1624-1625.

Williams, S., Knighton, W.B., Midey, A.J., Viggiano, A.A., Irle, S., Wang, Q.F., Morokuma, K., 2004. Oxidation of alkyl ions, CnH2n+1+ (n=1-5), in reactions with O-2 and O-2 in the gas phase. Journal of Physical Chemistry A., vol. 108(11), 1980-1989.

Winterhalter, R., Van Dingenen, R., Larsen, B. R., Jensen, N. R., and Hjorth, J., 2003. LC-MS analysis of aerosol particles from the oxidation of α-pinene by ozone and OH-radicals, Atmos. Chem. Phys. Discuss., vol. 3, 1–39.

Wisthaler, A. Jensenb, N.R., Winterhalterb, R., Lindingera, W., Hjorthb, J., 2001. Measurements of acetone and other gas phase product yields from the OH-initiated

oxidation of terpenes by proton-transfer-reaction mass spectrometry (PTR-MS), Atmospheric Environment, vol.35, 6181–6191.

Wohlfrom, K.-H., Hauler, T., Arnold, F., Singh, H., 1999. Acetone in the free troposphere and the lower stratosphere: aircraft-based CIMS and GC measurements over the North Atlantic and a first comparison. Geophysical Research Letters, vol. 26, 2849–2852.

Worton, D.R., Mills, G.P., Oram, D.E., Sturges, W.T., 2008. Gas chromatography negative ion chemical ionization mass spectrometry: Application to the detection of alkyl nitrates and halocarbons in the atmosphere. Journal of Chromatography A, vol. 1201, 112-119.

Wu, S., Mickley, L. J., Leibensperger, E. M., Jacob, D. J., Rind, D., Streets, D. G., 2008. Effects of 2000–2050 global change on ozone air quality in the United States. Journal of Geophysical Research - Atmospheres, vol. 113(D6), D06302.

Xia, A.G., Michelangeli, D.V., Makar, P.A., 2008. Box model studies of the secondary organic aerosol formation under different HC/NO_x conditions using the subset of the Master Chemical Mechanism for α-pinene oxidation. Journal of Geophysical Research, vol. 113, D10301.

Yu, J., Flagan, R.C., Seinfeld, J. H., 1998. Identification of Products Containing — COOH, —OH, and—C=O in Atmospheric Oxidation of Hydrocarbons, Environ. Sci. Technolology, vol. 32, 2357–2370.

Yu, J., Cocker III, D.R., Griffin, R.J., Flagan, R.C., Seinfeld, J.H., 1999. Gas-Phase Ozone Oxidation of Monoterpenes: Gaseous and Particulate Products. Journal of Atmospheric Chemistry, vol. 34, 207-258.

Yu, Y., Ezell, M.J., Zelenyuk, A., Imre, D., Alexander, L., Ortega, J., D'Anna, B., Harmon, C.W., Johnson, S.N., Finalyson-Pitts B.J., 2008. Photooxidation of α-pinene at high relative humidity in the presence of increasing concentrations of NOx. Atmospheric Environment, vol. 42, 5044-5060.

Zhang, S.H., Shaw, M., Seinfeld, J.H., Flagan, R.C, 1992. Photochemical Aerosol Formation from α-Pinene and β-Pinene. Journal of Geophysical Research, vol. 91(D18), 20717-20729.

Zhang, D., Lei, W., Zhang, R., 2002. Mechanism of OH formation from ozonolysis of isoprene: kinetics and product yields. Chemical Physics Letters, vol. 358, 171–179.

Zhang, J., Dransfield, Y., Donahue, N.M., 2004. On the Mechanism for Nitrate Formation via the Peroxy Radical + NO Reaction. Journal of Physical Chemistry A, vol. 108, 9082-9095.

Zhang, L., Jacob, D.J., Boersma, K.F., 2008. Transpacific transport of ozone pollution and the effect of recent Asian emission increases on air quality in North America: an integrated analysis using satellite, aircraft, ozonesonde, and surface observations. Atmospheric Chemistry and Physics, vol. 8(20), 6117-6136.

Zhang, Q., Jimenez, J.L., Canagaratna, M.R., Allan, J.D., Coe, H., Ulbrich, I., Alfarra, M.R., Takami, A., Middlebrook, A.M., Suni, Y.L., Dzepina, K., Dunlea, E., Docherty, K., DeCarlo, P.F., Salcedo, D., Onasch, T., Jayne, J., Miyoshi, T., Shimono, A., Hatakeyama, S., Takegawa, N., Kondo, Y., Schneider, J., Drewnick, F., Borrmann, S., Weimer, S., Demerjian, K., Williams, P., Bower, K., Bahreini, R., Cottrell, L., Griffin, R.J., Rautiainen, J., Sun, J.Y., Zhang, Y.M., Worsnop, D.R., 2007. Ubiquity and dominance of oxygenated species in organic aerosols in anthropogenically- influenced Northern Hemisphere mid latitudes. Geophysical Research Letters, vol. 34, L13801.

Zivkovic, B., Fujii, I., 2000. An analysis of isothermal phase change of phase change material within rectangular and cylindrical containers. Solar Energy, vol. 70(1), 51-61.